

High-Mobility TCO-Based Contacting Schemes for c-Si Solar Cells

Han, C.

DOI

[10.4233/uuid:d6f35adf-486e-453a-9ae9-679a81105bed](https://doi.org/10.4233/uuid:d6f35adf-486e-453a-9ae9-679a81105bed)

Publication date

2022

Document Version

Final published version

Citation (APA)

Han, C. (2022). *High-Mobility TCO-Based Contacting Schemes for c-Si Solar Cells*. [Dissertation (TU Delft), Delft University of Technology]. <https://doi.org/10.4233/uuid:d6f35adf-486e-453a-9ae9-679a81105bed>

Important note

To cite this publication, please use the final published version (if applicable).
Please check the document version above.

Copyright

Other than for strictly personal use, it is not permitted to download, forward or distribute the text or part of it, without the consent of the author(s) and/or copyright holder(s), unless the work is under an open content license such as Creative Commons.

Takedown policy

Please contact us and provide details if you believe this document breaches copyrights.
We will remove access to the work immediately and investigate your claim.

High-Mobility TCO-Based Contacting Schemes for c-Si Solar Cells

CAN HAN

韩 灿

High-Mobility TCO-Based Contacting Schemes for c-Si Solar Cells

Proefschrift

ter verkrijging van de graad van doctor
aan de Technische Universiteit Delft,
op gezag van de Rector Magnificus Prof. dr. ir. T.H.J.J. van der Hagen,
voorzitter van het College voor Promoties,
in het openbaar te verdedigen op
maandag 9 mei om 10:00 uur

door

Can HAN

Master of Engineering in Nonferrous Metals Metallurgy, Central South University, China
geboren te Zhoukou, China

Dit proefschrift is goedgekeurd door de promotoren.

Samenstelling promotiecommissie bestaat uit:

Rector Magnificus	voorzitter
Prof.dr. M. Zeman	Technische Universiteit Delft, promotor
Prof.dr. X.D. Zhang	Nankai University, China, promotor
Prof.dr.ir. O. Isabella	Technische Universiteit Delft, promotor

Onafhankelijke leden:

Prof.dr. I. Gordon	imec, Genk, Belgium / Technische Universiteit Delft
Prof.dr. E.C. Garnett	AMOLF Institute, Amsterdam
Dr. M. Bivour	Fraunhofer Institute for Solar Energy Systems, Freiburg, Germany
Prof.dr. F.C. Grozema	Technische Universiteit Delft
Prof.dr. P. Palensky	Technische Universiteit Delft, reservelid



Keywords: transparent conductive oxide (TCO), bifacial copper-plating, indium use reduction, c-Si solar cells

Printed by: Ipskamp Printing

Front & Back: Designed by Y. Chen and C. Han, inspired by a photograph of the bifacial solar cells from this research.

Copyright © 2022 by C. Han

All rights reserved.

No part of this material may be reproduced, stored in a retrieval system, nor transmitted in any form or by any means without the prior written permission of the copyright owner.

ISBN 978-94-6421-734-6

An electronic version of this dissertation is available at
<http://repository.tudelft.nl/>.

To my parents
Han Peixiang, Zhang Haolan

献给我的父母
韩培祥 张好兰

Contents

Summary	xi
Samenvatting	xiii
Nomenclature	xv
1 Introduction	1
1.1 Renewable energy demand	2
1.2 PV cell technologies	3
1.2.1 PV market choice	3
1.2.2 PV cell design and the TCO functions	6
1.3 Aim and outline of this thesis	8
1.4 Main contributions to the filed	9
2 TCO fundamentals	11
2.1 Host material choice	12
2.2 Trade-off between opto-electrical properties of TCOs.	13
2.2.1 TCO formation via degenerate doping of metal oxide	13
2.2.2 Scattering mechanisms	14
2.2.3 Trade-off between carrier mobility and carrier density.	16
2.2.4 Trade-off between opto-electrical properties	16
2.3 TCO deposition technologies	18
2.3.1 Magnetron sputtering	19
2.3.2 Other techniques	21
2.4 TCO utilization in PV devices	22
2.4.1 Optical perspective	22
2.4.2 Electrical perspective	22
2.4.3 Sputtering damage.	25
2.4.4 Material sustainability issue	28
2.5 Conclusions.	28
3 Experimental	31
3.1 TCO sputtering	31
3.2 Contact study and solar cell fabrication.	34
3.3 Characterizations	35
3.3.1 Opto-electrical properties of the TCO film	36
3.3.2 Other material characterizations.	42
3.3.3 Device characterization and contact study.	43
3.4 Modelling.	45
3.5 Conclusions.	46

4 High-μ_e IFO:H in low thermal budget c-Si solar cells with CSPCs	47
4.1 Introduction	48
4.2 Experimental	48
4.3 Results and discussion	49
4.3.1 H ₂ O vapor pressure influence on the as-grown films.	49
4.3.2 Optimized IFO:H analysis	49
4.3.3 Comparative opto-electrical properties with ITO	53
4.3.4 Solar cell applications	55
4.4 Conclusions.	57
5 IFO:H implementation in high thermal budget poly-Si solar cells	59
5.1 Introduction	60
5.2 Experimental	61
5.3 Results and discussion	62
5.3.1 Opto-electrical properties upon PDA treatments.	62
5.3.2 The IFO:H films under different PDA treatments.	64
5.3.3 Contact and device application	70
5.4 Conclusions.	75
6 RT-sputtered IWO for improved current in SHJ solar cells	77
6.1 Introduction	78
6.2 Experimental	79
6.3 Results and discussion	79
6.3.1 Optimization of 75 nm-thick IWO films on glass substrate	79
6.3.2 IWO on top of thin film Si layers and optical simulations	81
6.3.3 Devices performance	84
6.4 Conclusions.	88
7 Towards bifacial Cu-plated SHJ solar cells with reduced TCO use	89
7.1 Introduction	90
7.2 Experimental	91
7.3 Results and discussion	92
7.3.1 Optical evaluations regarding TCO reduction in SHJ solar cells	92
7.3.2 Electrical evaluations regarding TCO reduction	96
7.3.3 Bifacial SHJ solar cell results	100
7.4 Conclusions.	102
8 Conclusions and outlook	105
8.1 Conclusions.	105
8.2 Outlook	106
Appendices:	113
A IFO:H in high thermal-budget poly-Si solar cells	113
B RT-sputtered IWO in SHJ devices	117
C Towards bifacial SHJ solar cells with reduced TCO use	123
D Controllable bifacial Cu-plating for c-Si solar cells (I)	131

E Controllable bifacial Cu-plating for c-Si solar cells (II)	145
References	149
Acknowledgements	183
List of Publications	187
Curriculum Vitae	193

Summary

In the efficiency-driven photovoltaic (PV) industry, the market dominating crystalline silicon (c-Si) technology has been developing towards PV devices with carrier-selective passivating contacts (CSPCs). Especially, the silicon heterojunction (SHJ) solar cell, based on hydrogenated amorphous silicon (a-Si:H) contact stacks, and the poly-Si solar cell, based on ultrathin SiO_x/poly-Si passivating contacts, pave the way for power conversion efficiencies above 26%, approaching the theoretical limit of the c-Si solar cell. In case of front/back-contacted (FBC) architectures, to minimize the optical parasitic absorption at the emitter and/or surface field side(s), thin doped silicon layers are normally applied, which exhibit high sheet resistance. Accordingly, transparent conductive oxide (TCO) layers are required to ensure sufficient lateral carrier transport towards the metal electrodes. However, problems still exist in contacting schemes for high-efficiency solar cell design towards future multi-terawatt production of PV modules, regarding the development of TCO layer with high carrier mobility (μ), its integration into specific device structures, and more importantly, the material availability.

In this work, we present three types of TCO materials. They are tin-, fluorine- and tungsten-doped indium oxide layers, namely, ITO, IFO, and IWO. RF magnetron sputtering approach has been utilized to deposit the films. The TCOs are integrated into both low thermal-budget SHJ and high thermal-budget poly-Si solar cells. Further, to address the sustainability implication related to indium consumption, we propose a strategy of bifacial SHJ solar cell with reduced TCO use. Meanwhile, to reduce silver (Ag) consumption, as well as to reach good solar cell performance in our laboratory, we have developed a platform for bifacial copper (Cu)-plating metallization approach. Specific results are summarized as follows.

Chapter 4 reports on the hydrogenated IFO (IFO:H) layers with a remarkably high μ of 87 cm² V⁻¹ s⁻¹. To our knowledge, this is the highest mobility value among the as-sputtered In₂O₃-based TCOs at a temperature below 110 °C. When implemented into low thermal-budget SHJ solar cells, the IFO:H-based devices show significantly higher short-circuit current density (J_{SC}) values than our lab-standard ITO counterpart. The optical gain results from an outperformance of the IFO:H-based SHJ solar cell over the ITO-based device along the whole wavelength range of interest (300-1200 nm).

However, notable contact resistance increase occurs when integrating IFO:H layer into high thermal-budget poly-Si solar cells. This contact deterioration happens during a post TCO deposition treatment above 350 °C, which is required to restore the passivation quality of the poly-Si solar cell precursor (n^+ poly-Si/SiO_x/c-Si/SiO_x/ p^+ poly-Si) from sputtering damage.

Chapter 5 presents the alternatives to eliminate the contact degradation. Via appropriate post-annealing treatment in hydrogen atmosphere, the poly-Si solar cell precursors could restore their passivation quality while maintain low contact resistances of both n - and p -contacts. Besides, with such a post-annealing treatment, the μ of the IFO:H

layer is further improved to $108 \text{ cm}^2 \text{ V}^{-1} \text{ s}^{-1}$. The inherent electron scattering and doping mechanisms of the IFO:H layers are also explored.

Chapter 6 elaborates on the room temperature sputtered IWO layers, whose optimal μ is $34 \text{ cm}^2 \text{ V}^{-1} \text{ s}^{-1}$. The underlying thin-film silicon layers influence the TCO properties during the device fabrication process. With utilizing a multi-layer approach in spectroscopic ellipsometry characterizations, we are able to extract the optical parameters of TCO layers that mimic the practical SHJ solar cell use. In such a way, more accurate optical simulations at device level are performed, and the performance of the solar cell can be properly elucidated. By adding an additional magnesium fluoride layer on device, the champion IWO-based SHJ solar cell shows an active area cell efficiency of 22.92%.

Chapter 7 introducing the bifacial Cu-plated SHJ solar cells with reduced TCO use. The development of the simultaneous bifacial Cu-plating metallization approach is described in **Appendix D**. The bifacial Cu-plated SHJ solar cells outperform our lab-standard screen-printed Ag-based counterpart. The reason stays in avoiding the penetration of metals into silicon substrate, reduced optical loss from less metal coverage at each side, and favourable lateral carrier transport from lower finger spacing distance in the Cu-plated devices. To reduce the TCO use on both sides of the wafer, the TCOs (including ITO, IFO, and IWO) with varied film thicknesses are examined in bifacial SHJ solar cells, both optically and electrically. With appropriate contact engineering, Cu-plated bifacial SHJ devices, which have 25 nm-thick front IWO at *n*-contact, and 25 nm-thick rear ITO at *p*-contact, show front side efficiencies >22%. Moreover, with utilizing modified SHJ solar cell precursors (*n/i/c-Si/i/p*) and further TCO adjustment, our champion bifacial Cu-plated SHJ solar cell shows a front side efficiency of 22.84%. The bifaciality factor is 0.95.

Our findings in this work could provide important insights into high-mobility TCO development, optimal optical design of PV devices, and contact manipulations at the TCO/thin-film silicon interfaces. Combined with the controllable bifacial Cu-plating technique for c-Si solar cells, promising contacting schemes with less In and Ag consumptions become achievable.

Samenvatting

Dutch translation by David van Nijen.

De markt van de efficiëntie-gedreven fotovoltaïsche (*photovoltaic*, PV) industrie wordt gedomineerd door technologie gebaseerd op kristallijn silicium (*crystalline silicon*, c-Si). Binnen de markt van c-Si zonnecellen heeft er een verschuiving plaatsgevonden naar zonnecellen met ladingsdrager-selectieve passiverende contacten. Hiervan zijn er in het bijzonder twee type zonnecellen die de weg vrij maken voor efficiënties boven 26%, waarmee de theoretische limiet van de c-Si zonnecel wordt benaderd. Dit zijn de silicium heterojunctie (SHJ) zonnecel gebaseerd op gehydrogeneerd amorf silicium (*hydrogenated amorphous silicon*, a-Si:H) contacten en de polysilicium (poly-Si) zonnecel gebaseerd op ultradun siliciumoxide (SiO_x) / poly-Si passiverende contacten. Echter, in het geval van voorzijde/achterzijde gecontacteerde (*front/back-contacted*, FBC) structuren zijn er nog steeds nadelen aanwezig bij het maken van contacten voor hoog-efficiënte zonnecelstructuren. Om deze reden worden transparante geleidende oxide (*transparent conductive oxide*, TCO) lagen met een hoge ladingsdragers-mobiliteit (μ) geïmplementeerd. Hiernaast wordt de kwestie van materiele beschikbaarheid een belangrijk onderwerp wanneer productie van zonnemodules op multi-terawatt schaal wordt bereikt.

In dit werk presenteren wij drie typen TCO materialen. Dit zijn tin-, fluoride-, en wolfraam-gedoteerde indium oxide lagen, namelijk ITO, IFO en IWO. De lagen werden gedeponeerd met het RF-magnetron sputterproces. De TCO lagen zijn geïntegreerd in zowel laag-thermisch budget SHJ zonnecellen als in hoog-thermisch budget poly-Si zonnecellen. Verder doen wij een voorstel voor een strategie met tweezijdige zonnecellen en minder TCO gebruik om de duurzaamheidsimplicatie gerelateerd aan indiumconsumptie aan te pakken. Om tegelijkertijd zilver (Ag) consumptie te verminderen, ontwikkelden wij een tweezijdige koper (Cu)-geplateerde metallisatie aanpak. De specifieke resultaten hiervan kunnen als volgt worden samengevat.

Hoofdstuk 4 rapporteert over de gehydrogeneerde IFO (IFO:H) lagen met een opmerkelijk hoge μ van $87 \text{ cm}^2 \text{ V}^{-1} \text{ s}^{-1}$. Naar ons weten is dit de hoogste mobiliteitswaarde gemeten bij onbehandelde In_2O_3 -gebaseerde TCO's gesputterd op een temperatuur onder 110°C . Wanneer de IFO:H-gebaseerde zonnecellen zijn geïmplementeerd in laag-thermisch budget zonnecellen, laten ze significant hogere kortsluitstroombichtheid (*short-circuit current*, J_{SC}) waardes zien dan hun ITO tegenhangers. De optische winst is een gevolg van de betere prestatie van IFO:H-gebaseerde SHJ zonnecellen vergeleken met ITO-gebaseerde zonnecellen over de gehele golflengte van interesse (300-1200 nm). Echter, toen we probeerden om IFO:H te integreren in hoog-thermisch budget poly-Si zonnecellen, werd een noemenswaardige contactresistiviteit geobserveerd bij de poly-Si/TCO interface. Deze contactverslechtering treedt op nadat de TCO is gedeponeerd, namelijk wanneer een behandeling boven de 350°C wordt uitgevoerd om de passivatiekwaliteit van de poly-Si zonnecel precursor (n^+ poly-Si/ SiO_x /c-Si/ SiO_x / p^+ poly-Si) te herstellen van

schade door sputtering.

Hoofdstuk 5 presenteert alternatieven om de contactdegradatie te elimineren. Door achteraf een geschikte verhittingsbehandeling in waterstofomgeving uit te voeren, konden de poly-Si zonnecel precursors hun passivatiekwaliteit herstellen terwijl zij een lage contactresistiviteit behouden bij zowel de *n*- als de *p*-contacten. Hiernaast verbeterde deze verhittingsbehandeling de μ van de IFO:H lagen naar $108 \text{ cm}^2 \text{ V}^{-1} \text{ s}^{-1}$.

Hoofdstuk 6 wijdt uit over de op kamertemperatuur gesputterde IWO lagen, van welke de optimale μ $34 \text{ cm}^2 \text{ V}^{-1} \text{ s}^{-1}$ was. De onderliggende dunne film silicium lagen beïnvloeden de TCO eigenschappen tijdens het productieproces van de zonnecel. Wij waren in staat om de optimale parameters van de TCO lagen te vinden door tijdens karakterisatie met spectroscopische ellipsometrie een aanpak met meerdere lagen te gebruiken. Hierbij werd het praktische gebruik van de lagen in SHJ zonnecellen nagebootst. Op deze manier deden wij meer accurate optische simulaties op celniveau, waardoor de prestatie van de zonnecel goed kan worden uitgelegd. Door een additionele magnesium-fluoride laag toe te voegen aan de zonnecel, liet onze beste IWO-gebaseerde SHJ zonnecel een actieve-oppervlakte efficiëntie zien van 22.92%.

Hoofdstuk 7 introduceert onze tweezijdige Cu-geplateerde SHJ zonnecel met lager TCO gebruik. De ontwikkeling van een tweezijdige Cu-geplateerde metallisatie techniek is beschreven in **Appendix D**. De tweezijdige Cu-geplateerde SHJ zonnecellen overtreffen onze lab-standaard zeefgedrukte Ag-gebaseerde tegenhanger. De redenen hiervoor zijn dat penetratie van metalen in de functionele silicium lagen wordt vermeden, dat optische verliezen worden geminimaliseerd door kleinere oppervlakten aan de verlichte zijdes te bedekken met metaal, en dat voordelig lateraal transport van ladingsdragers plaatsvindt als gevolg van de verminderde afstand tussen de metalen contacten in de tweezijdige Cu-geplateerde zonnecellen. Om het gebruik van TCO aan beide kanten van de wafer te verminderen, zijn de TCO lagen (inclusief ITO, IFO en IWO) met gevarieerde laagdikte onderzocht in tweezijdige SHJ zonnecellen. Door contactoptimalisatie van Cu-geplateerde tweezijdige SHJ zonnecellen demonstreerden wij een voorzijde-efficiëntie van >22%. Hierbij waren de IWO laag van het *n*-contact aan de voorzijde en de ITO laag van het *p*-contact aan de achterzijde allebei 25 nm dik. Door aangepaste SHJ zonnecel precursors (*n/i/c-Si/i/p*) te gebruiken en verdere TCO aanpassingen te doen, hebben wij met onze tweezijdige Cu-geplateerde SHJ zonnecel een voorzijde-efficiëntie van 22.84% bereikt. De tweezijdigheidsfactor was 0.95.

Onze bevindingen in dit werk kunnen belangrijke inzichten verschaffen in de ontwikkeling van TCO lagen met hoge ladingsdragers-mobiliteit, optimaal optisch design van PV zonnecellen, en contactmanipulatie van de TCO/dunne film silicium interfaces. Gecombineerd met onze controleerbare tweezijdige Cu-geplateerde techniek voor c-Si zonnecellen worden veelbelovende contacteermogelijkheden met minder consumptie van In en Ag haalbaar.

Nomenclature

Abbreviations

TCO	transparent conductive oxide
ITO	indium tin oxide (or, tin-doped indium oxide)
IFO	fluorine-doped indium oxide
IFO:H	hydrogenated fluorine-doped indium oxide
IWO	tungsten-doped indium oxide
GBs	grain boundaries
MFP	mean free path, nm
UV	ultraviolet
Vis	visible
NIR	near infrared
FCA	free carrier absorption
<i>WF</i>	work function, eV
<i>EA</i>	electron affinity, eV
DT	direct tunnelling
TE	thermionic emission
TAT	trap-assisted tunnelling
B2BT	band-to-band tunnelling
PDA	post-deposition annealing
ARC	anti-reflection coating
DLARC	double-layer anti-reflection coating
CSPCs	carrier-selective passivating contacts
SHJ	silicon heterojunction
RT	room temperature
SP	screen printing
MF	monofacial
BF	bifacial
AR	aspect ratio of metal finger, -
CV	cyclic voltammetry
OPD	overpotential deposition
EQE	external quantum efficiency, -
MPP	maximum power point
iMPP	implied maximum power point

Letters

R_{sh}	sheet resistance, Ω/\square
ρ	resistivity, $\Omega \text{ cm}$
σ	conductivity, S/cm
μ	carrier mobility, $\text{cm}^2 \text{V}^{-1} \text{s}^{-1}$
μ_e	electron mobility, $\text{cm}^2 \text{V}^{-1} \text{s}^{-1}$
$\mu_{e,\text{Hall}}$	electron mobility from Hall measurement, $\text{cm}^2 \text{V}^{-1} \text{s}^{-1}$
μ_{opt}	optical mobility, $\text{cm}^2 \text{V}^{-1} \text{s}^{-1}$
τ	carrier relaxation time
m^*	carrier effective mass
m_e^*	electron effective mass
V_{O}	oxygen vacancy
V_{In}	indium vacancy
H_{i}	interstitial hydrogen
N	carrier density, cm^{-3}
N_e	electron density, cm^{-3}
λ	wavelength, nm
α	absorption coefficient, cm^{-1}
A	absorptance, %
R	reflectance, %
T	transmittance, %
n	refractive index, -
k	extinction coefficient, -
E_{g}	(optical) band gap, eV
E_{U}	Urbach energy, meV
E_{vac}	vacuum level energy
E_{F}	Fermi energy, eV
E_{c}	conduction band energy, eV
Δn	excess carrier density under illumination, cm^{-3}
V_{OC}	open-circuit voltage, mV
$i-V_{\text{OC}}$	implied open-circuit voltage, mV
J_{SC}	short-circuit current density, mA/cm^2
$J_{\text{SC,EQE}}$	EQE integrated short-circuit current density, mA/cm^2
FF	fill factor, %
pFF	pseudo fill factor, %
η	power conversion efficiency, %
ρ_{c}	contact resistivity, $\text{m}\Omega \text{ cm}^2$
$R_{\text{S,SunsVoc}}$	series resistance calculated from SunsVoc measurement, $\Omega \text{ cm}^2$

1

Introduction

1.1. Renewable energy demand

Modern society largely depends on the capability of humankind to convert energy from one to another more usable form. In terms of energy use, there are several problems: First, the growing world population and the increasing living standards lead to an increased energy demand. Second, the energy infrastructure heavily relies on fossil fuels like oil, coal and gas, which are not sustainable energy sources. Third, burning fossil fuels leads to greenhouse gas emissions, causing global warming and climate change [1]. Figure 1.1 shows world total energy supply by source during 1973-2018, according to the data reported in the Key World Energy Statistics 2020 released by the International Energy Agency (IEA) [2]. The overall energy capacity increased by 117% in the 45 years, due to the increased global energy consumption. However, in 2018, the fossil fuels still took up the largest fraction in the energy mix of primary energy sources, with a sum ratio of 81.3% from coal, oil, and gas. For comparison, the share of the renewable energy is quite limited with only 2.0% (see “Other” component in Figure 1.1).

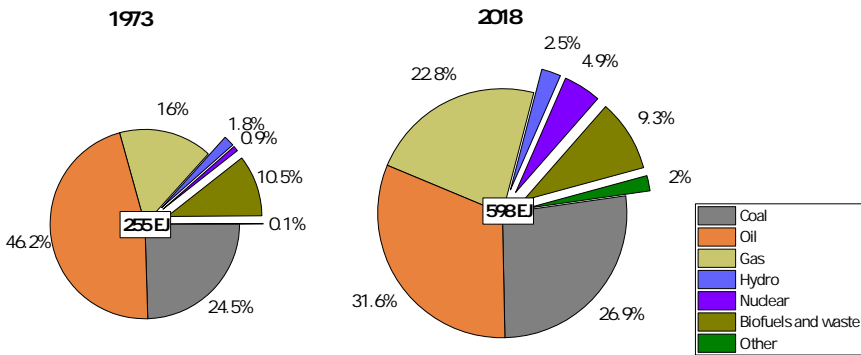


Figure 1.1: 1973 and 2018 source shares of world total energy supply [2].

According to Energy Outlook of the British Petroleum (BP) company in 2020 [3], the global primary energy consumption is predicted to continuously increase till 2040, but the share of fossil fuels will decrease. Related to that, the proportion of renewable energy is expected to keep rising. BP presented three scenarios upon different measures to predict the possible outcomes over the next 30 years, as shown in Figure 1.2(a). With respect to 2018, in 2050, the CO₂ emissions from energy use could be reduced by 70%, 95%, and 10% in *Rapid*, *Net Zero*, and *Business-as-usual* transition scenarios, respectively.

According to the talk from the United Nations Framework Convention on Climate Change (UNFCCC), the world was on track towards a global temperature rise of 3 degrees Celsius (°C) till January 2020, which is twice of the internationally accepted target established by the 2015 Paris Climate Change Agreement [4]. To effectively reduce CO₂ emissions and remain on a path compatible with the Paris Agreement, i.e., to limit the global temperature increase to 1.5 °C above the preindustrial level in 2100, we need a rapid transition to *Net Zero* [4]. In 2020, many countries established new or revised climate action plans to reach *Net-Zero* emission goals within the next 15–30 years [5]. Figure

1.2(b) illustrates BP's energy consumption prediction in the *Net Zero* scenario [3]. Till 2050, the renewables will take more than 50% of the human activity energy consumption. Therefore, the global energy system is very likely to undergo a fundamental restructuring in order to decarbonize, which will create challenges and opportunities for both academia and industry of the energy transition communities.

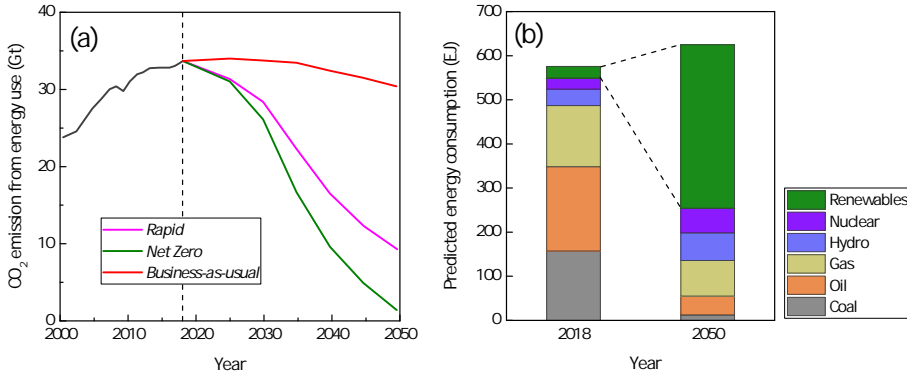


Figure 1.2: (a) CO₂ emissions from energy use, based on three scenarios to estimate the energy transition to 2050; and (b) energy consumption prediction by source in *Net Zero* scenario.

Typical renewable energy sources include hydro, wind, and solar energy, with which the energy can be replenished by natural processes at a rate comparable or faster than the consumption rate by humans. Solar energy holds an annual energy potential of 1575-49837 EJ (exajoules) [6], which is several times larger than the total world energy consumption (550-600 EJ, see Figure 1.1(b) and Figure 1.2(b)). Thus, solar energy is an enormous source of energy. Photovoltaics (PV) is the technology that converts solar energy into electricity. The energy conversion takes place within a semiconductor-based photovoltaic cell, which is called *solar cell*, *PV cell*, or *PV device* within the scope of this dissertation. In past decades, the production of solar cells and PV modules, as well as the installation of PV systems have grown fast. However, the proportion of PV electricity in the global total energy supply was only increased from 0.0056% in 1973 to 0.33% in 2018 [2]. Compared to the aforementioned huge demand prediction, there is plenty of room for PV technologies to grow for terrestrial application.

1.2. PV cell technologies

1.2.1. PV market choice

Wafer-based crystalline silicon (c-Si) solar cells have been dominating the PV industry with more than 90% of the market share [7]. From 1976 till 2020, the PV module price has maintained a learning rate of about 23.8%, i.e., for every doubling of cumulative PV module shipment, the average module sales price decreases by ~23.8% [7]. The drivers for the cost reduction of solar electricity include complex and interconnecting factors, such as the improvement in solar cell efficiency, the increase in silicon wafer size, the reduction in wafer thickness, the reduction in silver consumption, high-level of

automation, increased economies of scale [8]. Comprehensively, solar cell efficiency is a key lever for PV cost reduction: on the one hand, the increase in efficiency reinforces the reduction in silver, silicon, and non-silicon materials in the module; on the other hand, the increase in efficiency also automatically reduces the Balance-of-System (BoS) costs and all area-dependent soft costs at system level [8].

In such an efficiency-driven PV industry, the c-Si technology evolved from the traditional low-complexity full area aluminium back surface field (Al-BSF, till 2013) PV cell structure to the passivated emitter and rear contact (PERC) architecture, reaching the power conversion efficiency (PCE) of 23-24% at production level. However, PERC cells still feature localized metal-silicon contacts which suffer from relatively low open-circuit voltage due to high recombination. In this regard, the c-Si solar cells featuring carrier-selective passivating contacts (CSPCs) are promising options with attaining PCE well above 25%. Such solar cells enable low contact resistance as well as good passivation quality of the c-Si surface, thus appreciably enhancing the contact selectivity as compared to conventional diffused junctions or PERC technology. More details are included in Section 1.2.2.

The c-Si solar cells with CSPCs, typically include silicon heterojunction (SHJ) solar cell and c-Si solar cell with tunnel-oxide passivated contact (TOPCon, or SIPOS, or poly-Si, or POLO) [9, 10]. Due to an easier upgrade from PERC to TOPCon in industrial pipeline, the capacity of TOPCon cell is growing fast [7]. Meanwhile, SHJ is also gaining momentum due to its advantages in high efficiency potential [11], simple and low temperature process [12], favourable outdoor performance (low temperature coefficient, high bifaciality) [13, 14], and particular compatibility with thin wafers [15]. Figure 1.3 shows the worldwide market shares of different cell technologies [7]. The traditional Al-BSF technology only shared 15% of the market in 2020, and is predicted to disappear after 2025. Instead, PERx/TOPCon technologies has been quickly adopted by the industry, with a market share of around 80% in 2020. Meanwhile, the emerging SHJ solar cell has taken a share of around 2% in 2020, which is forecast to reach about 18% in 2031. The SHJ cell holds the record PCE of 26.6% on lab-scale cell [11]. In mass production, the competition between TOPCon and SHJ is quite fierce. During the preparation of the thesis, the cell efficiency records for industrial TOPCon and SHJ solar cells have reached 25.5% [16] and 26.30% [17], respectively. The poly-Si based FBC cell efficiency record is 26.0% at lab-scale [9].

The mentioned record efficiency of 26.6% on SHJ was based on an interdigitated back-contact (IBC) architecture. An IBC cell features no metal grids at the front illuminated side of the cell, thus removing the shadowing losses and yielding higher efficiencies than front and back contacted (FBC) cell [18]. However, the IBC cell faces increased level of complexity due to its exquisite workmanship required for making the two- or three-dimensional (rear) interdigitated contact patterns. On the other hand, the efficiency gap between FBC and IBC is progressively narrowing for CSPCs. A poly-Si based FBC cell efficiency of 26% was recently reported by Richter *et al.* [9], which is quite close to the 26.6% record on IBC-SHJ cell [11]. The market share of IBC cell is around 2% in 2020, which is expected to slightly increase in the next years [7].

Another promising concept to further increase efficiency is represented by the silicon based tandem solar cells. The efficiency of silicon solar cells is fundamentally limited by spectral losses. Basically, in a c-Si solar cell, the c-Si material acts as the absorber layer, in

which the photons of the incident radiation are absorbed and further utilized. c-Si is a semiconductor material with a bandgap energy of 1.12 eV. The definition of bandgap is in 1.2.2. On the one hand, photons with energy higher than the bandgap energy can be absorbed. However, the excess energy of photons above the bandgap energy of absorber is released as heat into the absorber material in the thermalization process, causing spectral loss. On the other hand, the photons with energy lower than the bandgap energy of the c-Si absorber are in principle not absorbed. This causes another amount of non-negligible spectral loss [19].

The non-absorption of photons carrying less energy than the silicon bandgap and the excess energy of photons above the bandgap (which transforms to heat), are the two main losses, which account for about 20% and 35% of the incident energy being lost, respectively [10]. These spectra losses can be substantially reduced by adding one or more solar cells with suitable bandgaps beside the silicon cell. In such a case, a tandem solar cell is built. A fundamental (detailed balance) efficiency limit for a tandem device with two *p/n* junctions could reach 42% [20]. While the theoretical efficiency of c-Si solar cell is normally considered as 29.43% [21], although a 31% is also predicted based on a broadband solar absorption beyond lambertian limit in certain thin silicon photonic crystals [22, 23]. Eventhough the current developments in the academic field of tandem solar cells are very promising, there are still many challenges to be solved and no market readiness can be expected in the short term [24]. By far, a champion efficiency of 29.8% has been reported on Si-based tandem solar cell [25]. From the PV industry roadmap, the tandem cell is expected to step into the market from 2023 onwards [7]. These two concepts, IBC and tandem, will not be discussed in the research work of the thesis.

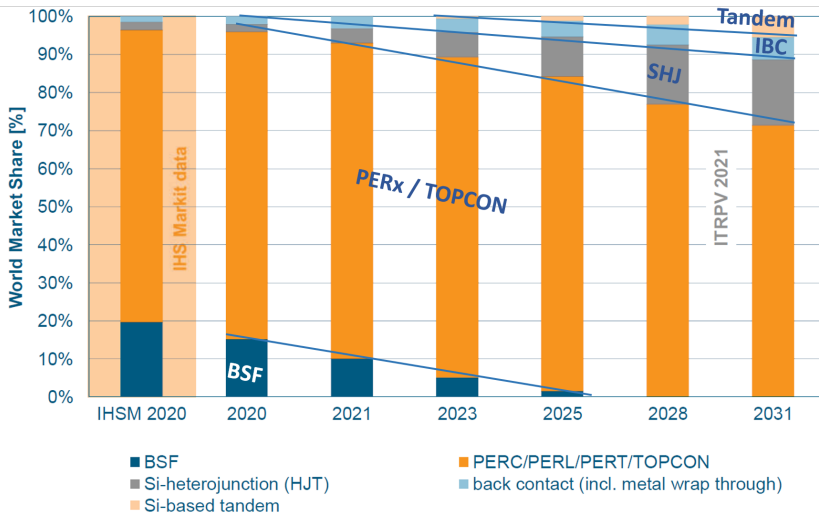


Figure 1.3: Worldwide market shares for different cell technologies [7]. Information Handling Services (HIS) market data are indicated for 2020 as reference for 2020.

Lastly, it is noteworthy to mention the bifacial solar cells. Compared to the monofacial configuration with a fully metalized rear side, the bifacial solar cell realizes double side

light illumination by including metal grid on both sides of the wafer, thus gives higher energy yields. Besides, with respect to the monofacial case, the bifacial solar cell could largely reduce the metal consumption, such as silver (Ag), due to the elimination of full-area metal use. Moreover, the indium (In) consumption may also be reduced in a bifacial cell, which will be elaborated in Chapter 7. According to the ITRPV 2021 report [7], the market share of the bifacial solar cell is around 30% in 2020, and is forecast to rapidly increase to around 80% in 2031.

1.2.2. PV cell design and the TCO functions

Photovoltaic devices convert solar irradiance into electric power. This process is achieved in two steps: first, the radiation from the sun is absorbed in the so-called absorber material and converted into populations of electrons and holes with distinct electrochemical potentials; second, these electrons and holes are separated and selectively transported to their respective electrodes [1]. A c-Si solar cell consists of a crystalline silicon wafer as the light absorber material. Upon illumination, the wafer generates electron-hole pairs by absorbing photons with energies larger than its *band gap*, which is the minimal energy that is needed to excite an electron from *valence band* to *conduction band*. The concepts of valence band and conduction band could be found in [1]. The maximal valence band energy and the minimal conduction band energy, are depicted as E_V and E_C , respectively.

According to the Fermi-Dirac statistics, the carrier distribution in a semiconductor (including electrons and holes), depends on the electrochemical potential of the carriers, which is referred to as the Fermi level (E_F). In thermal equilibrium conditions before illumination, the E_F of electrons and holes are the same in the c-Si material. Upon illumination, the Fermi level splits up into two quasi-Fermi levels for electrons and holes (E_{Fn} , and E_{Fp}), due to the high number of photogenerated electrons and holes. The difference of (E_{Fn} , and E_{Fp})/ q gives the maximum voltage that can be expected from the solar cell, which is usually known as the implied open-circuit voltage (iV_{OC}) of a solar cell precursor. While the open-circuit voltage (V_{OC}) is a measure of the maximum external voltage between the cathode and anode of a complete solar cell device.

Figure 1.4 shows a schematic silicon band diagram with a silicon absorber, in which three different electron and hole contact schemes are illustrated [10]. Note that the "contact" in Figure 1.4 includes all the contacting layer stacks, such as carrier transport layer, transparent electrode (if any), and metal electrode.

Figure 1.4(a) represents an ideal case where the iV_{OC} of a solar cell precursor is only limited by the recombination losses of the silicon absorber itself, and the V_{OC} measured at the terminals equals to the iV_{OC} value. However, it is not the real case in a practical PV cell. Basically, there are two types of limiting cases. Figure 1.4(b) illustrates the minority carrier recombination limited case, which represents the standard case of the industrially realized Al-BSF and PERC solar cells. In these cases, a low band bending in crystalline silicon, as well as a highly recombinative interface between the metal electrode and underlying contact stacks are unavoidable, which largely reduce the passivation quality of the PV devices. To eliminate the minority-related recombination issue, the PV community had devoted numerous efforts to minimize the metal-contacted area before 2013. However, these surfaces still dominate the overall recombination of the device, even though the metal coverage of the cell is reduced to less than 1% [26, 27].

In order to reach higher solar cell performance, the approach of “carrier selective passivating contacts (CSPCs)” has to be utilized, which avoids direct contact between metal and the silicon wafer, and allows a high band bending in crystalline silicon. Typical examples include SHJ solar cells, c-Si solar cells with tunnel oxide passivated contacts (TOPCon, or SIPOS, or poly-Si, or POLO), and c-Si solar cells with dopant-free carrier-selective contacts [10]. By far, all the single junction silicon solar cells with efficiencies above 25% are featuring CSPCs. The record efficiency of 26.6% is approaching the theoretical limit of 29.4% in silicon solar cells [11, 21, 28].

In principle, if the passivating contacts are realized perfectly, the solar cell performance is close to the ideal case as shown in Figure 1.4(a). However, the real scenario is likely to fall into a majority carrier transport limited case, as shown in Figure 1.4(c). In such a case, the iV_{OC} of the solar cell precursor is similar to the ideal case (Figure 1.4(a)), but the V_{OC} is less than the iV_{OC} value. This results from a voltage drop due to majority carrier transport losses, and stimulates tremendous research interests regarding the contacting schemes of c-Si solar cells with CSPCs.

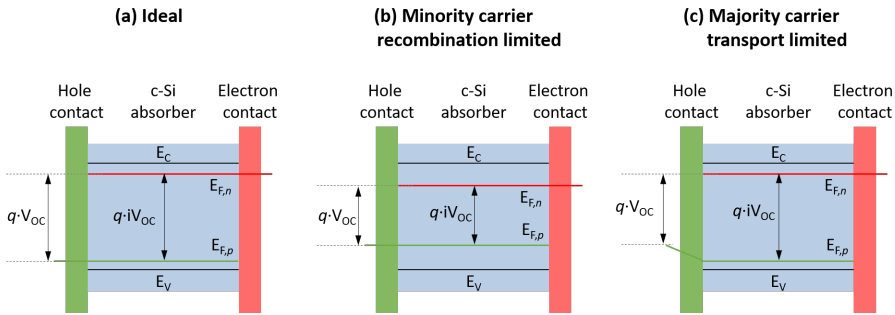


Figure 1.4: Schematic silicon band diagram with different electron and hole contact schemes, leading to (a) an ideal solar cell, (b) recombination or (c) transport limited solar cells. This picture is adapted from [10].

Different from the Figure 1.4(b) case, the electron and hole contact layers on the wafer absorber in Figure 1.4(c) are normally with a much higher sheet resistance [12, 29, 30], due to a thin layer use for the purpose of reducing parasitic absorption [31]. Thus a transparent conductive oxide (TCO) layer is required to be included in the contact layers to ensure the electrical properties of the device. On the one hand, a low sheet resistance of the TCO layer is needed to provide sufficient lateral carrier transport towards the metal electrodes, in which a trade-off between electrical and optical properties needs to be addressed. On the other hand, a low contact resistance between TCO and the underlying doped thin-film silicon layers should be maintained. These two aspects will be elaborated in Chapter 2. Moreover, optical functions (such as anti-reflection coating), need to be satisfied. In addition, the TCO coating should not introduce detrimental influence on the underlying thin-film silicon stacks.

To summarize, the ideal TCO layer should feature the following characteristics: (i) low lateral electrical resistivity (i.e. low R_{sh}) and simultaneously high transparency in the whole wavelength range of interest (normally 300-1200 nm); (ii) low contact resistance with the adjacent layers; (iii) appropriate refractive index for maximal light in-coupling in

the solar cell; (iv) appropriate process condition without degrading passivation quality or contact property of the solar cell.

1.3. Aim and outline of this thesis

The aim of this work is to develop TCO films that could satisfy the aforementioned opto-electrical requirements, explore the conduction mechanisms behind the carrier behaviors, implement the optimal TCO films into high-efficiency c-Si solar cells, and eventually utilize the films from a sustainable perspective.

This thesis is outlined in the following way.

Chapter 1. Introduction. This chapter gives a general introduction of the growing share of renewable energy, evolution of photovoltaic technologies in the market, fundamentals of high-efficiency c-Si solar cell design. Besides, the requirements of TCO layers are introduced.

Chapter 2. TCO fundamentals. This chapter discusses the TCO fundamentals, which include the physical understanding of the interaction between the optical and electrical properties of TCOs, the widely utilized deposition approaches and their comparison, and the challenges that need to be considered when practically integrating TCOs into PV devices.

Chapter 3. Experimental. This chapter lists experimental methods that are utilized in this work, including TCO deposition, solar cell fabrication and intermediate test sample preparation, as well as corresponding material, device, and sample characterizations. Moreover, modelling approaches regarding optical device simulation and atomistic density function theory calculation used in this thesis are introduced.

Chapter 4. High- μ_e IFO:H in low thermal-budget SHJ solar cells. High-mobility IFO:H film is fabricated with low temperature RF magnetron sputtering technique, and is implemented into front/back-contacted SHJ solar cells.

Chapter 5. IFO:H implementation in high thermal-budget poly-Si solar cells. In the attempt to restore the TCO sputtering damage on the poly-Si contacts, severe carrier transport degradation occurs. To address this problem, different post-annealing treatments after TCO deposition are investigated. The investigation on the inherent electron scattering and doping mechanisms in the IFO:H films is also presented.

Chapter 6. Room temperature (RT)-sputtered IWO in SHJ solar cells. RT-sputtered IWO film is optimized. Underlying thin-film silicon layers could influence the TCO properties, which is discussed and evaluated in solar cell performance.

Chapter 7. Towards bifacial Cu-plated SHJ solar cells with less TCO use. Strategies of designing and fabricating high-efficiency SHJ solar cells with reduced TCO use are proposed. The development of electrochemical bifacial Cu-plating metallization approach is elaborated in **Appendix D**.

Chapter 8. Conclusions and outlook. This chapter summaries the key results of this thesis and gives an outlook for the future research on high performance TCO development, investigation, and its deployment into high efficiency c-Si solar cells, as well as in other types of optoelectronic devices such as tandem solar cells.

1.4. Main contributions to the filed

This work contributes to the TCO-based contacting schemes for c-Si solar cells addressing the following aspects:

1. RF magnetron sputtered IFO:H films with high μ_e . A remarkably high μ_e of $87 \text{ cm}^2 \text{ V}^{-1} \text{ s}^{-1}$ was achieved in the IFO:H film. To our knowledge, it is the highest μ_e value among the previously reported IFO films, and among the as-sputtered In_2O_3 -based TCOs at a low temperature below $110 \text{ }^\circ\text{C}$. The μ_e of the as-deposited IFO:H film could be further improved $108 \text{ cm}^2 \text{ V}^{-1} \text{ s}^{-1}$ after appropriate post-treatment. These results demonstrate the possibility of developing high-mobility TCOs with anionic doping, rather than the widely reported cationic metallic doping.

2. The conduction mechanisms in IFO:H films. Combined with various material characterizations, we explored the inherent electron scattering and doping mechanisms in the as-sputtered and post-annealed IFO:H films. The findings provide insights for understanding the conduction mechanism in the high- μ_e IFO:H films.

3. Room temperature sputtered IWO film. Optimal polycrystalline IWO film is deposited with room temperature sputtering. Besides, its opto-electrical properties are evaluated on top of thin-film silicon layers. This part of work provides a more device-oriented material study of the TCO film.

4. Post H_2 annealing on TCO/poly-Si contact. Unlike N_2 or air annealing ($>350 \text{ }^\circ\text{C}$) inducing severe TCO/poly-Si contact degradation, H_2 annealing could effectively eliminate this detrimental contact degradation. This is likely due to the suppression of interfacial oxide formation at the TCO/poly-Si interface. These results demonstrate the potential of material manipulation and contact engineering strategy in high-efficiency photovoltaic devices endowed with TCOs.

5. Bifacial Cu-plated SHJ devices with less TCO use. Towards a sustainable development of PV technologies, metal consumptions (such as In, Ag), need to be minimized. We prove that bifacial solar cell design is the most effective way to reach this goal. However, intentionally reducing TCO thickness on both sides of wafer is challenging, due to a reduced lateral conductivity of TCO layer, and more importantly, a likely increased contact resistance between TCO and the underlying doped silicon layers. We compared the optical and electrical performances of TCOs (including ITO, IFO and IWO) with varied thicknesses, and found an optimal TCO use of combining 25 nm-thick front IWO in *n*-contact and 25 nm-thick rear ITO in *p*-contact. In such a way, we achieved front side efficiencies above 22% in bifacial Cu-plated SHJ devices. These results may provide insightful discussions on multifold research topics for future sustainable PV development, such as contact engineering, optical optimization, reduction of indium consumption, bifacial solar cell design, and bifacial Cu-plating.

2

TCO fundamentals

2.1. Host material choice

Various materials have been developed for transparent electrodes in optoelectronic devices, such as metal oxides, metal nanowires, carbon nanotubes (CNTs), organic semiconductors, and 2D materials such as graphene and MoS₂ [32–34]. Among the alternatives, metal oxides represent a conventional and competitive group because of the combination of high carrier mobility, good optical transparency, straightforward synthetic access, large-area electrical uniformity and mechanical flexibility [32]. In metal oxides, the opto-electrical (especially the electrical) properties depend critically upon the oxidation state of the metal component (stoichiometry of the oxide) and on the nature and quantity of impurities incorporated in the films, either intentionally or inadvertently [35, 36]. Perfect stoichiometric oxides are either insulator or ionic conductors. However, oxides such as indium oxide (In₂O₃), tin oxide (SnO₂), zinc oxide (ZnO), cadmium oxide (CdO), and gallium oxide (Ga₂O₃), are naturally nonstoichiometric and show intrinsic *n*-type conductivity [35, 37]. It is noteworthy that, it is quite challenging to change the conductivity type of these oxides from *n*-type to *p*-type. This is partly reflected by various attempts to develop *p*-type ZnO [38], In₂O₃ [39], and Ga₂O₃ [40], but no encouraging results have been achieved so far.

Among the prototypical *n*-type oxides, CdO is probably the first investigated TCO since 1907 [41]. But it is not widely used today, due to the toxicity of Cd and the relatively narrow bandgap of 2.3 eV that implicates low transparency in visible wavelength region. However, it is still of scientific interest because CdO has exhibited high electron mobility above 200 cm²V⁻¹s⁻¹ [42]. Regarding Ga₂O₃, it has an ultra-large bandgap of 4.8 eV, and is extensively investigated in the applications of power electronics [40]. As for the photovoltaic applications, only SnO₂-, ZnO- and In₂O₃-based TCOs have gained widespread attention, owing to their appropriate optical bandgap above 3 eV and low resistivity of around or below 1 × 10⁻³ Ω cm [43]. Another interesting candidate in photovoltaics is TiO₂-based TCO [44], but seemingly such a material is more famous as electron transport layer in perovskite solar cells to alleviate detrimental hysteresis phenomenon [45].

From the physical definition, the conductivity (σ), which depends on the carrier mobility (μ) and the carrier concentration (N), can be described as follows:

$$\sigma = N \cdot e \cdot \mu \quad (2.1)$$

where e is the elementary charge. Equation 2.1 tells that in order to improve the σ of the film, both high N and μ are beneficial. However, high N is detrimental to the optical transparency, thus is not desirable for our PV applications. Therefore, high μ is of critical importance to realize the trade-off between optical and electrical properties of the TCO material.

As mentioned, SnO₂-, ZnO- and In₂O₃-based TCOs are the widely utilized TCOs in PV applications. Compared to the former two candidates, the In₂O₃-based TCOs exhibit the most promising potential in developing high-mobility TCOs. The mobility of indium oxide single crystal could go as high as 180 cm²V⁻¹s⁻¹ [46]. Besides, mobilities of 170 cm²V⁻¹s⁻¹ [47], 141 cm²V⁻¹s⁻¹ [48] and 150 cm²V⁻¹s⁻¹ [49] are reported for Zr-, Ce-doped In₂O₃ and hydrogenated In₂O₃, respectively. Therefore, we chose In₂O₃ as the host material for developing high-mobility TCOs in this dissertation.

2.2. Trade-off between opto-electrical properties of TCOs

2.2.1. TCO formation via degenerate doping of metal oxide

Metal oxide-based TCOs are formed where the ionic character of the host oxides produces an oxygen 2p-derived valence band (VB) and the metal ns and oxygen 2p orbitals derived conduction band (CB) [37]. Figure 2.1(a) shows the cubic bixbyite structure of the indium oxide conventional unit cell [50]. It contains 80 atoms, composed of 32 In sites (two inequivalent sites of In-8b and In-24d), and 48 O sites (O-48e) in the Wyckoff notation [50, 51]. Both In-8b (labeled as In1) and In-24d (labelled as In2) are six-fold coordinated, surrounded by O atoms. But the local structure of In1 is highly symmetric, while that of In2 is less symmetric. The local structure of O is a distorted tetrahedron due to the inequivalent In-O bonds. Figure 2.1(b) displays the schematics of a typical TCO band structure, in which E_{g0} represents the intrinsic (or fundamental) band gap. According to traditional band theory, with a E_{g0} around 3 eV, the host material (In_2O_3) permits transparency in the visible spectrum, yet the great separation between valence band maximum (VBM) and conduction band minimum (CBM) decreases the probability of exciting an electron into conduction. Thus, high conductivity and optical transparency seem contradictory [52]. However, TCO materials have been proven to sidestep this conundrum by degenerate doping. The high energy dispersion of the conduction band, which originates from interactions between metal s and oxygen p states, provides the conduction path for electrons. Larger orbital overlap facilitates easier carrier drift [53]. Besides, in an *n*-type TCO, electrons can be injected from a nearby defect donor level directly into the conduction band in order to permit conductivity [52]. If there is sufficient conduction path (via orbital overlap), the electronic states in the conduction band can be filled by the delocalized electrons from defect sites, i.e., the Fermi level shifts above the conduction band minimum of the material. This makes the metal oxide host material degenerately doped, changing the electrical property of the metal oxide from insulator to metal-like (or, conductor) [37]. Therefore, the degenerately doped metal oxides become both transparent and conductive, i.e., TCOs.

On the other hand, such an upward Fermi energy displacement is also called the Moss-Burstein shift [54, 55]. Assuming parabolic bands, this shift ΔE can be calculated from the following equation [35]:

$$\Delta E = \frac{h^2}{8m^*} \left(\frac{3N}{\pi} \right)^{2/3} \quad (2.2)$$

where N denotes carrier density, h is plank constant, and m^* represents the effective mass of conduction electrons. The Moss-Burstein shift helps to broaden the optical transparency window and to keep the intense optical transitions from the valence band out of visible wavelength range. Therefore, the optical band gap, which is the separation of Fermi level and VBM (as shown in Figure 2.1(b)), is practically used in the TCO study, rather than the aforementioned E_{g0} . In addition, through Mott-criterion [56, 57], $n_c^{1/3} a_B = 0.26$ (in which n_c is the critical charge carrier density, a_B is the effective Bohr radius determined from $a_B = \frac{4\pi\epsilon_r\epsilon_0^2}{m_e^*e^2}$, with ϵ_r being the static dielectric constant of the host lattice, ϵ_0 the vacuum permittivity, m_e^* the effective electron mass and e the elementary charge), the n_c for In_2O_3 to induce degeneration could be calculated to be $\sim 6 \times 10^{18}$

cm^{-3} [58]. However, the electron density of the unintentionally doped In_2O_3 is $\sim 7 \times 10^{16} \text{ cm}^{-3}$ [58]. This means that extrinsic impurity needs to be introduced to reach the desirable degeneration for producing TCOs with desired properties. For the well-known tin-doped In_2O_3 (ITO), the electron density can be as high as $1 \times 10^{21} \text{ cm}^{-3}$ [58]. The TCOs investigated in this work basically have electron densities $> 1 \times 10^{19} \text{ cm}^{-3}$. The extrinsic impurities utilized are tin (Sn), fluorine (F), and tungsten (W), which are representatives of In_2O_3 -based TCOs with post-transition metal dopant, anionic dopant, and transition metal dopant, respectively. For simplicity, the TCOs are called ITO, IFO, and IWO, respectively. Among the layers, ITO, which has been widely used in academia and industry environment, acts as the reference TCO layer in our investigations. It is worth noting that, the so-called *reference* ITO layers in this dissertation only represent the layers that were optimized for our lab-standard use. The comparative results in all the chapters may differ with different laboratory conditions.

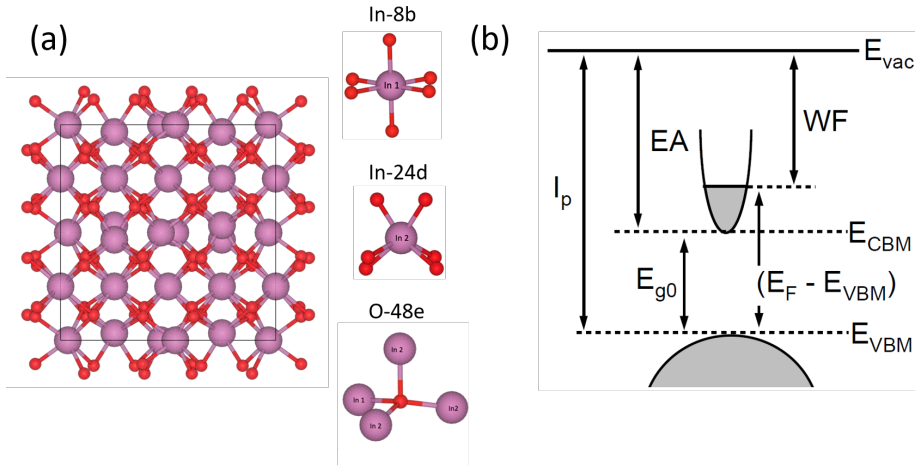


Figure 2.1: (a) Conventional cell of the In_2O_3 cubic bixbyite structure and local lattice structure of In and O atoms in the Wyckoff notation [50, 51]. (b) The schematics of typical TCO band structure, in which I_{p} , WF , EA , E_{g0} , E_{vac} , E_{CBM} , E_{VBM} , and E_{F} denote ionization potential, work function, electron affinity, intrinsic (or fundamental) band gap, vacuum level, conduction band minimum, valence band maximum, and Fermi level, respectively [59].

2.2.2. Scattering mechanisms

As indicated by equation 2.1, apart from carrier density (N), carrier mobility (μ) is a key metric of semiconductor performance, which represents the ability of carriers to move through the host lattice. Traditional band theory describes carrier transport of semiconductors in electronic structures in reciprocal space, with the CBM and VBM curvatures determining the electron and hole effective masses, respectively [32]. In an n -type semiconductor, the electron effective mass (m_e^*) expresses the mass that the electrons appear to have when moving within a periodic solid; while the electron mobility (μ) indicates how quickly the electrons can move through the material in an electric field. The electron mobility can be influenced by both m_e^* and the electrons' response to local

forces within the crystal [52]. On the one hand, low m_e^* facilitates high μ , i.e., μ is inversely proportional to m^* . On the other hand, μ is directly proportional to the carrier relaxation time (τ), via

$$\mu = \frac{e \cdot \tau}{m^*} \quad (2.3)$$

The parameter τ is determined by the various scattering mechanisms in the TCO material. Provided that the scattering from dislocations, acoustic phonons, and neutral impurities are negligible in the degenerate In_2O_3 -based TCOs [58], the total relaxation time τ_{total} could be estimated from relaxation time values from the polar optical phonon scattering (τ_{phonon}), charged center (or ionized impurity) scattering (τ_{cc}), and grain boundary scattering (τ_{GB}), via Matthiessen's rule [60]:

$$\frac{1}{\tau_{\text{total}}} = \frac{1}{\tau_{\text{phonon}}} + \frac{1}{\tau_{\text{cc}}} + \frac{1}{\tau_{\text{GB}}} \quad (2.4)$$

Accordingly, the τ_{total} could be estimated by

$$\frac{1}{\mu_{\text{total}}} = \frac{1}{\mu_{\text{phonon}}} + \frac{1}{\mu_{\text{cc}}} + \frac{1}{\mu_{\text{GB}}} \quad (2.5)$$

These three considered main scattering mechanisms are discussed as follows.

(i) Phonon scattering. Single crystals as well as polycrystalline materials can present an interaction with vibrational modes of the crystal lattice defined as phonons. Due to the polar nature of the In_2O_3 crystal with partly polar bonds between In and O atoms, optical phonon scattering and acoustic phonon scattering limit the electron mobility. The latter is less important due to the generally larger coupling constant for polar interactions than for an acoustic deformation potential [58]. The polar optical phonon scattering is characterized by the longitudinal optical phonon energy, parametrized as Debye temperature, and the number of longitudinal optical phonon modes. The large number of 80 atoms in the cubic bixbyite In_2O_3 unit cell results in a complex phonon spectrum with many longitudinal optical phonon modes of different phonon energies. Therefore, it is not realistic to assign specific phonon energy to specific Debye temperature or longitudinal optical phonon mode. Thus, only effective parameters are utilized in phonon scattering analysis [58]. Thanks to the temperature-dependence nature, the overall phonon scattering could be estimated from temperature-dependent mobility values (such as from Hall measurements) [61].

(ii) Charged center (or ionized impurity) scattering. Charged center (or ionized impurity) scattering is especially relevant in degenerate TCOs doped with oxygen vacancies and impurity atoms [62]. At every position of the crystalline structure where electrons become freely mobile, an ionized impurity is left behind. It is noteworthy that apart from the aforementioned metallic or anionic dopants to the IO host material, there is a special kind of dopant that could also contribute to the n -type conductivity, which is hydrogen-related dopant. It has been proven that both interstitial and substitutional hydrogen serve as shallow donors in In_2O_3 [63], hence such dopants also need to be taken into account in relevant TCO films. Furthermore, impurity clustering may occur in degenerate TCOs with high carrier concentrations [64, 65], which makes it more difficult to predict the μ_{cc} in a

quantitative way. In this work, we explored the open-volume defect information in the fluorine-doped IO film by Doppler broaden positron annihilation spectroscopy (DB-PAS). Combined with the analytical expression of Pisarkiewicz *et al.* [62], the μ_{cc} was calculated [61]. Detailed discussion can be found in Chapter 5.

(iii) Grain boundary scattering. The TCOs investigated in this work have a polycrystalline structure in their final state, thus the grain boundary (GB) scattering can limit the μ_{total} . The GBs could be considered as a quasi-two-dimensional disruption of the crystalline structure with surface states. These states can act as carrier traps at the GBs, where potential barriers are created to hinder the intergrain carrier transport [66]. Depending on the carrier density, the GB scattering can be either temperature-dependent thermionic emission or temperature-independent tunneling [66–68]. The former transport mechanism and relevant equations are elucidated in [66].

In this work, we performed temperature-dependent Hall measurements on the high-mobility hydrogenated fluorine-doped indium oxide films. Based on the data from various material characterizations (especially DB-PAS and spectroscopic ellipsometry), we decoupled the μ_{phonon} , μ_{cc} , and μ_{GB} out from the μ_{total} . The contributions from phonon scattering, charged center scattering, and grain boundary scattering in the films of interest were distinguished and discussed. The experimental results and corresponding analysis are elaborated in Chapter 5.

2.2.3. Trade-off between carrier mobility and carrier density

As described in section 2.2.1, degenerate doping is essential to realize the transition of insulating In_2O_3 host material to transparent and conductive TCOs. For quite some time, most efforts to improve the conductivity of TCO had been mainly focused on increasing the carrier density (N) via doping. However, this approach is somehow self-limiting since the carrier relaxation time could also be reduced due to dopant scattering when introducing many dopant sites. This is not favorable for obtaining high mobility value of the TCO material. Hence, obtaining the highest possible conductivity is a trade-off between N and the mobility (μ). For a complete degeneracy, the μ and N are no longer independent, but governed by a rule of $\mu \propto N^{-2/3}$ [36, 69].

This results in a highest conductivity of the order of 5000 S/cm [36], which is 2 orders of magnitude lower than that of metal such as Ag or Cu. Furthermore, at high dopant (such as Sn) concentrations, the observed N of ITO film normally appears to be lower than the expected value when assuming that every soluble tin atom contributes one free electron. This implies that a portion of the tin atoms remains electrically inactive [36].

To summarize this subsection, due to the limitations of dopant scattering and doping efficiency, there is an upper limit of the conductivity of TCOs. In other words, one cannot continuously improve the conductivity of TCO due to the trade-off between μ and N .

2.2.4. Trade-off between opto-electrical properties

Besides the electrical limitation, achieving the optimal performance in a TCO is also challenging because of the complex interplay between the electrical and optical properties. In the short wavelength range (below 400 nm), optical absorption occurs due to inter-band transitions from the partially filled conduction band. As mentioned in section 2.2.1, the optical band gap of degenerate TCOs are broadened by the so-called Moss-Burstein

shift. This is beneficial for PV application since a broader optical transparency window can be achieved, which allows for a more efficient utilization of the solar irradiance into the absorber material. However, numerous study on moderately and heavily doped TCOs reveals that their optical band gap has lower blue-shift than the theoretical value obtained from the well-known Moss-Burstein shift [70–72]. This means that band gap narrowing effects are happening. Different theoretical interpretations have been proposed, such as multi-body scattering including electron-electron and electron-impurity scattering within the random phase approximation [72, 73], and non-parabolic nature formation of the host conduction band due to the intrinsic electron doping or dopant hybridization with the host conduction states [74]. Besides, structural disorder yields band tailing/shift and localized states, resulting in a strong reduction of the optical band gap [75–77]. However, it is noteworthy that although there is a band gap shrinkage in amorphous TCOs, they could maintain the electrical properties as that of (poly-)crystalline materials. This is afforded by the small electron effective masses, thus efficient electron transport even in the amorphous state, since the spherically symmetrical metal s-orbital overlap is minimally affected by lattice distortions [77, 78]. In addition, the generally quoted optical band gap is > 3.7 eV, while weak absorption was experimentally observed at low energy levels ~ 2.5 eV. Such optical absorption in the short wavelength range could be related to: (i) energy levels of defects such as hydrogen-induced shallow donor states [79]; (ii) the formally forbidden transitions at the top of the valence band [80].

In the near-infrared (NIR) wavelength range (> 700 nm), optical absorption also occurs due to intra-band transitions within conduction band [37]. This contributes to the well-known parasitic free carrier absorption (FCA) in PV applications [33]. The FCA in metals and semiconductors is typically modelled by a Drude oscillator [35, 81]. The absorption coefficient is given by [33, 35]:

$$\alpha_{\text{FCA}} = \frac{\lambda^2 e^3 N_e}{4\pi^2 \epsilon_0 c^3 n (m_e^*)^2 \mu_{\text{opt}}} \quad (2.6)$$

where α_{FCA} is the absorption coefficient, N_e is the carrier concentration (assuming in n -type TCO), λ is the photon wavelength, e is elementary charge, ϵ_0 is the vacuum permittivity, c is the speed of light in vacuum, n is the refractive index, m_e^* is the effective electron mass, and μ_{opt} is the optical mobility. From equation 2.6, one can see that, higher N_e of the TCO layer accompanies more significant FCA in the NIR wavelength range. This is detrimental for high efficiency solar cells. As a device-relevant parameter, sheet resistance (R_{sh}) is usually utilized to evaluate the electrical properties of TCOs, rather than the conductivity as defined in equation 2.1 [33]. The R_{sh} could be calculated from

$$R_{\text{sh}} = \frac{1}{\sigma \cdot t} = \frac{1}{e \cdot N_e \cdot \mu \cdot t} \quad (2.7)$$

where t denotes the thickness of the TCO film. In solar cell utilization, low R_{sh} is required to ensure sufficient lateral carrier transport towards metal electrodes. Meanwhile, for the purposes of front anti-reflection coating (ARC) and back reflector (BR), the t values of 75 nm for front side use and 150 nm for rear side use in monofacial solar cells with passivating contacts are utilized in literature [82, 83] and in this dissertation. Both N_e

and μ act as the adjustable parameters to get a minimal R_{sh} . However, from equation 2.6, FCA is directly proportional to the carrier density. For this reason, high μ becomes a critical metric for reaching a trade-off between optical and electrical properties of the TCO film for high efficiency c-Si solar cell applications. In this dissertation, fluorine (F)- and tungsten (W)-doped In_2O_3 are developed for such a high μ purpose.

In addition, the collective motion of the conducting carriers make them behave as a kind of *plasma* in conductors. When light, namely an electromagnetic wave, is irradiated to the conductors, the carriers oscillate at the frequency of the light, which is called *plasma oscillation*. There is a characteristic threshold plasma frequency (ω_p) for causing plasma oscillation, which is determined by equation 2.8 [35, 53, 81]. One can also use the plasma wavelength (λ_p) given by equation 2.9. Basically, when the light is with higher frequency than ω_p , the carriers in the film cannot catch up with the fast electric field oscillation of the light. Thus, the light is transmitted through the conductors without causing the plasma oscillation or reflection at the film surface. However, when the light is with lower frequency than ω_p , plasma oscillation results in the reflection of the light at the surface of the conductors. Besides, an absorption peak could be observed in the long wavelength range due to the plasma resonance. Figure 2.2 shows the typical reflectance (R), transmittance (T), and absorptance (A) spectra of a metal oxide [84].

$$\omega_p^2 = \frac{N_e \cdot e^2}{\epsilon_0 \cdot m_e^*} \quad (2.8)$$

$$\lambda_p = \frac{2\pi c}{e} \sqrt{\frac{\epsilon_0 \cdot m_e^*}{N_e}} \quad (2.9)$$

where N_e , m_e^* , ϵ_0 and c denote carrier concentration (assuming in n -type TCO), effective electron mass, vacuum permittivity, and speed of light in vacuum, respectively. Like FCA, the plasma frequency is also dependent on the electrical parameter N_e of the TCO layer, which has been confirmed from experimental results [85].

In summary, degenerate doping is essential to realize TCO fabrication. In degenerately doped In_2O_3 -based TCOs, small electron effective mass resulting from great CBM hybridization affords large carrier mobilities. Besides, carrier scatterings coming from phonons, charged centers, and grain boundaries co-exist and obstruct the movement of the electrons in free pathways. Thus, the overall carrier mobility is determined from effective mass together with the free carrier scattering time. Furthermore, there is a trade-off between the carrier density and mobility within the TCO conduction mechanism. More importantly, there is another trade-off between the electrical and optical properties of TCOs. High carrier mobility is of critical importance to realize low sheet resistance, meanwhile maintain good transparency window. Developing In_2O_3 -based TCOs with high mobility, applying them in the crystalline silicon solar cells, and exploring efficient contacting schemes for the solar cells with passivating contacts, are the main objectives of this dissertation.

2.3. TCO deposition technologies

Rupprecht *et al.* [86] carried out one of the first investigations on an In_2O_3 semiconductor in 1954. Since then, a variety of thin film deposition techniques have been employed to

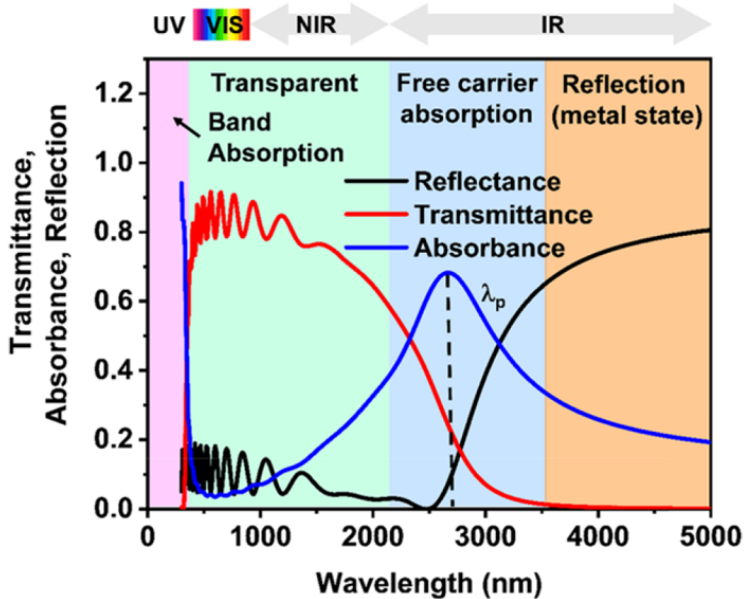


Figure 2.2: the typical reflectance (R), transmittance (T), and absorbance (A) spectra of a metal oxide [84].

deposit the In_2O_3 -based TCOs. As described in section 2.2, the properties of TCO films strongly depend on their stoichiometry, microstructure, and the presences of impurities. Thus, each deposition technique with its associated parameters yields films with different properties [35]. Depending on the deposition technique, the substrate can also have a significant influence on the properties of the films, which needs to be taken into account in device-oriented investigations [87–89].

Basically, TCOs can be deposited using a variety of vapour- or solution-phase techniques. Among the techniques, magnetron sputtering is an industrially mature technique and is the tool-of-choice for this thesis. A brief introduction of the magnetron sputtering approach is given in Section 2.3.1. Besides, other commonly used techniques for TCO deposition in PV field are listed in Section 2.3.2.

2.3.1. Magnetron sputtering

The term “sputtering” means the ejection of atoms from a usually solid target material due to the impact of highly energetic species. The primitive sputtering apparatus (discussed in 1852 [90] and invented in 1930s [91]) suffered from a low ionization efficiency of the electrons crossing the gap between the cathode (i.e., target) and the anode. Such drawback was circumvented using the magnetron configuration of the sputtering cathode (invented in 1970s [92]). This approach utilizes magnetic trapping of the electrons to confine the plasma close to the cathode. The magnetic trapping of the electrons and the corresponding ambipolar diffusion of the ions raises the plasma density in front of the target, hence the deposition rate is largely improved due to a much higher ion current. Moreover, reduced pressure could improve the film properties since less scattering in the

gas phase occurs [66, 93].

The highly energetic species are usually positive ions, which can be accelerated in the cathode sheath of a plasma discharge or in an ion source. The latter has limitations associated with scalability and power supply options [94], thus we exclude ion beam sources in this discussion. As for the plasma discharge, DC and Radio Frequency (RF, 13.56 MHz) excitations are commonly utilized in TCO depositions. In general, DC mode is typically used in the case of conductive materials, which prevents the accumulation of electric charge; while RF mode is versatile for depositing both conductive and non-conductive materials. Regarding the TCO sputtering growth, compared to DC sputtering, the RF sputtering could potentially produce good-quality films with better uniformity, homogeneity, less trap densities, and higher carrier mobility [66, 93, 95]. But utilizing RF sputtering can be more costly and limited to relatively smaller substrate sizes compared to DC sputtering. Possible interpretations on the comparison between DC and RF sputtering could be found in [95]. Besides, from the applicability point of view, both DC and RF sputtering could induce damage to the substrate surface in the TCO deposition process. The damage was reported to mainly result from particle bombardment in DC sputtering, yet ultraviolet radiation emission in RF sputtering [96]. However, the major sputtering induced damage can be recoverable by means of thermal treatment, which will be introduced in Section 2.4.3. Additionally, we note that the sputtering techniques are industrially applicable [97]. So far, high throughput production-scale sputtering tools are capable of processing up to 10,000 wafers per hour [98].

Furthermore, it is worth noting that virtually any material can be a candidate for sputtering growth. Films containing almost every solid element in the periodic table have been prepared by sputtering, and simple compounds can be sputtered with their stoichiometry preserved [66]. Therefore, sputtering can be applied to deposit a wide variety of materials. This may bring additional benefits when it is employed in PV industry, combining its advantages regarding ease of process integration, high productivity, no hazardous gas use, decent film uniformity, ease of in-situ doping, and guarantee of one-side deposition. Apart from TCO deposition, sputtering has also been developed at laboratory scale to deposit (doped) thin-film silicon layers [97, 99–101]. This can be beneficial from the following three aspects. Firstly, traditional LPCVD (Low Pressure Chemical Vapor Deposition) appears to be problematic in the pipeline of upgrading PERC to TOPCon, since double-side silicon layer deposition is unavoidable, leading to an extra procedure to etch away unwanted wrap-around on the wafer. This not only lowers production efficiency but also brings extra costs. Thanks to its single-side deposition nature, sputtering could perfectly circumvent such a dilemma. Secondly, due to the absence of hydrogen and low (or room) temperature deposition, blistering of the thin-film silicon layers is not an issue in sputtering, contrary to PECVD (Plasma Enhanced Chemical Vapor Deposition) techniques [102]. Thirdly, if so-desired, contacting schemes such as TCO and metal depositions could also be integrated in the thin-film silicon layer sputtering system. This may provide a possibility for highly modular platform design for PV device fabrication (for instance, with substrate pre-heating integration, without breaking vacuum).

Within this dissertation, we utilize RF magnetron sputtering approach to develop high-mobility In_2O_3 -based TCO films.

2.3.2. Other techniques

Other commonly used techniques for TCO deposition in PV field are briefly introduced in this section.

Evaporation

TCO films are deposited by thermal or electron beam evaporation of volatile source materials, under high vacuum. Both metallic and oxide sources can be employed. When pure or mixed oxides are evaporated, they reduce and form opaque films due to the presence of free indium in an In_2O_3 matrix. TCOs are subsequently obtained either by a post-oxidation step or by the oxygen introduction during evaporation. In order to realize decent opto-electrical properties for PV applications, a substrate or post-treatment temperature above 300 °C is normally required [35, 103]. This limits its application in low thermal-budget solar cells.

Pulsed-laser deposition (PLD)

PLD is an efficient flash-evaporation technique where a high power pulsed ultraviolet laser beam is utilized to vapourize the metal oxide target material in a plasma plume and deposit it as a thin film. This process can occur in vacuum or in a background gas, such as O_2 . As compared to sputtering, PLD can be a *soft* technique for TCO deposition, which could reduce the deposition damage on the underlying layers due to a lower kinetic energy of ablated species [104, 105]. Besides, PLD could operate at a relatively high deposition pressure, promoting thermalization of particles. This potentially leads to an easier stoichiometric mass transfer of the target material. For this reason, PLD could afford high-quality and high-performance films with well-controlled compositions and morphologies [104]. However, so far it is still not very applicable to production scales, because of limitations in large-area film uniformity, low deposition rates, and relatively high capital costs [32].

Reactive plasma deposition (RPD)

A generalized RPD technique could include a variety of methods in different terms, such as reactive ion plating [35, 106], arc plasma ion plating [107], ion plating with DC arc discharge [49], or high-density plasma-enhanced evaporation [108], reactive evaporation [109], reactive sputtering [110, 111]. Among the methods, the latter two are using reactive gas in the plasma environment, which limit the flux of plasma that involved in the deposition process. In a more common sense, the RPD method is treated as one of the evaporation-based ion-plating methods with an additional plasma generator. The evaporation source, which is the anode, is heated and evaporated by the electron beam via the magnetic field-controlled high-density plasma supplied from the pressure-slope type plasma gun. The evaporated particles are dissociated, activated and ionized in the high density plasma, so high reactivity can be achieved during film deposition, and high-quality TCO films can be fabricated at low temperature at substrate temperature below 200 °C or even at room temperature [107, 112, 113]. In particular, the utilization of shaped magnetic fields, which could generate a highly uniform plasma, provides the possibility to grow flat, uniform and large size thin films while the conventional plasma-related stability and repetitive problems are overcome. Schematic diagrams of RPD could be found in [106–108, 114]

Due to the aforementioned advantages, RPD is becoming a promising candidate for producing TCOs even in industrial environment [115]. Meanwhile, the plasma damage

issue has also been addressed in academic researches [116, 117].

Spray pyrolysis

Spray pyrolysis is a solution-based process in which a thin film is deposited by spraying a solution on a heated surface, where the constituents react to form a chemical compound. A post-annealing treatment is normally required to further improve the film quality. The chemical reactants are selected such that the products other than the desired compound are volatile at the temperature of deposition. So far, different kinds of TCOs have been formed by spray pyrolysis, such as ITO, IZO, AZO, IFO [118]. The biggest advantages of spray pyrolysis are non-vacuum technique (cost reduction), and tuneable composition of the target compound. However, the downside is that high temperature above 350 °C is generally needed to drive out solvents, or to induce reactions in film growth stage, or to crystallize the film in the post-annealing thermal treatment [119, 120]. This largely restricts its utilization in low thermal-budget solar cells.

2.4. TCO utilization in PV devices

2.4.1. Optical perspective

As mentioned in Section 1.2.2, the TCO films act as multi-functional layers in the c-Si solar cells with CSPCs. From the optical perspective, in our aimed SHJ and poly-Si solar cells, the TCO layers are deposited onto doped thin-film silicon layers (including both *n*-type and *p*-type). From optical perspective, the front side TCO layer in a solar cell acts as a transparent window and an antireflection coating (ARC). TCO, together with the entire front stack of layers, form a so-called refractive index grading stack. The front TCO thickness is commonly restricted to approximately 75 nm to obtain a light reflection minimum via destructive interference effects at about 600 nm, which is the wavelength at which one sun standard spectral irradiance peaks. Take ITO for example, using the equation $n_{\text{ITO}} \cdot d_{\text{ITO}} = \lambda/4$, where $\lambda = 600$ nm and $n_{\text{ITO}} \sim 2$, we obtain $n_{\text{ITO}} = 75$ nm [83].

Regarding the rear side TCO use in monofacial c-Si solar cells with CSPCs, a thick TCO is normally required to maximize the infrared response. Such a thick TCO layer helps to increase the internal reflectance at the rear surface of the solar cell, since it reduces the penetration of the evanescent waves to the metal reflector [82].

Alternatively, one can utilize a combination of TCO and dielectric layers (such as SiO_x) at the front and/or rear side(s) of the solar cell, to further reduce the reflection loss on the front side [121–123], and to lessen the parasitic absorption of the front and/or rear TCO layer(s) by decreasing the TCO thickness [123–125].

In this dissertation, our monofacial solar cell scheme was based on a setting with front 75 nm and rear 150 nm-thick TCO use, both sides 75 nm-thick TCOs were utilized in bifacial cell investigation, unless otherwise specified.

2.4.2. Electrical perspective

As elaborated in section 2.2, there is a trade-off between the optical and electrical properties of a TCO film. In_2O_3 -based TCOs with high carrier mobility may provide an ideal solution to maximize the function of TCO as transparent electrode in high-efficiency solar cells. Besides, RF magnetron sputtering, which is utilized in this thesis, could ensure a high-quality film deposition. However, at device level, more sophisticated considerations

need to be taken into account.

Figure 2.3 shows a typical set of TCAD Sentaurus simulated band diagram of a SHJ solar cell [126]. Specifically, for the n -contact, the TCO/doped silicon junction is isotype, which means that electrons are majority carriers on either side. For this side, a low work function (WF , $WF = E_{vac} - E_F$) of the TCO layer is preferable to lower down the transport barrier at the TCO/ n -type silicon layer interface. However, the TCO/ p -type silicon interface acts as a recombination junction. Holes in the p -layer valence band have to recombine with electrons in the TCO conduction band. Thus, for the p -contact, a high WF or electron affinity (E_{EA} , $E_{EA} = E_{vac} - E_c$) of the TCO layer is preferable to lower down the transport barrier at the TCO/ p -type silicon layer interface. Provided an electron affinity of ~ 3.9 eV for the thin-film silicon layer, with a band gap of 1.8 eV, and activation energy values of ~ 200 meV and ~ 400 meV in the n - and p -layer, respectively, ideal WF values of ~ 4.1 eV and ~ 5.3 eV could be roughly estimated for the TCOs in order to form preferable ohmic contacts at the n - and p -layer/TCO interfaces, respectively. The reported WF values for the n -type degenerate In_2O_3 -based TCOs basically fall into the range of 4.3–4.9 eV [127].

Contact resistivity (ρ_c) is a helpful metric for evaluating the contact properties. From our simulated results [126], the ρ_c of n -contact could be controlled below $20 \text{ m}\Omega \text{ cm}^2$ for an activation energy of below 190 meV in the n -type thin-film silicon layer, independent of normally used TCO carrier density ($1 \times 10^{19} \sim 1 \times 10^{21} \text{ cm}^{-3}$). This results from a low potential barrier and a favourable band bending in the n -contact side. While the ρ_c of p -contact can be orders of magnitude higher than that of n -contact. Therefore, the carrier transport at the p -contact normally interprets the main cause of the low fill factor in SHJ devices. Numerous efforts have been made to minimize the ρ_c of p -contact [128–132]. The high ρ_c of p -contact is mainly attributed to the intrinsic Schottky barrier that forms at the p -layer/TCO interface [133]. It is worth noting that with appropriate manipulation on the activation energy of p -layer and carrier density of TCO, tunneling is believed to facilitate an efficient carrier transport at the p -layer/TCO interface and result in minimal ρ_c values of the p -contact [129]. From simulation results, the ρ_c of p -contact could be minimized to below $30 \text{ m}\Omega \text{ cm}^2$ [126]. However, to the author's knowledge, no such low ρ_c value has been experimentally realized in the p -contact stack of SHJ devices so far. In addition, optical degradation may accompany the above-mentioned electrical engineering approaches, which needs to be considered in practical research.

Furthermore, there are other factors that need to be taken into account:

(i) Field effect passivation.

Field effect passivation is related to the band bending at the silicon surface. Take Figure 2.3 for example, for an n -type c-Si substrate, for the n -contact, the band bending at the c-Si surface favors its majority carriers (i.e., electrons) accumulating at the surface. It means the minority carriers (i.e., holes) are repelled from the surface towards the c-Si bulk, resulting in a decreased probability of recombination thus increased effective lifetime of the minority carriers.

While more complex case could occur at the c-Si surface in the p -contact. When a p -layer is deposited on top of an i -a-Si:H/ n -c-Si stack, a decreased passivation quality at low injection level and a decreased thermal stability of the passivation quality have been widely reported. Different reasons have been proposed [134, 135], such as defect-rich

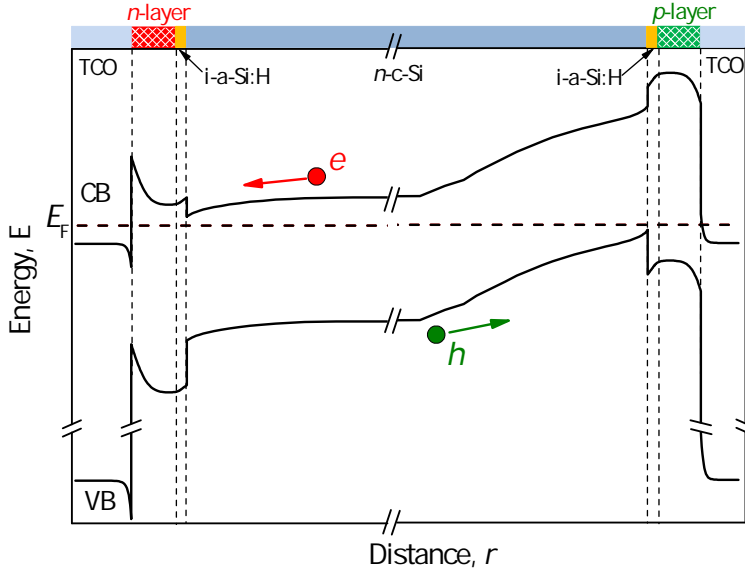


Figure 2.3: Schematic band diagram of a SHJ solar cell structure, from TCAD Sentaurus simulation [126].

p-layer acting as an effective recombination channel for the minority carriers, boron diffusion into the intrinsic layer, hydrogen effusing out from the underlying intrinsic film in *p*-layer growth process, and Fermi energy dependent defect generation at the *i*-a-Si:H/*n*-c-Si interface. When a TCO layer is deposited on the *p*-layer, the work function difference between *p*-layer and TCO further impacts the magnitude of the c-Si band bending. The band bending change is injection-dependent, thus it is observed that TCO on *p*-layer causes a reduction of charge carrier lifetime at low injection levels [136, 137], which leads to a decrease of the implied fill factor in the solar cell precursors.

In the dissertation work, we did not observe significant negative field effect influences after TCO deposition on the solar cell precursors of interest, thus it is assumed that such an effect is negligible or somehow hidden in the overall solar cell performances.

(ii) Interfacial oxide layer formation.

Unintentionally grown interfacial silicon oxide layer has been detected at the interface between TCO and silicon layers, since TCO acts as an oxygen source for the underlying silicon layer [138–140]. This is undesirable because such an interfacial insulating layer could hinder the carrier transport in device [130], and can even cause significant *S*-shape in device characteristics [141]. In recent years, the detrimental (or even fatal) influence of the interfacial oxide layer formation at the TCO/silicon interface is more reported on high thermal-budget poly-Si solar cells. Unlike low thermal-budget SHJ solar cell, the poly-Si solar cell experiences more severe deterioration in passivation quality after TCO sputtering step, which is hard to be recovered at post-annealing temperature of below 200 °C [142]. Under such circumstance, a post TCO deposition annealing treatment at above 350 °C was found to efficiently recover the passivation quality, whereas the contact resistivity at the poly-Si/TCO interface may increase by orders of magnitude

[142, 143], likely due to the interfacial oxide layer formation at the poly-Si/TCO interface [138, 144]. Additionally, the thermal treatment related interfacial oxide layer formation at the TCO/silicon interface also accompanies the opto-electrical properties change on the TCO layer, which needs to be taken into consideration in practical device fabrication. We provided a comprehensive investigation to address the above issues in high thermal-budget poly-Si solar cells, as interpreted in Chapter 5.

(iii) The material phase at the TCO/thin-film silicon layer interface.

Apart from doping capability, the material phase (such as amorphous, nanocrystalline, microcrystalline, or polycrystalline) also influences the interface properties when one material is in contact with other materials. It has been shown that the TCO/thin-film silicon interface properties are also correlated with the characteristics of both the thin-film silicon and TCO layers. Sheng *et al.* [145] examined the interface differences between TCO and thin-film silicon layers, found that amorphous silicon (n -a-Si:H) interfaces better with ITO film, while microcrystalline (n - μ c-Si:H) layer contacts better with ZnO film. The former result is somehow in agreement with our observation in fabricated SHJ devices, which shows a significant fill factor improvement when a thin n -a-Si:H layer is inserted between n -nc-Si:H and ITO [146]. We observed more oxygen presence at the n -nc-Si:H/ITO than the n -a-Si:H/ITO interface, and the doping capability of thin n -a-Si:H layer is higher than that in n -nc-Si:H layer, which could be the causes for the distinct difference in fill factor of devices. Besides, Silva *et al.* [147] reported that compared to the crystalline silicon, amorphous silicon film shows less reactivity with oxygen at the surface. The above results are mainly obtained from dedicated experimental explorations for different application purposes. Depending on different layers, layer stacks, and laboratory conditions, the results may differ. In addition, the material properties of the thin films can be thickness-dependent, which need to be taken into account in practical research. For instance, normally, a minimal layer thickness of (far) above 20 nm is required for the material characterizations such as Raman, FTIR, XRD, and DB-PAS. However, in device fabrication, the thin-film layer thickness may be less than 5 nm (or even lower) [146]. In such a case, the measured material properties on a thick film could be not representative for its practical use at device level. Accordingly, the deep understanding of the TCO/thin-film silicon layer interface is complicated and needs more *in situ* and high-resolution characterization techniques involved, which remains to be progressed in the future.

2.4.3. Sputtering damage

Apart from the aforementioned aspects, there is a widely-recognized challenge regarding the practical employment of sputtered TCOs in PV devices, namely, the sputtering damage. For a reference, the required energy to break the Si-H and Si-Si bonds in amorphous silicon layer are approximately 3.55 eV [148] and 2.5 eV [149], respectively. Whereas in sputtering process, the ion kinetic energy can be 7-70 eV [150], and the energy from particle bombardment could be up to 150 eV [151]. Therefore, the sputtering process could produce destructive influence in the material structure of thin-film silicon layers. Demaurex *et al.* [152] observed that the silicon-hydrogen configuration of the amorphous silicon film is permanently changed, although the electronic passivation quality of the a-Si:H/c-Si interface can be reversibly recovered.

Figure 2.4 depicts the electronic defects and carrier transport in a typical a-Si:H film

during plasma processing [153]. Electronic defects such as dangling bands (DBs) could be generated by ion bombardment, photon irradiation, radical exposure, particulate attachment, and surface charging. The former three are treated to be the main sources analyzed in literature [96, 137, 152]. Nunomura *et al.* [153] studied the defect kinetics in a-Si:H during Ar plasma treatment, and found that the defects are mainly generated by radical species such as metastable Ar atoms (Ar^*) in the plasma, rather than the Ar^+ ion bombardment. Meanwhile, the Ar^+ -ion bombardment creates residual defects, and the activation energy for the annihilation of defects is smaller for the plasma-induced defects (including radical exposure and ion bombardment), compared with that for photon-induced defects. Moreover, Demaurex *et al.* [152] experimentally compared the TCO sputtering damages at a-Si:H/c-Si interfaces by means of glass-shielding the plasma luminescence with photon energy above 4.7 eV or 7.8 eV. They found that the sample with no glass-shielding showed a 96% degradation in passivation, while the samples with glass-shielding only showed passivation degradation below 30%. Apart from the results from Nunomura *et al.* [153], this provides a more straightforward indication that both plasma- and photon-induced defects are contributors to the sputtering damage.

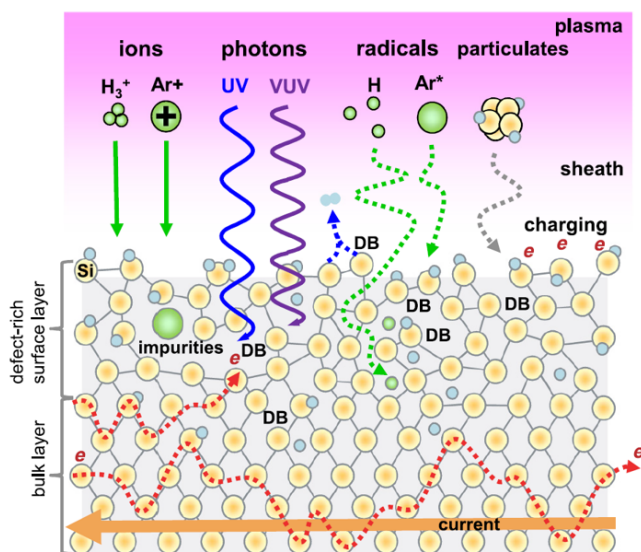


Figure 2.4: Electronic defects and carrier transport in a typical a-Si:H film during plasma processing [153]. The defects are distributed in a defect-rich surface layer, where weak Si-H and Si-Si bonds are broken and the local structure is disturbed. The carrier (electron) transport is highly limited in this layer, denoted by a zigzag line in the middle left. Underneath this, the bulk layer is located, where the local structure is intact. The carriers are transported mainly through this layer, denoted by a zigzag line in the lower part.

Thanks to the electronic reversibility, the sputtering damage could be cured with a post-annealing treatment, or post H₂ plasma treatment, or *in situ* deposition annealing process [96, 152–155]. However, it is worth noting that for different solar cell configurations, the activation energy requirement for the annihilation of defects can be different. We can take SHJ and poly-Si solar cells for examples. In a SHJ solar cell where TCO is

deposited on top of a-Si:H or nc-Si:H or $\mu\text{c-Si:H}$ thin films, it is widely reported that the sputtering damage could be almost fully restored by a low-temperature ($< 200\text{ }^\circ\text{C}$) post-annealing treatment [122, 155]. In other cases, TCO deposition on a heated substrate ($< 200\text{ }^\circ\text{C}$) could eliminate the sputtering damage on the SHJ solar cell precursor due to a self-curing process [122, 155]. Alternatively, with appropriate thin-film silicon layer use, such a self-curing process could occur even during room-temperature TCO sputtering process [156]. By contrast, in a poly-Si solar cell where TCO is grown on top of thin poly-Si layers, a curing temperature above $350\text{ }^\circ\text{C}$ is normally required [143]. These cases imply that the underlying layer of TCO also plays an important role in the origin of the defect generations, which was reported to be relevant to the subsequently required activation energy [153].

There are some interesting investigations that we would like to note: (i) the TCO sputtering damage in SHJ solar cell occurs regardless of the emitter doping level, but could depend on the thickness of the underlying thin film silicon layer [137, 157]; (ii) as mentioned, the Ar^+ ion kinetic energy can be 7-70 eV. However, Illiberi *et al.* [150] observed that the sputtering damage at the a-Si:H/c-Si interface is independent on the Ar^+ ion kinetic energy, but linearly proportional to the ion flux. Similar phenomenon was reported by Le *et al.* [158]. In addition, Nunomura *et al.* [153] attributed the dominance of Ar^* radicals in the defect generation over Ar^+ ions to the higher radical densities than ion densities. These observations might be a reflection that plasma-induced damage is more related to the flux, rather than the kinetic energy of the species; (iii) the impact of the sputtering-induced ion bombardment could reach the TCO/a-Si:H interface region through the TCO coating with a thickness of up to 20 nm [159]; (iv) The photon- and radical-induced defects could be recovered completely by a simple post-annealing treatment, but Ar^+ -ion-created defects may require an additional H_2 -plasma treatment beside post-annealing [153]; (v) hydrogen effusion from underlying thin-film silicon layers needs to be taken into account when analysing the passivation quality degradation upon TCO sputtering [160]; (vi) Si-Si bonds might account for the electronic reversibility in the curing step of sputtering damage, rather than the Si-H bonds [152]. These explorations may be beneficial to build up deep understandings of the sputtering-induced defect generation-annihilation mechanisms in the future.

Even though the defect generation-annihilation mechanisms on different solar cells are still not clear enough, various progresses have been made for putting the industrially applicable TCO sputtering technique into practice. Firstly, self-curing approaches have been widely used in SHJ device fabrications, i.e., the TCO is deposited on a heated substrate, such that the sputtering damage could be cured when TCO growth happens [122, 155]. Secondly, a two-step approach can be employed. For instance, one can apply consecutive low power and high power steps in TCO deposition, such that the sputtering damage on the cell precursors can be minimized, meanwhile optimal TCO properties could be maintained [159, 161]. Thirdly, air exposure of solar cell precursors before TCO sputtering might be helpful to reduce the detrimental sputtering damage [159, 162]. In addition, utilizing appropriate sputtering apparatus with favourable discharge excitation forms can be also helpful to realize free-damage sputtering [158, 163]. More recent studies can be found in [164–166].

In this dissertation, the sputtering damage issue is mainly addressed in the high

thermal-budget poly-Si solar cells (see Chapter 5). Under our lab-standard conditions, the thin poly-Si layer in poly-Si solar cells was observed to be more sensitive to the sputtering damage than the doped thin-film silicon layers in SHJ solar cells.

2

2.4.4. Material sustainability issue

As mentioned in Chapter 1, in the Paris Agreement in 2015, a target of limiting the global temperature increase to 1.5 °C above the preindustrial level in 2100 was set. In such a scenario, a rapid transition to *Net Zero* CO₂ emission needs to be reached by mid-century, and the global PV generating capacity is estimated to be about 70 terawatt (TW) by 2050 [167]. In early 2022, the PV industry has reached a cumulative capacity of 1 TW [168], which marks the dawn of TW era. Towards the TW scale utilization, sustainability issue regarding the material abundance needs to be addressed.

Indium is an element that is currently produced solely as by-products from the ores of other metals such as zinc, copper, tin [169]. As a by-product, indium benefits from sharing some production costs with its associated main product. Hence, the current indium price is lower than if it is produced by the host material of itself. However, in the long term, the availability of indium may still be problematic since it is one scarce element in the Earth's crust. The total reserves and resources of indium is approximately 50,000 tonnes, while the current global indium supply and use is around 1,000 tonnes per year [169]. Based on this estimation, the primary indium supply could only maintain roughly 50 years. Therefore, strategies to minimize the indium consumption need to be developed for PV technologies employed at TW-scale level.

Apart from indium, there are some other PV materials facing sustainability issues. One typical example is silver, which is utilized as the mainstream metal electrode in solar cells and the solderable metal for interconnection of solar cells in module production. The PV industry currently consumes about 20 tonnes of silver per gigawatt (GW). In 2019, 2,400 tonnes of silver was utilized in PV industry, which is more than 10% of the global silver production. Provided that 1 TW of PV production is reached at around 2028, the PV industry will use 100% of the global silver supply [167]. Strategies to minimize the silver consumption also need to be addressed.

So far, various alternatives have been developed regarding the material sustainability issues of indium and silver [170–172]. In this work, to reduce both the indium and silver consumptions in SHJ solar cells, we designed bifacial cell configuration with reduced TCO thickness, meanwhile, a bifacial electrochemical Cu-plating metallization approach was developed in our laboratory. Detailed investigations are elaborated in Chapter 7 and Appendix D.

2.5. Conclusions

This chapter gives an overview of the fundamental aspects involved in the TCO research. In order to reach a high carrier mobility, indium oxide is chosen as the host material in this work. Degenerate doping is essential to produce TCOs from the non-conductive host material. Moreover, extrinsic doping not only influences the carrier density, but also influences the carrier mobility. Different carrier scattering mechanisms could co-exist and determine the carrier mobility. In this work, to develop high-mobility TCOs, we

choose tin (Sn), fluorine (F), and tungsten (W) from different groups in the periodic table, as the dopants introduced into the In_2O_3 host material. Besides, RF magnetron sputtering is utilized to deposit the TCO layers, due to its advantages in producing high-quality films and industrial compatibility. The matters of interest regarding the TCO integration into PV devices are also briefly discussed.

3

Experimental

3.1. TCO sputtering

As mentioned, sputtering is based on ion bombardment of a target source material. To understand the physics behind the sputtering process, the interaction between the ions and the target comes as a first priority [94]. Figure 3.1 depicts a schematic picture of the sputtering mechanism [173]. In a simple sputtering system, the plasma glow discharge can be produced between two parallel plates in a vacuum chamber: the substrate (anode) and the target (cathode). Firstly, the process chamber is preventively evacuated up to high vacuum (1×10^{-7} mbar) to avoid contaminations. Then, the working gas (generally argon) is fluxed into the chamber, obtaining an appropriate equilibrium pressure (1-10 Pa). The plasma glow discharge is then ignited by applying a sufficiently intense electric field (E). This occurs through acceleration of the residual free electrons in the neutral working gas (produced by random event as cosmic rays or thermal collisions) that can eventually ionize neutral atoms. When ionization events are more frequent than recombination ones, an avalanche effect is produced, so that the plasma discharge is self-sustained [94]. Finally, the ion collisions with the target can give rise to a ballistic process that leads to the ejection of atoms. It is noteworthy that the E is normally realized by applying a high voltage (in the range of 2000 V). To define a glow discharge, one can follow the current-voltage (I - V) characteristics. Figure 3.2 shows the I - V characteristics of the plasma discharge for a wide range of currents [174]. Three general regions can be identified in the figure, namely, the dark discharge, the glow discharge, and the arc discharge. Each of these regions encompasses many interesting phenomena, and the sputtering is making use of the glow discharge. Detailed interpretation can be found in [94, 174]. In addition, it is important to realize that the plasma discharge also depends on the process parameters such as working gas(es), pressure, geometry of the electrodes (cathode and anode) and vacuum vessel, separation between cathode and anode, and the electrode material.

The sputtering yield is defined as the average number of atoms removed from the target surface per incident ion. According to a semiempirical model based on the linear

cascade collision theory, the sputtering yield can be estimated by the momentum transfer in the ion collision, and the surface binding energy of target material [94]. For a fixed energy and fixed target material, an optimal sputtering yield could be obtained when the masses of the projectile and the target atoms are equal. Argon could produce relatively high sputtering yield and high deposition rate due to its high molecular weight. Moreover, the inert argon gas does not react with the target material or combine with other process gases, making it an competitive candidate for working as sputtering gas.

3

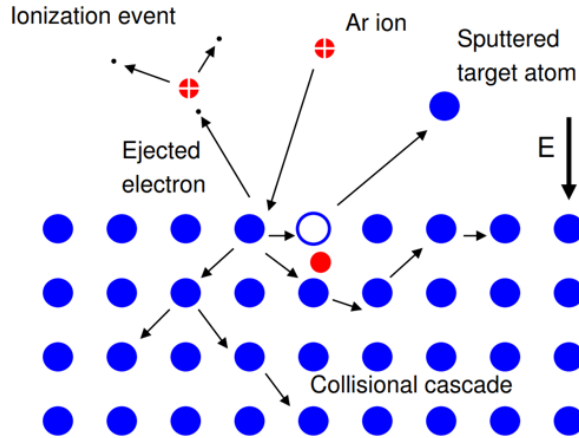


Figure 3.1: Schematic picture of the sputtering mechanism, in which E indicates the applied electric field [173].

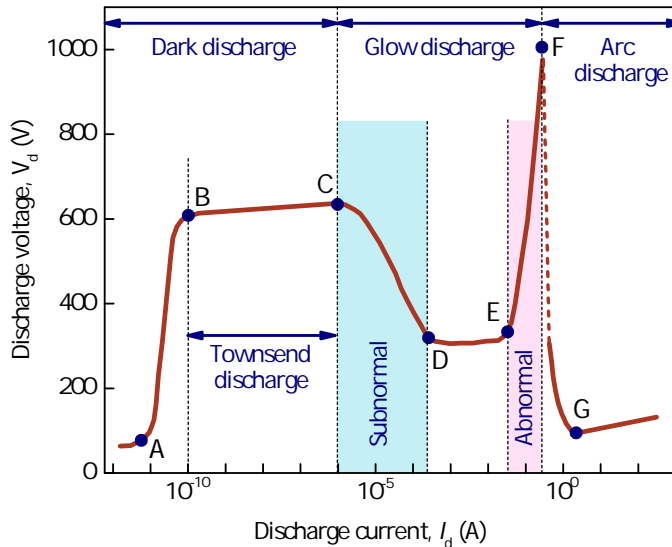


Figure 3.2: The current-voltage (I - V) characteristics of the plasma discharge for a wide range of currents [174].

In a simple glow discharge arrange, electron trajectories are only defined by the electric field between the cathode and the anode. Hence, the electrons are accelerated over the cathode sheath, and move with high velocity towards the anode. The classical approach to avoid the rapid loss of electrons from the discharge is to utilize the magnetron sputtering. Figure 3.3 shows the schematic diagram of a simple RF-magnetron sputtering system. In this strategy, magnets are applied behind the target, such that most of the kinetic energy of sputtered material can be transferred to the substrate, which reduces unwanted material erosion at other surfaces. Most importantly, the magnetron sputtering setting enhances the diffusion and reactivity of the species at the substrate surface, thus produces high-quality uniform TCO films at high growth rate [66]. The circular symmetry of the magnetic field typically produces the typical toroidal shape of the confined plasma region [173], which is also the case as we observed in the lab. Additionally, it is noteworthy that depending on the plasma excitation modes, the position and the float angle of the substrate can be tuned to reach an optimal plasma discharge and deposition result [163]. This is out of the discussion scope of this work. We performed our experiments in a RF-magnetron sputtering tool from Polyteknik AS, where the float angle of the substrate is approximately 45° with respect to the target surface, and the substrate holder is rotatable to ensure a good uniformity of the deposited film.

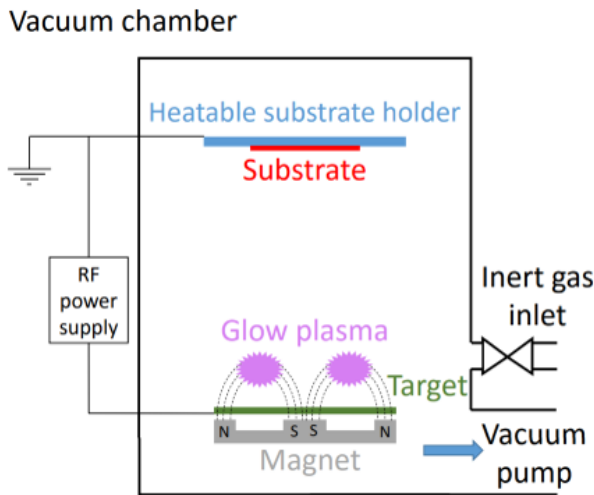


Figure 3.3: Schematic diagram of a simple RF-magnetron sputtering system [173].

In this work, TCO films were deposited on corning glass substrates by RF magnetron sputtering technique. The geometrical size of the corning glass piece is $10\text{ cm} \times 10\text{ cm} \times 0.7\text{ mm}$. Prior to sputtering, the glass substrates were cleaned in acetone and isopropyl alcohol sonication baths for 10 min, respectively. Commercially available 4-inch In_2O_3 -based targets were utilized. Specifically, the reference ITO films were deposited from a target containing 90 wt% In_2O_3 and 10 wt% SnO_2 ; the IFO films were grown from a so-called *SCOT* target product from Advanced Nano Products Co., Ltd. The F/(F+O) atomic ratio is measured to be 12% (see Chapter 4); the IWO films were prepared from a

target that consists of 95 wt% In_2O_3 and 5 wt% WO_3 . The process chamber was evacuated to a base pressure below 1×10^{-7} mbar before deposition to eliminate the contribution of the water during the processing. Argon was employed as the sputtering gas since it does not react with the target material or combine with other process gases, meanwhile it produces relatively high deposition rate due to its high molecular weight. Before deposition, the target was pre-sputtered for 5 min to remove any contaminants and eliminate any differential sputtering effects. The TCO film thickness is 75 nm unless otherwise specified. In addition, the TCO properties were found to be influenced by underlying thin-film silicon layers, thus we also prepared TCO films on top of Corning glasses which were coated with thin-film silicon layers. In such a way, we could obtain more realistic data to evaluate the TCO performance at device level.

3.2. Contact study and solar cell fabrication

Due to its strong dynamics in developing top efficiencies [7] and less susceptibility to carrier induced degradation [175], *n*-type solar cells were investigated in this work. The samples for contact study utilize the same functional layer thicknesses as that used in corresponding solar cells. Apart from that, in order to extract the contact resistivities of *n*- and *p*-contacts from vertical dark *I-V* measurements, *n*- and *p*-type wafers were utilized as substrates, respectively [143, 176]. Moreover, full-area PVD metal electrode was employed, rather than the metal grids as that used in solar cell fabrications. Figure 3.4 show an overview of SHJ and poly-Si monofacial solar cell configurations and the corresponding samples for contact study. For bifacial solar cell fabrication, the rear side contacting scheme (including TCO and metal) is the same as that utilized on the front side. In our experiments, there are multiple solar cells designed on one wafer. The cells have full-area emitter and FSF (or BSF) layers, and are separated with patterned TCO area by using hard masks in TCO sputtering step. The active area of the solar cells are described in corresponding chapters.

The procedure of extracting the contact resistivity (ρ_c) value is as follows. First, the resistance of the symmetric sample (R_{sample}) is measured via a Kelvin connection. Then, the contact resistance from all the contact interfaces (R_c) is obtained from $R_c = R_{\text{sample}} - R_{\text{bulks}}$, where R_{bulks} denotes the resistance from the c-Si absorber and thin-film layers in the contact stack. Finally, the ρ_c of the c-Si/*i/n*(or *p*)/TCO/Ag stack is calculated from $\rho_c = (R_c/2) \times S$, where S denotes the sample area, and the term “2” is utilized due to the symmetric nature of the sample. Since all the functional layers (including metal) are full-area prepared. The calculated ρ_c represents the overall contact resistivity at the contact stack which corresponds to the layer stack in the emitter or FSF (or BSF) side of the solar cell. Furthermore, considering that the TCOs are *n*-type degenerated semiconductor (behaving close to metal), and $\rho_{c,\text{metal/TCO}}$ values below $5 \text{ m}\Omega \text{ cm}^2$ are commonly reported in the literature [177, 178], we assume that the $\rho_{c,\text{metal/TCO}}$ variations are negligible in our samples. In such a way, the observed ρ_c differences mainly indicate the contact property change at the TCO/doped silicon layer interface.

To exclude the influences of metallic impurities and crystallographic defects in wafer base, high purity float zone (FZ) wafers were utilized in our lab [179]. Besides, for various solar cell concepts, parameters such as wafer thickness, bulk lifetime and base resistivity may also affect the optimal cell performances [180]. In the dissertation, we used a constant

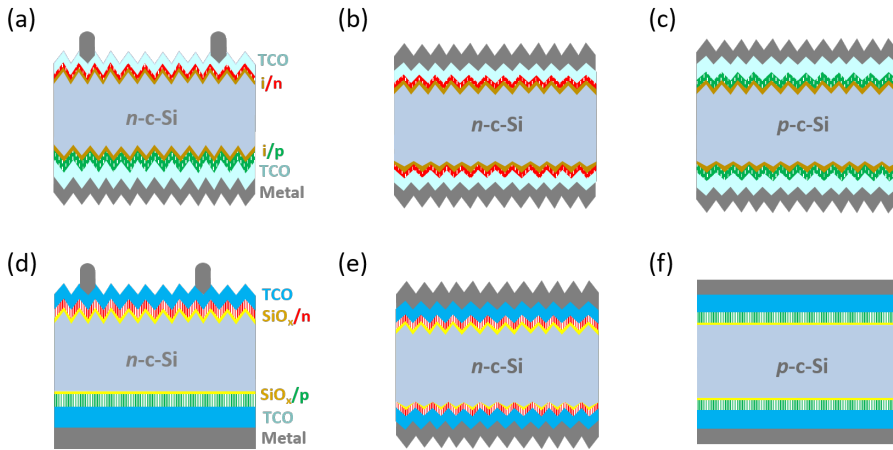


Figure 3.4: (a) Monofacial SHJ solar cell configuration and corresponding samples for (b) n -, and (c) p -contact study; (d) monofacial poly-Si solar cell configuration and corresponding samples for (e) n -, and (f) p -contact study.

type of 4-inch double-side polished FZ 280 μm -thick n -type flat (100) oriented wafers as the substrates for device fabrication, with a resistivity of 1-5 $\Omega\text{ cm}$. The wafers were randomly pyramidally-textured in a heated solution composed of 5% TMAH and 2.4% ALKA-TEX 8 from GP-Solar-GmbH. In such a manner, the incident sunlight is randomized inside the semiconductor in order to take maximum advantage of light-trapping in the high index of refraction absorber [181]. The pyramid feature size in our textured wafers was in the range of 1-6 μm . The (textured) wafer substrates were subsequently cleaned in two subsequent baths of a HNO_3 99% bath (RT, 10 min) and HNO_3 69.5% (110 $^\circ\text{C}$, 10 min) to remove the organic and inorganic contaminations, respectively. Wafers were freshly dipped in 0.55% HF for 4 min to remove the superficial oxide layer before loading for device fabrication procedures. To reach the nominal (reported) layer thickness, for the thin-film silicon layer growth in PECVD and TCO sputtering on textured wafer surface, the deposition time was chosen as the deposition time on a flat substrate multiplied by a factor of 1.7. For the thin-film silicon layer growth in LPCVD, a factor of 1.25 was utilized. The solar cell precursor optimizations (before TCO coating) are out of the scope of the discussion in this thesis, which will be only briefly described in the Experimental part of corresponding chapters.

3.3. Characterizations

During the thesis work, various approaches were utilized to measure the optical and electrical properties of the TCO films (including ITO, IFO, and IWO). To better understand the TCO properties, the structural, morphological, compositional, defect-related characterizations were also carried out. These aspects will be addressed in sections 3.3.1 and 3.3.2. Besides, device-related performances were evaluated in terms of contact study, cell precursor quality, as well as final solar cell parameters. Related measurements will

be briefly introduced in section 3.3.3. Furthermore, preliminary modelling work was performed to gain insights into the TCO materials and relevant contact properties, which will be introduced in section 3.4.

3.3.1. Opto-electrical properties of the TCO film

This subsection describes characterization approaches of the TCO film.

Part I. Thickness determination and optical characterization of the TCO film

The thickness of the TCO film can be determined from two approaches: (i) direct detection, such as step-profiler, scanning electron microscope (SEM); (ii) optical measurement with the assistance of appropriate model fitting. The latter strategy was utilized in our work, which is also widely employed for TCO characterizations in literature. Moreover, apart from the film thickness, the optical properties of TCO layers can also be evaluated simultaneously with the optical measurement approach.

In our work, the TCO film thickness (t) was determined by a Steag ETA-Optik mini-RT setup or a spectroscopic ellipsometry (SE) M-2000DI system (J.A. Woollam Co., Inc.). The sample is the deposited single TCO layer on Corning glass substrate. For mini-RT measurement, the film thickness value was obtained from Scout software fitting [182] on the quickly-measured measured reflectance (R) and transmittance (T) curves of the sample. With respect to mini-RT, the SE measurement is more powerful since it could provide multiple film parameters such as bulk thickness (t_b), surface roughness (t_s), optical mobility (μ_{opt}), Urbach energy (E_U) and complex refractive index (including refractive index, n , and extinction coefficient, k), and absorption coefficient spectra (α). The optical band gap (E_g) could also be extracted from Tauc plot based on the SE-fitted α curve [61]. In addition, SE also provides a solution to extract the TCO optical properties when deposited on top of thin-film silicon layers. In other words, both single and multi-layer strategy could be realized in SE modelling. This is of special importance for device-oriented investigations.

Figure 3.5 schematically depicts the basic principle of spectroscopic ellipsometry (SE) [183, 184]. Basically, SE is a reflection-type optical measurement, which utilizes the change in polarization state of light upon reflection to determine the optical properties of the samples. The sample induces a phase shift (Δ) between the polarization components of the reflected light which are parallel (subscript p) and perpendicular (subscript s) to the plane of light incidence. In addition, the corresponding absolute values of the reflection coefficients r_p and r_s are generally not equal. Therefore, linearly polarized light in general is converted into elliptically polarized light upon reflection. The complex reflection coefficients of the film are defined as the ratio of the reflected to incident electric field for both polarization, and can be extracted by mathematic fitting on the detected (Ψ , Δ) data. Besides, the most prominent features in SE data are oscillations when the film is transparent. The measured spectra exhibit peaks and valleys, referred to as *interference features*, due to constructive and destructive interference as the light recombines. The number and position of interference features depend on film thickness (t) and refractive index (n), while the oscillation amplitude is affected by optical contrast between film and substrate. Therefore, the SE approach is more flexible in using opaque sample substrates than mini-RT, but requires a distinct optical difference (such as refractive index) between film and substrate.

The SE setup consists of several optical elements, which are used to direct a beam with a defined polarization. In our measurements, to prevent backside reflections with transparent substrates, cloudy tape was applied on the backside of the glass substrates [185]. The measured photon energy range was 0.75-6.5 eV, while the incidence angles were 55°, 60°, 65°, and 70°. The spectra showed similar features with different angle variations on one sample. The data from 70° were selected for analysis due to its ideal graphing depolarization conditions near zero, which indicates that little light is reflected from the backside into the detector. For the SE analysis, the dielectric function of the TCO film was considered to be homogeneous in depth and modeled by a combination of a Cody-Lorentz oscillator and a Drude oscillator, to account for the absorption across the optical bandgap in ultraviolet (UV) range and the free carrier absorption (FCA) in the near infrared (NIR) part of the spectrum, respectively [186, 187].

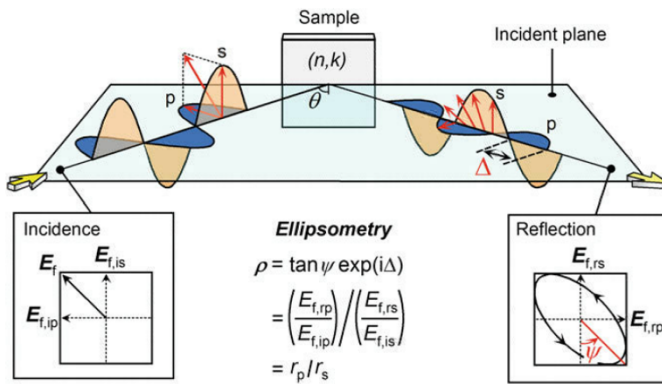
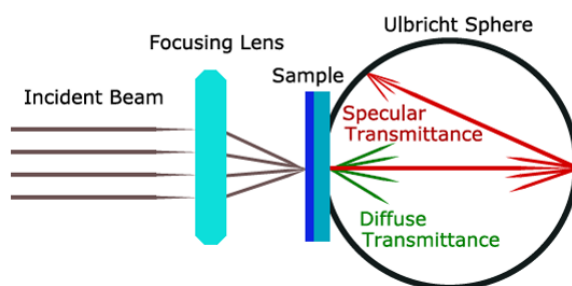


Figure 3.5: Basic principle of spectroscopic ellipsometry (SE) [183]. The waves indicated as “s” and “p” represent s- and p-polarized light waves. The oscillatory direction of the p-polarization is parallel to the incident plane of samples. SE measures the amplitude ratio Ψ and the phase difference Δ between the p- and s-polarizations. The n and k show the refractive index and extinction coefficient of the sample, whereas θ indicates the incident angle. The E_f shows the electric field vector and the subscripts “i”, “r”, “s” and “p” for E_f denote the incidence, reflection, s-polarization and p-polarization, respectively. The synthesized vectors for the p- and s-polarizations are indicated by red arrows. The SE parameters (Ψ , Δ) are defined by the amplitude reflection coefficients for p-polarization (r_p) and s-polarization (r_s).

Besides, the transmittance (T) and reflectance (R) spectra were obtained from a spectrophotometric PerkinElmer Lambda 950 or 1050 system. Figure 3.6 shows the schematic diagram of the configurations of the photo spectrometer [188]. The setups are capable of producing light beam in a broad wavelength range of 250-2450 nm, which covers the ultraviolet, visible, to near infrared (UV-Vis-NIR) wavelength range. The dual beam photo spectrometer is utilized, in which a deuterium lamp produces the UV light beam (till 319 nm), and a halogen Wolfram lamp that is in charge of the beam for the Vis-NIR light. Before measurements, the lamps are warmed up for 30 minutes to assure the desired intensity, and a calibration run without loading any sample on the device is executed to obtain the baselines for 100% and 0% transmission or reflection. In measurement, the light beam is divided in a reference beam and the beam that falls on the sample which are compared by the system. The detected intensity difference between the two beams

is collected. The incident beam goes through several lenses for the correct focusing and falls on the sample on a constant perpendicular path in both of the probable positioning of the samples. An Ulbricht sphere is installed to keep the reflected and scattered photons so that a photodetector can perceive the intensity of the light and yield the value of transmission or reflection. It is worth noting that there is a detector transition from photomultiplier to lead sulphide detector at 870 nm, which normally leads to a noticeable signal fluctuation upon this wavelength. The fluctuation is small, thus is generally not considered in the analysis of the measured spectral curves. In our measurements, the wavelength range of interest is 300-1200 nm, since it basically covers all the usable fraction of solar spectrum that the c-Si absorber can utilize. We did the measurements with a scanning step-size of 10 nm.

(a) Total/diffuse Transmittance



(b) Total Reflection

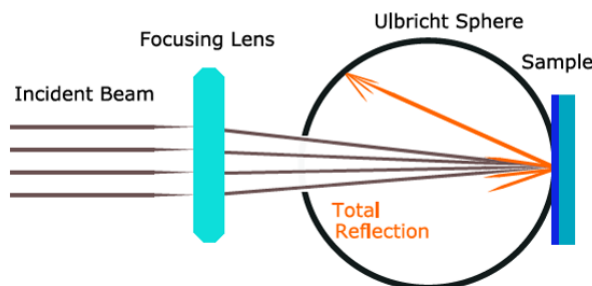


Figure 3.6: Schematic diagram of the configurations of the photo spectrometer [188]. (a) Total or diffuse transmittance. (b) Total reflection.

Besides the R/T data visualization of the TCO film, the spectrophotometric measurements also provides supplementary information in the following two aspects: (i) the reflective type SE has limited sensitivity for weak light absorption [183, 189]. Under such circumstance, one can calculate the absorptance (A) of the TCO film by $1-R-T$, which provides a direct analysing measure to evaluate the absorptive property of the transparent TCO film; (ii) the aforementioned Scout software fitting in mini-RT method can also be

employed here, such that the complex refractive index of the film can be extracted. The data on the optical properties of the TCO films from mini-RT, SE and spectrophotometry should be mutual-corroborative.

Part II. Electrical characterization of the TCO film

As described in Chapter 2, the main parameters to evaluate the electrical properties of the TCO film include: sheet resistance (R_{sh}), resistivity (ρ , $\rho = 1/\sigma$), carrier density (N), and carrier mobility (μ). In this subsection, the approaches to obtain these parameters will be introduced.

The R_{sh} of the TCO film is determined from the four-point probe (4PP) method, whose schematic diagram is illustrated in Figure 3.7. The 4PP technique is more accurate than the two-point method since independent contacts are employed for the applied current flow and the voltage measurement. Four equidistantly positioned contacts are linearly distributed in 4PP method. The two outer probes are used to enter small measurement currents, while the two inner contacts are utilized to detect the potential difference between them. In such a way, any voltage drop due to the resistance of the first pair of leads and their contact resistances is ignored by the meter. For the ideal case of an infinite extended film whose thickness is much smaller than the distance between the contacts, the R_{sh} is calculated after:

$$R_{sh} = \frac{U}{I} \cdot \frac{\pi \cdot t}{\ln 2} \quad (3.1)$$

The magnitude of R_{sh} is with the unit of Ω/\square to distinguish it from the conventional resistance R , whose unit is Ω . Further details on the 4PP method can be found in [190].

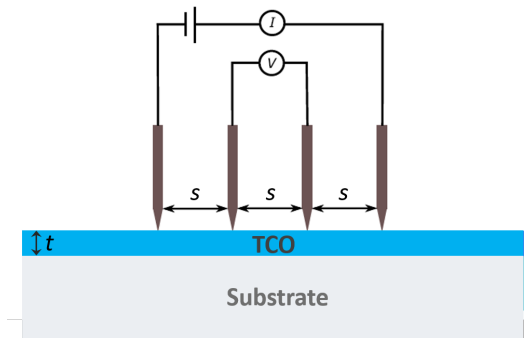


Figure 3.7: Schematic diagram of the four-point probe (4PP) method. I is the applied current, V is the voltage, t is the thickness of the TCO film, and s is the distance between the probe contacts.

The conduction type of the TCO films in this dissertation is n -type, which is confirmed from Hall measurements. Further, the electrical parameters of the TCO films, such as ρ , N and μ , are also measured from Hall measurements, in which ρ is measured by the so-called van der Pauw method, and N and μ are extracted combined with the Hall effect. Detailed information is described as follows.

In Hall measurements based on a traditional Hall bar geometry, the accuracy of the resistivity measurements is sensitive to the geometry of the sample. Van der Pauw found that the sample geometry can be extended to arbitrary shape, as long as the

contacts are small and at the edge of the sample, the sample layer is homogeneous, of uniform thickness, and geometrically holes free [191]. The commonly used van der Pauw geometries include square, circle, cloverleaf shaped structure. A qualitative sketch of the specimen we used in this thesis is shown in Figure 3.8(a). In this approach, the resistivity is automatically given by the expression from combined voltage-current readings and sample thickness value. The current is applied in the diagonal direction (such as A to C) in Hall effect work mode. In such a square structure, the measurement errors for resistivity and Hall coefficient are roughly proportional to $(c/L)^2$ and (c/L) respectively. Therefore, we kept a constant size with (c/L) below $1/20$, such that the measurement errors for resistivity and Hall coefficient could be reasonably kept below 0.1% and 5%, respectively. Besides, to make it safe, the offset voltage due to possible thermoelectric effects and misalignment in geometric symmetry and infinitesimal contact was corrected by reversing the direction of current flow and magnetic field during the automated measurements [192].

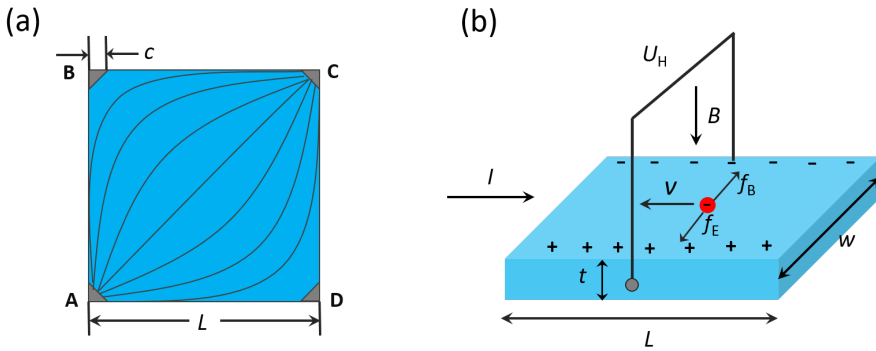


Figure 3.8: (a) The square shaped van der Pauw geometries in this work. (b) Schematic diagram of Hall effect. In our measurements, the sample length (L) equals the sample width (w) due the square shaped sample use.

The Hall effect was discovered by Hall in 1879 [193]. Initially, we shall assume a rectangular sample with constant thickness t , where a current I flows parallel to the sides as sketched in Figure 3.8(b). The resistivity (ρ) has been obtained from voltage-current reading based on the van der Pauw method as described above. When a magnetic field (B) is normally applied to the surface of the sample, a Lorentz force is formed, which could be expressed by $f_b = qvB$. This f_b is compensated by the electric field (E) resulted from the distributed mobile charge carriers in the sample. When $f_E = f_b$, the voltage between the opposite sides of the sample could be measured, which is called Hall voltage (U_H). Considering $f_E = qE = qU_H/w$, and $I = nqvwt$, then $U_H = IB/nqt$. The Hall coefficient R_H is defined as $R_H = U_H t / IB$, and n is deduced by $n = -1/qR_H$ (for n -type sample). This derivation is obtained under simplifying assumptions of energy-independent scattering mechanisms. With this assumption relaxed, the Hall scattering factor r , which accounts for the energy-dependence of the carrier scattering rate, needs to be introduced (typically between 1 and 2). In this case, the electron density is formulated from

$$n = -\frac{r}{qR_H} = -\frac{rIB}{qU_H t} \quad (3.2)$$

and

$$\mu = \frac{\sigma}{|n|q} = \frac{1}{|n|q\rho} \quad (3.3)$$

In the Hall measurements, as r is typically unknown, a “Hall mobility (μ_{Hall})” and accordingly “Hall carrier density (n_{Hall})” are defined by choosing $r = 1$. In this convention, the physically conductivity related mobility and carrier density correspond to $\mu = \mu_{\text{Hall}}/r$, and $n = r n_{\text{Hall}}$, respectively. In this thesis, we neglected r in our reported values since r is close to unity at degenerate semiconductors such as doped In_2O_3 [58].

We note that, according to the physical definition, $R_{\text{sh}} = \rho/t$. Theoretically, the measured ρ from the van der Pauw method in Hall measurement should be strictly consistent with the calculated data from 4PP measurements. However, discrepancy can happen from two aspects: (i) the probe contact issue in Hall measurement. For samples that are too resistive to make a good ohmic contact between the probe and sample surface needs to be ensured in Hall measurement, the measured ρ in Hall measurement could be higher than the actual value of the sample [194, 195]; while 4PP could give more reliable ρ values since it measures the potential difference in an independent loop, where the contact barrier between probe and sample surface is negligible [190]; (ii) the anisotropy of the material. The traditional van der Pauw method employs a four-point probe placed around the perimeter of the sample, in contrast to the linear four point probe. This allows the van der Pauw method to provide an average resistivity of the sample, whereas a linear array provides the resistivity in the sensing direction. This difference becomes important for anisotropic materials. In our work, we only observed the discrepancy in ρ values from 4PP and Hall measurement for not well-conductive TCO samples, such as the air-annealed IFO:H layer in Chapter 5. For most conductive TCO layers of interest for solar cell applications, the ρ values from 4PP and Hall measurement were quite comparable (equal or a few Ω/\square difference). Therefore, we assume that our In_2O_3 -based TCO films are basically isotropic and might be related to the high-quality film growth from RF magnetron sputtering technique. Moreover, good ohmic contact between the probe and sample surface needs to be ensured in Hall measurement, otherwise the contact barrier needs to be considered in the electrical measurement of a resistive sample.

Another thing is that, the electrical property of a TCO film is interactive with its optical property (see Section 2.2.4). As mentioned in SE measurement, a combination of a Cody-Lorentz oscillator and a Drude oscillator were employed in the SE data fitting. The latter accounts for the free carrier absorption (FCA) in the near infrared (NIR) part of the spectrum. According to equation 2.6, the FCA is proportional to the carrier density (N) value. Hence, the measured N values in Hall measurements should also be mutual-corroborative. In addition, by assuming the effective electron mass $m^* = 0.30 m_e$ and $N_{\text{opt}} = N_e$ from Hall measurements [37, 58, 60, 196], the optical mobility (μ_{opt}) could be extracted from the Drude fitting in SE data, via $\mu_{\text{opt}} = e\tau_{\text{opt}}/m^*$, in which e is the elementary charge, and τ_{opt} is optical relaxation time from Drude fitting [186, 196]. Such that the effect of grain boundaries (GBs) in the electron scattering mechanisms can be evaluated from the ratio between $\mu_{e,\text{Hall}}$ and μ_{opt} , because $\mu_{e,\text{Hall}}$ reflects all scattering phenomena, while μ_{opt} is not affected by GB scattering [60, 197].

Furthermore, apart from room temperature measurements, temperature dependence

of the electrical properties could be evaluated from Hall measurements. As described in section 2.2.2, the carrier scattering mechanisms in the TCO film are affected by thermal activation energy. Thereby, the inherent conduction mechanisms in the TCO film could be indicated by means of temperature-dependent Hall measurements, combined with the μ_{opt} extracted from SE fitting and defect (or doping) analysis strategies such as Doppler broadening positron annihilation spectroscopy (DB-PAS). The DB-PAS technique will be introduced in the following material characterization part. In this work, we carried out temperature-dependent Hall measurements on the IFO:H films that undergo different annealing treatments, which will be elaborated in Chapter 5. The temperature range in the Hall measurement was 200 K to 350 K. First, the measured film was cooled down to 200 K with liquid nitrogen, and the electrical properties were measured during heating up to 350 K [186].

3.3.2. Other material characterizations

Apart from the opto-electrical measurements, we also carried out various material characterizations on the TCO samples, to better understand the TCO properties.

Firstly, the crystalline nature of the films was studied with the X-ray diffraction (XRD) technique. The XRD spectra were obtained on an XPERT-PRO diffractometer system with spinning stage (Spinner PW3064), and a Cu $K\alpha$ radiation from the X-ray tube with normal focus was used (Cu $K\alpha=1.5406 \text{ \AA}$). The characterization was operated at 45 kV with a 2θ scan range of 10-90°.

Secondly, surface morphology scanning was carried out in NTEGRA PNL configurations from atomic force microscopy (AFM) mode at room temperature. A high accuracy non-contact composite probe consisting of a silicon body, polysilicon lever and silicon high resolution tip was utilized, whose resonant frequency is $120 \pm 10\%$ kHz. The scan area was set at $1 \times 1 \mu\text{m}^2$, and a topographic image consisted of 256 lines. Statistical roughness and grain analysis were conducted in NOVA program. Alternatively, morphological images of the samples (including TCO layers, metal fingers, wafer surfaces) were detected from field-emission scanning electron microscope (FE-SEM) via Hitachi Regulus 8230, or a low resolution SEM system from JEOL Ltd.. Besides, a confocal laser microscope (Keyence VK-X250) was utilized to obtain the optical microscope images of the metal fingers. Additionally, it is noteworthy that in Chapter 4, with the AFM setup, we also attempted to carry out some Kelvin probe force microscope (KPFM) measurements in air to estimate the TCOs' work function (WF) from the observed contact potential difference (CPD) considering gold as reference. Samples are based on cleaned 280 μm -thick n -type flat (111) oriented wafers as substrates, in order to mimic the (111) oriented crystal plane of the pyramids facets exposed after surface texturing for device fabrication. A conductive silicon-SPM-Sensor probe was utilized as the standard tip and the Z -position of tip was 10 nm. In order to minimize the temporary influence from the ambient air atmosphere on the static charging effect and to get clear comparative CPD values, repeated measurements were carried out [198].

Thirdly, fourier transform infrared spectroscopy (FTIR) was used to confirm the presence of hydrogen in the IFO:H film in Chapter 4, and to evaluate interfacial silicon oxide formation on TCO-coated c-Si wafers in Chapter 5. The measurements were performed in the NICOLET 5700 setup with a scanning range of 4000 - 400 cm^{-1} in nitrogen atmosphere.

A KBr beam-splitter and a transmission accessory were used. The measurements were done under dry nitrogen ambience with 1200 scans at a 4 cm^{-1} resolution. In Chapter 4, specified 500- μm -thick wafers with resistivity of 1-10 $\Omega \text{ cm}$ were used as substrates and reference. In Chapter 5, we firstly measured the FTIR spectra for all the four samples with one standard c-Si wafer piece as the reference sample, and the background spectra of the reference wafer was collected before each sample measurement. From this step, four measured spectra on four samples were obtained accordingly. Then, the measured spectra were analyzed by using the as-deposited IFO:H coated poly-Si stack as a baseline in the Omnic program. Based on such a baseline correction, signals regarding the IFO:H/poly-Si interfacial silicon oxide, which represents the most distinct part among the samples, were enlarged and can be easily recognized.

Fourthly, the chemical composition of the IFO film was studied using X-ray photoelectron spectroscopy (XPS) at the initial stage of this thesis work, since the target information was not disclosed by the supplier. Spectra were measured at 45° take-off angle relative to the surface plane with a PHI 5600 Multi Technique System (base pressure of the main chamber was 1×10^{-8} Pa). Samples were excited with Al $K\alpha$ X-ray radiation using a pass energy of 5.85 eV. Structures due to the $K\alpha$ satellite radiations were subtracted from the spectra prior to data processing. The XPS peak intensities were obtained after Shirley background removal [199]. The atomic concentration analysis was performed by taking into account the relevant atomic sensitivity factors. The instrumental energy resolution was ≤ 0.5 eV. Spectra calibration was achieved by fixing the main C 1s signal at 285.0 eV [200].

Further, to unveil the mystery of the magnetron-sputtered IFO film and its thermally annealed state, Doppler broadening positron annihilation spectroscopy (DB-PAS) was employed to explore the presence of open volume defects in relevant films. We did DB-PAS measurements using the mono-energetic low energy positron beam VEP at Delft University of Technology [201]. A liquid-nitrogen-cooled high-purity Ge (HPGe) detector with an energy resolution of 1.3 keV was utilized to determine the energy of the emitted positron-electron annihilation γ -rays. The line shape parameter S was calculated as the ratio of the central region ($|\Delta E| < 0.8 \text{ keV}$) of the 511 keV annihilation γ -ray photopeak to the total area, and the wing parameter W was defined as the ratio of wing regions ($2.1 \text{ keV} < |\Delta E| < 6.0 \text{ keV}$) to the total area. The Doppler depth-profiles collected in the range of 0.1-24 keV were fitted to extract S and W parameters of corresponding samples, using the VEPFIT program [201].

3.3.3. Device characterization and contact study

Part I. Passivation quality - minority carrier lifetime measurement

The effective minority carrier lifetime τ_{eff} was measured using the photoconductance decay (PCD) technique with the lifetime tester WCT-120 from Sinton Instruments, in a fast, contactless, non-destructive way. The tool illuminates the sample with a white light flash lamp and corresponding photoconductance decay, $\Delta\sigma$, of the sample is measured contactless with a calibrated radio-frequency circuit, which is inductively coupled to the sample's conductivity [202]. The decay of Δn generated by a short illumination is determined from the measured decay of the excess photoconductance $\Delta\sigma$, which is directly related to Δn :

$$\Delta\sigma = e\Delta n(\mu_n + \mu_p)W \quad (3.4)$$

where e is the elementary charge, W is the wafer thickness, μ_n and μ_p are the electron and hole mobility, respectively. For silicon, the variation of the carrier mobility with the carrier concentrations is well known, thus equation 3.4 can be solved iteratively to find Δn for each measured $\Delta\sigma$. The PCD measurements were either performed in the transient mode for samples with high passivation quality, or in the quasisteady-state mode (QSSPC) using a generalized analysis for samples with lower lifetime values [202]. Due to a minimum flash lamp decay time of 30 μs in the WCT-120 tool, transient-PCD measurements are limited to samples with τ_{eff} above $\sim 200 \mu\text{s}$. The lifetime curve is informative on the recombination mechanisms in the wafer bulk or the on the wafer surface, detailed elucidation could be found in [203–206]. The i - V_{OC} is calculated at one-sun illumination [188].

The maximum power point of a solar cell depends on both the wafer doping and the carrier injection level [207]. In this work, our wafer doping is approximately $1.5 \times 10^{15} \text{ cm}^{-3}$, and the reported the lifetime and i - V_{OC} values in this work corresponds to an injection level of $1.5 \times 10^{15} \text{ cm}^{-3}$.

Part II. SunsVoc measurements

SunsVoc measurements were performed for evaluating the electrical properties in our devices, via a Sinton Suns-Voc-150 Illumination-Voltage Tester. The principle of the SunsVoc technique is to measure the open-circuit voltage as a function of the light intensity. With a few assumptions, the data can be further analyzed to indicate the potential I - V curve that the solar cell/precursor would have if it could be made and measured with no series resistance. This can be extremely useful, since the presence of shunt and series resistance effects on the final device performance can be easily separated. Because the measurement is done under open-circuit conditions, the requirements of low-series resistance wiring and probes that would normally make cell measurements complex are avoided.

A comparison between SunVoc and the measured I - V data on final solar cell allow one to extract the series resistance of the device [208]. Combining the contact resistivity values obtained from the contact study samples, the carrier transport in vertical can lateral directions could be decoupled. The vertical carrier transport implies the TCO/doped thin-film silicon interface properties, and the lateral carrier transport is indicative of whether the R_{sh} is sufficiently low for device use.

Part III. I - V measurements

I - V measurements were utilized to obtain the solar cell parameters, with an AAA class Wacom WXS-90S-L2 solar simulator. For the bifacial solar cell measurements, a dedicated in-house sample stage was utilized, unless otherwise specified. Within this dissertation, the front side is depicted for the i/n side, and the rear side is meant for the i/p side of a bifacial SHJ solar cell. Besides, in the dedicated sample stage for the bifacial device measurements, one type of special substrate which shows a reflectance of below 3.5% along the wavelength range of 700-1200 nm was utilized. By directly mounting the wafer on the substrate in the I - V measurements, the rear side illumination, when measuring front side of the wafer, could be effectively controlled below 3 W/m^2 [209]. The I - V data were obtained on both sides of the SHJ devices separately. Subsequently, the bifaciality

factor, φ , was determined as the minimum of the ratios of the rear and front short-circuit current and maximum power, i.e., $\varphi = \min(I_{SC,back}/I_{SC,front}, P_{max,back}/P_{max,front})$ [209].

Furthermore, dark I - V measurements have been widely utilized in contact studies of various methodologies (such as transfer-length-method [177], circular-transfer-length-method [210], and the vertical sample measurement [142, 143]). The key point in these measurements is that, the overall resistance is very small (m Ω scale). Under this circumstance, the influence in the circuit loop as well as the contact resistance between the chuck(or the contacting probe) and the sample surface may not be negligible anymore, which arouse uncertainties in the resistance measurements. In this work, we utilized a Cascade33 Microtech setup in Else Kooi Lab at Delft University of Technology, with the electrical connections as sketched in Figure 3.9, unless otherwise specified. Symmetric samples as shown in Figure 3.4 were prepared for contact study, and vertical I - V measurements were carried out. The total resistance (R_{total}) of the symmetrical sample for contact study is measured from $R_{total} = (V_H - V_L)/I_{force}$. Similar in a four-point probe measurement, the potential difference ($V_H - V_L$) of the sample is collected separately without the influence of the applied current (I_{force}). Moreover, the influence from the sample chuck is eliminated, thus the accuracy of the resistance measurement could be ensured. Subsequently, the contact resistivity values of corresponding contact stacks were calculated following the procedure as described in Section 3.2.

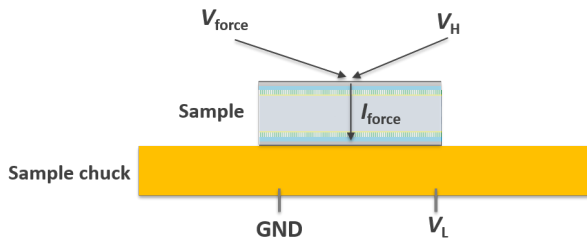


Figure 3.9: Schematic diagram of electrical connections in the I - V measurement for contact study.

Part IV. External quantum efficiency (EQE) measurement

The External quantum efficiency (EQE) is the ratio of the number of carrier collected by the solar cell to the number of photons of a given energy incident on the solar cell. If all photons of a certain wavelength are absorbed and the resulting minority carriers are collected, then the quantum efficiency at that particular wavelength is unity. EQE curve is indicative on the spectral response of the solar cell, and the short-circuit current density that derived from the EQE integration is denoted as $J_{SC,EQE}$. An in-house EQE setup was utilized in this work, with the wavelength range of interest of 300-1200 nm. We note that in this work, the *active area power conversion efficiency* of the devices was calculated from the product of V_{OC} , FF , and $J_{SC,EQE}$.

3.4. Modelling

In order to evaluate the optical performance of the TCO films (ITO, IFO, and IWO) at device level, we performed simulations via ray-tracing GenPro4 optical model [211]. The

simulations of our SHJ device structures were performed based on double-side textured c-Si wafer with SE-fitted complex refractive index of each functional layer as input. For the simulations on bifacial cells in Chapter 7, we used a rear side irradiance of 100 W/m^2 . A superposition principle was employed to calculate the implied photocurrent densities in c-Si absorber ($A_{\text{c-Si}}$). Specifically, $A_{\text{c-Si}}$ values of the front and rear side illumination were separately obtained at a default 1000 W/m^2 , which were $A_{\text{c-Si,front}}$ and $A_{\text{c-Si,back,0}}$. Then the overall $A_{\text{c-Si}}$ value was calculated via $A_{\text{c-Si}} = A_{\text{c-Si,front}} + 0.1 \times A_{\text{c-Si,back,0}}$.

Besides, we attempted to interpret the observed carrier transport behaviours in contact study by combining simulation work (see Chapter 7). A first-principles density-functional theory (DFT) study was carried out via the Vienna Ab initio Simulation Package (VASP). Based on the projector augmented wave (PAW) method, the equilibrium geometric and electronic structures of In_2O_3 (IO), ITO, IFO, and IWO were calculated. The Perdew-Bruke-Ernzerhof (PBE) exchange-correlation functional was applied. The conventional cell of bixbyite In_2O_3 of 80 atoms was subjected to a geometrical optimization. A 400 eV plane wave cut-off energy and a Γ -centred k-point grid of $3 \times 3 \times 1$ were utilized. The convergence criterion was below 0.01 eV/\AA . To mimic the materials as we utilized in the lab, for ITO, three In 8b sites were replaced by Sn atoms; for IFO, five oxygen sites were replaced by F atoms; and in IWO, one In 24d site was replaced by W atom. The effective electron mass was obtained in the ab initio calculation through fitting the curvature of the conduction band [73]. The work function (WF) of a TCO was obtained from an additional simulation, in which a vacuum slab was added in the input file and the WF was extracted by taking the potential at the center of the vacuum [212].

3.5. Conclusions

This chapter provides a brief introduction of the experimental details in this dissertation, including the deposition conditions of the TCO films, device fabrication, various characterizations of the samples, and the modelling details regarding optical device simulations and density functional theory calculations of the TCO materials.

4

High- μ_e IFO:H in low thermal budget c-Si solar cells with CSPCs

This chapter was published in *ACS Applied Materials & Interfaces** [213]

Abstract

Broadband transparent conductive oxide layers with high electron mobility (μ_e) are essential to further enhance crystalline silicon solar cells performances. While metallic cation doped In_2O_3 thin films with high μ_e ($> 60 \text{ cm}^2 \text{V}^{-1} \text{s}^{-1}$) have been extensively investigated, the research regarding anion doping is still under development. Here, we investigate the properties of hydrogenated fluorine-doped indium oxide (IFO:H) films processed at low substrate temperature and power density by varying the water vapour pressure during deposition. The optimized IFO:H film shows a remarkably high μ_e of $87 \text{ cm}^2 \text{V}^{-1} \text{s}^{-1}$, carrier density of $1.2 \times 10^{20} \text{ cm}^{-3}$ and resistivity of $6.2 \times 10^{-4} \Omega \text{ cm}$. We analyzed compositional, structural, and opto-electrical properties of the optimal IFO:H film. Besides, we implemented the IFO:H film into different front/back-contacted solar cells with passivating contacts. With respect to our lab-standard ITO counterpart, a significant short-circuit current gain of 1.53 mA/cm^2 was observed in the IFO:H-based silicon heterojunction solar cell. The best solar cell shows a conversion efficiency of 21.1%.

*C. Han, L. Mazzarella, Y. Zhao, G. Yang, P. Procel, M. Tijssen, A. Montes, L. Spitaleri, A. Gulino, X. Zhang, O. Isabella, and M. Zeman, "High-Mobility Hydrogenated Fluorine-Doped Indium Oxide Film for Passivating Contacts c-Si Solar Cells," *ACS Applied Materials & Interfaces*, 11(49), 45586-45595, 2019. November 22, 2019, doi: 10.1021/acsami.9b14709.

4.1. Introduction

Metal-doped and/or hydrogen-doped In_2O_3 thin films with high μ_e ($> 60 \text{ cm}^2 \text{ V}^{-1} \text{ s}^{-1}$), such as H [76], Ce [49], Zn [214], Ti [215], Zr [216], W [217], Mo [218], Hf [219], have attracted considerable attention. In these cases, the metallic cation doping species substituting In atoms mainly act as a donor; besides, they decrease the residual strain and the contribution of the grain boundary scattering to carrier transport, which could be enhanced by the co-doping with hydrogen [49]. On the other hand, the study with respect to anion doping is, to our knowledge, still not fully developed, even though fluorine dopant has been found to present high mobility in the early 1980s [220].

Different approaches have been utilized to fabricate conductive fluorine doped indium oxide (IFO) films, such as chemical vapour deposition at $350 \text{ }^\circ\text{C} - 450 \text{ }^\circ\text{C}$ [221], pyrosol approach at $310 \text{ }^\circ\text{C} - 500 \text{ }^\circ\text{C}$ [120, 220], electron-beam evaporation at $450 \text{ }^\circ\text{C} - 520 \text{ }^\circ\text{C}$ [222, 223]. Some reports on reactive ion plating [194] and RF magnetron sputtering [224] at room temperature showed rather high initial resistivity ($> 1 \times 10^{-3} \text{ } \Omega \text{ cm}$), requiring an annealing step at temperature above $400 \text{ }^\circ\text{C}$ for yielding a highly conductive and transparent film. The ion radius of F^- (1.36 \AA) is close to that of O^{2-} (1.40 \AA) and substitutional replacement of F^- with O^{2-} is expected to cause minor distortion to the In_2O_3 lattice [224, 225]. In terms of material properties, IFO film was found to have comparable conductivity and better optical transmission in comparison with indium tin oxide (ITO) [120, 226]. It is noteworthy that Untila *et al.* have applied the pyrosol synthesized IFO film to IFO/*p*-Si heterojunction and bifacial c-Si solar cells for low-concentration systems [120, 227, 228]. Such high-temperature process limits the application of IFO in low-thermal budget architectures; furthermore, the process is prone to develop an insulating SiO_x between the IFO film and doped layers [227]. At present, the low-temperature deposition method of IFO film has not been well explored, and there has been little work on its application in solar cells with passivating contacts.

In this paper, we prepared high- μ_e hydrogenated fluorine-doped indium oxide (IFO:H) films with RF sputtering at low substrate temperature and low power density. The compositional, structural, and opto-electrical properties were characterized. Furthermore, we validated the use of IFO:H in different solar cells with CSPCs, with indium tin oxide (ITO) as reference. Experimental improvements were observed. Especially the SHJ cell with double-side IFO:H demonstrates distinct optical enhancement without any losses in fill factor (FF) and V_{OC} , making IFO:H a strong candidate for multi-purpose applications such as FBC and IBC c-Si solar cells or perovskite/silicon tandem solar cells.

4.2. Experimental

The experimental section includes the following parts.

Materials. The IFO:H film was sputtered at substrate temperature $105 \text{ }^\circ\text{C}$, Ar flow 50 sccm , chamber pressure 2.50 Pa , power density 1.8 W/cm^2 , and variable water vapour partial pressure. For comparison purpose, ITO films were deposited at substrate temperature $105 \text{ }^\circ\text{C}$, Ar flow 40 sccm , chamber pressure 2.20 Pa , power density 1.7 W/cm^2 .

Contact samples. The contact resistivity between the 75 nm -thick TCOs and screen-printed silver (SP, Ag) was studied with the transfer length method (TLM) on the samples [177] as shown in Figure 4.1 (a). Wafers with insulating SiO_x coating layer were used as

substrates to restrict the lateral current flow to the subsequently deposited TCO layers.

Device fabrication. The tested solar cell structures are illustrated in Figure 4.1 (b). Two are so-called hybrid type [229, 230], combining high- and low- thermal budget processing routes (poly-Si_x hybrid and poly-Si hybrid), and one is SHJ type. The i-a-Si:H, nc-Si(O_x) and n-poly-SiC_x layers were grown by plasma enhanced chemical deposition (PECVD). The n-poly-Si layers were prepared via low pressure chemical vapor deposition (LPCVD). Further details about the fabrication process can be found elsewhere [231]. Both front and rear metal contacts were screen printed obtaining cells with area of 7.84 cm².

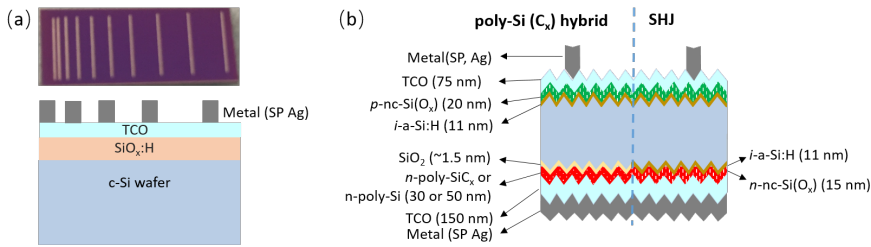


Figure 4.1: Sketches of (a) TLM samples (picture inset), and (b) solar cell structures (poly-Si(C_x) hybrid on the left-hand side, SHJ on the right-hand side). SP Ag stands for screen-printed silver.

4.3. Results and discussion

4.3.1. H₂O vapor pressure influence on the as-grown films

Water (H₂O) vapour was intentionally introduced in the system during deposition as hydrogen source, which has been found to be favourable to promote high mobility TCOs, such as IO:H, ICO:H, IWO:H, etc [197]. Hall measurements show that all the fabricated films are *n*-type. Figure 4.2 shows the electrical properties of as-deposited layers under different H₂O vapour conditions. It can be seen that the resistivity (ρ) decreases significantly with the introduction of H₂O vapor from 1.6×10^{-2} Pa to 2.2×10^{-2} Pa caused by simultaneous improvement of both carrier density (N_e) and electron mobility (μ_e). The ρ value reaches a plateau for H₂O vapour pressure $> 1.8 \times 10^{-2}$ Pa; the minimum ρ (6.2×10^{-4} Ω cm) appears at the H₂O vapour pressure of 1.8×10^{-2} Pa, with a maximum μ_e ($87 \text{ cm}^2 \text{ V}^{-1} \text{ s}^{-1}$) and an N_e of $1.2 \times 10^{20} \text{ cm}^{-3}$. The μ_e value is remarkably high and to our knowledge, it is the highest mobility value among the as-sputtered In₂O₃-based TCO materials at low temperature below 110 °C.

4.3.2. Optimized IFO:H analysis

XPS was carried out to study the electronic structure of materials and identify the chemical composition of the optimal as-grown film. It should be noted that, sputtered In₂O₃-based materials have rather good uniformity in depth profiling [232], thus XPS results could represent the bulk quality although it provides the near surface region information [199]. Figure 4.3(a) shows the wide scanning XPS spectrum in the binding energy range of 0-1200 eV. The In 3d, O 1s and F 1s signals were detected, and C 1s signal came from the adventitious contamination from the air environment [200]. No signals of other elements

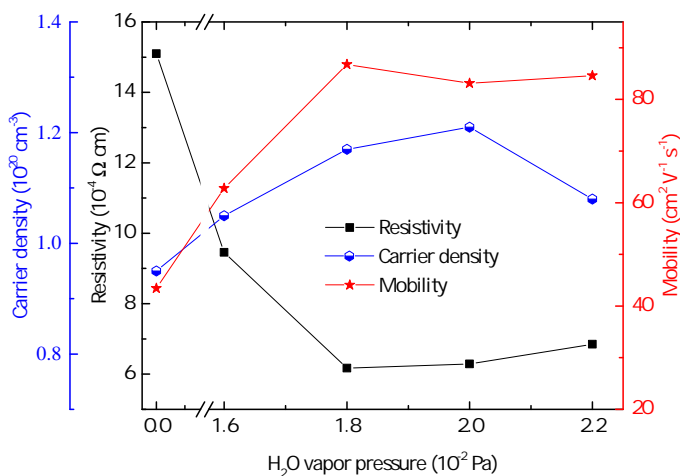


Figure 4.2: Resistivity(ρ), carrier density (N_e) and Hall mobility (μ_e) of as-grown In_2O_3 -based films as function of variable H_2O vapor pressure.

were detected. In particular, the observed energies at $\text{In } 3d_{5/2}$ and $3d_{3/2}$ states are located at 444.8 and 452.4 eV, respectively (as shown in the inset of Figure 4.3(a)), which closely match the binding energy of In^{3+} in In_2O_3 [233], and confirm the fluorine doped In_2O_3 composition of the film [234].

Figure 4.3(b) shows the O 1s XPS spectrum of the IFO:H film, which is fitted using three Gaussian components centered at 530.4, 532.2, and 533.7 eV. In_2O_3 crystallizes with a bixbyite structure in which each indium atom is surrounded by six oxygen atoms at the corners of a distorted cube, vacancies form at the unoccupied sites. According to the reported data [225], the lower energy peak located at 530.4 eV corresponds to O^{2-} ions which have neighbouring In atoms with their full octahedral coordination environment, whereas the higher energy peak located at 532.2 eV is assigned to O^{2-} ions in oxygen-deficient sites. Besides, the 533.7 eV peak is attributed to -OH groups, either from the film itself or from the air exposure, which will be further discussed by FTIR approach. Figure 4.3(c) shows the F 1s XPS spectrum of the IFO:H film. It has been discussed that a fluorine atom substitutes an oxygen atom generating a free electron or occupies an oxygen vacancy site eliminating an electron trap site. Fluorine ions with strong electronegativity could form hydrogen bonds with hydroxyl groups thus passivate the hole trap sites of the hydroxyl groups [225]. The F 1s spectrum was fitted using three Gaussians at 684.8, 686.0 and 688.2 eV. Correspondingly, the component at 684.8 eV is related to fluorine of the In-F bond in the IFO film; the component at 686.0 eV is due to fluorine that occupy the oxygen vacancies; finally, the component at 688.2 eV is related to the F ions that form hydrogen bonds with surface hydroxyl groups [225, 235].

The composition results show that the atomic ratio of $\text{In}/(\text{O}+\text{F})$ is 0.69, similar to the reported values of In_2O_3 films [226]. An oxygen deficiency of 3% has been observed with respect to the stoichiometric composition. Moreover, the $\text{F}/(\text{F}+\text{O})$ atomic ratio indicates a 12% fluorine-doping, and F/In atomic ratio was calculated to be 17.4%. It has

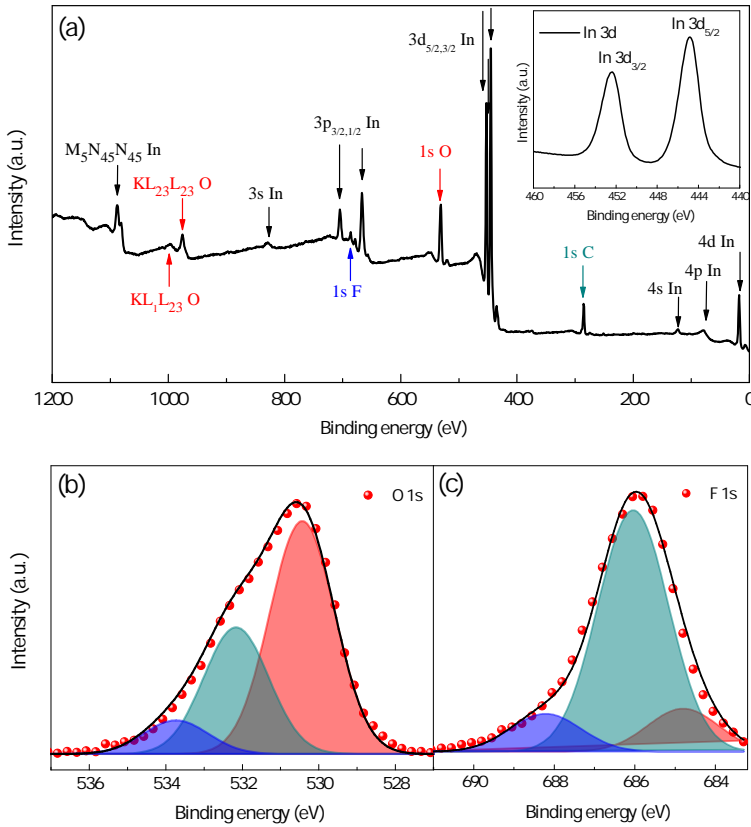


Figure 4.3: (a) XPS wide scan, with inset of In 3d core-level XPS spectra, (b) O 1s, and (c) F 1s core-level XPS spectra of the as-sputtered IFO:H film. The scatter plots in red colour represent the experimental profiles and the solid lines refer to the Gaussian components.

been reported that the F/In ratio has a significant influence on the contact properties between IFO and *p*-/*n*-type *c*-Si, regardless of the possible oxygen content variation [236]. According to Untila et al. [236], the ratio of 17.4% is in a region that IFO film forms ohmic contact with *n*-type *c*-Si, yet rectifying contact with *p*-type *c*-Si. We have to note that the properties of TCOs are affected by various deposition technologies. The contact issues between our IFO film and adjacent layers will be discussed in the following sections.

FTIR measurements were carried out to verify the existence of hydrogen. By comparison, a reference IFO sample with the same thickness without water vapour in the deposition was also measured. Figure 4.4(a) shows the FTIR spectra of the as-deposited samples. The bands at around 1600 cm^{-1} and 3400 cm^{-1} could be attributed to bonded OH bending and stretching vibrations, respectively [237, 238]. The bands may come from either the films or physically adsorbed water [239], yet from a comparison between the sample with and without water vapour in the growth process (especially at 3400 cm^{-1}), shift and intensity of the peaks changed significantly upon H_2O vapour introduction, indicating strengthened hydrogen bonds and related redistribution in the IFO:H film [237].

Thus, the existence of hydrogen could be proved. Besides, the observed bands in the 400-800 cm^{-1} region may be attributed to the characteristic M-O vibrations corresponding to In-O in the films [237, 240]. No fluorine-related band was observed.

Furthermore, FTIR is also an informative method to estimate the conduction band electrons in *n*-type semiconductors. The absorbance exhibited by IFO:H in mid-IR region ($> 1000 \text{ cm}^{-1}$) has positive correlation with the number of conduction band electrons in the film [241]. The results clearly indicate that water vapour in the deposition process can increase the conduction band electrons in the IFO:H film, and hence, improve the conductivity of the film. The results are in good agreement with the data reported in Figure 4.2, and the higher N_e could be attributed to the hydrogen acting as shallow donors [60, 63]. The above results indicate that the higher μ_e of the IFO:H film might be presumably attributed to contributions from the elimination of electron trap sites from fluorine doping [66, 225] and possible grain-boundary passivation by hydrogen [33, 60], both of which lower the potential barriers thus benefit the carrier transport in the film [60, 66].

Figure 4.4(b) shows the XRD spectrum of the optimal IFO:H film. All peaks can be assigned to the cubic bixbyite structure of In_2O_3 , which matches with ICDD database version PDF4+ reference code no. 04-004-8968, indicating that the IFO film retains the polycrystalline cubic In_2O_3 structure [242]. The strongest (222) diffraction peak at 30.55° is conspicuous, other peaks were assigned accordingly [224, 243]. Besides, the broad background peak at around $2\theta=22.28^\circ$ is related to the glass substrate [244]. Furthermore, the mean crystallite size was calculated to be 29.85 nm from full width at half maximum (FWHM) of X-ray peak of (222) following Scherrer's formula [245].

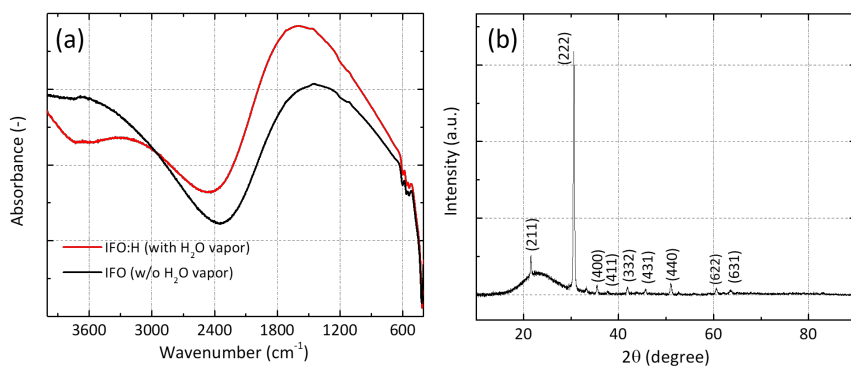


Figure 4.4: (a) FTIR spectra of the IFO:H and IFO films, (b) X-ray diffraction pattern of the optimized IFO:H film.

To understand the surface quality and growth morphology, the surface morphology and roughness of the IFO:H film were measured by atomic force microscope (AFM), as shown in Figure 4.5. The film exhibits a rather smooth surface with a root-mean-square (RMS) roughness of 0.52 nm.

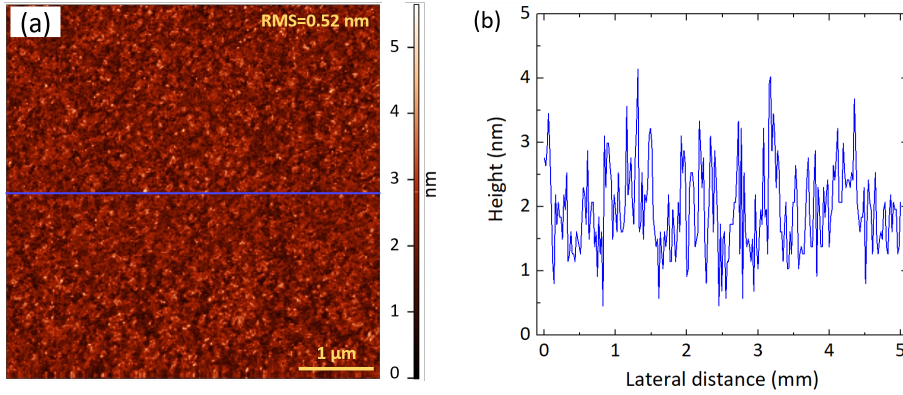


Figure 4.5: (a) AFM micrograph of the optimal IFO:H film, (b) cross-sectional profile along the line in (a).

4.3.3. Comparative opto-electrical properties with ITO

The electrical properties of the optimized IFO:H layer are listed in Table 4.1 and compared to those of our lab-standard ITO reference. It was found that introduction of fluorine causes an abrupt increase of μ_e in fluorine-doped tin oxide (FTO) film, due to fluorine dopant lowering the transport barrier at the grains' boundaries [246]. In terms of physical definition, $\mu_e = e\tau/m_e^*$, where μ_e is the electron mobility, τ and m_e^* are carrier relaxation time and electron effective mass, respectively. It has been theoretically [37] and experimentally [197] found that high- μ_e TCO films exhibit a similar m_e^* to those of conventional polycrystalline ITO and amorphous In_2O_3 -based TCO films, indicating that high μ_e is mainly achieved through a larger τ rather than a smaller m_e^* [197]. Therefore, as we mentioned above, the high μ_e in IFO:H might be interpreted by various scattering mechanisms (influencing τ) such as little distortion in crystal structure [220], low barrier height at grain boundaries by fluorine doping [236], grain-boundary passivation by hydrogen, as well as the fact that hydrogen atoms in the film do not significantly contribute to ionized or neutral impurity scattering [33, 60].

Table 4.1: Electrical parameters of the as-deposited 75 nm-thick IFO:H and ITO films.

TCO type	Sheet resistance [R_{sh} , Ω/\square]	Carrier density [N_e , cm^{-3}]	Electron mobility [μ_e , $\text{cm}^2\text{V}^{-1}\text{s}^{-1}$]	Film resistivity [ρ , $\Omega\text{ cm}$]
IFO:H	74	1.2×10^{20}	87	6.2×10^{-4}
ITO	50	4.9×10^{20}	28	4.7×10^{-4}

Figure 4.6(a) shows the transmittance and reflectance spectra of 75 nm-thick IFO:H and ITO films. Comparable transmittance was observed in Vis-NIR region, while in UV range the transmittance edge of IFO:H film shows a blue shift relative to ITO, indicating a possible wider bandgap in IFO:H film. Further, the IFO:H film displays higher reflectance in both UV and NIR region, which is related to the tail states and plasma oscillations of the free carriers, respectively [235, 247]. Figure 4.6(b) illustrates the absorption coefficient (α) of the TCOs with an ASTM G173-03 solar spectrum provided in the background. The

absorption coefficient was calculated from $\alpha = \ln[(1-R)^2/T]/d$, where T and R are the measured transmittance and reflectance spectra, respectively, and d is the film thickness. As it can be seen, the IFO:H film shows lower α along the whole wavelength range, allowing an augmented light incidence to the absorber material of the PV devices. As previously mentioned, the absorption edge shifts towards lower wavelength, indicating a wider band gap of the IFO:H film. The optical band gap (E_g) for allowed direct electronic transition was calculated from the plot of $(\alpha h\nu)^2$ versus $(h\nu)$ in Figure 4.6(c) [214]. The IFO:H film has an E_g of 3.85 eV, which is wider than that of ITO (3.76 eV). The wider band gap value should not be explained by Moss-Burstein effect [54], since the carrier density of IFO:H film is lower than that of ITO. It has been proposed that the optical transitions in a specific material system are influenced by the disorder in the material phase [76], as well as the various interaction effects either between free carriers or between free carriers and ionized impurities [248].

4

In low crystalline, disordered and amorphous materials, an exponential tail called Urbach tail appears near the optical band edge along the absorption coefficient curve. The Urbach tail is generated due to localized states in the band gap caused by perturbation in the structure and by disorder of the system [247]. We thus extracted the Urbach energy (E_U) to estimate the width of the tail states, following the Urbach relation that $\ln\alpha = \ln\alpha_0 + (h\nu/E_U)$, where α_0 is a pre-exponential constant, and $(h\nu)$ is the incident photon [247]. The fitting results showed an E_U of 197 meV for the IFO:H film and 444 meV for ITO, respectively. Compared to ITO, higher E_g and mobility can be expected from IFO:H due to its lower Urbach energy [247]. Besides, the E_U value of the IFO:H film is closer to the reported data of the high mobility IO:H and IZO films (~ 130 meV) [214], indicating similar changes upon ITO, where the fluorine doping accompanies less disorder and defect states in the In_2O_3 -based film. It is notable that the E_U for ITO is higher than the reported value of 300 meV extracted from PDS measurements by Morales-Masis *et al.* [214], the reason may be attributed to the ITO material quality deposited by different sputtering technologies.

Furthermore, another particularly attractive feature of all In_2O_3 -based materials is that their refractive index is close to 2 at around 600 nm wavelength where solar radiation intensity is maximum. This is approximately the geometric mean of the refractive indices of air and typical solar cell absorber such as silicon, and gives such materials very good anti-reflective coating (ARC) properties [33]. The wavelength-dependent refractive index (n) and extinction coefficient (k) curves from Scout software fitting are shown in Figure 4.6(d). n decreases with the wavelength, which is consistent with the expectation from Kramers-Kronig analysis [243]. It is noticeable that the IFO:H has a relatively gentler variation in n than ITO, which may have a better ARC potential than the ITO film considering the wavelength-dependent phase changes in the light interference [249]. Furthermore, k values are in accordance with the α curves in Figure 4.6(b), which can be interpreted by the correlation of $\alpha = 4\pi k/\lambda$, whereas the inconsistency between α and k in the UV region in the two figures should be attributed to the software fitting error in the region.

To summarize, compared to ITO, the IFO:H film has lower N_e , higher μ_e and n (especially in NIR range), which contributes to FCA reduction [250]. Combined with the potential as ARC, decent optical performance of the IFO:H film as a front electrode can be expected at the device level. Furthermore, considering its low absorption in the long

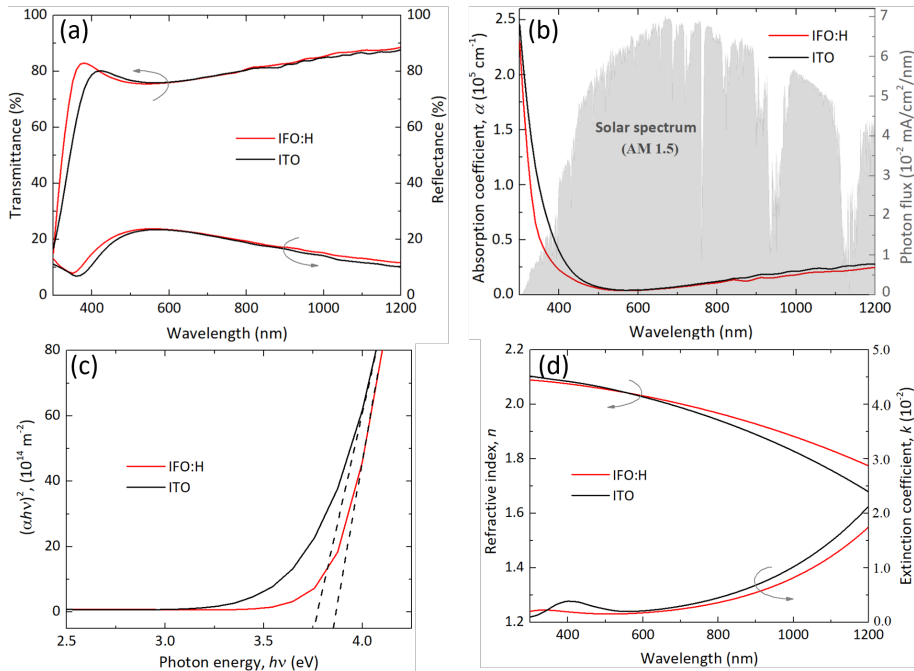


Figure 4.6: Optical properties of the IFO:H and ITO films: (a) transmittance and reflectance spectra, (b) calculated absorption coefficient curves, (c) optical band gap plot curves, and (d) wavelength-dependent refractive index (n) and extinction coefficient (k) curves.

wavelength region, the IFO:H film deployment at the rear side of a PV device may also produce an additional optical gain [82].

4.3.4. Solar cell applications

Before applying the TCOs in solar cell devices, we experimentally evaluated the work function ($WF = E_{\text{vac}} - E_F$) values of the TCOs under test via KPFM approach. The recorded CPD values were -895 mV, -475 mV and -720 mV for gold (reference), IFO:H, and ITO films, respectively. Accordingly, the WF values were calculated to be 4.68 eV for IFO:H and 4.93 eV for ITO [198], indicating a possibly preferable contact of IFO:H for collecting electrons from the n -contact stack in solar cell device [251]. However, we note that the interpretation of different contact properties could be linked not only to the WF value of the specific TCO layer but also to the specific stack of materials in which a (thin) TCO layer might be embedded. To this end, more sophisticated investigation remains to be carried out to get conclusive evaluation on the contact properties.

The contact resistivity (ρ_c) between 75 nm-thick TCOs and screen-printed silver (Ag) was studied using transfer length method (TLM) [177]. Fitting results show that ohmic contacts form between TCOs and Ag, which can be expected from the metal-like electronic behaviour of the degenerated In_2O_3 -based TCOs. The ρ_c values are 0.22 $\text{m}\Omega \text{ cm}^2$ for ITO/Ag stack, and 1.13 $\text{m}\Omega \text{ cm}^2$ for IFO:H/Ag stack. The higher ρ_c in IFO:H/Ag

stack is related to the much lower carrier density (N_e) in the IFO:H film [33, 252]. This drawback might be circumvented by deploying a TCO bi-layer prior metallization (e.g. transport layer/IFO:H/ITO/Ag) [253].

Based on Figure 4.1(b), three groups of solar cells with CSPCs were designed. Note that the IFO:H films were applied on the n -contact stack at the rear sides of poly-Si(C_x) hybrid solar cells, with a thickness of 150 nm to ensure a good infrared response [82], and on both sides of SHJ solar cells (75 nm and 150 nm-thick, respectively). Figure 4.7(a)-(c) show the corresponding EQE results. For the poly-Si(C_x) hybrid devices, rear IFO:H contributes to the IR response, resulting from a higher R and in accordance with higher n in IR range (as shown in Figure 4.6). In case of SHJ solar cells, optical improvement along the whole wavelength range was detected for the IFO:H cell, with a $J_{SC,EQE}$ increase of 1.53 mA/cm^2 compared to the ITO-based reference cell. It is worth noting that, the good optical performance of the IFO:H film in the long-wavelength range might make it a potentially competitive TCO for the bottom cell use in perovskite/silicon tandem solar cells [254].

4

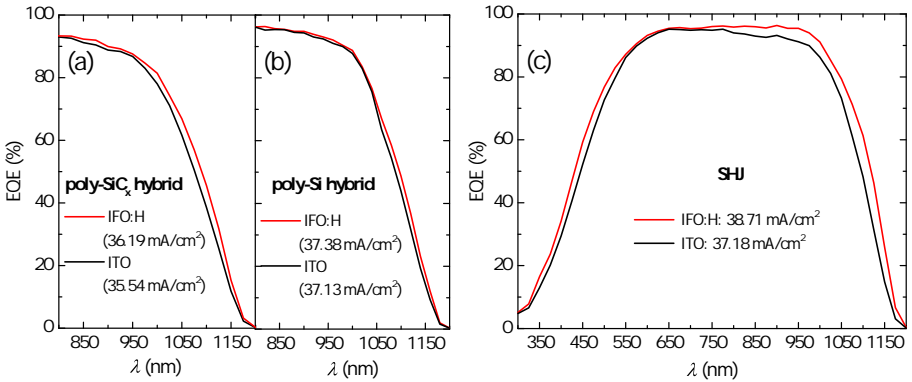


Figure 4.7: External quantum efficiency (EQE) curves of (a) poly-Si C_x hybrid, (b) poly-Si hybrid, and (c) SHJ solar cells, respectively. $J_{SC,EQE}$ were provided accordingly.

Figure 4.8(a) shows the corresponding FF comparison of the above solar cells. As it can be seen, for different front metal coverage cases (12.5% and 6%), poly-Si(C_x) hybrid solar cells with rear IFO:H exhibited more than $1\%_{abs.}$ FF improvements compared to the ITO counterpart. These indicate different n -contact properties between TCO and poly-Si(C_x) layers, for which further research is needed. As for the SHJ solar cells, double-side IFO:H films result in a comparable FF with respect to ITO-ITO cell films arrangement. Furthermore, Figure 4.8(b) displays the $i-V_{OC}$ change caused by TCO deposition. Compared with initial solar cell precursors (without TCO or metallization), the loss of $i-V_{OC}$ are found to be less than 5 mV, for both sputtered ITO and IFO:H films.

Additionally, upon further optimization on cell design, with a front metal coverage of 4.4%, the 3.92 cm^2 device performances based on three SHJ cells are shown in Table 4.2. The best SHJ solar cell with double-side IFO:H films illustrated an efficiency of 21.1%, whose current-voltage characteristic is presented in Figure 4.8(c), and the best reference ITO-based SHJ solar cell showed an efficiency of 20.3%, with $V_{OC} = 702 \text{ mV}$, $J_{SC} = 37.00$

mA/cm^2 , $FF = 78.00\%$.

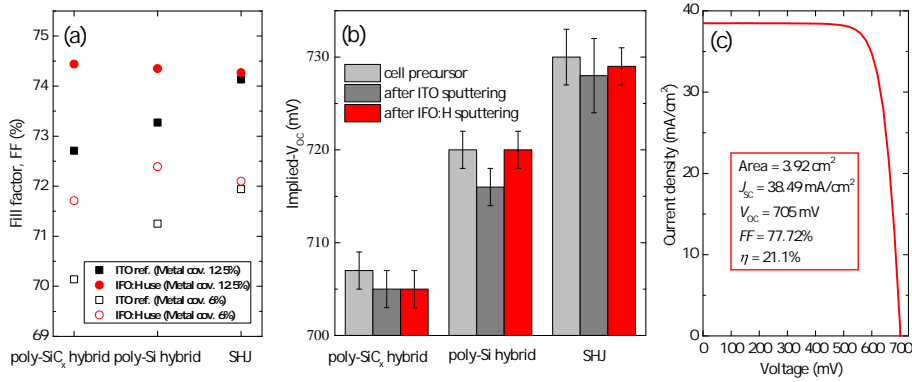


Figure 4.8: (a) Fill factor (FF) of different types of solar cells with IFO:H applied on the n -contact stack at the rear sides of poly-Si(C_x) hybrid, and on both sides of SHJ solar cells, compared to ITO-based devices as references. Results from different metal coverage are provided. (b) Implied- V_{OC} variation with TCOs' sputtering processes based on four series of experimental data, and (c) Current-voltage characteristic of the best SHJ solar cells integrating double-side IFO:H films.

Table 4.2: Solar cell parameters of 3.92 cm^2 SHJ devices with IFO:H and ITO. The values reported are the average based on three cells. The standard deviation is calculated for each cell parameter.

TCO	Open-circuit voltage [V_{OC} , mV]	Short-circuit current density [J_{SC} , mA/cm^2]	Fill factor [FF , %]	Efficiency [η , %]
IFO:H	702 ± 2.7	38.32 ± 0.17	78.08 ± 0.36	21.01 ± 0.08
ITO	699 ± 3.0	36.90 ± 0.10	78.18 ± 0.18	20.17 ± 0.12

4.4. Conclusions

We demonstrate RF-sputtered hydrogenated fluorine-doped indium oxide (IFO:H) films at low substrate temperature ($< 110 \text{ }^\circ\text{C}$) and power density ($< 2.0 \text{ W}/\text{cm}^2$). By varying the water vapour pressure during the deposition, we obtain optimized IFO:H film with a remarkable high electron mobility ($\mu_e = 87 \text{ cm}^2 \text{V}^{-1} \text{s}^{-1}$), the optimal IFO:H film shows cubic In_2O_3 polycrystalline structure with a F/In atomic ratio of 17.4%. Compared to our lab-standard ITO reference, the IFO:H film displays wider optical band gap (3.85 eV), lower Urbach energy (197 meV), higher μ_e and appropriate refractive index for ARC purpose in Si-based devices. The SHJ device with double-side IFO:H gave a $J_{SC,EQE}$ gain of $1.53 \text{ mA}/\text{cm}^2$ within the whole wavelength range without inducing FF loss. The optimized SHJ solar cell showed a conversion efficiency of 21.1%, featuring J_{SC} of $38.49 \text{ mA}/\text{cm}^2$, V_{OC} of 705 mV, and FF of 77.72%.

5

IFO:H implementation in high thermal budget poly-Si solar cells

This chapter was published in *ACS Applied Materials & Interfaces** [61]

Abstract

Considerable deterioration in passivation quality occurs for thin poly-Si-based devices owing to the sputtering damage during transparent conductive oxide (TCO) deposition. Curing treatment at temperatures above 350 °C can recover such a degradation, whereas the opto-electrical properties of the TCO are affected as well, and the carrier transport at the poly-Si/TCO contact is widely reported to degrade severely in such a procedure. Here, we propose straightforward approaches to tailor the material properties of the hydrogenated fluorine-doped indium oxide (IFO:H) film, via post-deposition annealing at 400 °C in nitrogen, hydrogen, and air ambience. Structural, morphological, and opto-electrical properties of the IFO:H films are investigated, as well as their inherent electron scattering and doping mechanisms. Hydrogen annealing treatment proves to be the most promising strategy for the following reasons: (i) the annealed IFO:H layer exhibits both optimal opto-electrical properties (carrier density = $1.5 \times 10^{20} \text{ cm}^{-3}$, electron mobility = $108 \text{ cm}^2 \text{ V}^{-1} \text{ s}^{-1}$, and resistivity = $3.9 \times 10^{-4} \text{ } \Omega \text{ cm}$), and (ii) remarkably low contact resistivities ($20 \text{ m}\Omega \text{ cm}^2$ for both *n*- and *p*- contacts) are achieved in the poly-Si solar cells. Even though the presented cells are limited by the metallization step, the obtained IFO:H-based solar cell shows an efficiency improvement from 20.1 to 20.6% after the hydrogen annealing treatment, demonstrating the potential of material manipulation and contact engineering strategy in photovoltaic devices endowed with TCOs.

*C. Han, G. Yang, A. Montes, P. Procel, L. Mazzarella, Y. Zhao, S. Eijt, H. Schut, X. Zhang, M. Zeman, and O. Isabella, "Realizing the Potential of RF-Sputtered Hydrogenated Fluorine-Doped Indium Oxide as an Electrode Material for Ultrathin SiO_x/Poly-Si Passivating Contacts," *ACS Applied Energy Materials*, 3(9), 8606-8618, 2020. August 12, 2020, doi: 10.1021/acsaem.0c01206.

5.1. Introduction

To push forward the power conversion efficiency, c-Si solar cells featuring carrier-selective passivating contacts (CSPCs) are developed, which have demonstrated viable novel cell concepts with PCE well above 25% [255]. Such CSPCs enable low contact resistance and passivation quality of the c-Si surface, thus appreciably enhancing the contact selectivity as compared to conventional diffused junctions [255]. Applying CSPCs based on ultrathin SiO_x /poly-Si in front/back-contacted (FBC) silicon solar cells remains to be further exploited, due to the significant optical loss caused by parasitic absorptive doped layers [143, 256]. In fact, in FBC c-Si solar cells featuring ultrathin SiO_x /poly-Si passivating contacts at both front and rear sides (so-called *poly-Si* solar cell), parasitically absorptive poly-Si layers cannot be deposited thick enough to provide sufficient lateral conductivity for the current transport toward the metal grid. To solve this dilemma, transparent conductive oxide (TCO) layers on top of a thin poly-Si layer ensure the required lateral conductivity and constitutes a more transparent front window [10, 144]. However, commonly used sputtering technology is known to degrade the passivation quality of thin poly-Si contacts [143]. Owing to the high thermal stability of poly-Si contacts, an effective curing can be achieved at 350 °C to restore the passivation [143]. Nevertheless, carrier transport at the poly-Si/TCO contact is widely reported to degrade severely for temperatures above 250 °C [143], likely due to the formation of an interfacial SiO_x with oxygen effusing from the TCO [130, 138, 143, 144, 257]. Such drawbacks in carrier transport need to be solved to achieve a high PCE in FBC poly-Si solar cells.

In Chapter 4, we developed a high- μ_e hydrogenated fluorine-doped indium oxide (IFO:H) film, in which fluorine and hydrogen act as co-dopants in a bixbyite In_2O_3 structure. Specifically, fluorine dopants enhance the electrical properties of In_2O_3 film via (i) substituting for oxygen atoms thus generating free electron carriers, (ii) occupying oxygen vacancy (V_O) sites thus eliminating electron trap sites, (iii) lowering the transport barrier at the grain boundaries; while the introduction of hydrogen further could enhance the electrical properties of the fluorine-doped In_2O_3 film by acting as shallow donors and passivating defects in the film. The application of the IFO:H film in low thermal-budget SHJ solar cells has been demonstrated in Chapter 4. However, it remains elusive to realize the potential of the IFO:H film in high thermal-budget devices, especially due to the aforementioned carrier transport problem for poly-Si passivating contacts in a passivation restoring step. It has been reported that the electrical behavior of polycrystalline In_2O_3 from room temperature to 800 °C is influenced by impurities and oxygen vacancies that act as donor states in degenerated TCO layers [51, 186, 258]. In addition, amphoteric hydrogen provides donor states in metal oxide, inducing alteration and changing the opto-electrical properties in the host matrix [63, 79, 186, 259]. On the other hand, in the case of semiconductor application with Si/ SiO_2 interface, atomic hydrogen is found to simultaneously passivate and depassivate silicon dangling bonds [260], resulting in different passivation qualities at the device level. Furthermore, hydrogen effused from TCO could help to passivate interfacial defects [261]. Therefore, engineering these defect states is of vital importance in tailoring both the opto-electrical properties of the TCO and contact at specific poly-Si polarity.

In this study, we demonstrated different straightforward approaches to alter the opto-electrical properties of the IFO:H film. Particularly, we examined the influence of

post-deposition annealing (PDA) treatment in different gaseous ambiances on the IFO:H structure, morphology, and opto-electrical properties. Corresponding inherent electron scattering mechanisms were also elucidated. We found that a specific PDA treatment provides the most promising strategy to tailor material's properties while retaining a good contact for carrier transport across poly-Si/TCO contact. As a proof of that, FBC poly-Si solar cells were then manufactured and those that underwent the PDA treatment exhibited increased fill factor (FF).

5.2. Experimental

The experimental section includes the following parts.

A. TCO deposition and post-deposition annealing (PDA) treatments

The deposition parameters for the sputtered IFO:H film are: Ar flow 50 sccm, substrate temperature 100 °C, chamber pressure 2.50 Pa, water vapour partial pressure 1.6×10^{-2} Pa, and power density ~ 1.8 W/cm². These conditions yielded a IFO:H deposition rate of ~ 6.0 nm/min. The deposition parameters for the sputtered ITO film are: Ar flow 50 sccm, substrate temperature 100 °C, chamber pressure 2.2×10^{-3} Pa, and power density 1.8 W/cm². The ITO deposition rate was ~ 6.5 nm/min. Approximately 80 nm-thick IFO:H thin films were deposited on Corning glass substrates unless otherwise specified.

Samples were subject to different post-deposition annealing (PDA) treatments as tabulated in Table 5.1. We note that in our various annealing tests regarding the single TCO layer, our IFO:H films were stable up to 300 °C in N₂, H₂, and air ambiances, and annealing temperature above 400 °C facilitated considerable changes in electrical properties (a duration of 10 min was used in the annealing tests, “stable” means that the sheet resistance change upon annealing is within 5% compared to the as-deposited film). To avoid overheating of our poly-Si cell precursors (n^+ poly-Si/SiO_x/ n -c-Si/SiO_x/ p^+ poly-Si), 400 °C was chosen to stimulate opto-electrical properties change in TCO and to maintain the passivation quality at the Si/SiO₂ interface [260, 262].

Table 5.1: Post-deposition annealing (PDA) treatments on different IFO:H samples.

Sample	Treatment temperature [T_{PDA} , °C]	Ambience [-]	^a Pressure [P_{PDA} , Pa]	^b Time [t_{PDA} , min]
as-deposited (as-dep.)	-	-	-	-
N ₂ -annealed (N ₂ -ann.)	400	pure nitrogen	50	10
H ₂ -annealed (H ₂ -ann.)	400	pure hydrogen	50	60
air-annealed (air-ann.)	400	air	atmospheric	10

^a We did annealing tests in different tools, such as rapid thermal annealer at Kavli nanolab Delft, Mapper annealing tube, and different multi-chamber PECVD systems in Else Kooi Lab (EKL) at Delft University of technology. The results from the same ambience showed similarity, even though the pressure control levels were different among the annealing tools. The results from Cascade PECVD were used in this article for a better gas pressure controllability, and 50 Pa was used to keep a constant oxygen-deficient environment in the annealing treatment.

^b Hydrogen annealing with durations of 10 min up to 30 min did not cause observable changes in the opto-electrical properties of the IFO:H film, and the duration of 60 min gave comparable improvements with the N₂-ann. sample in electrical properties; thus, the duration of the H₂-ann. sample was set to be 60 min. An even longer hydrogen annealing time was deemed not industrially appealing.

B. Contact study and solar cell fabrication.

The solar cell schematic is shown in Figure 3.4(d), and the test structures for contact study are illustrated in Figure 3.4(e-f). After dipping the c-Si wafers into 0.55% HF for 4 min to remove the native oxide, the tunnelling SiO_x layer was formed by the method of Nitric Acid Oxidation of Silicon (NAOS) [263]. In our case, we dipped the wafers in 68% HNO_3 bath for 1 hour at room temperature. In order to obtain 250 nm-thick p^+ poly-Si layer for utilization at the rear side in our FBC poly-Si solar cells, a Varian Implanter E500HP was used to implant boron (B) atoms into the low pressure chemical vapour deposition (LPCVD) intrinsic a-Si layer, with a fixed implantation energy of 5 keV and implantation dose of $5 \times 10^{15} \text{ cm}^{-2}$. Afterwards, an annealing step in N_2 and O_2 mixed ambience at 950 °C for 3 min was conducted to activate and drive-in the dopants. The ramping rate for heating or cooling was 10 °C/min, and the doping level in the p -type poly-Si layer after activation and drive was around $1 \times 10^{20} \text{ cm}^{-3}$ [263]. For getting 24 nm-thick n^+ poly-Si layer on a textured surface for utilization at the front side in our FBC poly-Si solar cells, we firstly textured the c-Si bulk in mixture solution of TMAH and ALKA-TEX 8 from GP-Solar-GmbH followed by NAOS; then intrinsic a-Si growth and subsequent doping by POCl_3 diffusion were carried out with N_2 as carrier gas in LPCVD at 800 °C for 43 min. The doping level in the n -type poly-Si layer after diffusion was measured by electrochemical capacitance-voltage (ECV) as around $2 \times 10^{20} \text{ cm}^{-3}$. Forming gas (10% H_2 in N_2) annealing was used to hydrogenate the poly-Si passivating contacts in solar cell precursor samples (400 °C, 30 min). Further details about the fabrication process can be found elsewhere [263, 264]. For solar cell fabrication, the samples were single-side textured prior realizing rear and front ultrathin SiO_x /poly-Si CSPCs and received 4-min HF dip before depositing TCO in order to remove any eventual present surface oxide. In order to extract the contact resistivity of n -contact (n^+ poly-Si/TCO/metal) and p -contact (p^+ poly-Si/TCO/metal) from vertical dark current-voltage (I - V) measurements [142, 143], full-area 1 μm -thick Ag was evaporated on both sides of test structures of Figure 5.1(b), in which n -type and p -type c-Si were utilized as substrates, respectively. Screen-printing Ag was used for solar cells metallization, the curing condition was 170 °C for 30 min with a subsequent 350 °C for 5 min to restore the passivation in samples without TCO PDA treatments.

5.3. Results and discussion

5.3.1. Opto-electrical properties upon PDA treatments

Figure 5.1 illustrates data points of $(N_e, \mu_{e,\text{Hall}})$ of the IFO:H films under different PDA treatments, i.e., Hall mobilities ($\mu_{e,\text{Hall}}$) versus corresponding carrier densities (N_e) plot. Resistivity (ρ) lines are also provided according to the relation $\log(\mu_{e,\text{Hall}}) = -\log(N_e) + \log(1/\rho e)$ [53]. Hall measurements show that all the films exhibit n -type conductivity. The $\mu_{e,\text{Hall}}$ are plotted versus the corresponding carrier densities (N_e), with our lab-standard 80 nm-thick ITO data serving as reference. Compared to the ITO reference, the as-dep. IFO:H film shows a bit higher resistivity, while the N_2 -ann. and H_2 -ann. layers show lower resistivity values. We note that the properties of ITO layer also change with PDA treatments, but the topic is outside the scope of this article thus will not be elaborated here. Among the IFO:H films, with respect to the as-dep. film, the reduced resistivity

values in the N_2 -ann. and H_2 -ann. films result from improvements in both N_e and $\mu_{e,Hall}$. In sharp contrast, the air-ann. sample shows instead an obvious deterioration in electrical properties, caused by largely reduced N_e and $\mu_{e,Hall}$. The specific data of N_e , $\mu_{e,Hall}$ and sheet resistance (R_{sh}) of the IFO:H films under PDA are summarized in Table 5.2. The optimal material properties were obtained after PDA in hydrogen, with carrier density $1.5 \times 10^{20} \text{ cm}^{-3}$, electron mobility $108 \text{ cm}^2 \text{ V}^{-1} \text{ s}^{-1}$, and resistivity $3.9 \times 10^{-4} \Omega \text{ cm}$. Besides, the N_2 -ann. sample shows comparable electrical properties as the H_2 -ann. film. Detailed elucidation will be discussed in the following sections.

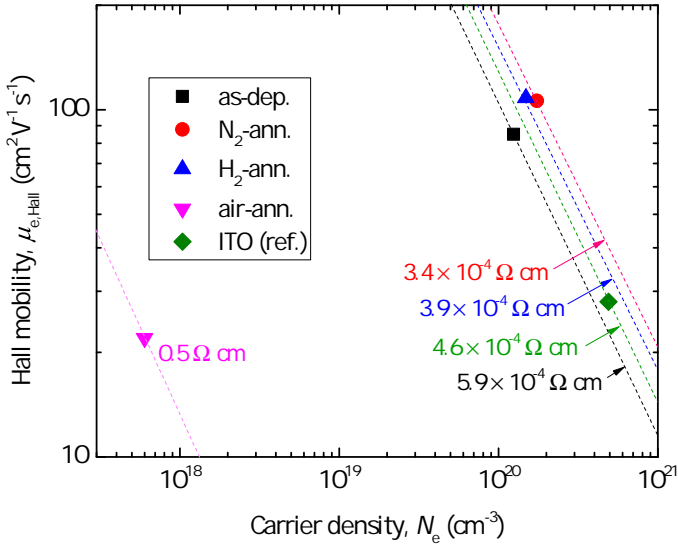


Figure 5.1: Hall mobilities ($\mu_{e,Hall}$) versus corresponding carrier densities (N_e) of the IFO:H films under different PDA treatments. Lab-standard ITO layer is provided as reference data point. Symbols are the measured (N_e , $\mu_{e,Hall}$) pairs while the dashed lines indicate corresponding resistivity values.

Furthermore, the optical properties of the IFO:H films were evaluated, as compared to the commonly used ITO. Figure 5.2(a) displays the measured wavelength-dependent transmittance/reflectance of the IFO:H films under different PDA treatments, with our lab-standard ITO layer as reference. In ultraviolet (UV) range, the transmittance edge of the ITO film and the air-ann. IFO:H sample basically showed a red shift with respect to the other IFO:H layers. These results imply optical band gap (E_g) differences of the IFO:H films, which are illustrated Figure 5.2(b). The transmittance/reflectance differences around 400-600 nm region among the IFO:H films might be caused by the different film thicknesses after PDA treatments (as shown in Table 5.2). Figure 5.2(b) shows the absorption coefficient curves extracted from ellipsometry (SE) fittings. As one can observe, contrasting with the ITO film, the IFO:H layers show a marked sharper transition at the absorption edge in UV part, and visible lower absorption in NIR region, which is in accordance with our previous report and underlines the great potential of IFO:H film in allowing an augmented light in-coupling into the absorber material of PV devices [213]. Among the IFO:H films, with respect to the as-dep. film, the absorption edges of the

N_2 -ann. and H_2 -ann. samples show blue shifts, while that of the air-ann. layer illustrates a red shift, indicating changes in E_g . The E_g for allowed direct electronic transition was extracted according to Tauc relation in Figure 5.2(b) inset [220, 247]. The E_g values of 3.85 eV, 3.94 eV, 3.87 eV, 3.76 eV and 3.78 eV were obtained corresponding to as-dep., N_2 -ann., H_2 -ann., air-ann., and ITO reference samples, respectively. The results of IFO:H films are in accordance with the N_e changes in Hall measurements (as shown in Table 5.2), which can be explained by the Moss-Burstein effect in the degenerate semiconductors ($\Delta E_g \propto N_e^{2/3}$) [54]. The wavelength-dependent complex refractive index of the films are reported in Figure A.1, repeated experimental opto-electrical parameters of IFO:H films under different PDA treatments can be found in Table A.1.

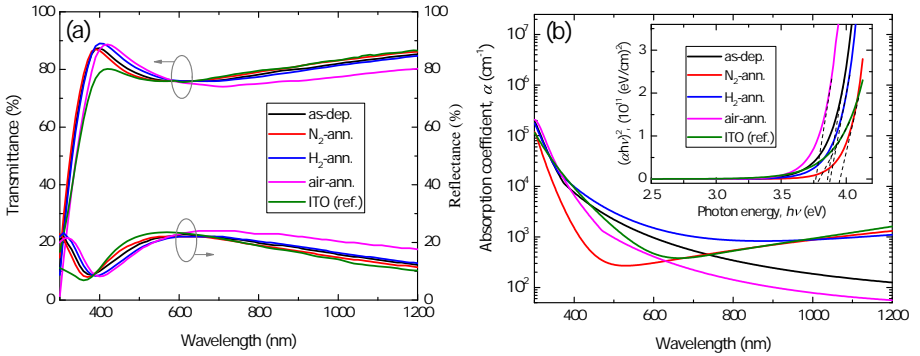


Figure 5.2: Optical properties of IFO:H films after various PDA treatments. (a) transmittance/reflectance spectra, and (b) absorption coefficient curves from SE fitting, inset is optical band gap plots.

To evaluate the conduction and valence band tail states change in the IFO:H film after various PDA treatments, we extracted the Urbach energy (E_U) which is presumed as the width of the tail of localized defect states in the band gap in low-crystalline, disordered or amorphous materials [247]. We followed the equation that $\ln \alpha = \ln \alpha_0 + (h\nu/E_U)$, where α_0 is a pre-exponential constant, and $(h\nu)$ is the incident photon [247]. The fitting results show E_U values of 229 meV, 224 meV, 256 meV, 224 meV, and 420 meV with as-dep., N_2 -ann., H_2 -ann., air-ann. IFO:H films, and reference ITO layer, respectively. The data for the as-deposited layers are at similar levels with our previous report [213]. Among the IFO:H films, with respect to the as-dep. sample, a relatively higher E_U value was observed in the H_2 -ann. layer, implying increased band tail states and promoted atomic structural disorder [79]. This is plausibly caused by the hydrogen-induced defects such as interstitial H_i dopants and V_OH shallow donor states (generated by hydrogen occupation on V_O sites), but the position of the corresponding subgap states is still under debate [79, 214, 265, 266]. By contrast, the N_2 -ann. and air-ann. samples exhibit a bit lower E_U values with respect to the as-dep. sample, which might be attributed to the improved material quality during the annealing process.

5.3.2. The IFO:H films under different PDA treatments

This section provides structure, morphology, and electron scattering mechanism of the IFO:H films under different PDA treatments.

Structural/morphological changes under PDA.

Figure 5.3 shows the X-ray diffraction (XRD) patterns of the IFO:H thin films under various PDA treatments. All films display XRD peaks at $2\theta = 21.3^\circ, 30.6^\circ, 35.5^\circ, 41.7^\circ, 51.0^\circ,$ and 60.6° , corresponding to (211), (222), (400), (332), (440) and (622) planes of polycrystalline In_2O_3 with cubic bixbyite structure [197, 213, 222, 243], with the preferred (222) orientation. No crystalline orientation change was observed along with different PDA treatments. Furthermore, from Gaussian fitting, all the annealed layers exhibited smaller full-width at half-maximum (FWHM) value of X-ray peak of (222) than the as-deposited film, indicating larger crystallite sizes and smaller strains in the annealed films [197, 245]. According to Scherrer's formula [245], the mean crystallite size ($D_{\text{crystallite}}$) values from (222) orientation are calculated to be 22.08 nm, 27.67 nm, 25.03 nm, and 25.91 nm for as-dep., N_2 -ann., H_2 -ann., and air-ann. samples, respectively, as summarized in Table 5.2. The small peaks appearing at 43° probably originate from substrate contamination, since they can hardly be assigned to indium oxide/fluoride materials. We further measured the as-deposited samples which were done previously and 1 month later, no such signals were detected anymore.

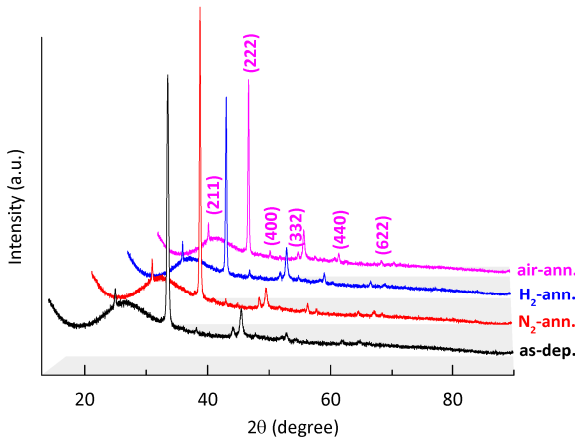


Figure 5.3: X-ray diffraction patterns of IFO:H films under different PDA treatments.

Figure 5.4(a)-(d) shows AFM images of the as-deposited, N_2 -ann., H_2 -ann., and air-ann. samples, respectively. In contrast to as-dep. film, the annealed layers exhibit rougher surface along with densely distributed granular structures. Enlarged grain sizes were observed in annealed samples compared to as-dep. film, we ascribe the observed agglomerated trend to the heating effect [79]. These spontaneously formed nanostructures have a size range of 20-30 nm. The grain size (D_{grain}) as well as the root-mean-square (RMS) roughness values of the samples are reported in Table 5.2.

Electron scattering mechanism in IFO:H films upon PDA.

The carrier scattering mechanism responsible for conductivity of the IFO:H thin films under different PDA treatments has been investigated. Note that in terms of physical definition, $\mu = e\tau / m^*$, where μ is the carrier mobility which directly correlates the conductivity parameter, τ and m^* are carrier relaxation time and electron effective mass, respectively. It

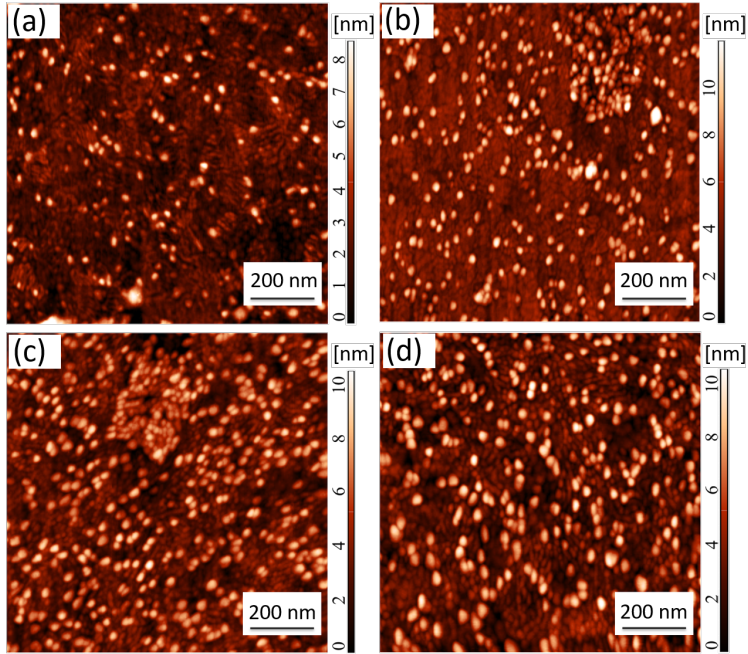


Figure 5.4: AFM micrograph of the (a) as-dep., (b) N₂-ann., (c) H₂-ann., and (d) air-ann. IFO:H films, respectively.

has been theoretically [37] and experimentally [197] found that high- μ TCO films exhibit a similar m^* regardless the material phase, and high μ is mainly achieved through a larger τ rather than a smaller m^* [197]. In polycrystalline films, the overall relaxation time is determined by scattering induced by grain boundaries (GBs), stacking faults, dislocations, charged centres such as ionized impurities, and phonons (lattice vibrations) [197].

Firstly, to distinguish whether GBs play roles on carrier scattering in the IFO:H films under different PDA treatments, we made a comparison between $\mu_{e,Hall}$ and μ_{opt} , as summarized in Table 5.2. One can clearly see that $\mu_{e,Hall} / \mu_{opt} < 1$ occurs for all the samples, yielding information that grain boundary scattering contributes to the carrier scattering in both as-deposited and annealed IFO:H films (especially for air-ann. sample). To corroborate that, we further calculated the mean free path (MFP) of the charge carriers, which might represent an estimation of the upper limit for the distance between scattering centres [60, 81]. Using the Fermi velocity $v_F = \hbar(3\pi^2 N_e)^{1/3} / m^*$, where \hbar is the reduced Planck constant, and the scatter frequency $\omega_\tau = e / (m^* \mu_{opt})$, MFP = v_F / ω_τ values were found to be 10.38 nm, 13.79 nm, 15.92 nm and 2.33 nm for as-dep., N₂-ann., H₂-ann., and air-ann. samples, respectively. The MFP values are of the same order of magnitude as $D_{crystallite}$ and D_{grain} , implying that GBs could play a role in the conduction mechanisms of the IFO:H films. We note that for the air-ann. film, in which grain boundary scattering might be a dominating factor, the MFP value is less meaningful since grain boundaries do not really act as scattering centers in the intra-grain analysis.

Table 5.2: Material parameters of the IFO:H films under different PDA treatments.

Sample	^a d_b [nm]	^a d_s [nm]	^b N_e [$1 \times 10^{20} \text{ cm}^{-3}$]	^b $\mu_{e,\text{Hall}}$ [$\text{cm}^2 \text{ V}^{-1} \text{ s}^{-1}$]	^c R_{sh} [Ω/\square]	^d $D_{\text{crystallite}}$ [nm]	^e D_{grain} [nm]	^e RMS [nm]	^a μ_{opt} [$\text{cm}^2 \text{ V}^{-1} \text{ s}^{-1}$]	^a E_U [meV]
as-dep.	81.68	2.71	1.24	85	67	22.08	20.00	1.24	102	229
N ₂ -ann.	89.91	4.90	1.74	106	35	27.67	23.53	1.75	121	224
H ₂ -ann.	93.38	4.53	1.49	108	40	25.03	27.45	1.82	153	256
air-ann.	93.21	4.28	0.01	22	760	25.91	27.45	1.69	135	224

^a Determined from SE-fitting. ^b Obtained from Hall measurement. ^c Tested by the four-point probe technique.

^d Calculated from XRD data using Scherrer's formula. ^e Evaluated from AFM images in NOVA program.

Secondly, we carried out DB-PAS measurements to identify the open-volume defects thus understand the doping mechanisms in the PDA treated IFO:H layers. The positron is the antiparticle of the electron. The annihilation between positron and electron produces γ -quanta, which forms the detected signal. Since positrons are repelled by the positive charge of the atom cores, neutral and negatively charged vacancy defects usually act as positron traps. In particular, we used DB-PAS as additional tool to examine whether V_O or $V_O\text{H}$ vacancy defects are present, as they are well known to act as donors in In_2O_3 -based TCOs. While the positively charged V_O (or $V_O\text{H}$) alone does not trap positrons, V_O defects are detectable in DB-PAS when they are complexed with cation vacancies (namely, $V_{\text{In}}-nV_O$ complex) [64, 65]. Figure 5.5(a) shows the collected best-fit positron Doppler broadening W -parameters as a function of S -parameters of the IFO:H films using VEPFIT analysis, in which the as-dep. film denotes a S - W reference point, and error bars were calculated as the average deviation of fitted values to measured data in the energy range of 1–2.5 keV where the targeted IFO:H film is probed (see Figure A.2 and Table A.1). Specifically, the S -parameter provides sensitivity to the presence of open volume defects, while the W -parameter is more dependent on the type of atoms surrounding the annihilation site [65, 201]. From Figure 5.5(a), the S -parameter of the N₂-ann. layer and of the as-dep. sample are basically the same within the error bar region, indicating similar defect concentrations in the films or possibly saturation trapping of positrons at the vacancy sites. This phenomenon does not explain the notable increase in carrier density N_e of 40% as shown in Table 5.2. The discrepancy plausibly results from the effective interstitial H_i dopants generated during annealing procedure [60], which contribute to the increased density in conduction band electrons, but are invisible in DB-PAS measurements. Besides, the resulting S -parameter of the H₂-ann. sample is decreased by 2.1% compared to the as-dep. layer, implying a less vacancy-related defective film structure [201]. The reduced S may come from: (i) a decrease in the size of V_O sites due to their occupation by H, making singly charged $V_O\text{H}$ the major donor states in the film together with interstitial H_i [60, 197, 265, 267], which could explain the increased carrier density N_e in Table 5.2 [186, 265] and is in accordance with the increased subgap states from Urbach energy calculation in Section 5.3.1, or (ii) a reduction in the size of V_{In} sites due to their interaction with H impurities [267]. The above results outline the role of hydrogen-related donors as dominant singly charged dopant in our IFO:H films, especially in N₂-ann. and H₂-ann. films. Furthermore, in the case of the air-ann. sample, the S -parameter is 2.5% lower than that of the as-dep. sample, indicating elimination of $V_{\text{In}}-nV_O$ complex due to local oxidation [65, 268], which is also supported by reported

phenomenon [262] and the degraded electrical properties as shown in Hall measurements (Figure 5.1). On the other hand, all the W -parameters of the annealed samples show increased values with respect to the as-dep. layer, demonstrating a change in local environment of vacancy defects, such as O occupying the V_O sites, or more effective fluorine impurities that order on neighbouring V_{In} sites with improved crystallinity upon annealing (the fluorine impurities alone cannot act as positron annihilation sites). The experimental S - and W -parameter depth profiles and fit curves as a function of positron implantation energy for the IFO:H films under PDA are illustrated in Figure A.2, and the VEPFIT fitting parameters are provided as Table A.2.

Thirdly, we performed temperature-dependent Hall measurements to analyse the specific scattering mechanisms in the IFO:H films under different PDA treatments, as shown in Figure 5.5(b). One can see that the N_e of the films does not show a temperature dependence as expected given the degenerate nature of the semiconductor [67, 269]. Besides, the temperature dependence of mobility of IFO:H greatly varies with different PDA treatments. Apart from air-ann. sample, films exhibited marked increase in $\mu_{e,Hall}$ with cooling direction with negligible change in N_e , implying phonon scattering plays notable role in the as-dep., N_2 -ann., and H_2 -ann films [197].

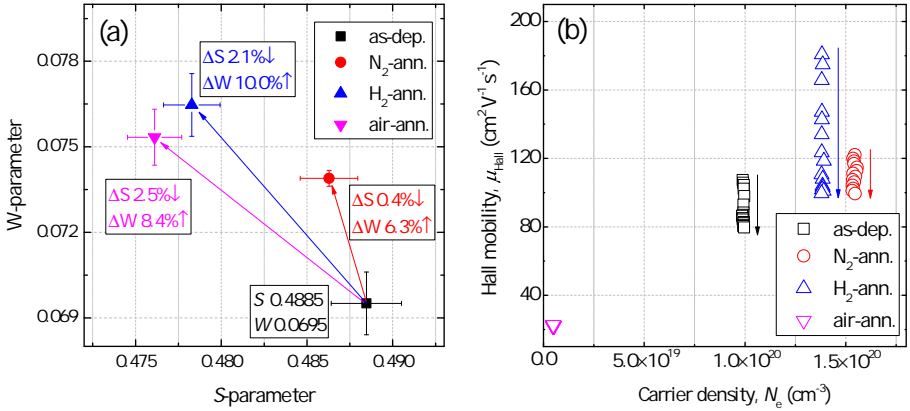


Figure 5.5: (a) S - W parameters of the IFO:H films extracted from DB-PAS measurements, and (b) Hall mobilities versus carrier densities in the IFO:H films in temperature-dependent Hall measurements, the arrows indicate the increasing direction of measurement temperature from 200 K to 350 K.

Since mobility is inversely related to scattering, the separation into scattering processes is intuitively difficult. The interpretation becomes easier when using the inverse mobility [60, 81]. According to Preissler et al [58] and Macco et al [60], charged scattering centres from ionized impurities together with phonon scattering were found to be the dominant scattering mechanisms in both single-crystalline In_2O_3 and polycrystalline hydrogenated In_2O_3 films. Combined with the previous proven grain-boundary scattering in our IFO:H films, we assume the temperature-dependent mobility can be expressed as follows from Matthiessen's rule [60].

$$\frac{1}{\mu} = \frac{1}{\mu_{GB}} + \frac{1}{\mu_{cc}} + \frac{1}{\mu_0} \left(\frac{T}{T_0} \right)^p \quad (5.1)$$

In this equation, μ_{GB} represents the mobility results from grain-boundary scattering, and μ_{cc} is from charged scattering centres (such as V_{O} , $V_{\text{O}^{\text{H}}}$). The last component in equation 5.1 is inverse phonon mobility (μ_{phonon}), in which μ_0 denotes the phonon mobility at a reference temperature T_0 . The parameter p exponential fits temperature-dependent mobility data (see Figure A.3(a)). According to literature, the fitted p values should be in the range of 2-4 if the temperature is below the Debye temperature (reported range for In_2O_3 is 420 to 811K) [58, 60]. While our converged parameter p values were determined to be 1.35, 1.76, and 2.25 for as-dep., N_2 -ann. and H_2 -ann. samples, respectively. No converged p value was obtained for the air-ann. layer.

We note that at the grain size range and carrier densities of interest ($1 \times 10^{20} \sim 2 \times 10^{20} \text{ cm}^{-3}$), the grain boundary scattering can be either temperature-independent tunnelling or temperature-dependent thermionic emission [60, 66–68]. By assuming μ_{GB} as a temperature-independent component in equation 5.1, the latter case would not be displayed. That is why our obtained $1/\mu_{\text{phonon}}$ varies for different IFO:H films. On the other hand, the possible presence of thermionic emission can be roughly evaluated by the deviation on fitted p values from the above mentioned reasonable range of 2-4 according to equation 5.1. From the above results, only the p value of H_2 -ann. film is above 2 and is in accordance with the reported values for (un)intentionally hydrogen doped In_2O_3 films [60, 270]. This evidences that in H_2 -ann. film, grain boundary scattering is in tunnelling mode, while in as-dep. and N_2 -ann. layers, thermionic emission and tunnelling current may coexist at GBs. Additionally, we plotted $\mu_{\text{e,Hall}}\sqrt{T}$ versus inverse temperature for the air-ann. sample (see Figure A.3(b)), which showed exponential dependence that well matches the scattering mechanism described by the Schottky-barrier model in thermionic emission [269]. It agrees with the report that in TCO film with rather low carrier densities ($< 1 \times 10^{18} \text{ cm}^{-3}$), transport across grain boundaries would be mainly through thermionic emission [67]. Hence we can conclude that thermionic grain-boundary scattering is the dominant mechanism in the air-ann. layer.

Figure 5.6 plots a rough estimate on the inverse mobilities that accounts for carrier scattering from charged centres, phonons, and GBs, based on equation (1). We decoupled components from the above mathematic fitting for the H_2 -ann., film, and the fitted phonon mobility is $\sim 150 \text{ cm}^2 \text{ V}^{-1} \text{ s}^{-1}$, which is basically in accordance with the results that predicted by Preissler et al In the cases of as-dep. and N_2 -ann. films, thermionic emission at GBs results in converged p values deviating from expected range for phonon scattering component. The $1/\mu_{\text{phonon}}$ components in these films were assumed based on their p deviation from H_2 -ann., film (uncertainties therein). In air-ann. film, thermionic emission at GBs dominates in the film, and phonon scattering is assumed to be negligible. Besides, for statistically homogeneously distributed scattering centres, the charged centre limited mobility (μ_{cc}) were calculated following the equation 5.2 [60, 62].

$$\mu_{\text{cc}} = \frac{3(\epsilon_r \epsilon_0)^2 h^3 N_e}{Z^2 m^{*2} e^3 N_i F_{\text{cc}}(\xi_0)} \quad (5.2)$$

In this equation, h is Planck's constant, ϵ_0 and ϵ_r are the vacuum and relative permittivity (for In_2O_3 , $\epsilon_r = 8.9$), respectively, and $\xi_0 = (3\pi^2)^{1/3} \epsilon_r \epsilon_0 h^2 N_e^{1/3} / m^* e^2$. Z is the charge state of the ionized impurity, and N_i the concentration of ionized impurities (taken to be N_e/Z , i.e., full ionization is assumed). $F_{\text{cc}}(\xi_0)$ is the N_e -dependent screening

function for charged centre scattering given non-parabolicity of the band structure [62]. Considering the DB-PAS analysis in Figure 5.5(a), it is well possible that singly charged hydrogen-related dopants are prevalent in our IFO:H films (especially in N_2 -ann. and H_2 -ann. films). Hence, we assume singly charged donors dominate in the IFO:H films, i.e. $Z=1$.

From Figure 5.6, we note that μ_{cc} almost stays at the same level for all the IFO:H films under different PDA treatments. Besides, in as-dep. layer, μ_{GB} , μ_{phonon} , and μ_{cc} co-play in the film, which is in accordance with reported electron scattering mechanisms on polycrystalline hydrogenated indium oxide films [271]. In contrast to the as-dep. film, the N_2 -ann. sample shows a decreased μ_{GB} contribution accompanied by increased μ_{phonon} component, which is presumably caused by diminished GBs from crystallite growth and increased GB passivation by diffused hydrogen during heating process [186, 265]. Furthermore, in H_2 -ann. film, a pronounced μ_{phonon} component is observed (as expected), indicating a further improved hydrogen passivation on GBs with respect to N_2 -ann. sample. Besides, in air-ann. sample, μ_{GB} absolutely dominates in the film.

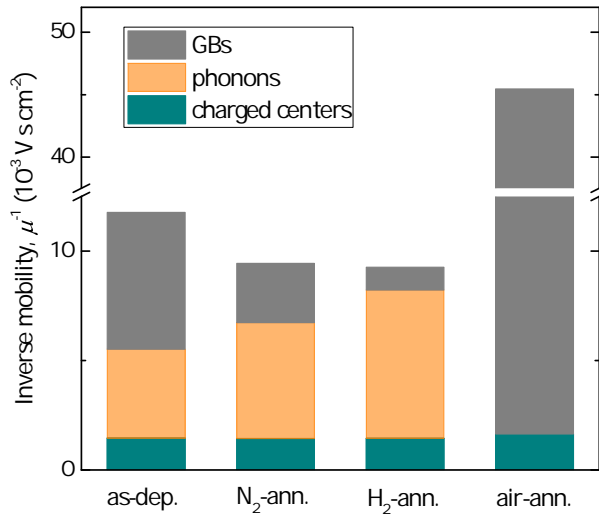


Figure 5.6: Inverse electron mobility components of IFO:H films under different PDA treatments.

5.3.3. Contact and device application

FTIR measurements were carried out to evaluate the interfacial oxide formation on symmetric structures with n^+ poly-Si/IFO:H stacks on both sides of the wafer, note that the FTIR results are collected on TCO coated poly-Si stacks. Figure 5.7(a) shows the baseline corrected FTIR transmittance spectra of the IFO:H films under different PDA treatments, by using the as-dep. sample as a reference baseline. In such a way, the noisy signals resulting from free carrier absorption of the TCOs in the infrared region were removed in the data reading so that the signal of our wanted n^+ poly-Si/TCO interfacial oxide formation was enlarged and became recognizable. The vibrations of Si-O-Si network were observed at 1076 cm^{-1} and/or 1236 cm^{-1} in N_2 -ann. and air-ann. samples, corresponding

to its transverse mode (TO) and longitudinal mode (LO) [272], respectively. According to Ishikawa *et al.* [273] and Liu *et al.* [272], the LO mode becomes lower when the film thickness decreases and the TO may become so weak with decreased SiO_x film thickness or changed chemical composition that TO can be hardly recognized on the spectrum. Thus the decreased LO intensity and undetected TO mode in the air-ann. sample might indicate a thinner interfacial SiO_x layer compared to the N₂-ann. sample. Moreover, both the LO and TO characteristics were not detectable in H₂-ann. samples, implying a basically unchanged interfacial composition with respect to the as-dep. sample baseline.

The interfacial oxide has been assumed as a legitimate explanation for forming a transport barrier on TCO/doped silicon layer and should be avoided in device application [130, 142–144]. Figure 5.7(b) displays the passivation test results on symmetric structures. In contrast to 24 nm-thick *n*-poly stack, the 250 nm-thick *p*-poly stack shows a higher stability against sputter-induced degradation and PDA treatments. The thickness-dependent characteristic can be attributed to the role of the poly-Si film as shielding of the critical *c*-Si/SiO_x/poly-Si interface from emerging harmful species [143]. The poly-Si thickness of 24 nm is in the reported range of 10–28 nm, in which the lifetime samples are dramatically sensitive during subsequent process [143]. Hence, one can see a clear implied- V_{OC} ($i-V_{OC}$) drop of around 20 mV on the thin *n*-poly stack samples after sputtering, which goes further down after PDA in N₂ ambiance while almost get fully restored after PDA in H₂ and air atmosphere. Hydrogen has been widely accepted as a crucial factor for ensuring good passivation quality in the poly-Si passivating contacts [274, 275], thus we attribute the passivation recovery to a sufficient hydrogen supplement to the *n*⁺ poly-Si/SiO_x/*c*-Si interfaces for H₂-ann. sample. As for the air-ann. sample, with the existence of moisture (H₂O), the exchange of hydrogen at the *n*⁺ poly-Si/SiO_x/*c*-Si interfaces do not harm the passivation qualities, since water vapour has been reported to effectively hydrogenate the poly-Si passivating contacts [276]. While for the N₂-ann. contacts, the passivation degradation is plausibly caused by a de-hydrogenation of the passivating contacts, in other words, hydrogen effuses from the *n*⁺ poly-Si/SiO_x/*c*-Si interfaces. Additionally, we extracted one group of contact resistivity values (ρ_c) of *n*-contact (*n*⁺ poly-Si/TCO/metal) regarding to different PDA treatments, which showed the results of 21.68 mΩ cm², 598.76 mΩ cm², 22.05 mΩ cm², and 265.05 mΩ cm², for as-dep., N₂-ann, H₂-ann, and air-ann. sample, respectively. These values are basically in accordance with Figure 5.7(a), namely, thicker interfacial oxide layer results in higher ρ_c values. From all the above results regarding both TCO opto-electrical properties and device application, we can conclude that H₂ annealing treatment provides a promising contact engineering approach in the high thermal-budget poly-Si solar cell design.

To verify that, we extracted ρ_c values of *n*-contact (*n*⁺ poly-Si/TCO/metal) and *p*-contact (*p*⁺ poly-Si/TCO/metal) with and without hydrogen annealing procedure, as shown in Figure 5.7(c-d). Results on lab-standard ITO layer were also provided for the audience's reference. As it can be seen, low ρ_c values below 40 mΩ cm² were observed for the contacts with as-deposited TCOs, which decreased further to around (or below) 20 mΩ cm² after hydrogen annealing treatment. For the *p*-contact which will be used on rear side of the device ((sample structure is shown in Figure 3.4(f))), all the $\rho_{c, p\text{-contact}}$ values after annealing were observed well below 30 mΩ cm², which will add negligible transport and *FF* losses when this stack is applied as a full-area contact [130]. As for the *n*-contact

(sample structure is shown in Figure 3.4(e)), to make a comparison, our $\rho_{c, n\text{-contact}}$ with as-deposited ITO are comparable with the reported data with 35 nm-thick n^+ poly-Si layer [142]. However, carrier transport at the poly-Si/TCO contact have been widely reported to degrade severely for temperatures above 350 °C (even $>10^4$ m Ω cm 2) [130, 142, 144]. According to Tutsch *et al.*, exposure at 380 °C in air significantly increased the ρ_c of n -contact from 50 m Ω cm 2 to above 700 m Ω cm 2 [143], and Wietler *et al.* reported the unfavourable ρ_c of ~ 800 m Ω cm 2 on a metal/ZnO:Al/poly-Si stack after air annealing at 400 °C [144]. To our knowledge, the $\rho_{c, n\text{-contact}}$ values are among the lowest values reported so far for poly-Si/TCO/metal stack with < 30 nm thin polysilicon layer, especially after thermal annealing at high temperature.

It is widely accepted that parasitic growth of the interfacial oxide in thermal annealing might be the reason for the reported high contact resistivity at poly-Si/TCO after annealing procedure [130]. According to the simulated results from Messmer *et al.* [130], there is a critical parasitic oxide thickness of about 1.4 nm, below such value the electron tunnelling through the oxide is expected to be efficient to yield a low contact resistivity. Above this threshold, the contact resistivity grows exponentially with linear increase in interfacial oxide thickness. Under this hypothesis, the unincreased contact resistivity values after our hydrogen annealing treatment at 400 °C probably result from the depression on the mentioned parasitic growth of interfacial oxide, which is also evidenced by our FTIR measurement results (Figure 5.7(a)). However, electric states at the interface between TCO and silicon can be very complicated (interface region can be even up to 50 nm [277]), thus detailed investigation remains to be carried out. Additionally, we noticed that for n -contact, ITO showed a lower ρ_c and a more preferable contact compared to IFO:H, which is inconsistent with our previous results [213]. This discrepancy might be explained by the high doping levels of doped silicon layer and ITO [126, 130], which facilitate electron tunnelling at the n^+ poly-Si/TCO interface, thus the work function matching becomes not as dominant as the case in reference [12] [213].

Considering that H $_2$ annealing at 400 °C ensures good contact properties for both n -contact and p -contact, we tested the performance on completed devices. Figure 5.8(a) displays the poly-Si solar cell parameters of devices using IFO:H and ITO, with and without H $_2$ annealing treatment, respectively. The devices experienced a general severe passivation loss accompanying our lab-standard screen-printing procedure, which brought a big drop from i - V_{OC} (~ 710 mV) on solar cell precursors to V_{OC} values (~ 665 mV) in devices. This could result from the damage of metallization procedure on the (thin) poly-Si layer [263, 278]. Apart from the general V_{OC} limitation on our devices, one can see that all the poly-Si solar cells showed similar V_{OC} values. This is in accordance with the results as shown in Figure 5.7(b). Besides, the FF was clearly improved by 0.9% $_{\text{abs}}$. (from 78.6% to 79.5%) with H $_2$ annealing treatment for IFO:H-based cells. To elaborate this, we performed SunsVoc measurements and calculated the series resistance ($R_{S, \text{SunsVoc}}$) values of the devices according to equation 5.3 [208].

$$R_{S, \text{SunsVoc}} = (pFF - FF) \frac{V_{OC} \cdot J_{SC}}{J_{\text{mpp}}^2} \quad (5.3)$$

In equation 5.3, pFF and J_{mpp} represent the pseudo fill factor and current density at maximum power point condition in SunsVoc measurements.

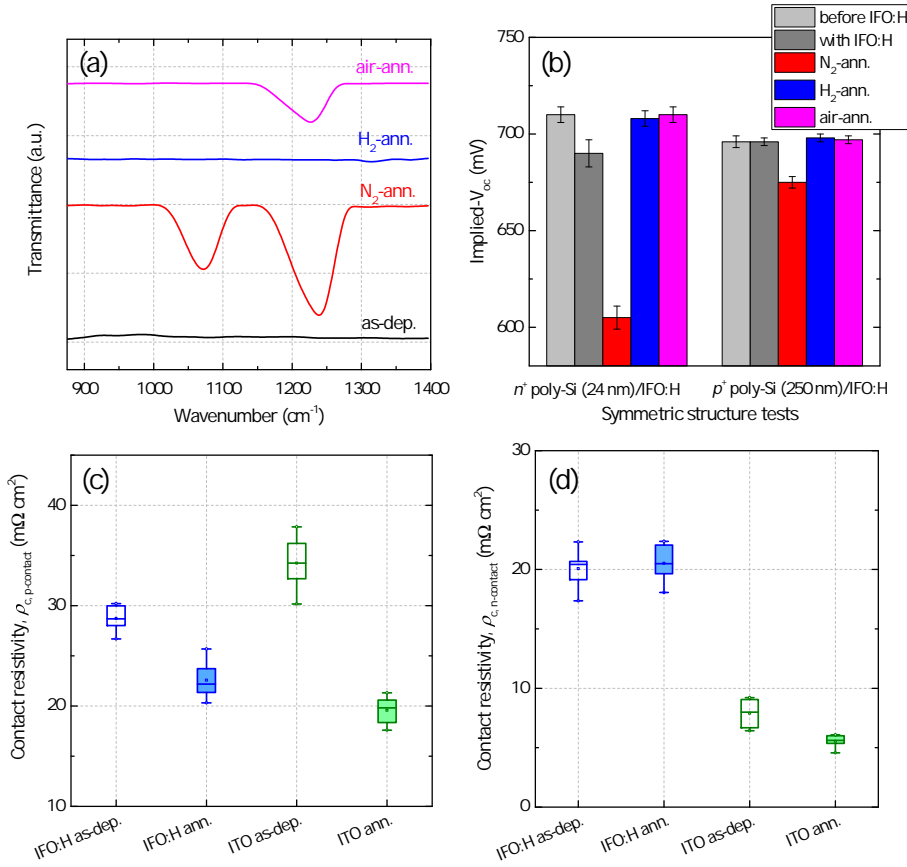


Figure 5.7: (a) baseline corrected FTIR spectra and (b) implied- V_{OC} change of the poly-Si/IFO:H stack under different PDA treatments. Contact resistivity values of (c) n -contact (n^+ poly-Si/TCO/metal) and (d) p -contact (p^+ poly-Si/TCO/metal) using IFO:H and ITO, with and without H₂ annealing treatment, respectively. The results in (c) and (d) are collected based on 6 groups of experimental data.

The specific vertical resistance ($R_{S,vertical}$) and lateral resistance ($R_{S,lateral}$) in our devices were then derived according to equation 5.4 and equation 5.5, respectively. Figure 5.8(b) illustrates the calculative $R_{S,vertical}$ and $R_{S,lateral}$ results corresponding to the devices in Figure 5.9(a).

$$R_{S,vertical} = \left(\frac{\rho_{c,n-contact}}{A_{front}} + \frac{\rho_{c,p-contact}}{A_{front}} + \rho_{wafer} \frac{t_{wafer}}{A_{cell}} \right) \cdot A_{cell} \quad (5.4)$$

In equation 5.4, $\rho_{c,n-contact}$ and $\rho_{c,p-contact}$ are corresponding average results from Figure 5.7(c-d). A_{front} , A_{rear} , and A_{cell} , denote the front metal coverage area, rear metal coverage area, and specific cell area, respectively. In our case, $A_{rear} = A_{cell} \cdot \rho_{wafer}$ is wafer resistivity (we took 3 Ω cm in the calculation), and t_{wafer} is wafer thickness (we took 270 μm as the single-side textured wafer). The vertical resistance values from our n^+ poly-Si, p^+ poly-Si, and TCO were negligible in the calculation.

$$R_{S,lateral} = R_{S,SunsVoc} - R_{S,vertical} \quad (5.5)$$

From Figure 5.8(b), the FF increase in IFO:H ann. sample as compared to IFO:H as-dep. sample is mainly caused by a decreased $R_{S,lateral}$ value, which can be reasonably attributed to the improved lateral conductivity of IFO:H film (as shown in Table 5.2). While the $R_{S,vertical}$ almost stays unchanged in both kinds of samples, indicating that the small contact resistivity change as shown in Figure 5.7(c-d) did not bring observable FF increase upon IFO:H ann. devices with respect to IFO:H as-dep. cells. As for the comparative results on ITO-based devices, an average FF drop of 0.4%_{abs.} after hydrogen annealing treatment was observed. As it can be interpreted in Figure 5.8(b), the FF drop is mainly caused by a decreased lateral conductivity of ITO film, which plausibly results from stability issues of ITO layer during the thermal treatments such as the firing steps in screen-printing process. Such stability issues of ITO is beyond the scope of this article and will not be discussed here.

Furthermore, the as-deposited ITO-based devices showed a higher average FF of 79.0% than the 78.6% of the as-deposited IFO:H cell, which are consistent with our previous data (Figure 5.1(a) and Figure 5.7(c-d)). While in the optical perspective, for specific TCO utilizations, slight $J_{SC,EQE}$ improvements were observed after H_2 annealing treatment, which might be interpreted by the compensation between E_g , n and FCA with PDA treatment (Figure 5.2, Figure A.1). However, all the IFO:H cells outperformed ITO cells due to the optical advantage of the high- μ_e IFO:H film [197, 213]. Subsequent improvements are under investigation regarding further reducing poly-Si layer thickness on illuminated side, increasing internal reflection, etc.

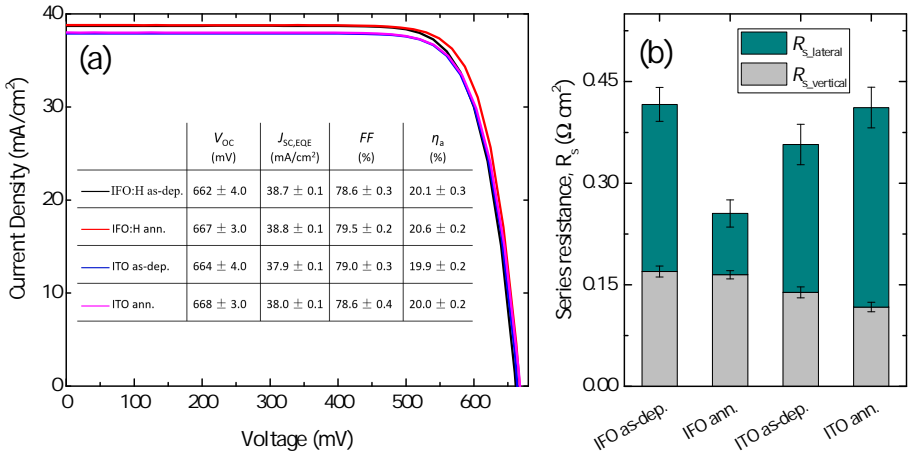


Figure 5.8: (a) Current-voltage characteristics of the best 3.92 cm^2 poly-Si solar cell devices using IFO:H and ITO, with and without H_2 annealing treatment, respectively. The values reported are the average based on three cells from the same batch, more device results from different experimental batches can be found in Table A.3, and (b) the decomposition of series resistance ($R_{S,SunsVoc}$) that corresponds to Figure 5.8(a).

To summarize, the PDA with H_2 annealing at 400 °C was successfully utilized in high thermal budget poly-Si solar cells, no obvious FF loss was observed. An absolute 0.5% gain

in active-area power conversion efficiency (η_a) was observed on IFO:H solar cell after PDA treatment in H_2 ambience, mainly due to the FF improvement (0.9%_{abs.}). Additionally, with respect to the widely used ITO, the PDA-treated IFO:H layer maintains its optical advantages in terms of higher E_g (T) and lower FCA while improves its lateral conductivity. This makes it a competitive transparent electrode for photovoltaic devices especially for high thermal-budget solar cells.

5.4. Conclusions

In summary, we studied the opto-electrical properties of the hydrogenated fluorine doped indium oxide (IFO:H) by means of post-deposition annealing (PDA) treatments at 400 °C in N_2 , H_2 , and air ambiances. Through detailed analyses of crystal structure, surface morphology, optical properties and temperature-dependent electrical properties, the inherent electron scattering and doping mechanisms of the IFO:H films were proposed and compared. Hydrogen annealing treatment was proved to favorably alter the opto-electrical properties of the TCO film, meanwhile achieve a good carrier transport at the poly-Si/TCO contact. It is noteworthy that the low contact resistivity of around (or below) 20 m Ω cm² was achieved on both n - and p - contacts with poly-Si/TCO stack after hydrogen annealing, which to our knowledge is among the lowest values especially on thermally annealed contacts at 400 °C. Beyond this, we implemented the hydrogen-annealed IFO:H films on FBC poly-Si solar cells. With respect to the solar cells with as-deposited IFO:H films, we observed a 0.9%_{abs.} improvement in average fill factor, which leads to an absolute 0.5% gain in active-area power conversion efficiency.

6

RT-sputtered IWO for improved current in SHJ solar cells

This chapter was published in *Solar Energy Materials and Solar Cells** [122]

Abstract

The window layers limit the performance of front/back-contacted silicon heterojunction (SHJ) solar cells. Here, we optimized tungsten-doped indium oxide (IWO) film deposited by radio frequency magnetron sputtering at room temperature (RT). The opto-electrical properties of the IWO were manipulated when deposited on top of thin-film silicon layers. The optimal IWO on glass shows carrier density and mobility of $2.1 \times 10^{20} \text{ cm}^{-3}$ and $34 \text{ cm}^2 \text{ V}^{-1} \text{ s}^{-1}$, respectively, which were tuned to $2.0 \times 10^{20} \text{ cm}^{-3}$ and $47 \text{ cm}^2 \text{ V}^{-1} \text{ s}^{-1}$, as well as $1.9 \times 10^{20} \text{ cm}^{-3}$ and $42 \text{ cm}^2 \text{ V}^{-1} \text{ s}^{-1}$, after treated on *i/n*/glass and *i/p*/glass substrates, respectively. Using the more realistic TCO data that were obtained on thin-film silicon stacks, optical simulation indicates a promising visible-to-near-infrared optical response in IWO-based SHJ device structure, which was demonstrated in fabricated devices. Additionally, by adding an additional magnesium fluoride layer on device, the champion IWO-based SHJ device showed an active area cell efficiency of 22.92%, which is an absolute 0.98% efficiency gain compared to the ITO counterpart, mainly due to its current gain of 1.48 mA/cm^2 .

*C. Han, Y. Zhao, L. Mazzarella, R. Santbergen, A. Montes, P. Procel, G. Yang, X. Zhang, M. Zeman, and O. Isabella, "Room-temperature sputtered tungsten-doped indium oxide for improved current in silicon heterojunction solar cells," *Solar Energy Materials and Solar Cells*, 227, 111082, 2021. April 14, 2021, doi: /10.1016/j.solmat.2021.111082.

6.1. Introduction

By far, the choice of dopants that induce high mobility in TCOs has largely been empirical, in which In_2O_3 doped with transition metal elements (such as Zr [104, 279], Ti [280], Mo [281], Ce [49], Hf [219], W [107, 121, 197, 282]) represent an attractive group. As suggested by Zhang *et al.* [283], the high mobility potential of the transition metal doped In_2O_3 could be explained by the high Lewis acid strength, which can be calculated from $L = Z/r_2 - 7.7\chi_z + 8.0$, where r is the ionic radius related to the electrostatic force due to the oxidation state Z of the ion and χ_z is the electronegativity of the element in the respective oxidation state. W^{6+} exhibits a high L of 3.158 due to its low ionic radius and high oxidation state. The W dopant with higher L compared to In^{3+} (1.026) in the host compound attracts electronic charge from the O^{2-} 2p valence band, resulting in the screening of the dopant's effective charge (Z). This screening effect weakens the interaction between the carriers and dopant ions, which means that the dopant's activity as a scattering center is receded thus high mobility is achievable. In addition, the ion radii of W^{6+} and In^{3+} are 0.6 Å and 0.8 Å, respectively, the tungsten dopant can substitute indium site in the lattice of In_2O_3 , high crystallinity of IWO in In_2O_3 polycrystalline structure has been reported [284]. Moreover, W^{6+} substituting for In^{3+} can still provide an electron even when associated with interstitial oxygen impurities (O^{2-}) in the lattice by forming charged complexes, $[(\text{W}_{\text{In}}^{\cdots})\text{O}_i^{\cdots}]$, as oppose to Sn^{4+} dopants in ITO, which become deactivated by forming neutral complexes, $[(2\text{Sn}_{\text{In}}^{\cdots})\text{O}_i^{\cdots}]$. This means that for the same number of carrier concentration, there may exist much less of dopant scattering centers in IWO film than in the commonly used ITO film [113]. All the above factors contribute to a high carrier mobility potential in IWO film [285]. Furthermore, tungsten doped indium oxide (IWO) shows complementary features in combining the advantages of indium oxide and tungsten oxide; thus it provides possibilities in manipulation of different contact characters [127]. As a consequence, IWO is a promising candidate for transparent electrode in photovoltaic devices [121].

For the fabrication of IWO layers, a wide range of deposition techniques have been utilized, such as pulsed laser deposition (PLD), reactive plasma deposition (RPD, or arc plasma ion plating, or high-density plasma-enhanced evaporation), magnetron sputtering [49, 107, 285]. In order to obtain decent carrier mobility above $60 \text{ cm}^2 \text{ V}^{-1} \text{ s}^{-1}$, a deposition temperature of above $300 \text{ }^\circ\text{C}$ was utilized for quite a long time [285]. This is not suitable for SHJ devices, which require a process temperature below $250 \text{ }^\circ\text{C}$, or even lower [12, 132]. Since 2013, Liu *et al.* have been working on developing SHJ-targeted IWO film via RPD approach [113, 121, 217, 282]. Similar technique was also utilized by Koida *et al.* [197, 286]. Besides, Lerat *et al.* applied radio frequency (RF) magnetron sputtered hydrogenated IWO for SHJ application [287]. The above-mentioned techniques were using a deposition or post-deposition annealing treatment above $150 \text{ }^\circ\text{C}$.

Accordingly, it is imperative to study the opto-electrical properties and the application of a low thermal budget IWO layer. Herein, we present an IWO optimization at room temperature (RT) by RF magnetron sputtering. The opto-electrical properties of the optimized IWO film are evaluated on top of thin-film silicon layers. Finally, the performances of IWO-based SHJ solar cells are tested and compared to reference devices with ITO.

6.2. Experimental

The experimental section includes the following parts.

Deposition of TCO films. In IWO film sputtering, argon and 1% oxygen in argon were utilized as the process gas. All depositions were performed at room temperature without any intentional heating, with the chamber pressure of 4.0×10^{-3} mbar, (Ar+O₂) flow of 20 sccm, and power density of ~ 0.8 W/cm². The deposition rate of the optimized IWO films was ~ 2 nm/min. The ITO depositions were done at substrate temperature of 110 °C, chamber pressure of 2.0×10^{-2} mbar, Ar flow of 50 sccm (0.05% O₂), and power density of ~ 1.8 W/cm². The deposition rate of ITO layer was ~ 6 nm/min.

Fabrication of SHJ solar cells. SHJ cell precursors with front 10 nm-thick *i/n* stack and rear 26 nm-thick *i/p* stack thin-film silicon layers were prepared. Nominal 75-nm and 150 nm-thick TCO films were sputtered on the front and rear sides of the wafers, respectively, through hard mask, which defines different cell areas on each wafer. After sputtering, the IWO-based cell precursors were annealed in air at 180 °C for 5 min for curing purposes. We note that ITO-based devices maintained good passivation qualities after ITO sputtering; thus no subsequent post annealing treatment was applied on corresponding cell precursors. Front metal contacts were RT electroplated Cu fingers, with an underlying 100 nm-thick Ag as seed layer [288]. The photolithography process with organic photoresist (AZ ECI3027 from Microchemicals) was used to define the contact area for metallization. The rear metal contact was 500 nm-thick thermally evaporated Ag. For a double layer anti-reflection coating purpose, 90 nm-thick MgF₂ layer was e-beam evaporated on the front side of the completed SHJ devices.

6.3. Results and discussion

6.3.1. Optimization of 75 nm-thick IWO films on glass substrate

Hall measurements show that the IWO films are *n*-type semiconductor. Figure 6.1(a) shows their carrier density (N_e), mobility (μ_e), and resistivity (ρ) change as function of O₂-to-Ar flow ratio (X). For X increasing from 0 to 0.50%, N_e monotonously decreases, while μ_e first rises and then goes slightly down. Consequently, the ρ value first decreases and then rises up. The highest μ_e of 34 cm²V⁻¹s⁻¹ was obtained at $X = 0.25\%$. This is higher than the reported < 20 cm²V⁻¹s⁻¹ of RT-sputtered IWO layer at room temperature [289]. However, we note that both N_e and μ_e of our as-deposited layer are lower than that of reported RT grown IWO films from RPD approach [107, 113]. Possibly, as compared to the sputtering process, the high-density plasma density in RPD technique provides higher reactivity of the evaporated species from the tablet material, which promotes higher effective doping of W dopant and thus produces excess electrons and higher N_e in the IWO film [107, 290, 291]. The charge screening effect of more effective W dopant and the plausibly increased densification/crystallization of the film, contribute to a higher μ_e in the IWO film [107, 113, 285].

Furthermore, the electrical properties of the TCOs correlate their optical properties. Figure 6.1(b) displays the complex refractive index of the IWO films. The IWO deposited at $X = 0.25\%$ yields the largest optical bandgap (E_g) in UV range and low absorption in NIR range, while the IWO deposited at $X = 0.50\%$ shows a E_g shrinkage (Moss-Burstein effect [55]) and rather high ρ due to its lowest N_e . Thus, it was not considered for use in

devices.

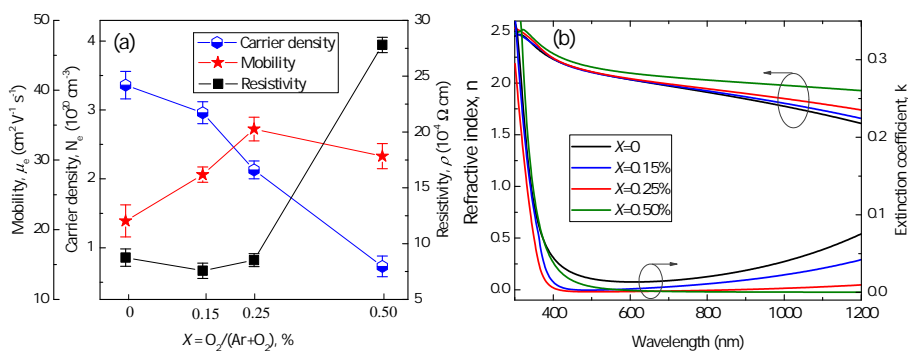


Figure 6.1: (a) N_e , μ_e , and ρ of the as-grown IWO films with a variable O_2 -to-Ar flow ratio (X), based on six groups of experimental data. (b) Complex refractive index of the IWO films for different X .

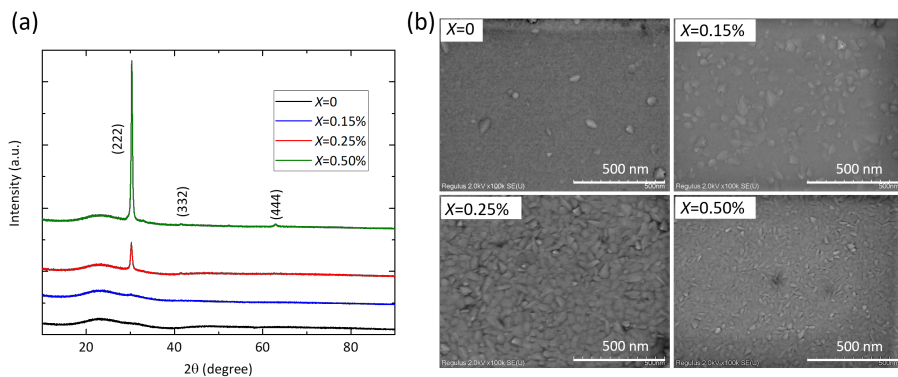


Figure 6.2: (a) X-ray diffraction patterns, and (b) scanning electron microscope images of IWO films deposited with different O_2 -to-Ar flow ratios (X).

Figure 6.2 (a-b) present the XRD patterns corresponding to an In_2O_3 cubic bixbyite crystal structure and SEM images of the IWO layers grown with different X . One can see from both figures that, with increasing X from 0 to 0.50%, the crystallization of the as-deposited IWO films largely improves. This is possibly due to the increased stoichiometric composition of the film [292]. For the XRD results with $X = 0$ and $X = 0.15\%$, the absence of diffraction peaks is indicative of mostly amorphous films. Further, from corresponding SEM images, we additionally observe the characteristic crystalline grain evolution, indicating a limited sensitivity of the XRD measurement in detecting low crystalline materials [104]. From Figure 6.2(b), the grain size of the IWO films shows a decreasing trend with increased X , indicating more grain boundaries (GBs) that act as carrier scattering defects. Therefore, combined with the data shown in Figure 6.1, the monotonously decreased N_e from $X = 0$ to $X = 0.50\%$ is mainly caused by a continuously increased oxygen incorporation, which occupies oxygen vacancies (V_O) that provide additional electrons in the IWO

films [51]. Whereas the μ_e could be influenced by the compensation of decreased point defect scattering from V_O elimination, and GB scattering as mentioned above in Figure 6.2 (b) [285]. In addition, the carrier transport at GBs is also influenced by the N_e change [66, 293, 294]. As a consequence, μ_e firstly rises from $X = 0\%$ to $X = 0.25\%$, then drops with a further increased X to 0.50%.

Figure 6.3 compares the absorption coefficient spectra of the optimal IWO grown from $X = 0.25\%$ to the ITO reference, with the inset table showing the parameters of N_e , μ_e , ρ and E_g . Notably, in the short wavelength range, the IWO with lower N_e shows a larger optical bandgap (E_g) than ITO, which is opposite to the well-known Moss-Burstein effect [55]. Presumably, it indicates a smaller effective electron mass in the IWO film structure [281, 285]. Besides, with respect to ITO film, the lower absorption coefficient (α) of IWO layer in the NIR region could be explained by the classical Drude theory [33, 196]. In addition, to further confirm the observations, we compared the absorbance curves of IWO and ITO films which were calculated from 1- R - T , as shown in Figure B.2, which shows the same trend as we observed from Figure 6.3.

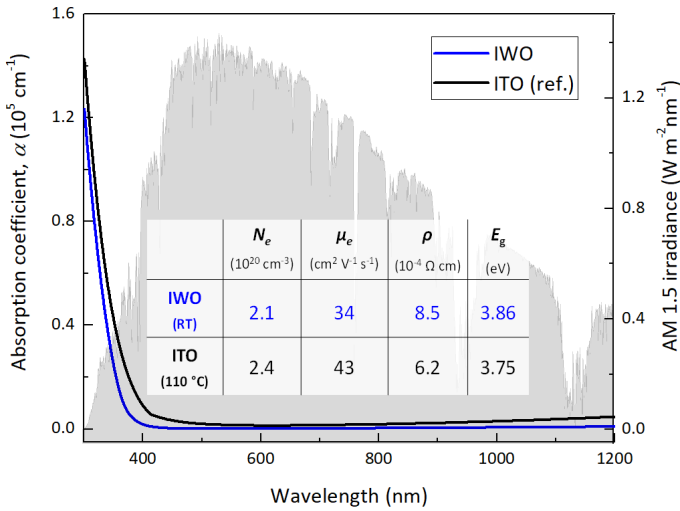


Figure 6.3: SE-fitted absorption curves and inset table with opto-electrical properties of the optimized IWO and ITO reference films deposited at RT and 110 °C, respectively.

6.3.2. IWO on top of thin film Si layers and optical simulations

Figure 6.4(a-d) show the N_e and μ_e values of nominal 75 nm-thick TCOs on glass and on i/n /glass and i/p /glass, respectively. Our lab-standard ITO film acts as a reference, and the i/n and i/p thin-film silicon layer stacks are in the same layer thickness as used in SHJ devices. We note that a hot-plate annealing at 180 °C for 5 min was performed on the RT-deposited IWO samples. This is a required step to recover the sputter damage of the passivation quality of the SHJ cell precursors (see Figure B.3), which could also potentially improve the electrical property of the IWO/ p -layer interface [176]. For the IWO layers, deposition on either glass or thin-film silicon does not influence μ_e , whilst it mildly

adjusts N_e . After annealing, the IWO films show a slightly lower N_e from $2.1 \times 10^{20} \text{ cm}^{-3}$ on glass substrate to $2.0 \times 10^{20} \text{ cm}^{-3}$ on *i/n*/glass and $1.9 \times 10^{20} \text{ cm}^{-3}$ on *i/p*/glass substrates, respectively. The N_e decreases reflect oxygen incorporation during the annealing process. On the other hand, upon annealing, the μ_e increases from $34 \text{ cm}^2\text{V}^{-1}\text{s}^{-1}$ on glass substrate to $47 \text{ cm}^2\text{V}^{-1}\text{s}^{-1}$ on *i/n*/glass and $42 \text{ cm}^2\text{V}^{-1}\text{s}^{-1}$ on *i/p*/glass substrates, respectively. This phenomenon could be associated with an increased Lewis acid strength (L) as introduced in Introduction part. After annealing treatment, tungsten dopant with a higher L could be reached due to a higher oxidation state of tungsten ions, which leads to an increased carrier mobility [285, 292, 295, 296]. Additionally, with respect to as-deposited states, the μ_e increases in annealed IWO layers on *i/n*/glass and *i/p*/glass substrates are different, indicating that the μ_e is also influenced by (i) increased crystallization, as implied by the XRD patterns and SEM images in Figure B.4, and (ii) possible defect passivation of thermally effused hydrogen from underlying thin-film silicon layers [87, 195]. Furthermore, with respect to glass substrate, the as-deposited ITO film on *i/n* stack shows constant μ_e and mildly increased N_e , while the ITO layer on *i/p* stack displays distinct μ_e drop together with N_e rise. The N_e change could be partially owing to the diffused hydrogen from the thin film underneath, which has been elucidated by Cruz *et al.* [87] and Ritzau *et al.* [195]. Regarding the observed μ_e drop for the ITO on *i/p* stack, we exclude the cause from the substrate surficial roughness as observed by Cruz *et al.* [87]. In fact, AFM measurements show quite similar root-mean-square roughness values of 1.11 nm and 1.23 nm for our *i/n* and *i/p* stacks, respectively. Plausibly, our N_e and μ_e change is also correlated with additional features, such as crystallizations of both TCOs and thin-film Si layers and their inherent interactions, hydrogen effusion behaviour in dependence of temperature/ambience, TCO/Si interfacial oxide influence on carrier transport. Elaborated study still needs to be carried out to fully understand the interaction between IWO and doped thin-film layers. Additionally, it is worth pointing out that the substrate topology such as textured wafer surface might also have an impact on the TCO properties [88, 89], which remains to be investigated via appropriate characterization approaches.

Figure 6.5 shows the corresponding absorption coefficient (α) curves versus wavelength of TCOs on different substrates. Basically, all the IWO layers show favourable lower α than reference ITO films along the Vis-NIR range. Regarding the IWO layers on thin-film silicon layers, with respect to the IWO films on *i/n*/glass and *i/p*/glass substrates, the different α transition in the UV range is possibly related to the thermally-effused hydrogen from underlying thin-film silicon layers, since both interstitial and substitutional hydrogen have been proven to act as shallow donors in In_2O_3 system [63, 87, 195]. Additionally, the α changes of the TCOs in the NIR region could be aligned with the classic Drude theory [33, 196]. Overall, we may conclude that with thin-film silicon layer underneath, the top TCO film could be manipulated both electrically and optically, which needs to be considered in device simulations as well as in practical cell fabrication.

Figure 6.6(a-c) show GenPro4 optical simulation results of comparative SHJ devices based on IWO and ITO counterpart. Figure 6.6(a-b) are the simulated absorptance curves of IWO- and ITO-based SHJ structure, in which the TCO data obtained from thin-film silicon stacks were used. The results based on TCO data obtained on glass substrates were provided in Figure B.5(a-b). From Figure 6.6(a-b), the implied photocurrent density in c-Si absorber was calculated to be 40.3 mA/cm_2 in IWO cell and 38.5 mA/cm_2 in ITO

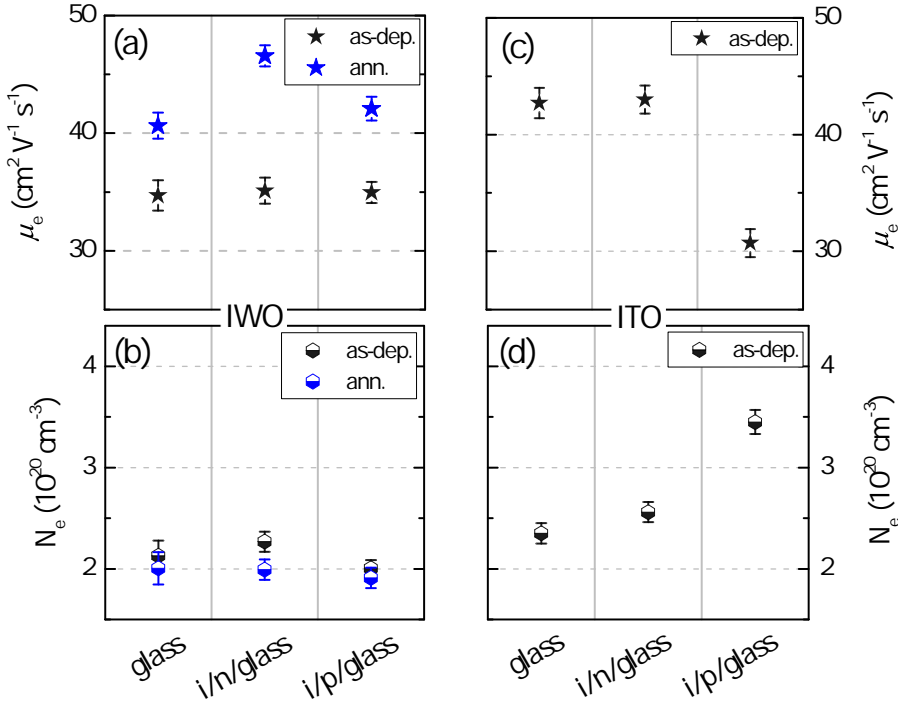


Figure 6.4: (a) μ_e and (b) N_e of the as-deposited and annealed IWO films on different substrates; (c) μ_e and (d) N_e of as-deposited ITO layers on different substrates. The results are based on three groups of experimental data.

cell. As compared to ITO cell, the outstanding optical advantage of IWO cell is ascribed to the much less parasitic absorption in IWO layer. Figure 6.6(c) displays the optical losses corresponding to reflection, parasitic absorption from thin-film silicon, TCO, and rear metal components. In Figure 6.6(c), the results from simulations based on TCO data obtained on glass substrates are also included. With respect to the results from data on glass substrates, the IWO cell shows a lower parasitic absorption in TCO layer, while ITO cell shows an increased parasitic absorption in TCO layer. This is related to their different changing trends in N_e , as shown in Figure 6.4 [33]. In addition, we notice that the total reflection loss in IWO cell is visibly higher than in ITO cell. Following the approach as utilized in [297], we decomposed the total reflectance into front side reflectance (R_1) and rear side internal reflectance (R_2), which are indicated in Figure 6.6(d). The R_1 and R_2 are 1.3 mA/cm^2 and 1.6 mA/cm^2 for IWO cell, and 1.5 mA/cm^2 and 0.5 mA/cm^2 for ITO cell, respectively. This means that the high reflection loss in IWO cell comes from its high R_2 value, indicating that large amount of NIR light escapes after passing through the cell. While in ITO cell such NIR light is mainly absorbed in the TCO, this is not displayed in the reflection loss. In this regard, the higher R_2 in IWO cell may not be optically detrimental since there is still possibility to make use of it with appropriate manipulation strategy. To summarize, the interactive opto-electrical properties of TCO with underlying layers

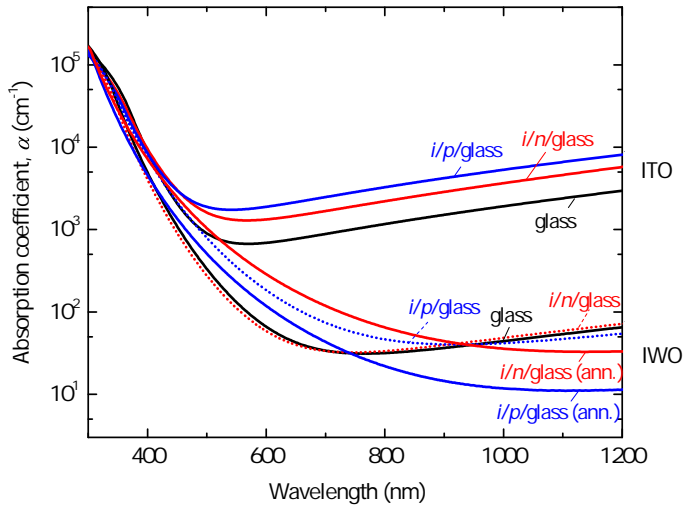


Figure 6.5: SE-fitted absorption coefficient (α) curves of TCOs on top of different substrates.

need to be considered in device design, and our IWO layer indicates a promising optical outperformance in SHJ cell over our lab-standard ITO counterpart.

6

6.3.3. Devices performance

Figure 6.7(a-d) depict the measured IWO- and ITO-based SHJ cell parameters. The metallization approach is room temperature Cu-plating. For each batch, we tested variable devices in different metal design, all the devices in the same design showed similar comparative trend, and only the optimal 8.97 cm²-cell results are summarized in Figure 6.7. The implied- V_{OC} of the SHJ cell precursors varied from 720 to 735 mV (not shown here). From Figure 6.7(a), the average V_{OC} , especially for IWO cells, is approaching 730 mV, due to the RT Cu-plating metallization [288]. As for the optical response in Figure 6.7(b), all the IWO cells showed notably higher J_{SC} than ITO devices, which agrees with the previous optical simulation results as shown in Figure 6.6. We notice that the J_{SC} improvement from reference ITO cell to IWO cell was generally 0.8-1.4 mA/cm², which is smaller than the 1.8 mA/cm² as predicted from Genpro4 simulation. This may be ascribed to the electrical carrier transport/collection difference in the two kinds of devices, or possible underestimation on the simulated parasitic absorption of IWO layers, since reflection-type spectroscopic ellipsometry has been reported to present limited sensitivity for weak light absorption [183, 189]. Additionally, from Figure 6.7(c), the IWO cells showed slightly higher FF and lower series resistance ($R_{S,SunsVoc}$) than the ITO-based counterpart. This possibly originates from a favourable band alignment at the IWO/doped Si layer interfaces, as the IWO exhibit different work-function than ITO [126, 127]. The IWO cells outperformed ITO devices due to their advantage in both optical and electrical aspects, as displayed in Figure 6.7(d). With respect to ITO-SHJ cells, the averaged cell efficiencies of IWO-SHJ cells show absolute improvements of 0.98%. Our comparative cell results are in agreement with the observations from Ding *et al.* [298]. It is noteworthy that Ding *et al.*

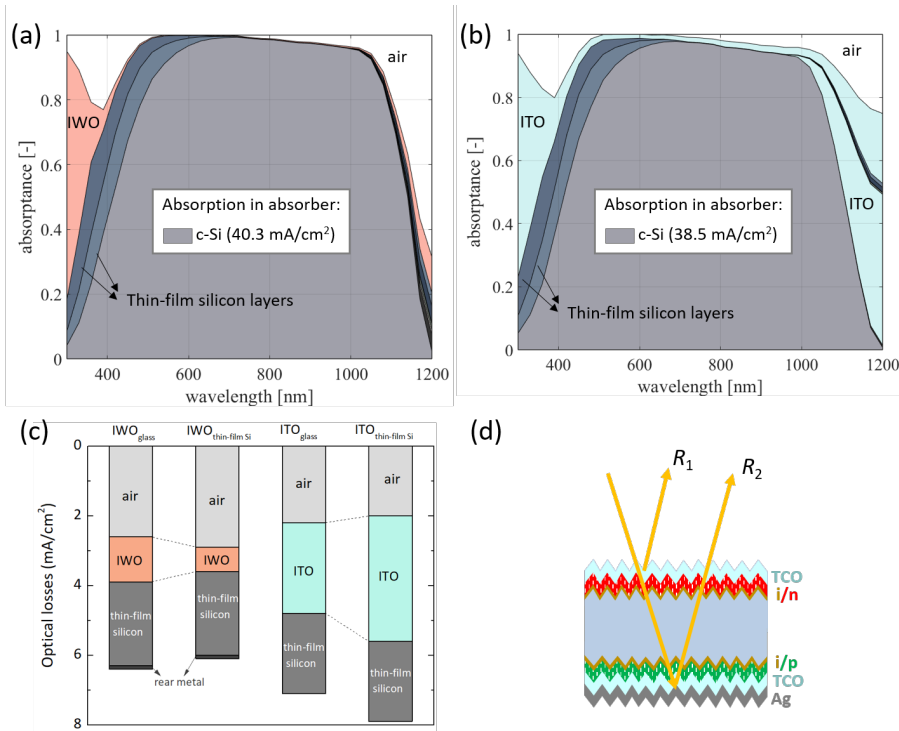


Figure 6.6: Optical simulations performed by GenPro4 software of (a) IWO- and (b) ITO-based SHJ solar cells, in which the TCO data gathered from thin-film silicon layers were taken into consideration. (c) Overview of optical losses from different components. The simulations are performed using the TCO n, k data set obtained as indicated on the x -axis. (d) Sketch of individual reflection losses corresponding to the front and rear sides of our SHJ cell structure.

used hydrogenated IWO layers, which presented both higher μ_e and N_e as compared to our IWO film. According to Ding *et al.* [298], as compared to ITO cell, their J_{SC} increase is less, and FF increase is higher in IWO cell than in our case. Plausibly, the phenomena are related to the hydrogen inclusion in their IWO layer, which generates more dopants to ensure a good conductivity, yet results in a probability to compensate its optical property [35, 267]. Additionally, we note that the measured J_{SC} in our $I-V$ measurements was a bit higher than the integrated $J_{SC,EQE}$ from EQE curve, similar phenomenon is also seen in [155]. Below we report the active area power conversion efficiency to avoid such a measurement error from the different light sources and metal fractions in the illumination area.

To minimize the above-mentioned high reflection loss in IWO cell (Figure 6.6), we further introduced the so-called double layer anti-reflection coatings (DLARC). By adding an additional non-absorptive layer with appropriate thickness and refractive index of ~ 1.5 @ 600 nm, we can further decrease the reflection losses on device level [121, 123, 279, 299]. Figure 6.8 and Table 6.1 show the EQE, $1-R$ and cell parameters of our optimized IWO-based SHJ device and its ITO counterpart, with and without (w/o) a 90 nm-thick MgF_2 top

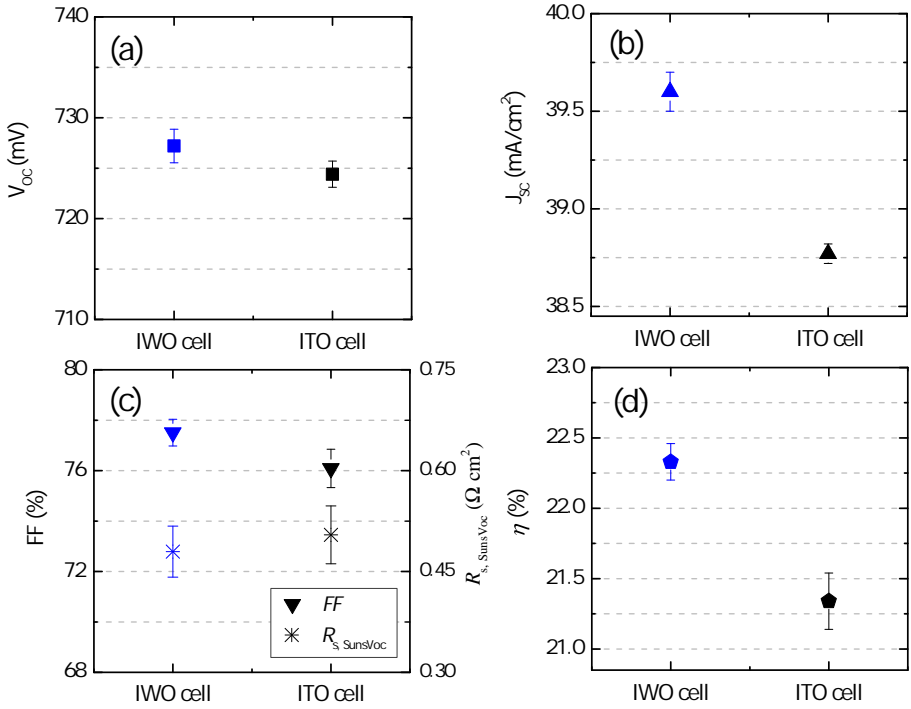


Figure 6.7: (a) Open-circuit voltage, V_{OC} , (b) short-circuit current density, J_{SC} , (c) fill factor, FF , and series resistance, $R_{S, \text{SunsVoc}}$, and (d) illuminated area power conversion efficiency, η of the IWO- and ITO-based SHJ devices. The cell area is 8.97 cm^2 and the designed metal coverage is 1.93%. The results are based on five batches of cells.

layer. The MgF_2 optical parameters and the simulative optimization with MgF_2 thickness on our IWO cell structure are shown in Figure B.6(a-b). From Figure 6.8, compared to the devices without MgF_2 on top, the cell with MgF_2 layer showed significantly improved optical responses. Especially the $J_{SC, \text{EQE}}$ of the IWO cell was improved from $39.41 \text{ mA}/\text{cm}^2$ to $40.16 \text{ mA}/\text{cm}^2$. This is mainly caused by a boosted performance in the short wavelength range (300-550 nm), resulting from the decreased reflectance of the cell surface, as we can clearly see from the 1- R curve. Finally, with adding a MgF_2 layer on top of the IWO device, the active area power conversion efficiency was improved from 22.52 to 22.92%.

Now we look at the EQE curves of the IWO cell and ITO cell in Figure 6.8. Before applying the MgF_2 top layer, the IWO cell displays lower blue response in 300-600 nm ($-0.46 \text{ mA}/\text{cm}^2$) and significantly higher response in vis-NIR region in 600-1200 nm ($+1.74 \text{ mA}/\text{cm}^2$), as compared to ITO cell. After adding the top MgF_2 layer, the IWO/ MgF_2 cell outperformed ITO/ MgF_2 cell in the whole wavelength range, which corresponds to a $0.44 \text{ mA}/\text{cm}^2$ gain in the 300-600 nm region and a $1.04 \text{ mA}/\text{cm}^2$ gain in 600-1200 nm region, respectively. According to Figure 6.3, the IWO layer has a higher optical band gap (E_g) value of 3.86 eV than the 3.75 eV of ITO layer, while the IWO cell shows a lower blue response, as compared to ITO cell. To elaborate that, we performed E_g plots of the

TCOs on top of thin-film silicon stacks at the illuminated side of our SHJ device, as shown in Figure B.7. The extracted E_g values are 3.81 eV and 3.87 eV for IWO and ITO layers, respectively. Combined with Figure 6.4, this more realistic comparison is in accordance with the Moss-Burstein effect [55] and well explains why the IWO cell shows a lower blue response than ITO cell. Additionally, this difference is not existing after applying MgF_2 , and the $J_{\text{SC,EQE}}$ improvement of ITO/ MgF_2 cell over ITO cell is 0.55 mA/cm^2 , which is lower than the 0.75 mA/cm^2 in IWO case. This is related to the non-ideal DLARC use [123]. Optimization on the DLARC design and corresponding experimental validation are out of the scope of this work, thus will not be further elucidated.

Furthermore, according to Ding *et al.* [298] and Lerat *et al.* [287], significantly improved blue response in IWO cell accounts for the J_{SC} increase with respect to ITO cell while no NIR contribution was observed. This is different from our observations that improved NIR response contributes to the $J_{\text{SC,EQE}}$ increase of the as-fabricated IWO cell over ITO cell. Considering that the reference ITO film used by Lerat *et al.* was in a similar N_e range as the one we use in our work, we speculate the rationale of the different optical response in IWO cells may lie in the microstructure and carrier conductive mechanism difference in the IWO films [35, 285].

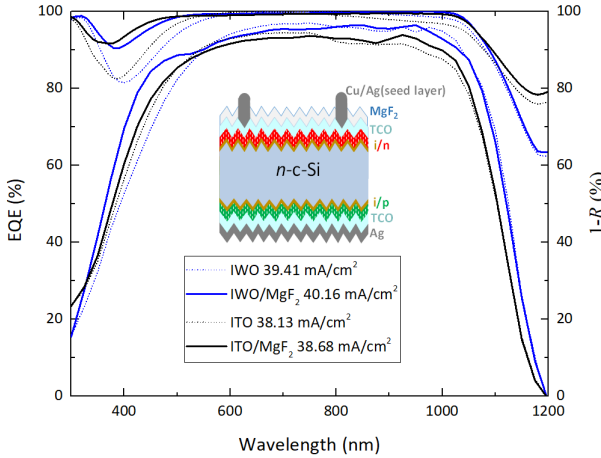


Figure 6.8: EQE and $1-R$ of the optimal IWO-based SHJ device and its ITO counterpart, with and without MgF_2 top layer. Inset is the final device structure.

Table 6.1: Solar cell parameters of the optimal IWO-based SHJ device and its ITO counterpart, before and after MgF_2 top layer deposition (cell area 8.97 cm^2).

TCO	Open-circuit voltage [V_{OC} , mV]	EQE-short circuit current density [$J_{\text{SC,EQE}}$, mA/cm^2]	Fill factor [FF , %]	Efficiency [η , %]
IWO	730	39.41	78.27	22.52
IWO/ MgF_2	731	40.16	78.07	22.92
ITO	728	38.13	78.00	21.65
ITO/ MgF_2	728	38.68	77.91	21.94

6.4. Conclusions

We optimized RF magnetron sputtered IWO layer at room temperature by adjusting the O₂-to-Ar gas flow ratio during deposition process. The opto-electrical properties of the TCO layers were found to be sensitive to the substrate materials and post-annealing process. The opto-electrical properties of the IWO were manipulated when deposited on top of thin-film silicon layers. This needs to be considered in practical simulation and experimental work. The optimal IWO on glass shows carrier density and mobility of $2.1 \times 10^{20} \text{ cm}^{-3}$ and $34 \text{ cm}^2\text{V}^{-1}\text{s}^{-1}$, which were tuned to $2.0 \times 10^{20} \text{ cm}^{-3}$ and $47 \text{ cm}^2\text{V}^{-1}\text{s}^{-1}$, as well as $1.9 \times 10^{20} \text{ cm}^{-3}$ and $42 \text{ cm}^2\text{V}^{-1}\text{s}^{-1}$, after treated on *i/n*/glass and *i/p*/glass substrates, respectively. Further, GenPro4 simulations implied a clearly increased visible-to-near-infrared optical response in IWO-based SHJ cell with respect to our ITO-based reference cell, which was demonstrated in practical comparative SHJ devices. By applying an additional MgF₂ layer on top of the optimal device, the EQE-integrated short-circuit current density was improved from 39.41 mA/cm^2 to 40.16 mA/cm^2 . Our final IWO/MgF₂-based SHJ solar cell showed an active area cell efficiency of 22.92%, which is an absolute 0.98% efficiency gain compared to the ITO counterpart, mainly due to its current gain of 1.48 mA/cm^2 .

7

Towards bifacial Cu-plated SHJ solar cells with reduced TCO use

This chapter was published in *Progress in Photovoltaics: Research and Applications** [125]

Abstract

In this work, based on a newly developed bifacial Cu-plating platform (see Appendix D), we explored bifacial SHJ solar cells with less TCO use. We present three types of In_2O_3 -based TCOs, tin-, fluorine-, and tungsten-doped In_2O_3 (ITO, IFO, and IWO). These are In_2O_3 -based TCOs, from post-transition metal doping, anionic doping, and transition metal doping and exhibit different opto-electrical properties. We performed optical simulations and electrical investigations with varied TCO thicknesses. The results indicate that (i) Reducing TCO thickness could yield larger current in devices; (ii) our IWO and IFO are favorable for n -contact and p -contact, respectively; and (iii) our ITO could serve well for both n -contact and p -contact. Interestingly, for the p -contact, with the ITO thickness reducing from 75 nm to 25 nm, the average contact resistivity values show a decreasing trend from $390 \text{ m}\Omega \text{ cm}^2$ to $114 \text{ m}\Omega \text{ cm}^2$. With applying 25 nm-thick front IWO in n -contact, and 25 nm-thick rear ITO use in p -contact, we obtained front side efficiencies above 22% in bifacial SHJ solar cells. This represents a 78% TCO reduction with respect to our lab-standard monofacial SHJ solar cell, and a 67% TCO reduction with respect to a reference bifacial solar cell with 75 nm-thick TCO on both sides.

*C. Han, R. Santbergen, M. van Duffelen, P. Procel, Y. Zhao, G. Yang, X. Zhang, M. Zeman, L. Mazzarella, and O. Isabella, "Towards high efficiency bifacial silicon heterojunction solar cells with reduced TCO use," *Progress in Photovoltaics: Research and Applications*, 2022. March 14, 2022, doi:10.1002/pip.3550.

7.1. Introduction

Silicon heterojunction (SHJ) solar cells have exhibited high efficiencies above 25% in both academia and industry [11, 115]. Key challenges to be addressed in the upscaling process are the cost and the relative scarcity of certain utilized materials, such as indium, silver, and bismuth [300, 301]. Indium is widely used in the transparent electrodes of SHJ devices. For the purpose of reducing indium consumption, basic strategies include: (i) use of In-free transparent electrode (TE), including In-free transparent conductive oxide (TCO) such as aluminum-doped zinc oxide (AZO) [172, 302, 303], and other TE material such as graphene [304]; (ii) reduction of the TCO thickness; (iii) development of TCO-free SHJ devices (extreme case). For the AZO use in (i), challenges may lie in low carrier mobility and stability issues [269, 299, 305], and the promise of non-traditional TE material use still needs to be tested and developed. For (iii), proof-of-concept TCO-free SHJ cells have been demonstrated lately [170], but efforts have been hampered from the passivation deterioration and contacting problems [170, 306, 307]. For instance, a thick thin-film silicon layer was reported to reduce the passivation deterioration, but it accompanies additional optical loss due to the parasitic absorption from the thin-film silicon layer [170]; titanium (Ti) was reported to maintain a low contact resistance between silicon layer and metal, but Ti can easily react with thin-film silicon layer and depassivate the solar cell [306]. The issues remain to be tackled in the future. Besides, it is still an open question whether TCO-free design could potentially give optimal device performance. Moreover, a TCO layer is practically needed to act as a barrier layer against Cu diffusion during plating processes [112, 308]. To circumvent these limitations, we focus on the solution with reducing TCO use in SHJ solar cells.

From the optical point of view, front and rear TCO layers function as anti-reflection coating (ARC) and back reflector (BR) layers, respectively [82]. However, parasitic free carrier absorption (FCA) from both sides TCOs is unavoidable, which is directly proportional to the carrier density [35]. The use of a thinner TCO layer could considerably reduce FCA. However, the functions of ARC and BR are weakened. As for the ARC purpose, an additional optical capping layer (OCL), such as MgF_2 [122], SiO_x [121, 299], SiN_x [82, 170], TiO_x [309], could be utilized to reach an optimal light in-coupling. It has been well proven that as compared to a SHJ device counterpart with only TCO layer acting as ARC at illumination side(s), the device with a double layer anti-reflection coating could produce an even higher current output [123] and meanwhile potentially improve the device stability [299]. Besides, considering the BR loss when reducing rear TCO use in SHJ solar cell, Holman *et al.* [310] and Cruz *et al.* [124] have reported that implementing an OCL between the rear TCO and the full-area rear metal could quench optical losses in the near-infrared wavelength range. Nevertheless, in order to find out what are the minimal TCO thicknesses for different TCOs to maintain/reach good optical responses at device level, an elaborate study on both sides TCO/OCL optimizations with varied TCOs is still to be carried out.

Meanwhile, the optical optimization should be addressed without detrimentally affecting the electrical performance of the device [311]. It is known that a high quality wafer absorber could itself provide substantial lateral transport of majority carriers [312]. However, for efficient utilization of absorber's lateral transport, very low contact resistances in the vertical directions are essential [313]. In general, for the monofacial SHJ solar cells, the

electrical problem exists at the TCO/doped silicon layer interfaces, where carrier transport barrier forms mainly due to the work function differences between TCO and doped silicon layers [126, 306, 314]. The work function defines the difference between the energy of the vacuum level and the Fermi level, which changes with the carrier density (N) in specific TCOs [59]. Considering the electrical properties (including N) of TCOs generally vary with the thickness of the TCO layer, it is imperative to investigate the thickness-dependent TCO/doped silicon layer contact properties when designing SHJ solar cells with reduced TCO thicknesses.

In this work, we choose three types of TCOs. These are tin-, fluorine-, and tungsten-doped indium oxides (namely, ITO, IFO, and IWO). They are In_2O_3 -based TCOs that exhibit different opto-electrical properties from post-transition metallic cationic doping, anionic doping, and transition metallic cationic doping, respectively. From optical simulations, different required minimal TCO thicknesses for maintaining good optical performance are calculated. Further, we evaluate the lateral and vertical carrier transport behaviors in solar cells with varied TCO thicknesses. Finally, different bifacial SHJ devices with reduced TCO use are fabricated.

7.2. Experimental

The experimental section includes the following parts.

Deposition of TCO films. All the TCO films were deposited at room temperature, and power density of $\sim 0.8 \text{ W/cm}^2$. The ITO films were grown with a chamber pressure of 3.2×10^{-3} mbar, and Ar flow of 20 sccm; the IFO films were deposited at a chamber pressure of 4.0×10^{-3} mbar, water vapor partial pressure 1.6×10^{-5} mbar, and Ar flow of 20 sccm; the IWO films were fabricated at a chamber pressure of 4.0×10^{-3} mbar, and Ar flow of 20 sccm (mixed with 0.25% O_2). The deposition rates were around 2 nm/min on flat surface. For one specific type of TCO layer, only the deposition time was changed to vary the TCO thickness. To mimic the TCOs as used in SHJ device fabrications, a post annealing procedure was performed in oven at 180 °C for 5 min, which was required to cure the sputter damage on our SHJ solar cell precursors (n -a-Si:H/ n -nc-Si:H/ i -a-Si:H/ n -c-Si/ i -a-Si:H/ p -nc-SiO_x:H/ p -nc-Si:H) during TCO deposition at room temperature [122].

Fabrication of SHJ solar cells and samples for contact study. Unless otherwise specified, SHJ solar cell precursors with front 10 nm- thick i/n stack and rear 26 nm-thick i/p stack thin-film silicon layers were prepared, based on n -type wafer. The precursor difference between Chapter 7 and Chapter 6 lies in the intrinsic layer adjustment. TCO films with specified thicknesses on both sides of the wafers were sputtered, through hard masks, which define different cell areas on each wafer. After sputtering, the solar cell precursors were annealed in air at 180 °C for 5 min for curing purposes. For monofacial cells, front metal contacts were room temperature electroplated Cu fingers, with an underlying full-area sputtered 100 nm-thick Ag as seed layer. Photolithography was utilized for patterning the metal grid area [288]. The rear metal contact was 500 nm-thick PVD Ag. For bifacial cells, both sides were Cu-plated metal contacts. In addition, for a double layer anti-reflection coating purpose, 100 nm-thick SiO_x layer was e-beam evaporated on the illuminated side(s) of the completed SHJ devices. The fabricated solar cells feature a designated illumination area of $2 \times 2 \text{ cm}^2$. The designed metal coverage is 1.6%, and the finger distance is 915 μm . We applied the same metal design on both sides

of the wafer. The patterning was done with photolithography. The metallization approach for bifacial solar cell is electrochemical copper plating on a 200 nm-thick evaporated silver seed layer. The contact width is 15 μm and the finger height is around 25 μm . For monofacial solar cell fabrication, we firstly did Cu-plating on the front side (i.e., n -side) of the wafer, with the rear side protected by a full area photoresist layer; then, a full area 500 nm-thick evaporated silver was deposited through hard masks as rear metal. For fabricating samples for contact study, we used contact stacks consisting of (i)a-Si:H, (n)nc-Si:H, (n)a-Si:H, TCO and metal for n -contact, and (i)a-Si:H, (p)nc-SiO_x:H, (p)nc-Si:H, TCO and metal for p -contact, respectively. The layers were kept the same as that used in SHJ device fabrication, except TCO variations. n -type wafer with symmetric n -contact layer stacks was used to extract the contact resistivity of n -contact ($\rho_{c,n}$). Similarly, p -type wafer was utilized to obtain $\rho_{c,p}$ values. Further details about the sample fabrications for contact study can be found in Section 3.2 or elsewhere [61, 132].

Solar cell measurements. For monofacial solar cell measurements, the front side (i/n) was the illuminated side, the front side (i/p) was covered with full-area metal electrode. For the bifacial cell measurements, a piece of black velvet was used to minimize the influence of rear side illumination. The solar cell was mounted on top of the black velvet, with the probe contacting through a small hole across the black velvet on the back side of the cell. In the bifacial solar cell measurements, we got I - V curves for the front and rear side of one cell, which corresponded to the front side efficiency and rear side efficiency, respectively. In addition, for the contact study, vertical dark I - V measurements were performed with four-point probes to obtain the total resistance of the sample, which was subsequently utilized to calculate $\rho_{c,n}$ and $\rho_{c,p}$ values [61].

7.3. Results and discussion

7.3.1. Optical evaluations regarding TCO reduction in SHJ solar cells

A. Opto-electrical properties of TCOs on top of thin-film silicon layers

Hall measurements show that all the TCO films are n -type semiconductor. Figure 7.1(a-b) shows the carrier density (N_e) and electron mobility (μ_e) values of nominal 75 nm-thick TCOs on glass and on i/n /glass and i/p /glass, respectively. The i/n and i/p thin-film silicon layer stacks have the same layer thickness as used in SHJ devices. To mimic the layer performance in actual device fabrication, a hot-plate annealing at 180 °C for 5 min was performed after the deposition of TCO at RT, which is a required step to recover the damage of the passivation quality of our SHJ solar cell precursors due to sputtering [122]. For the ITO and IFO films, with respect to the layers deposited on glass substrates, we observed increased N_e and decreased μ_e on the layers deposited on top of thin-film silicon layers. The N_e increase indicates a more absorptive nature in the TCO layers, and could be mainly owing to the diffused hydrogen from the thin film underneath, as it was elucidated by Cruz *et al.* [87] and Ritzau *et al.* [195]. While the reason for the μ_e decrease is still unclear. We exclude the cause from the substrate surficial roughness as observed by Cruz *et al.* [87], Erfurt *et al.* [89], and Tutsch *et al.* [88]. In fact, AFM measurements show similar root-mean-square roughness values of ~ 1 nm for both of our i/n and i/p stacks. Due to the N_e increase and μ_e decrease with respect to the layers deposited on glass substrates, the overall the resistivity (ρ) of the ITO and IFO layers decreases when

deposited on *i/n*/glass while slightly increases when deposited on *i/p*/glass (as shown in Figure 7.1(c)). In contrast, for the IWO layers, with respect to the layers deposited on glass substrates, a slightly decreased N_e and mildly increased μ_e were observed on layers deposited on thin-film silicon layers. As elucidated in our previous work [122], the N_e decrease indicates more oxygen incorporation during the post-deposition annealing process, and the μ_e increase could be associated with an increased Lewis acid strength of the tungsten dopants, increased crystallization, and possible defect passivation of thermally effused hydrogen from underlying thin-film silicon layers. With respect to the layer deposited on glass substrates, the ρ of the IWO layers decreases when deposited on *i/n*/glass, while increases when deposited on *i/p*/glass, which is in accordance with the cases in ITO and IFO layers.

Figure 7.1(d) displays the absorbance (A) spectra of the TCO films deposited on glass substrates. The results were calculated from $1-R-T$, and exhibit the same trend as observed in ellipsometry measurements (data not shown). In the short wavelength range, the sharp transition range of A varies with different TCOs, indicating varied optical band gap (E_g) values. From Tauc plots [61], the E_g values were obtained as 3.78 eV, 3.80 eV, and 3.86 eV for ITO, IFO, and IWO, respectively. We performed density function (DFT) theory calculations to obtain the band structures and density of states (DOS) of the host indium oxide (IO), ITO, IFO and IWO materials. Interestingly, the calculated IFO shows significantly higher effective electron mass and notably lower fundamental band gap than the other two types of TCOs, which are inconsistent with experimental observations [61, 213, 315]. Tentative interpretations of the discrepancy are provided in Supporting Information (Figure C.1 related part). From Figure 7.1(d), in the near infrared wavelength range, according to the classical Drude theory, the lower absorbance of the IFO and IWO films could be attributed to their lower N_e values as shown in Figure 7.1(a) [35]. In addition, with the multi-layer strategy from spectroscopic ellipsometry fittings as described in [122], we extracted the refractive index (n) and extinction coefficient (k) curves of the TCOs deposited on *i/n*/glass and *i/p*/glass, respectively, as shown in Figure C.2. The data is the input for our subsequent optical simulations.

B. Optical simulations on bifacial SHJ solar cells

Figure 7.2(a-c) shows GenPro4 optical simulation results of bifacial SHJ devices based on different TCO/SiO_x stacks [211]. For comparison, we provide the optical simulation results on monofacial cells in Figure C.3. We applied the same type of TCO at the front and rear sides. The thicknesses of the front TCO and rear TCO are variables. In bifacial cell simulations, constant 100 nm-thick SiO_x layers were utilized on top of TCO and on both sides of the wafer. This thickness was chosen from the procedures as described in the Supporting Information. From Figure 7.2(a), for ITO-based devices, thinner ITO continuously leads to higher implied photocurrent densities in c-Si absorber (J_{c-Si}) values. The optimal optical response of 43.5 mA/cm² appears when 20 nm-thick front ITO and 0 nm-thick back ITO layers are applied. Within the range of 0 ~ 50 nm-thick front ITO and 0 50 nm-thick back ITO, the J_{c-Si} could be kept above 43.0 mA/cm². Above this range, the increased parasitic absorption due to thicker ITO use compensates the optical gain from decreased reflectance due to DLARC use. As a result, J_{c-Si} decreases with further increase of front ITO and rear ITO thicknesses. From Figure 7.2(b), the IFO-based devices show highest J_{c-Si} of 43.9 mA/cm², for 40 nm-thick and 20 nm-thick IFO layers at front and rear

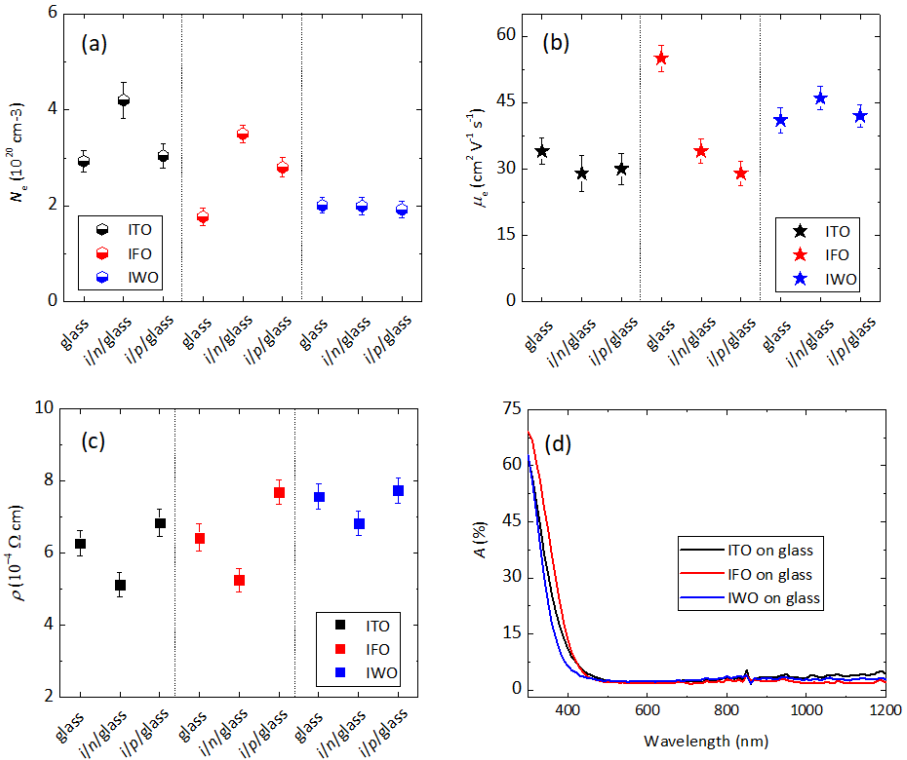


Figure 7.1: (a) Carrier density, N_e , (b) electron mobility, μ_e , and (c) resistivity, ρ , of the 75 nm-thick TCOs on top of different substrates. The results are based on three groups of experimental data. (d) Absorbance (A) curves of the TCO layers deposited on glass substrates.

sides of the wafer, respectively. As compared to Figure 7.3(a), J_{c-Si} of above 43.5 mA/cm^2 could be achieved in a wider range of IFO thicknesses, which is $20 \sim 70 \text{ nm}$ for front IFO and $0 \sim 70 \text{ nm}$ for rear IFO. Among the simulated devices, the IWO-based cells exhibit the best optical response within the widest range of TCO thicknesses, as shown in Figure 7.2(c). The highest J_{c-Si} of IWO-based devices is 44.3 mA/cm^2 , which corresponds to a front side 50 nm - and rear side 10 nm -thick IWO layers use. The J_{c-Si} is calculated to be above 44.0 mA/cm^2 in a broad range of IWO thickness, namely, 40 -to- 80 nm for front IWO and 0 -to- 100 nm for rear IWO (entire range investigated). Furthermore, it is noteworthy that considering the front side is dominating in the current contribution in the bifacial device, the results show more tolerance in the rear side TCO use. However, one should also take into consideration of the bifaciality factor change upon rear TCO variations in practical device design.

To summarize, from the optical point of view, the optimal front TCO thicknesses are dependent on the TCO type. For the ITO-based SHJ devices, the thinner, the better. While for IFO- and IWO-based devices, appropriate thicknesses are required to ensure good optical performance. Table 7.1 shows the optical evaluations of SHJ devices with reduced TCO thicknesses, in which the DLARC optimizations for both mono- and bi-facial cells

are included. The cases of single-layer ARC of TCO act as the references. One can see that, with respect to the reference devices, applying DLARC on the front side of monofacial device helps to reduce the TCO consumption to some extent, which is typically below 33% reduction. At the same time, the J_{c-Si} could be improved by up to 1.0 mA/cm^2 for ITO-based devices and 0.7 mA/cm^2 for IFO- and IWO-based devices, respectively. By contrast, the bifacial device design provides the most effective way to reduce the TCO consumption, meanwhile boost the optical performance of the device. Assuming a rear side illumination of 100 W/m^2 , with respect to the reference cell, the bifacial cell could potentially improve the J_{c-Si} by up to 5.0 mA/cm^2 , 4.3 mA/cm^2 , and 4.0 mA/cm^2 , for ITO-, IFO- and IWO-based devices, respectively. We note that with favourable albedo settings, the current improvements could be even higher [316].

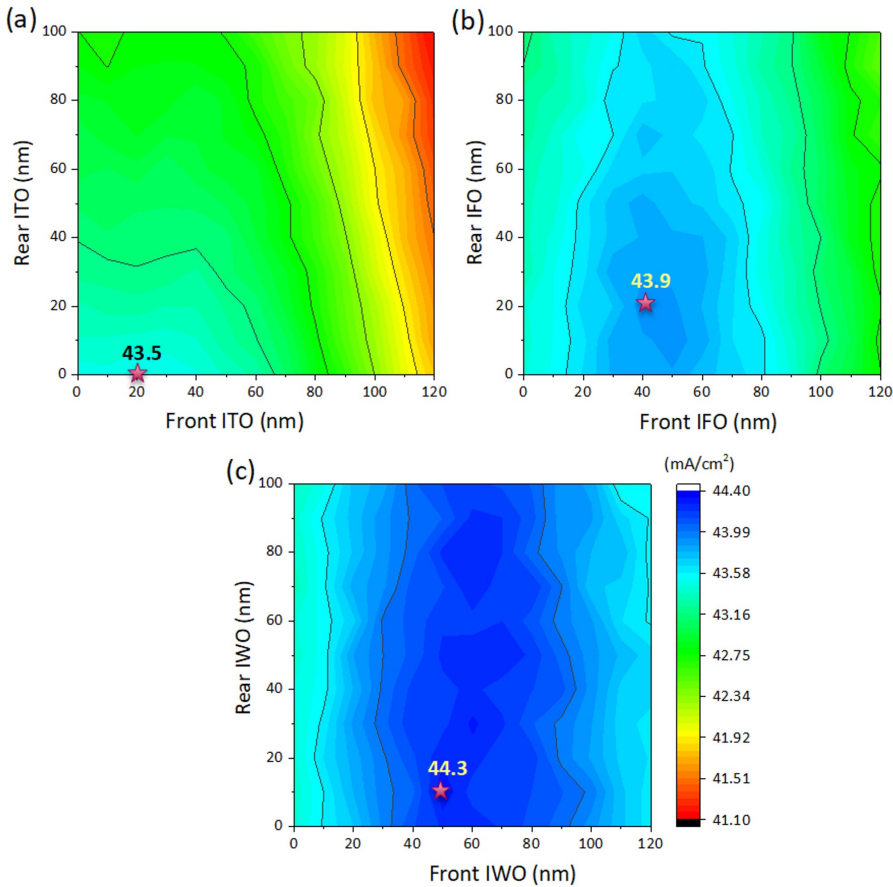


Figure 7.2: The simulated implied photocurrent densities in c-Si absorber (J_{c-Si}) as a function of front side TCO and SiO_x thicknesses for (a) ITO-, (b) IFO-, and (c) IWO-based bifacial SHJ devices. Constant 100 nm-thick SiO_x layers were utilized on top of TCO and on both sides of the wafer. The stars show the positions corresponding to the highest J_{c-Si} values.

Table 7.1: Optical evaluations of monofacial (MF) and bifacial (BF) SHJ devices with reduced TCO thicknesses. MF cells with single-layer ARC act as the reference cells.

TCO	Device type	Front TCO thickness [$t_{\text{TCO,front}}$, nm]	Back TCO thickness [$t_{\text{TCO,back}}$, nm]	Δt_{TCO} reduction	$\Delta J_{\text{c-si}}$ gain
ITO	MF(ARC)	75	150	-	-
	MF(DLARC)	0-40	150	16-33%	0.5-1.0
	BF(DLARC)	0-50	0-50	56-100%	4.5-5.0
IFO	MF(ARC)	75	150	-	-
	MF(DLARC)	0-40	150	16-33%	0.3-0.7
	BF(DLARC)	20-70	0-70	38-91%	3.9-4.3
IWO	MF(ARC)	75	150	-	-
	MF(DLARC)	10-60	150	7-29%	0-0.7
	BF(DLARC)	40-80	0-100	20-82%	3.7-4.0

7.3.2. Electrical evaluations regarding TCO reduction

This subsection elaborates the electrical assessments regarding the lateral and vertical transport, respectively.

A. Lateral transport

To realize such optical potential in device level, the electrical properties regarding the charge carrier transport behaviours need to be considered. Figure 7.3(a) illustrates the electron and hole transport paths towards the metal grid in the SHJ structure. As for the electron contact at the front side (n -contact), the lateral carrier transport layer can be either the c-Si absorber or the front TCO layer. Similarly, for hole contact at the back side (p -contact), the lateral carrier transport layer can be either the c-Si absorber or the rear TCO layer. In dark condition, the resistivity of c-Si bulk is normally higher than that of TCO layer. However, thanks to the excess carriers that are generated with illumination, the resistivity of the c-Si material bulk could be largely reduced. For a more practical evaluation on the lateral conductivity of the materials, the parameter of sheet resistance (R_{sh}), rather than the resistivity (ρ), was utilized in this section. Figure 7.3(b) illustrates the calculated sheet resistance (R_{sh}) versus excess carrier density (Δn) of our lab-use wafer under illumination, following $R_{\text{sh}} = 1 / [(qn\mu_n + qp\mu_p)t]$, in which q is elementary charge, n and p are electron and hole concentrations, respectively, μ_n and μ_p are the electron and hole mobilities, respectively, t is the thickness of the layer (wafer in this case). The μ_n of $1300 \text{ cm}^2 \text{V}^{-1} \text{s}^{-1}$ and μ_p of $450 \text{ cm}^2 \text{V}^{-1} \text{s}^{-1}$ were utilized in the calculation. The separate R_{sh} curves for electrons and holes are also included in Figure 7.3(b). Figure 7.3(c) shows the measured R_{sh} data for TCOs on glass with varied thicknesses at 25 nm, 50 nm, and 75 nm. All the films show a decreasing trend with thickness reduction, which is expected since R_{sh} is thickness-dependent ($R_{\text{sh}} = \rho / t$, where t is the thickness of the TCO layer). Figure 7.3(d) illustrates the data points of (N_e , μ_e) of the TCO layers from Hall measurements, i.e., electron mobility (μ_e) versus corresponding carrier densities (N_e) plot. Resistivity (ρ) lines are also provided according to the relation $\log(\mu_e) = -\log(N_e) + \log(1/\rho e)$ [53]. One can see that, with the TCO thicknesses reducing from 75 nm to 25 nm, the ρ values decreases to different extents for different TCOs. Therefore, the R_{sh} change in Figure 7.3(c) is related to the changes of both ρ and t .

Furthermore, from a comparison between Figure 7.3(b) and Figure 7.3(c), one can

see that, the $R_{sh,e}$ in the wafer is comparable with that of 75 nm-thick TCO layers at the Δn region that corresponds to implied maximum power point (iMPP) appearing at 0.2 suns illumination. When the iMPP appears at the Δn region of 1 sun illumination, the $R_{sh,e}$ in the wafer is lower than that of the standard 75 nm-thick TCO layers. This implies that the c-Si absorber is able to provide efficient lateral electron transport towards metal contacts during operation, which has been proven in literature [170, 306, 313]. On the other hand, for the lateral hole transport, the $R_{sh,h}$ of the wafer is above $350 \Omega/\square$ at 0.2 suns illumination, which is comparable with that the R_{sh} of 25 nm-thick TCO layers. The $R_{sh,h}$ of the wafer could be reduced to below $200 \Omega/\square$ at 1 sun illumination. This implies that with the development of high quality SHJ solar cell precursor, the c-Si may also be able to provide effective lateral hole transport. Looking back to Figure 7.3(a), a large portion of the lateral charge carrier transport towards local metal contacts could be accomplished by the silicon wafer itself during operation, question remains for the evaluation on the vertical carrier transport, i.e., whether the contact resistivity (ρ_c) is sufficiently low to ensure an effective charge carrier transport through the SHJ device [313].

B. Vertical transport: contact study

Figure 7.4(a-b) display the contact resistivity values of n -contact ($\rho_{c,n}$) and p -contact ($\rho_{c,p}$) stacks in our SHJ device structure, respectively. The cross symbols represent non-ohmic contacts in our dark current-voltage measurements. For the n -contact, the $\rho_{c,n}$ values of ITO- and IWO- based samples show almost TCO thickness-independent characteristic. The $\rho_{c,n}$ values are maintained at $\sim 120 \text{ m}\Omega \text{ cm}^2$ and $\sim 80 \text{ m}\Omega \text{ cm}^2$ for ITO- and IWO-based samples, respectively. These values basically fall into the reported value range in Ref. [306]. Interestingly, the IFO-based samples show non-ohmic behaviours in n -contacts when 25 nm- and 50 nm-thick IFO layers are applied. With increasing the IFO layer thickness to 75 nm, ohmic contact is detected. However, the IFO-based samples with 75 nm-thick IFO layer use show a relatively high average $\rho_{c,n}$ values of $411 \text{ m}\Omega \text{ cm}^2$.

For the p -contact, all the $\rho_{c,p}$ values show significant TCO thickness-dependent characteristics. Interestingly, the ITO- and IFO-based samples show opposite trends, i.e., with increasing the TCO thickness from 25 nm to 75 nm, the average $\rho_{c,p}$ values of the ITO-based samples increase from $114 \text{ m}\Omega \text{ cm}^2$ to $390 \text{ m}\Omega \text{ cm}^2$, while that of IFO-based samples decrease from $471 \text{ m}\Omega \text{ cm}^2$ to $175 \text{ m}\Omega \text{ cm}^2$. As for the IWO-based samples, we observed an average $\rho_{c,p}$ value of $148 \text{ m}\Omega \text{ cm}^2$ with 75 nm-thick IWO layer use, yet non-ohmic features when using 25 nm- and 50 nm-thick IWO layers. It may be worth noting that when the standard 75 nm-thick ITO is applied, the $\rho_{c,p}$ of $390 \text{ m}\Omega \text{ cm}^2$ is higher than our previously reported $222 \text{ m}\Omega \text{ cm}^2$ with the same thin-film silicon layer thickness use [132]. This might be mainly caused by the fine-tuned intrinsic layer in our laboratory [317]. Besides, the ITO deposition parameters also changed, which might also induce a change in the $\rho_{c,p}$ values.

Combined with the band diagrams of the n - and p -contact stacks from TCAD simulations [126] as shown in Figure 7.5(a), we provide our interpretation on Figure 7.4(a-b) as follows.

Regarding the n -contact (or electron contact), the TCO/doped silicon junction is isotype, in which the transport of electrons is simple since it only occurs in the conduction band. From the left part of Figure 7.5(a), a low work function of the TCO layer is preferable

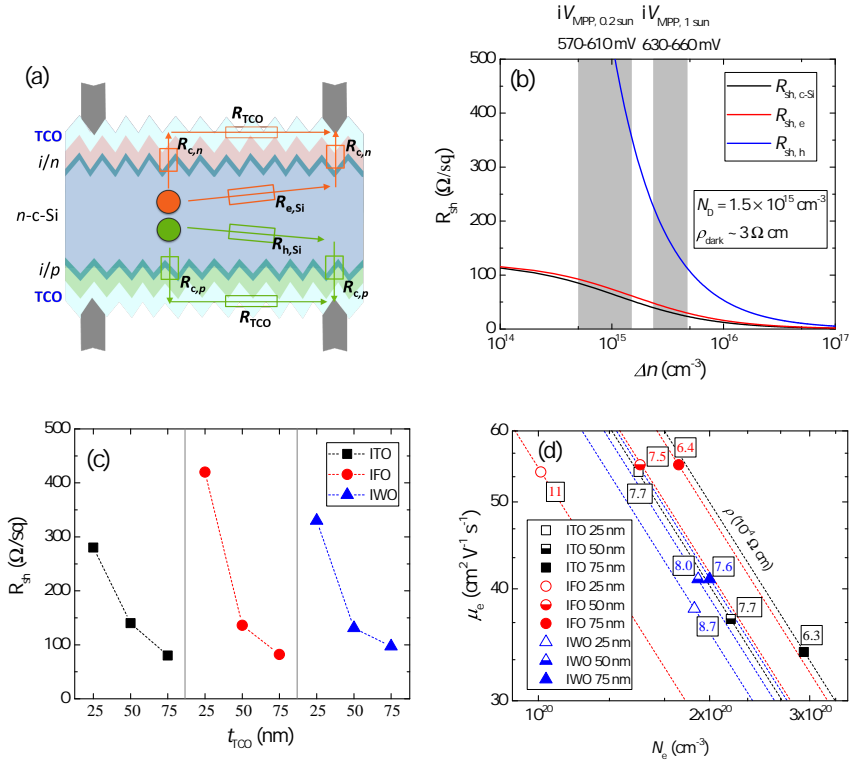


Figure 7.3: (a) Electron and hole transport paths towards the metal grid in the bifacial SHJ structure. (b) Calculated sheet resistance (R_{sh}) versus excess carrier density (Δn) of our lab-use c-Si absorber under illumination. The separate R_{sh} curves for electrons and holes are also presented. The grey shadowed areas show the normally used Δn regions that maximum power point (MPP) appears. (c) Thickness-dependent R_{sh} of our ITO, IFO, and IWO layers. (d) Electron mobilities (μ_e) versus corresponding carrier densities (N_e) of the TCO layers with varied thicknesses, from Hall measurements. The resistivity (ρ) values of the TCOs are also provided in (d).

due to a low electron transport barrier (Φ_{BN}) at the TCO/*n*-layer interface. Therefore, the observation of lower $\rho_{c,n}$ values of IWO than that in ITO samples in Figure 7.4(a) may indicate a lower work function of IWO layer than ITO layer at the interface. While the IFO layer is speculated to hold the highest work function values among our tested lab-use TCO layers since the IFO-based samples show the highest $\rho_{c,n}$ values.

Figure 7.5(b) depicts the simulated band structures of the ITO, IFO, IWO materials, respectively. The work function values of ITO, IFO, and IWO are calculated to be 4.42 eV, 4.26 eV, and 4.29 eV, respectively. The lower work function of IWO than ITO layer is in line with the observation that the IWO-based samples show lower $\rho_{c,n}$ values than ITO-based samples. While compared to ITO, the IFO material shows a slightly higher work function, but a visibly higher electron affinity (lower CBM position in Figure 7.5(b)). This makes it challenging to interpret the comparative properties between ITO- and IFO-based contact samples. Detailed investigation is ongoing. It is important to mention that our simu-

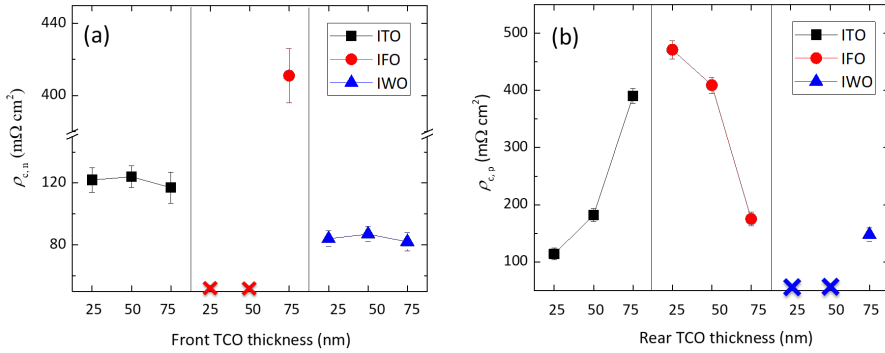


Figure 7.4: The contact resistivity of (a) n -contact, $\rho_{c,n}$, stack at the front and (b) p -contact, $\rho_{c,p}$, stack at the rear of our SHJ device structure for different TCO and variable thicknesses. The cross symbols represent non-ohmic contacts in the dark current-voltage measurements. The results are based on three groups of experimental data from one batch.

lated work function data as shown in Figure 7.5(b) helps to some extent in qualitatively exploring the intrinsic material properties. However, one cannot directly associate the calculated data with the measured individual data, since the real deposited TCO thin films are influenced by multi-factors, such as deposition condition (target composition, temperature, pressure, O $_2$ flow, residual water in the chamber) [35], substrate morphology [87–89] and the adjacent doped silicon layers [87, 122] or dielectrical layer [318, 319] in practical conditions [176, 320].

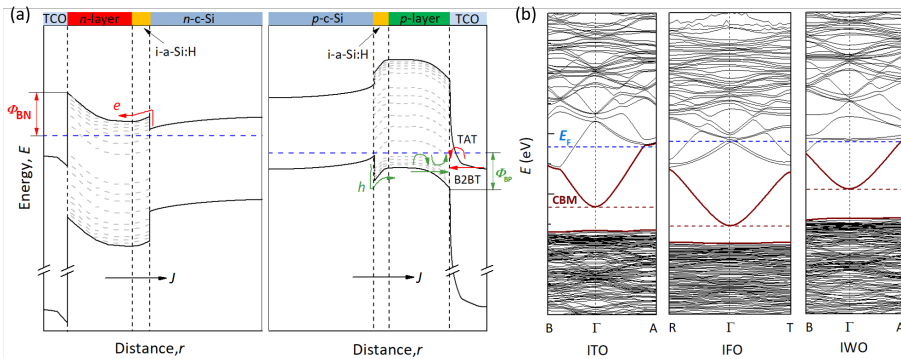


Figure 7.5: (a) Schematic band diagram of the charge carrier transport for n -contact (left part) and p -contact (right part). Corresponding transport barrier height of electrons (e) and holes (h) are marked as ϕ_{BN} and ϕ_{BP} , respectively. In p -contact, carrier transport mechanisms of band-to-band tunnelling (B2BT) and trap-assisted tunnelling (TAT) are indicated [126]. (b) Band structures of ITO, IFO, and IWO layers from density-functional theory simulations. The calculations were performed based on the Perdew-Burke-Ernzerhof (PBE) exchange-correlation functional, and the results are used for qualitative comparison analysis purposes among different TCO types.

For the p -contact (or hole contact), whose band diagram is shown in the right part

of Figure 7.5(a), the carrier transport is more complex than that in n -contact. In general, the TCO/ p -layer interface acts as a recombination junction. Holes in the p -layer valence band recombine with electrons in the TCO conduction band. As elaborated by Procel *et al.* [126], the $\rho_{c,p}$ variations could follow different combinative trends, depending on the dominating carrier transport mechanism(s). In this scenario, $\rho_{c,p}$ can be significantly influenced by the energy alignment of the p -layer with the TCO, which is affected by the hole transport barrier (Φ_{BP}) and/or different tunnelling mechanisms, as indicated in the right part of Figure 7.5(a). Presumably, for the ITO-based samples, with reducing ITO thickness, the energy alignment at the TCO/ p -layer interface is improved due to a possibly increased work function of ITO layer. The better the alignment, the better the transport of carriers (i.e., lower $\rho_{c,p}$) [251]. As for the IFO and IWO cases, we speculate that with increasing the TCO thickness, the Ne change negligibly affects the energy alignment at the TCO/ p -layer interface. However, Ne increase allows more energy states available for collecting holes from the p -layer [126], thus facilitates a reduction of $\rho_{c,p}$ for thicker TCO use. Further research remains to be carried out to confirm the above hypothesis.

7.3.3. Bifacial SHJ solar cell results

From previous observations, for the n -contact, the n -type c-Si absorber could provide sufficient lateral electron transport towards local metal contacts. Besides, low vertical contact resistance could be ensured by utilizing the ITO or IWO layers, since they show low WF values and the $\rho_{c,n}$ is observed to be independent of the TCO thickness. This means that, ITO and IWO layers are promising options for the n -contact side of the SHJ solar cell design with reduced TCO use. To verify this hypothesis, we fabricated monofacial rear emitter ITO-, IFO, and IWO-based SHJ devices, with varying the front TCO layer thickness from 25 nm to 75 nm. 100 nm-thick SiO_x layers are applied on the illuminated side. The results are shown in Figure C.4. It can be seen that, among the monofacial cells, IFO- and IWO-based SHJ devices show best optical performance; while ITO- and IWO-based devices show best fill factor values (electrical properties). Consequently, the best monofacial cell was observed in the IWO-based devices, in which the 50 nm-thick front IWO layer is applied. Elaborate analysis on the monofacial cells is provided in Appendix C, in which the comparison between simulated J_{c-Si} and measured $J_{SC,EQE}$ is also included. Considering the high ρ_c values in IFO-based contact samples and the low FF values in IFO-based monofacial SHJ devices, we only included ITO and IWO layers in our final bifacial cell fabrications. Besides, the IWO cells are proven to show the best optical performance (Figure 7.2 and Figure C.4), and 25 nm-thick ITO shows the most promising results in the hole-collecting p -contact (as shown in Figure 7.4(b)), thus we included a hybrid type of IWO/ITO-based bifacial cell in this work.

We fabricated Cu-plated bifacial SHJ devices, with front and rear TCOs of ITO/ITO, IWO/IWO, and IWO/ITO. For each type, three TCO thicknesses were tested on both sides of the device, which are 25 nm, 50 nm, and 75 nm. 100 nm-thick SiO_x layers are applied on top of the TCOs on both sides. Figure 7.6(a-d) show the measured bifacial SHJ solar cell results from n -side illumination. From Figure 7.6(a), the V_{OC} values are similar as that are observed in monofacial cells (as shown in Figure C4(a)). From Figure 7.6(b), the average J_{SC} values of ITO/ITO- and IWO/ITO-based devices show decreasing trends with increasing the TCO thicknesses on both sides. Especially, the ITO/ITO-based

solar cell show a dramatic J_{SC} decrease with TCO thickness increase, reflecting a notably higher parasitic absorption in the thick TCO film. This could be related to the fact that as compared to the thin ITO film, thick ITO film is more absorptive in nature (i.e., higher absorption coefficient, as indicated by a higher N_e in Figure 7.3(d)) and higher TCO thickness induces higher absorptance. As for the IWO/IWO-based devices, the average J_{SC} values does not show significant change among the tested cells, which are 38.95 mA/cm², 39.19 mA/cm², and 39.00 mA/cm², for devices with double-side 25 nm-, 50 nm-, and 75 nm-thick IWO layers, respectively. Combining our optical simulation results in Figure 7.2, the decreasing trend in the average J_{SC} values of ITO- and IWO/ITO-based devices could be attributed to the increasing parasitic absorption when increasing the ITO layer thickness.

From Figure 7.6(c), surprisingly, with increasing the ITO thickness from 25 nm to 75 nm, we observed slightly decreased FF values in the ITO-based devices. We note that the FF of a real solar cell is not only influenced by the vertical contact resistance, but also lateral carrier transport contributions on both sides of the wafer. According to Figure 7.4, with increasing the ITO thickness from 25 nm to 75 nm, the $\rho_{c,n}$ almost remains constant yet the $\rho_{c,p}$ notably increases. We presume that the increasing trend in $\rho_{c,p}$ in the vertical hole transport is somehow compensated by the decreasing trend in R_{sh} in the lateral hole transport (as shown in Figure 7.3(c)). The overall results from lateral and vertical hole transports at the p -contact side could be the driving force behind our observed FF trend in the ITO-based devices. As for the IWO-based devices, with increasing the IWO layer thickness from 25 nm to 75 nm, the FF shows an increasing trend. The high FF in the 75 nm-thick IWO-based devices could be attributed to both the low $\rho_{c,p}$ in the vertical hole transport (Figure 7.3(b)) and the low R_{sh} in the lateral hole transport (as shown in Figure 7.3(c)). Furthermore, with increasing the TCO thickness from 25 nm to 75 nm, the IWO/ITO-based devices show similar FF trend with ITO-based devices. This can be expected from previous observations in Figure 7.3, Figure 7.4, and the separate ITO and IWO cases in Figure C.4(c). Figure 7.6(d) shows the overall efficiencies of the bifacial devices from front side illumination. Efficiencies above 22% were obtained in the IWO/ITO-based devices in the 25 nm/25 nm case. The best cell performance in this batch is shown in Table 7.2. With respect to a reference bifacial solar cell with 75 nm-thick TCO on both sides, such a total TCO thickness of 50 nm represents a 67% TCO reduction.

It is worth noting that: (i) regarding the hybrid IWO/ITO use, we also performed optical simulations on the IWO/ITO-based bifacial cell structures (data not shown). Results show that the optimal J_{c-Si} (44.3 mA/cm²) is the same as that obtained in Figure 7.2(c), which appears when 50 nm-thick front IWO and 0 nm-thick back ITO are applied; (ii) regarding the J_{SC} reading in Figure 7.6(b), the values were collected from single-side illumination, thus are even lower than that of monofacial solar cells (opposite to the expectation from Table 1). Besides, the possible optical overestimations in our simulation results (in Figure C.3 and Figure 7.2) are discussed in monofacial case (see Figure C.5); (iii) regarding the further improvement, the FF of our bifacial SHJ solar cells in Figure 7.6 are generally below 80%. Considering our n -c-Si absorber possibly provides sufficient lateral electron transport for the n -contact (see Section 7.3.1), and the contact resistance between IWO and n -type doped silicon layer is sufficiently low (see Section 7.3.2), we suspect that the carrier transport of our bifacial cell is still somehow limited by the p -contact.

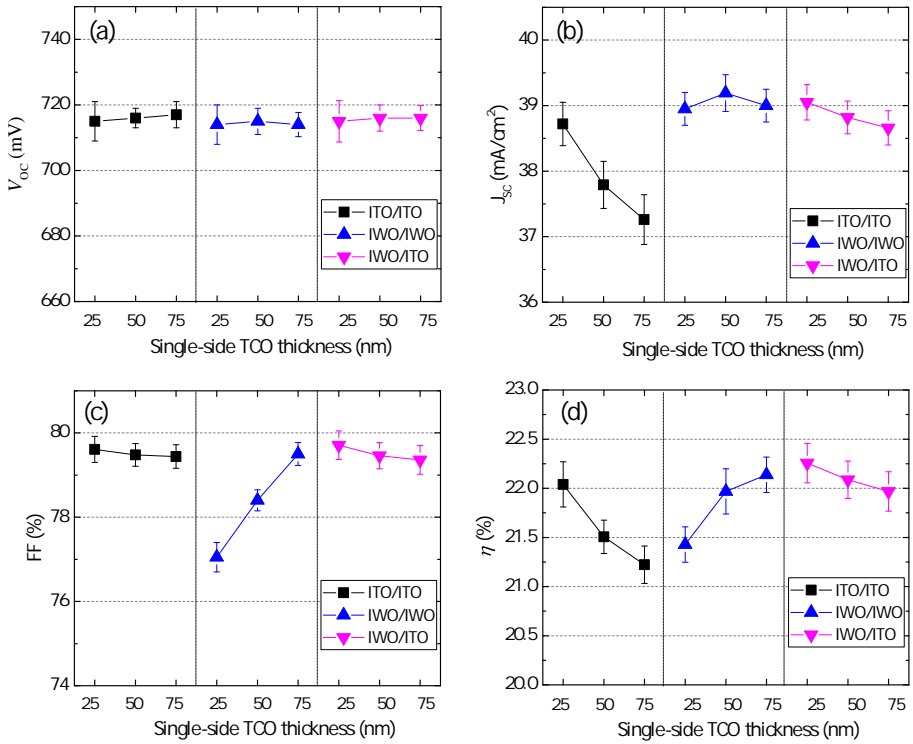


Figure 7.6: The measured (a) open-circuit voltage, V_{OC} , (b) short-circuit current density, J_{SC} , (c) fill factor, FF , and (d) power conversion efficiency, η , of bifacial SHJ device with varied TCO thicknesses of 25 nm, 50 nm, and 75 nm on both sides. The results are based on three devices on the same wafer from the one batch of processes. The data are the results from front side illumination.

Table 7.2: The device parameters of the best bifacial SHJ solar cell in the experimental series with using the same TCO thickness on both sides of the wafer. 25 nm-thick front ITO in n -contact and 25 nm-thick rear ITO in p -contact were applied.

TCOs	TCO thicknesses [t_{TCOs} , nm]	Illuminated side	Open-circuit voltage [V_{OC} , mV]	Short-circuit current density [J_{SC} , mA/cm ²]	Fill factor [FF , %]	Efficiency [η , %]
IWO/ITO	25/25	front	721	39.20	79.57	22.50
		rear	717	38.72	79.91	22.19

Furthermore, with utilizing a modified SHJ solar cell precursor and increasing the ITO thickness on the p -side to 75 nm, we realized notably increased FF and further improved solar cell efficiencies. The certified solar cell parameters of our champion bifacial SHJ device are shown in Figure 7.7. The front side efficiency is 22.84%, and bifaciality factor is calculated to be 0.95.

7.4. Conclusions

We utilized TCOs with different opto-electrical properties, which are tin-, fluorine-, and tungsten-doped indium oxides, namely, ITO, IFO, and IWO. By introducing a double layer

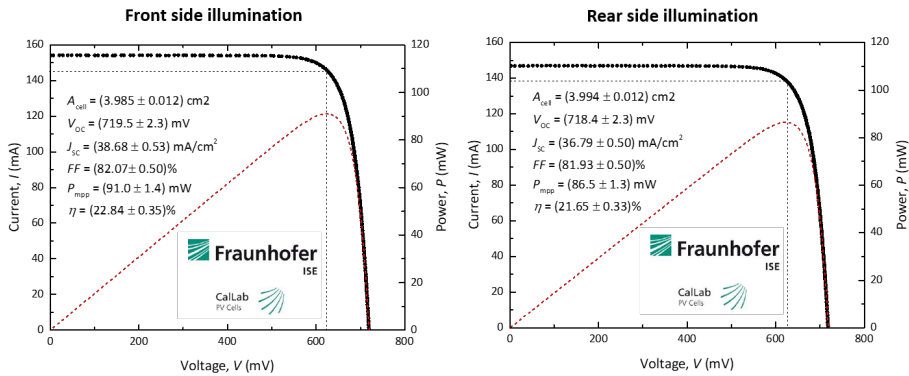


Figure 7.7: Certified solar cell parameters of our champion bifacial SHJ device, in which 25 nm-thick front IWO in *n*-contact and 75 nm-thick rear ITO in *p*-contact were utilized.

anti-reflection coating formed by TCO/SiO_x layer stacks on the illumination side(s), we performed optical simulations with varied TCO/SiO_x stacks on both mono- and bi-facial SHJ solar cells. Results show that bifacial solar cell architecture provides the most effective way to reduce the TCO usage, and appropriate TCO thicknesses are needed to ensure optimal optical response. Furthermore, with applying TCO thicknesses of 75 nm, 50 nm, and 25 nm, we performed electrical evaluations from both lateral and vertical charge transport perspectives. Based on our specific thin-film silicon layer stacks, our IFO and IWO films are found to be favorable for *p*-contact and *n*-contact, respectively. While for our ITO film, it can work well in both *p*-contact and *n*-contact, but thinner ITO shows lower contact resistance in *p*-contact, although its sheet resistance becomes higher. TCO thickness-dependent contact properties for both *n*-contact and *p*-contact were tentatively interpreted based on a preliminary first principles density-functional theory study. Based on the observations, preferable bifacial SHJ solar cells with reduced TCO use are designed and fabricated. With applying 25 nm-thick IWO on the front side and 25 nm-thick ITO on the rear side of the device, we obtained front side efficiencies >22%. This represents a 78% TCO reduction with respect to our lab-standard monofacial SHJ solar cell, and a 67% TCO reduction with respect to a reference bifacial solar cell with 75 nm-thick TCO on both sides. Moreover, with utilizing modified SHJ solar cell precursors and further TCO adjustment, our champion bifacial SHJ solar cell showed front side efficiency of 22.84%. The bifaciality factor is 0.95.

8

Conclusions and outlook

8.1. Conclusions

This thesis describes developing In_2O_3 -based transparent conductive oxide (TCO) films for high efficiency c-Si solar cell applications, and how to make use of them from a sustainable perspective. The main conclusions are summarized below.

Firstly, we developed RF-sputtered hydrogenated fluorine-doped indium oxide (IFO:H) films with high carrier mobility (μ_e). In Chapter 4, we describe the IFO:H films deposited at low substrate temperature below 110 °C. By varying the water vapour pressure during the deposition, we obtained an optimized IFO:H film with a remarkable high μ_e of $87 \text{ cm}^2 \text{ V}^{-1} \text{ s}^{-1}$. Besides, the IFO:H film displays an optical band gap of 3.85 eV and a carrier density of $1.2 \times 10^{20} \text{ cm}^{-3}$. With respect to the ITO counterpart, the IFO:H-based SHJ solar cell shows a $J_{\text{SC, EQE}}$ gain of 1.53 mA/cm^2 within the whole wavelength range of interest, without inducing FF loss. The best IFO:H-based front-emitter SHJ solar cell shows a power conversion efficiency of 21.1%.

Secondly, we implemented the RF-sputtered IFO:H in high thermal-budget poly-Si solar cells. In Chapter 5, we present the opto-electrical properties of the IFO:H layers after post-deposition annealing (PDA) treatments at 400 °C in N_2 , H_2 , and air ambiances. Through analyses on the crystal structure, surface morphology, optical properties and temperature-dependent electrical properties, the inherent electron scattering and doping mechanisms of the IFO:H films were proposed. In addition, hydrogen annealing provides an effective PDA strategy that could simultaneously improve the opto-electrical properties of the TCO film, restore the passivation quality of the poly-Si solar cell precursor (n^+ poly-Si/ SiO_x /c-Si/ SiO_x / p^+ poly-Si), and maintain a low vertical contact resistance at the poly-Si/TCO contact. Low contact resistivity values of around $20 \text{ m}\Omega \text{ cm}^2$ (or below) was achieved on both n - and p -contacts with poly-Si/TCO stack after hydrogen annealing, which to our knowledge, are among the lowest values especially on thermally annealed contacts at 400 °C. Furthermore, we implemented the hydrogen-annealed IFO:H films on FBC rear-emitter poly-Si solar cells. The IFO:H-based poly-Si solar cells show an average power conversion efficiency improvement from 20.1% to 20.6% after adding the hydrogen annealing PDA treatment, mainly due to a $0.9\%_{\text{abs}}$ improvement in FF .

Thirdly, we investigated the room temperature sputtered IWO material in a SHJ device-oriented approach. In Chapter 6, we describe the IWO property change along with underlying thin-film silicon layers and post-annealing treatment. The optimal IWO film on glass shows carrier density and mobility of $2.1 \times 10^{20} \text{ cm}^{-3}$ and $34 \text{ cm}^2\text{V}^{-1}\text{s}^{-1}$, which were tuned to $2.0 \times 10^{20} \text{ cm}^{-3}$ and $47 \text{ cm}^2\text{V}^{-1}\text{s}^{-1}$, as well as $1.9 \times 10^{20} \text{ cm}^{-3}$ and $42 \text{ cm}^2\text{V}^{-1}\text{s}^{-1}$, after treated on *i/n/glass* and *i/p/glass* substrates, respectively. Further, GenPro4 simulations implied a clearly increased visible-to-near-infrared optical response in IWO-based SHJ solar cell with respect to our ITO-based counterpart, which was demonstrated in practical rear-emitter SHJ devices. Applying MgF_2 as double-layer antireflection coating on top of the optimal device, the $J_{\text{SC,EQE}}$ was improved from 39.41 mA/cm^2 to 40.16 mA/cm^2 . The best IWO/ MgF_2 -based SHJ solar cell shows an active area power conversion efficiency of 22.92%.

Finally, bifacial Cu-plated SHJ solar cells with reduced TCO use are explored. In Chapter 7, we present TCOs with different opto-electrical properties, namely, ITO, IFO, and IWO. By introducing a double layer anti-reflection coating formed by TCO/ SiO_x layer stacks on the illumination side(s), we performed optical simulations with varied TCO/ SiO_x stacks for both mono- and bi-facial SHJ solar cells. Results show that bifacial solar cell architecture provides the most effective way to reduce the TCO usage, and appropriate TCO thicknesses are needed to ensure optimal optical response. Furthermore, with applying TCO thicknesses of 75 nm, 50 nm, and 25 nm, we performed electrical evaluations from both lateral and vertical charge transport perspectives. Our IFO and IWO are found to be favorable for *p*-contact, and *n*-contact, respectively. While for ITO, it can work well in both *p*-contact and *n*-contact, but thinner ITO shows lower contact resistance in *p*-contact, although its sheet resistance becomes higher. TCO thickness-dependent contact properties for both *n*-contact and *p*-contact were tentatively interpreted based on a preliminary first principles density-functional theory simulation. Based on the observations, preferable bifacial SHJ devices with less TCO use are designed. To minimize the resistive losses caused by a high metal finger pitch in our lab-standard screen-printing metallization approach, as well as to reduce the silver consumption, a bifacial Cu-plating experimental platform is developed (see Appendix D-E). Based on the platform, with applying 25 nm-thick IWO on the front and 25 nm-thick ITO use on the rear side of the device, we obtained front side efficiencies >22% on bifacial Cu-plated SHJ solar cells. This represents a 67% TCO reduction as compared to a reference bifacial solar cell with 75 nm-thick TCO on both sides. Further, with utilizing modified SHJ solar cell precursors (*n/i/c-Si/i/p*) and further TCO adjustment, our champion bifacial cell shows a front side efficiency of 22.84%. The bifaciality factor is 0.95.

8.2. Outlook

Along this PhD research, many ideas have been conceived and developed. The following recommendations are offered for future research.

1. Further reducing TCO use to less than 10 nm per side.

In this work, we managed to reduce the TCO use in SHJ solar cell to 25 nm per side. However, such a reduction is still not enough towards a TW-scale installation capacity. Zhang *et al.* [301] predicted the indium consumption as a function of its percentage in global annual supply. Assuming ITO is utilized as the TCO option and one wants to keep

the consumption-to-supply ratio of indium at 20%, the ITO use on per side of the cell needs to be controlled to less than 9 nm and 3 nm for 1 TW and 3 TW scale, respectively [301]. In this scenario, we should at least reduce the ITO use to less than 10 nm per side. For this purpose, there are some aspects that need to be considered as follows.

(i) Metal evaluation. According to Bivour *et al.* [306], with reducing the ITO thickness to less than 10 nm, the vertical contact resistance at the *n*-contact shows significantly increasing trend when using metal contacts of screen-printed silver and evaporated silver. However, titanium could provide an option to maintain a low contact resistance at the *n*-contact. The investigation at the *p*-contact with <10 nm-thick ITO use is still lacking.

(ii) Thin-film silicon layer adjustment. According to the results in Chapter 7, when applying 25 nm-thick TCO on both sides of the wafer, although solar cell efficiencies >22% were obtained, the *FF* of the solar cell is still limited by the electrical transport from the *p*-contact side. Such an electrical limit from the *p*-contact can be more severe with thinner TCO layer use. According to Wu *et al.* [302], the vertical contact resistance of the *p*-contact could be tuned by the doping level of the *p*-type thin film silicon layer. Our previous simulation results [126, 251] also give a similar indication.

(iii) Thin TCO layer manipulation. As indicated by Figure 7.3(d), the material parameter of a TCO layer is thickness-dependent. In this regard, the TCO material study aiming for <10 nm-thick TCO layer use should be performed on such thin TCO layers. Different deposition techniques and deposition parameters could be utilized. Besides, from the application point of view, additional influencing factors may need to be taken into account, such as underlying thin-film silicon layers [122, 124, 188], overlying dielectric layers [318, 319], substrate roughness [88, 188], interfacial oxide between TCO and underlying thin-film silicon layers [138, 140, 146, 277], reactivity between TCO and metal electrode during thermal treatment [321], and the work function changes of the adjacent layers in practical processing steps [176]. Besides, it is worth noting that simulation work provides beneficial perspectives in understanding the experimental results as well as in designing materials/contacts/devices. In this work, we did preliminary DFT calculations to tentatively interpret the contact properties between TCO and doped silicon layers. The TCAD simulation results from the research group [126, 251] also provide important insights in the TCO-related contact design. The DFT calculation was based on a perfectly conventional bixbyite In_2O_3 crystal structure, defect states still need to be introduced to mimic the real deposited film. Moreover, to get more accurate band structures and dielectric functions of the TCOs, adjustments on the simulation settings such as exchange-correlation functional and k-point grid remain to be carried out [322]. In addition, Knight *et al.* [323] reported the so-called nanowire-enhanced ITO by combining silver nanowires with thin ITO for the front contact use of silicon heterojunction solar cells. Such nanowire-enhanced ITO could notably improve the conductivity of thin ITO layer, meanwhile maintain equivalent transparency. This approach might also provide some possibilities for PV device design with reduced TCO use.

(iv) High quality solar cell precursors utilization *. A prerequisite to realize high efficiency c-Si solar cell with reduced TCO use is that the lateral charge carrier transport towards local metal contacts can be largely accomplished by the silicon wafer bulk. Herein,

*The *solar cell precursor* here refers to any c-Si wafer coated on each side with a passivating layer and one or more transport layers but without TCO or metallization.

we assume that the sheet resistance of the wafer absorber in dark condition is comparable with that of TCO, and the vertical contact resistance in the solar cell stacks can be ignored (i.e., only lateral conductivity is taken into account). In monofacial solar cell, one can easily use rear emitter design to reduce TCO thickness without sacrificing PCE, since the majority carriers could support the required lateral conductivity on the illuminated side, while full area TCO and metal are applied in rear side to ensure vertical one-dimension carrier transport for minority carriers (little lateral transport is needed). However, in bifacial solar cell, the lateral transports of both majority and minority carriers are required. In this regard, high quality solar cell precursor which features the following conditions is of critical importance in bifacial solar cell design with thin TCO layer use.

(a) high passivation quality. Figure 8.1(a-b) shows the calculated sheet resistance (R_{sh}) versus excess carrier density (Δn) of our lab-use n -type and p -type wafers under illumination, respectively. The electron sheet resistance ($R_{sh,e}$) and the hole sheet resistance ($R_{sh,h}$) are also presented. Excess carrier injection under illumination condition reduces the electron sheet resistance ($R_{sh,e}$) and the hole sheet resistance ($R_{sh,h}$) of the wafer, which eases the TCO requirement at device level. Hence, the injection level at maximum power point ($\Delta n @MPP$) determines the feasibility of reducing TCO thickness in solar cell design. The higher the $\Delta n @MPP$, the more feasible of thin TCO use in device design (for both electron and hole carriers). Provided the wafer doping is fixed, the $\Delta n @MPP$ is in a positive correlation with the open-circuit voltage of the device [207], whose upper limit is set by the passivation quality of the solar cell precursors. Therefore, solar cell precursors with high passivation quality is essential for ensuring a solar cell operating at high injection level, thus facilitates high performance bifacial solar cells.

(b) high quality wafer. In bifacial solar cells, both the emitter and BSF(or FSF) sides of the wafer are illuminated sides of the device. Most of the charge carriers are generated close to the front surface under illumination. This means that one type of carriers can almost straightforwardly transport towards metal electrodes, whereas the other type of carriers have to move through the entire wafer thickness before they reach the rear metal electrodes. This requires a sufficiently long diffusion length for the carriers (especially for minority carriers). In this sense, high quality float-zone wafers are desirable.

(c) p -type wafer utilization. From Figure 8.1, in both n - and p -type wafers, the R_{sh} of the minority carriers is the dominating factor that determines the electrical properties of the bifacial cell. However, the reduction of the $R_{sh,e}$ in p -type wafer under illumination goes much faster than that of $R_{sh,h}$ in n -type wafer, due to the higher electron mobility than hole mobility in c-Si materials. As a consequence, with the MPP appearing at high injection levels, the $R_{sh,e}$ in p -type wafer can be comparable to the $R_{sh,h}$, indicating a low resistive loss in bi-directional transport of the carriers. In this regard, p -type wafer can be recommendable for the future high performance bifacial solar cell design with thin TCO layer use. More specifically, to avoid the boron-related degradation problem with p -type wafer use, gallium-doped p -type wafer could be a good option for such a purpose [324]. In March 2022, Chinese solar PV manufacturer LONGi has reported 25.47% efficiency of p -type bifacial SHJ solar cell based on a M6 size gallium-doped wafer [325].

2. Investigating In-free TCOs.

For the purpose of high carrier mobility, we have chosen In_2O_3 as the host material in this thesis. However, the development of In-free TCOs is still worth a try, due to the low

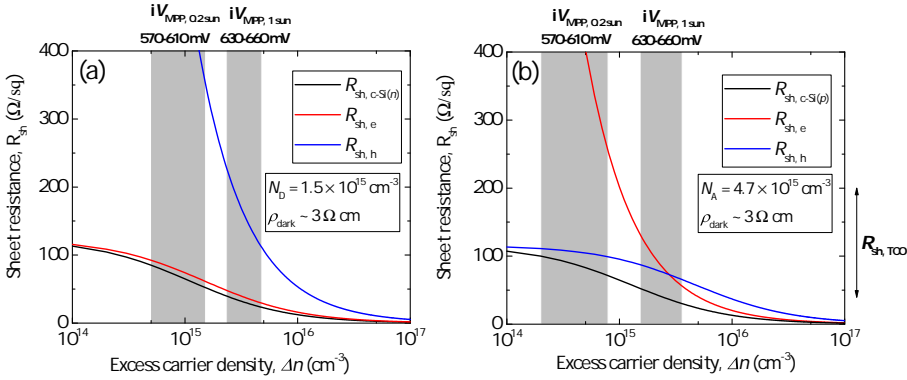


Figure 8.1: The calculated sheet resistance (R_{sh}) versus excess carrier density (Δn) of our lab-use (a) n -type and (b) p -type wafers under illumination. The R_{sh} curves for electrons and holes are also presented. The grey shadowed areas indicate the Δn regions where maximum power point (MPP) normally appears. The $R_{sh,TCO}$ range is also provided on the right side of (b) for comparison purpose.

abundance and the rapidly increased cost of indium raw material in the last two decades. The following alternatives could be investigated.

(i) **ZnO-based TCOs**, such as B-, Al-, Ga-, In-, Si-, Ge-, Sn-, Zr-, Ti-, and V-doped ZnO [326]. Among the layers, AZO (Al:ZnO) is widely utilized and the atomic layer deposited AZO layer has been proven to exhibit good passivation quality on thin poly-Si based cells [327]. For ZnO-based TCOs, the low carrier mobility (below $30 \text{ cm}^2 \text{ V}^{-1} \text{ s}^{-1}$) may be problematic for sufficient carrier collection, and the stability issue needs to be addressed [299, 328];

(ii) **TiO_x-based TCOs**, such as Nb-, or Ta-doped TiO_x [184], or even undoped TiO_x [329]. The latter is actually formed by an insulating amorphous TiO₂ matrix mixed with monocrystalline grains of metallic Ti, thus might not be suitable for PV applications due to the elusive contact engineering and possible metallic light absorption. As for the doped TiO_x, a main characteristic of such TCOs is that, the dopant activation can easily occur, independent of the dopant concentration. For this reason, the preferred (n -type) degenerate doping can be easily realized, enabling electron densities (N_e) above $2 \times 10^{21} \text{ cm}^{-3}$ even in amorphous state. This value is higher than the achievable N_e of below $1 \times 10^{21} \text{ cm}^{-3}$ scale in conventional In₂O₃-based TCOs. For this reason, the Nb-doped a-TiO₂ with resistivity below $3 \times 10^{-4} \Omega \text{ cm}$ received considerable attention since it was firstly reported in 2005 [44]. However, the high effective electron mass (derived from the 3d-character of CBM in host structure [52]), as well as the normally low crystallinity (since its charge transport is susceptible to crystalline structure [330], while TiO_x is not easy to be crystallized), result in low electron mobilities (μ_e) of below $30 \text{ cm}^2 \text{ V}^{-1} \text{ s}^{-1}$ in the PLD or epitaxial grown, and below $15 \text{ cm}^2 \text{ V}^{-1} \text{ s}^{-1}$ in the sputtering deposited TiO_x-based TCOs [184]. The undesirable high N_e and low μ_e hinder its application as TCOs in various PV devices, due to possible severe parasitic absorption caused by the high N_e . However, the TiO_x-based materials may embrace two new aspects:

(a) Doped/undoped TiO_x stack for TCO use. Specifically, a super thin TiO_x-based TCO layer is utilized for electrical transport, while the additional undoped TiO_x layer is

applied for ARC purpose. It is noteworthy that the undoped TiO_x ARC has been used in silicon-based solar cell for decades [309, 331, 332]. Compared to the other commonly utilized dielectric ARC materials (such as SiO_x , SiN_x , Al_2O_3), TiO_x has a relatively higher refractive index (n) of 2.45 [83]. Following the equation $n_{\text{ARC}} = \sqrt{n_{\text{glass}} \times n_{\text{Si}}}$ [83], in which glass is a representative encapsulation material. Provided $n_{\text{glass}} = 1.5$, and $n_{\text{Si}} = 4$, the optimal n_{ARC} could be calculated to be 2.45. In this regard, TiO_x is almost the ideal ARC material for encapsulated PV devices; Besides, it may serve as plating mask for dedicated Cu-plating metallization approach [331].

(b) electron transport layer (ETL) use. Either Nb-doped TiO_x [45] or undoped TiO_x [333] could be utilized as ETL in PV devices. Compared to the undoped TiO_x ETL, doped TiO_x , which possesses higher conductivity while maintains transparency, reduces the series resistance in solar cell devices. Hence, higher fill factor could be realized at device level [45]. To sum up, TiO_x -based materials could function as TCO in an optimal doped/undoped TiO_x layer stack format for silicon solar cells. Furthermore, the doped TiO_x may serve as an effective ETL layer for PV devices.

(iii) ***p*-type TCOs**, such as CuMO_2 (where M can be Al, Ga, or Cr) [334] with a delafossite structure. We note that, the commonly used oxides (such as In_2O_3) is intrinsically not suitable for producing effective *p*-type conductivity for two main reasons: (a) the localized nature of O 2p orbitals at the VBM, resulting in a large effective hole mass thus limiting the hole mobility; (ii) the valence bands are deep in energy, and holes are easily compensated by defects such as V_{O} , leading to a low *p*-type dopability thus limiting the carrier concentration [335]. By contrast, copper oxide can be a host material for producing *p*-type TCOs. Because the Cu 3d¹⁰ level is close to that of an O 2p⁶ level, it is expected that the Cu 3d¹⁰ can form strong covalent bonding with O 2p⁶. This results in a large dispersion at the top of VB and reduction of the localization of positive holes. Meanwhile the closed shell d¹⁰ orbitals also avoids coloration due to d-d excitations, ensuring the optical transparency for visible light. Take CuAlO_2 for example, depending on the deposition/treatment conditions, its reported band gap varies from 2.7 [336] to 3.86 eV [337], and the reported work function varies from 4.48 [336] to 5.3 eV [338]. So far, challenge in such *p*-type TCOs lies in its relatively high resistivity ($\sim 10 \text{ } \Omega \text{ cm}$). More effective doping may be introduced in future study. On the other hand, due to its inherent hole conducting capability, high transparency, good stability, and earth-abundant elements involved, CuAlO_2 has been explored as a hole transport layer (HTL) material for PV devices such as perovskite solar cells in recent years [338, 339]. The *p*-type materials (such as CuAlO_2) may also provide interesting topics for c-Si solar cells in the future, either in *p*-type TCO development or in HTL employment.

3. Developing novel Cu-plated TCO-free devices.

In this thesis, we described the employment of SHJ solar cells with reduced TCO use. There are three reasons: (i) the adhesion of plated Cu on bare wafer (coated with Ag seed layer) was observed to be poor; (ii) the contact resistivity at the PVD Ag / thin-film silicon layer interface was observed to be high ($> 1000 \text{ m}\Omega \text{ cm}^2$); (iii) Cu diffuses fast in Si, thus requires TCO acting as a diffusion barrier layer [112, 308]. Among the reasons, (i) has been solved with appropriate plating control in our lab; (ii) could be fixed by introducing Ti as the contacting layer with thin-film silicon layer [170, 306]. For (iii), different diffusion barrier layers in literature may facilitate a reliable Cu utilization without TCO employment.

Alternatives for diffusion barrier layer can be Ni [340], W [341], Ta [342], Ru [343], C [344], MnSiO_3 [345], $\text{Ta}_x\text{Mn}_y\text{O}_z$ [346], CoTi_x [347], and even CuAl [348]. Apart from that, long-term-stability issue of the Cu-plated PV devices and modules remains to be addressed [282, 349, 350].

4. Addressing TCO use in tandem solar cells.

As mentioned in section 1.2.1, the efficiency of silicon solar cells is fundamentally limited by spectral losses. Such spectral losses can be circumvented by using multiple junction solar cell concepts. The fundamental (detailed balance) efficiency limit for a double-junction tandem solar cell could reach 42% [20]. A typical configuration is represented by the perovskite/Si tandem solar cell, which has shown prosperous development after firstly reported in 2015 [10, 351]. A record efficiency of 29.8% [25] has been realized after only several years of progress. This strong dynamics also motivate us to further address aspects regarding TCO utilization in the advanced perovskite/Si tandem concept.

In a monolithic perovskite/silicon tandem device, TCOs could function as transparent electrode (TE) on top of the perovskite top cell or tunnelling recombination junction (TRJ) between the perovskite top cell and the silicon bottom cell. For the TE use, a minimal thickness of around 100 nm is normally required to ensure sufficient lateral conductivity, which accompanies significant parasitic absorption through the entire wavelength range of interest [352]. The TCO thickness of TE use could be potentially reduced without harming fill factor of the device. Besides, from an optical perspective, depositing an additional dielectric layer with appropriate refractive index could also be beneficial to minimize the reflection losses. Such additional dielectric layer can be MgF_2 , CaF_2 , PDMS [353]. Therefore, the designing rules for TCO as TE in perovskite/silicon tandem can be similar to what we have utilized in the single-junction c-Si solar cell scenario, except that perovskite absorber possesses different opto-electrical properties as compared to c-Si absorber, and the current in a two-terminal monolithic tandem solar cell can be reduced by half with respect to a single-junction c-Si solar cell [354]. In addition, the perovskite cell can be more susceptible to damage than the c-Si cell when facing TCO sputtering conditions, due to the moisture and temperature sensitivity of its functional materials (such as perovskite, Spiro-OMeTAD). This calls for low temperature (or even room temperature) deposition of TCO layer [355], and normally requires a thin buffer layer (such as MoO_x , SnO_2) utilized between the perovskite top cell and sputtered TCO film [356]. Besides, according to equation 2.1, high-mobility TCO is promising to realize the wanted trade-off between optical and electrical properties of the film. Thereby, for the purpose of TCO acting as TE on top of perovskite cell, the challenge lies in how to “softly” realize high mobility TCO deposition. Different TCO deposition techniques may be considered. In addition, it might be worth noting that new inspirations might also be obtained from the single-junction semi-transparent perovskite research. For instance, one can fabricate the TE in the form of a transparent conductive adhesive (TCA) material, which is separately accomplished to the tandem cell, and then simply laminate the TE and cell at room temperature [357]. However, in this case, the electrical contact between TCA and the solar cell is likely to be problematic, which remains to be investigated.

As for the TRJ use in tandem devices, the widely utilized alternatives include TCO-assisted [358, 359] and Si-based tunnelling junctions (such as nc-Si(O_x):H [360–362], poly-Si(C_x) [363]). From the light management point of view, as compared to TCO-

assisted TRJ, the Si-based TRJs were reported to have benefits of low reflection and parasitic absorption losses in the NIR wavelength range of interest [359, 360, 364]. Besides, from the electrical perspective, the Si-based TRJs could feature a highly anisotropic film conductivity, providing sufficient vertical conductivity while maintaining low lateral conductivity. This potentially reduces the shunt paths through pinholes or defects present in the perovskite top cell [360]. However, the TCO-assisted TRJ still deserves investigation due to its flexibility in work function manipulations, which is important to minimize voltage losses in the tandem cell [365]. Regarding the TCO-assisted TRJ, a more resistive TCO layer is observed to produce better electrical transport, owing to the suppression of shunt paths in the perovskite top cell [366]. In this regard, the TCO requirements on TRJ could be quite different from that on TE. Meanwhile, the lateral conductivity, as well as the parasitic absorption of the TCO layer, need to be minimized. Depending on the tandem polarities, sophisticated contact engineering via simulation work may provide insightful guidance for the optimal TRJ choice in tandem devices.

A

IFO:H in high thermal-budget poly-Si solar cells

This appendix provides supporting information of Chapter 5, which was included in the publication of *ACS Applied Materials & Interfaces** [61]

A.1. Properties of the IFO:H films under different PDA treatments

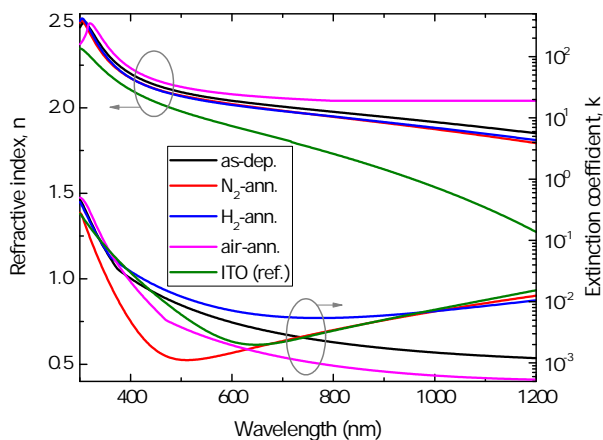


Figure A.1: Wavelength-dependent complex refractive index of the PDA treated IFO:H films from spectroscopic ellipsometry (SE) characterization.

*C. Han, G. Yang, A. Montes, P. Procel, L. Mazzarella, Y. Zhao, S. Eijt, H. Schut, X. Zhang, M. Zeman, and O. Isabella, "Realizing the Potential of RF-Sputtered Hydrogenated Fluorine-Doped Indium Oxide as an Electrode Material for Ultrathin SiO_x/Poly-Si Passivating Contacts," *ACS Applied Energy Materials*, 3(9), 8606-8618, 2020. August 12, 2020, doi: 10.1021/acsaem.0c01206.

Figure A.1 displays the wavelength-dependent complex refractive index of the IFO:H films under different PDA treatments, with our lab-standard ITO layer as reference. Basically, the refractive index (n) of the films shows lower values with increasing N_e (as shown in Figure 5.2). The extinction coefficient (k) curves are in accordance with Figure 5.2(b) due to the physical relation $\alpha = 4\pi k/\lambda$, where α is the absorption coefficient, and λ is corresponding wavelength. Specially, the k curves in UV part shows the optical band gap differences of different films, while the NIR region correlates with free carrier absorption differences of the layers.

Table A.1 shows the repeated results of the opto-electrical parameters of IFO:H films under different PDA treatments.

Table A.1: Opto-electrical parameters of the IFO:H films under different PDA treatments.

PDA	t [nm]	R_{sh} [Ω/\square]	N_e [$1 \times 10^{20} \text{ cm}^{-3}$]	$\mu_{e,Hall}$ [$\text{cm}^2 \text{ V}^{-1} \text{ s}^{-1}$]	ρ [$1 \times 10^{-4} \Omega \text{ cm}$]	T_{550} [%]	E_g [eV]
	80.6	67	1.22	88	5.81	76.32	3.84
as-dep.	79.7	66	1.22	85	6.02	76.28	3.85
	81.0	67	1.24	88	5.72	76.26	3.85
	78.8	71	1.24	86	5.85	76.35	3.85
	91.6	36	1.70	106	3.46	76.04	3.94
N_2 -ann.	89.0	38	1.74	104	3.45	76.10	3.92
	90.3	36	1.72	106	3.42	76.09	3.94
	89.8	38	1.74	104	3.45	76.06	3.93
H_2 -ann.	91.3	41	1.48	111	3.80	77.27	3.87
	90.5	43	1.44	110	3.94	77.30	3.85
	92.0	40	1.49	108	3.88	77.28	3.87
	90.0	44	1.48	108	3.91	77.32	3.86
air-ann.	92.1	760	0.060	22	472	77.78	3.76
	91.7	680	0.065	20	480	77.79	3.74
	92.4	700	0.047	20	664	77.83	3.76
	90.2	760	0.056	21	531	77.80	3.76

A.2. S- and W-parameter curves in DB-PAS measurements

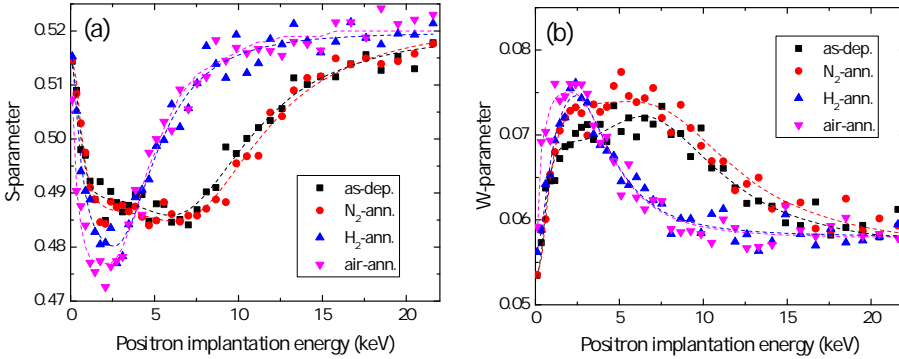


Figure A.2: (a) S-parameter and (b) W-parameter as a function of implantation energy for the IFO:H films under PDA. Dashed lines represent best-fit curves using VEPFIT analysis.

Table A.2: Fitting parameters and standard deviations extracted from VEPFIT analysis for the four different IFO:H films under PDA.

Sample	Layers	^a Thickness [nm]	S	W	^b Density [g/cm ³]
as-dep.	top film	70	0.4885 ± 0.0003	0.0695 ± 0.0003	5.80
	film bulk	210	0.4817 ± 0.0006	0.0743 ± 0.0005	5.80
	substrate	-	0.5220 ± 0.0004	0.0577 ± 0.0005	2.33
N ₂ -ann.	top film	70	0.4863 ± 0.0003	0.0739 ± 0.0003	7.18
	film bulk	210	0.4827 ± 0.0006	0.0756 ± 0.0010	7.18
	substrate	-	0.5215 ± 0.0004	0.0565 ± 0.0005	2.33
H ₂ -ann.	top film	90	0.4783 ± 0.0004	0.0765 ± 0.0005	7.18
	substrate	-	0.5198 ± 0.0002	0.0580 ± 0.0002	2.33
air-ann.	top film	80	0.4761 ± 0.0003	0.0753 ± 0.0003	6.33
	substrate	-	0.5205 ± 0.0002	0.0578 ± 0.0002	2.33

^a The VEPFIT thickness provides qualitative values, that are consistent with the quantitative values extracted from spectroscopic ellipsometry.

^b The density values for the as-dep. and air-ann. IFO:H films were tuned from the starting point of 7.18, which corresponds to the reported In₂O₃ bulk material, to reach a qualitative agreement in film thickness with the quantitative spectroscopic ellipsometry.

Figure A.2 shows the S- and W-parameter curves versus positron implantation energy for the IFO:H films under PDA. The peaks in S- and W-parameter are not exactly at the same positions for different samples since the thicknesses of the IFO:H layers differs. In order to realize a good fitting in the VEPFIT analysis, a three-layer model (top film/film bulk/substrate) was used for the ~ 280 nm-thick as-dep. and N₂-ann. films, and a two-layer model (top film/substrate) was utilized for the ~ 80 nm-thick H₂-ann. and air-ann. layers, respectively. The S-W values collected in Figure 5.5(a) were based on the mentioned

“top film” values for appropriate comparison. The best-fit parameters of the different layers and substrate are listed in Table A.2.

A.3. Temperature-dependent mobilities of IFO:H films under PDA

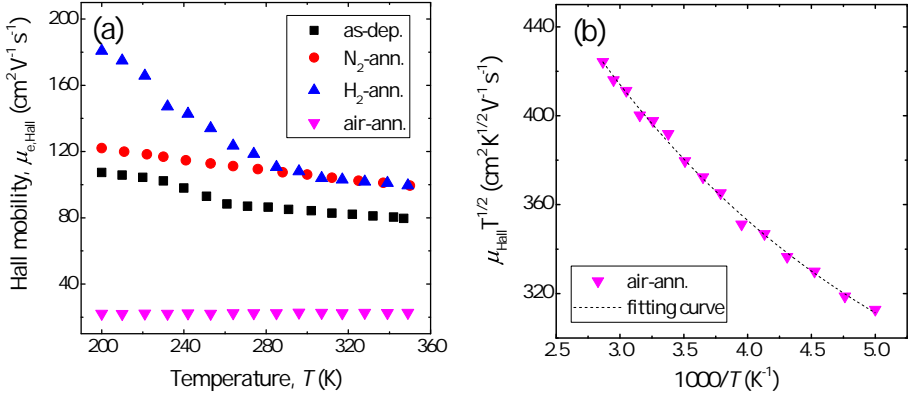


Figure A.3: (a) Temperature-dependent Hall mobilities of IFO:H films under PDA, (b) plot of $\mu_{e,Hall}\sqrt{T}$ versus inverse temperature in air-ann. sample, with the exponential fitting line.

Figure A.3(a) displays the temperature-dependent mobilities of IFO:H films under different PDA treatments, which has been used for the mathematical exponential fitting to extract different scattering components. The as-dep., N₂-ann., and H₂-ann. samples follow Matthiessen’s rule as expressed by equation 5.1, while air-ann. sample do not. Figure A.3(b) shows the plot of $\mu_{e,Hall}\sqrt{T}$ versus inverse temperature in air-ann. sample, with the exponential fitting line. The results on air-ann. film well match the scattering mechanism described by the Schottky-barrier model in thermionic emission.

A.4. Solar cell results from different batches

Table A.3 shows our solar cell results from different batches.

Table A.3: Poly-Si solar cell parameters of 3.92 cm² devices using IFO:H and ITO, with and without H₂ annealing treatment, respectively. The values reported are the average based on twelve cells. The standard deviation is calculated for each cell parameter.

TCO	Open-circuit voltage [V_{OC} , mV]	Short-circuit current density [J_{SC} , mA/cm ²]	^a Fill factor [FF , %]	Efficiency [η , %]
IFO:H as-dep.	670 ± 8	38.69 ± 0.21	74.24 ± 0.38	19.1 ± 0.3
IFO:H ann.	670 ± 7	38.76 ± 0.23	75.13 ± 0.31	19.5 ± 0.3
ITO as-dep.	669 ± 8	37.54 ± 0.19	74.51 ± 0.48	18.7 ± 0.2
ITO ann.	670 ± 6	37.69 ± 0.20	74.20 ± 0.38	18.7 ± 0.2

^a Fill factor showed a general decreased level compared to the FF data in Figure 5.8, plausibly due to the uncertainties occurring in our cell precursor fabrication process after equipment maintenance. However, the resulting trends upon TCO variations were basically repeated, as observed in Figure 5.8.

B

RT-sputtered IWO in SHJ devices

This appendix provides supporting information of Chapter 6, which was included in the publication of *Solar Energy Materials and Solar Cells** [122]

B.1. Multi-layer strategy in spectroscopic ellipsometry fittings

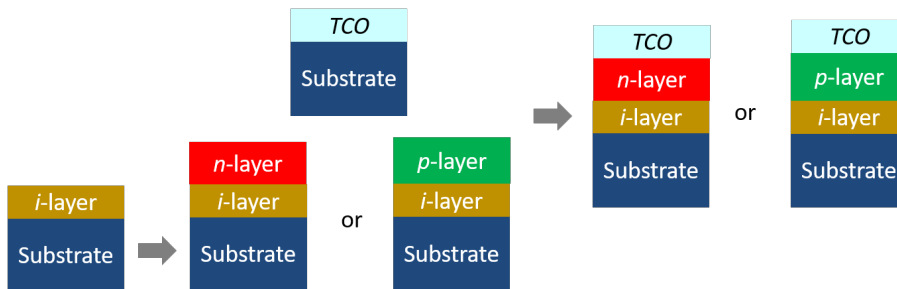


Figure B.1: Multi-layer strategy in spectroscopic ellipsometry fittings.

Figure B.1 displays the multi-layer strategy in our spectroscopic ellipsometry fittings: (i) measure n , k for i/n or i/p stack with previous i -layer fixed, using Cody-Lorentz dispersion models; (ii) measure n , k for a single TCO layer, using a combination of a Cody-Lorentz oscillator and a Drude oscillator to account for the absorption across the optical band gap in ultraviolet range and the free carrier absorption in the near infrared part of the spectrum, respectively; (iii) measure n , k for the TCO layer on top of i/n or i/p stack, with an effective medium approximation (EMA) layer inserted between TCO and underlying doped silicon thin film, to account for the interfacial mixing between

*C. Han, Y. Zhao, L. Mazzarella, R. Santbergen, A. Montes, P. Procel, G. Yang, X. Zhang, M. Zeman, and O. Isabella, "Room-temperature sputtered tungsten-doped indium oxide for improved current in silicon heterojunction solar cells," *Solar Energy Materials and Solar Cells*, 227, 111082, 2021. April 14, 2021, doi: /10.1016/j.solmat.2021.111082.

layers. In this step, oscillator parameters from previous i/n or i/p stack are fixed except doped silicon layer thickness. The variable modelling parameters also include the silicon and interfacial silicon oxide volume fraction in EMA constitution, EMA thickness, TCO oscillator parameters based on that from (ii), and TCO thickness.

B

B.2. Wavelength-dependent absorbance of the optimal IWO and ITO reference layers

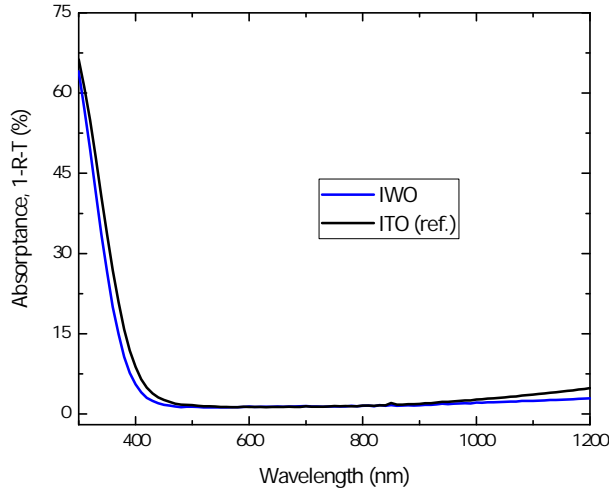


Figure B.2: Absorbance spectra of the optimal IWO film and ITO reference layers.

Considering the reflection- n -type SE has limited sensitivity for weak light absorption, samples were further measured via from UV-Vis-NIR spectroscopy. Figure B.2 illustrates the supplementary absorbance curves of the optimal IWO and ITO reference layers, which was calculated from $1-R-T$. Figure B.2 and Figure 6.3 show comparable trend in both E_g -related UV and FCA-related NIR ranges.

B.3. Minority carrier lifetime measurements of SHJ cell precursors

Figure B.3 shows the minority carrier lifetime measurements of SHJ cell precursors. The cell precursor maintains a high passivation quality after ITO sputtering at 110 °C. However, RT IWO deposition induces a severe sputter damage that could not be restored in the TCO sputtering procedure. Therefore, a subsequent hot-plate annealing at 180 °C for 5 min was utilized to recover the passivation quality of the IWO-based cell precursors.

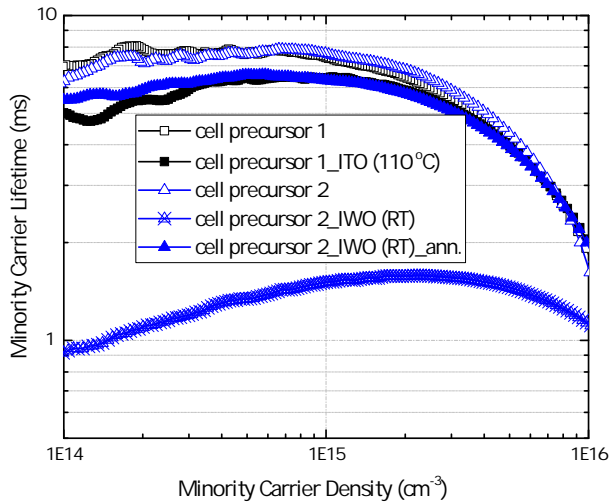


Figure B.3: Minority carrier lifetime measurements of SHJ solar cell precursors.

B.4. XRD patterns and SEM images of annealed IWO and reference ITO films

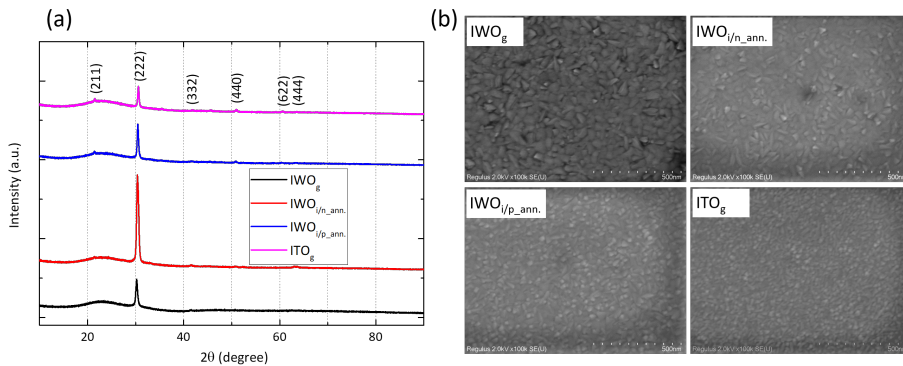


Figure B.4: (a) X-ray diffraction patterns, and (b) scanning electron microscope images of annealed IWO and reference ITO films. Subscript g stands for glass substrate.

Figure B.4 shows the XRD patterns and SEM images of annealed IWO and our reference ITO films. With respect to the as-deposited IWO film on glass substrate, both the annealed IWO layers on top of thin-film silicon show increased crystallinity and more prominent preferred (222) orientation. The reference ITO layer is also in polycrystalline structure, whose surface morphology shows more densely distributed fine grains than that of the IWO films.

B.5. Optical simulations from TCO data obtained on glass substrate

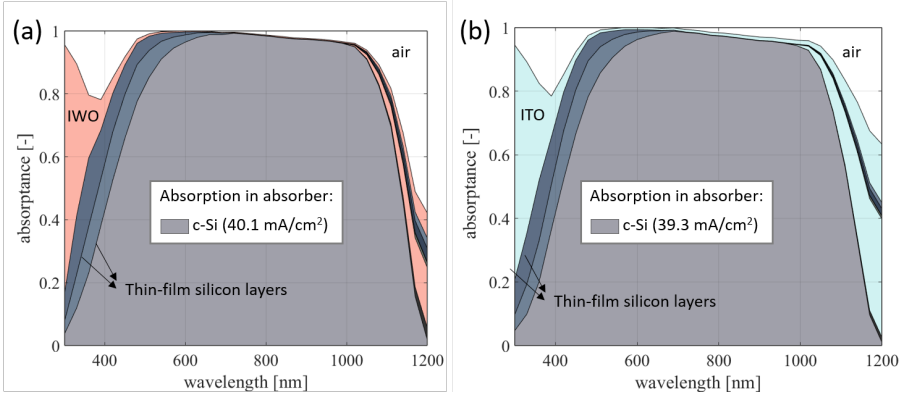


Figure B.5: Optical simulations performed by GenPro4 software of (a) IWO- and (b) ITO-based SHJ solar cells. TCO data were gathered from glass substrates.

Figure B.5(a-b) show the optical simulation results based on TCO data obtained from glass substrates. Specific optical losses from different layer components are included in Figure 6.6(c).

B.6. MgF₂ complex refractive index and its thickness optimization based on our existing device structure

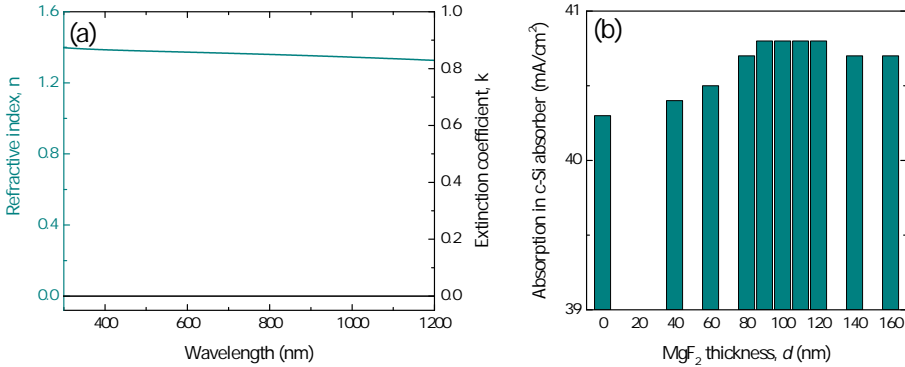


Figure B.6: MgF₂ complex refractive index and optical simulative results on our IWO-based SHJ device structure.

Figure B.6(a) shows the complex refractive index of MgF₂ on a flat wafer as measured by spectroscopic ellipsometry. Figure B.6(b) displays the MgF₂ thickness optimization on top of our existing IWO-based SHJ device structure, obtained from optical Genpro4 simulations. From Figure B.5(b), adding 90-120 nm-thick MgF₂ could reach an utmost absorption in our absorber material, which is also in accordance with the general $n_{MgF_2} \cdot d_{MgF_2} = \lambda/4$ rule in designing anti-reflection coating. We note that this optimization does

not represent the optimal results on double layer anti-reflection coating (DLARC) design, since the thickness of the front TCO was fixed at 75 nm in our device fabrication.

B.7. Optical band gap plots of TCOs on top of thin-film silicon stacks at illuminated side of devices

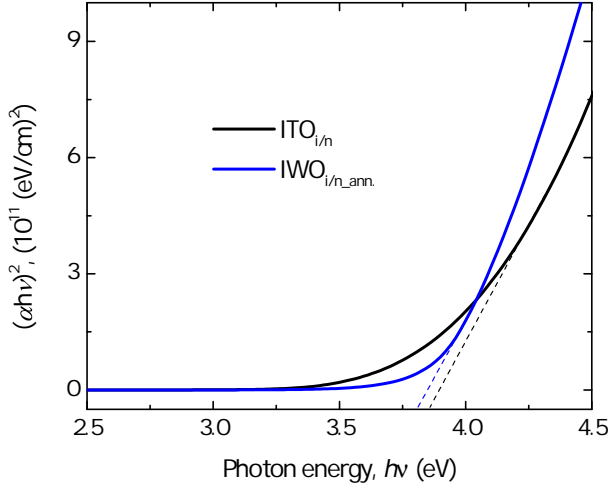


Figure B.7: Optical band gap plots of ITO on i/n stack (denoted as $\text{ITO}_{i/n}$), and IWO on annealed i/n stack (denoted as $\text{IWO}_{i/n,ann.}$).

Figure B.7 shows the optical band gap plots of TCOs on top of thin-film silicon stacks at illuminated side of our SHJ devices. The extracted optical band gap values for corresponding IWO and ITO layers are 3.81 eV and 3.87 eV, respectively.

C

Towards bifacial SHJ solar cells with reduced TCO use

This appendix provides supporting information of Chapter 7, which was included in the publication in *Progress in Photovoltaics: Research and Applications** [125]

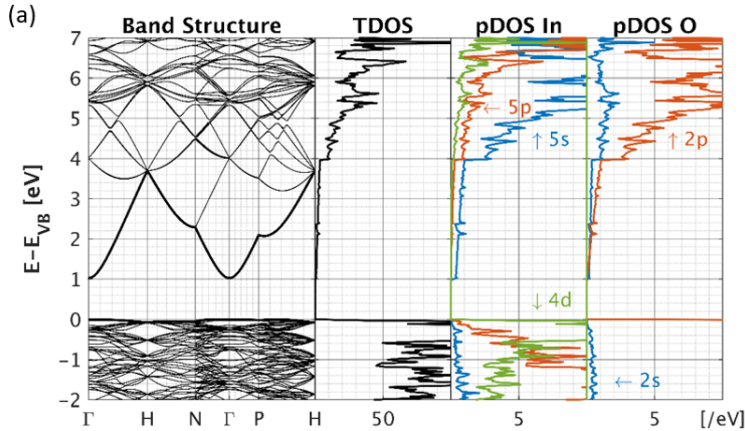
C.1. Electrical structures of TCOs from density-functional theory (DFT) simulations

Figure C.1(a-d) shows the band structure, total density of states (TDOS), and partial density of states (pDOS) of indium oxide and Sn-, F-, and W-doped indium oxides, i.e., IO, ITO, IFO, and IWO, respectively. The band structures are with respect to the fermi levels, and the valence band maximum (VBM) levels were set to 0 eV. From Figure C.1(a), the TDOS and pDOS reveal that the conduction band minimum (CBM) is primarily of In 5s and O 2p character, which implies a wide and dispersive conduction band that facilitates high electron mobility [367]. The calculated band gap (E_g) is 1.0 eV, much smaller than the experimental value (above 2.7 eV). Such an intrinsic underestimation in the calculated band gap of the TCO materials is caused by the lack of the discontinuity and errors in the single-particle eigenvalues resulting from the approximative nature of the Perdew-Burke-Ernzerhof (PBE) exchange-correlation functional [367, 368]. The effective electron mass (m_e^*) of IO is calculated to be $0.33 m_e$, which is within the reported value region [74]. From Figure C.1(b), the Sn dopant significantly hybridizes with the host CBM. This strong perturbation has been proven to be detrimental to the electrical properties of the ITO film [281]. From Figure C.1(c), the F dopant also hybridize with the host CBM. In contrast, one can see from Figure C.1(d) that, the enhanced doping behaviour arises from W 5d donor states being negligibly perturbing the host CBM. This phenomenon is similar with the case of molybdenum (Mo)-doped In_2O_3 [281], probably because W and Mo are from the same group in the Periodic Table of Elements. The m_e^* values are $0.24 m_e$, 0.31

*C. Han, R. Santbergen, M. van Duffelen, P. Procel, Y. Zhao, G. Yang, X. Zhang, M. Zeman, L. Mazzarella, and O. Isabella, "Towards high efficiency bifacial silicon heterojunction solar cells with reduced TCO use," *Progress in Photovoltaics: Research and Applications*, 2022. March 14, 2022, doi:10.1002/pip.3550.

m_e , and $0.23 m_e$, for ITO, IFO, and IWO, respectively. The corresponding fundamental E_g values are calculated to be 0.77 eV, 0.55 eV, and 0.94 eV.

Interestingly, the IFO material, which is calculated to show large m_e^* value and low E_g , exhibits higher electron mobility (μ_e) and comparable E_g as compared to ITO from experimental data [61, 213, 315]. We presume this could be related to two aspects. On the one hand, from physical definition, (μ_e is calculated by $\mu_e = e\tau/m_e^*$ (in which e is elementary charge, and τ denotes the carrier relaxation time. Plausibly, the IFO could show a high τ in nature due to a possibly less unit cell distortion than other TCOs, since the ion radius of F^- is quite close to that of O^{2-} [225]. Besides, F has reported to passivate defects such as oxygen vacancies and grain boundaries [225, 246], which is also beneficial to get a high τ . On the other hand, the shape of conduction band needs to be taken into consideration when we interpret E_g . It is well known that, in degenerated semiconductors, the E_g is influenced by the fundamental E_g and a E_g widening due to the well-known Moss-Burstein shift [54]. However, a so-called band-gap re-normalization can also occur in doped TCOs, that would offset the widening effect from the Moss-Burstein shift [74]. In addition, the properties of experimentally deposited TCOs are influenced by multiple factors, such as deposition techniques, deposition conditions, substrates, and source material purities. These factors makes it more complex to align calculated and experimental data on the opto-electrical properties of the TCO materials. Thus, we only tried to apply the calculated results for qualitative comparison purposes within the scope of this dissertation.



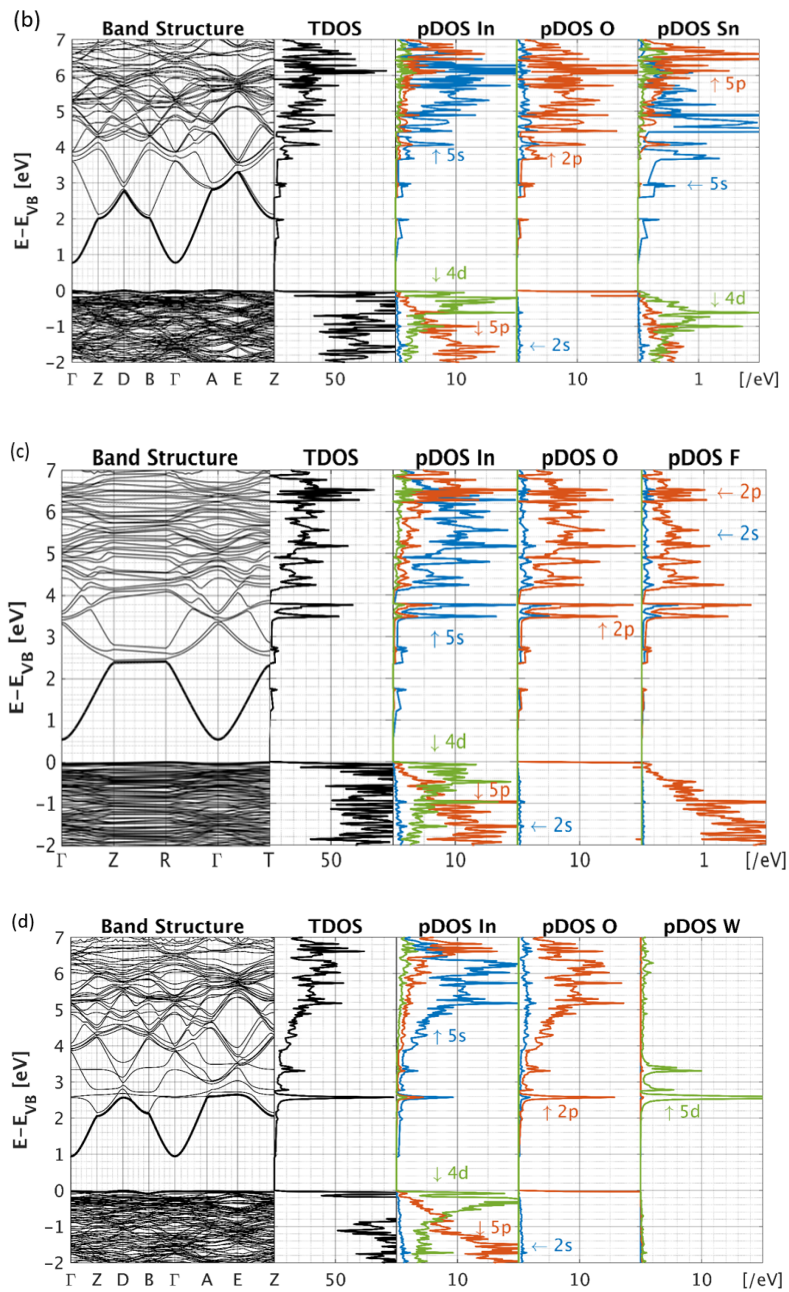


Figure C.1: The band structure, and projected total density of states (TDOS), and partial density of states (pDOS) of (a) indium oxide and (b) Sn-, (c) F-, and (d) W-doped indium oxides.

C.2. Complex refractive index of the TCOs on top of thin-film silicon layer stacks

Figure C.2 shows the complex refractive index of the TCOs on top of thin-film silicon layer stacks.

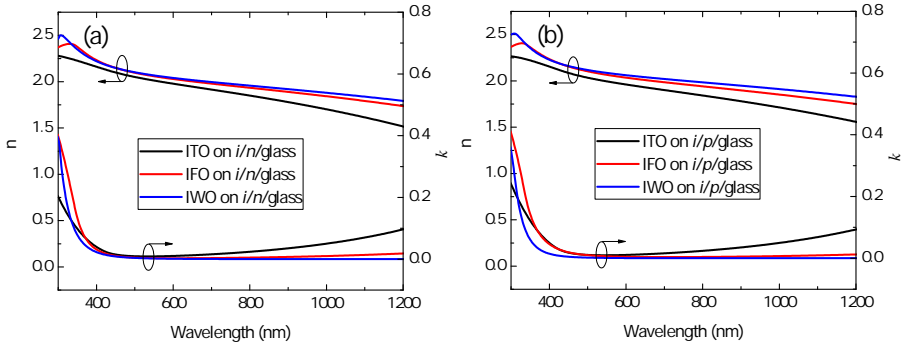


Figure C.2: Refractive index (n) and extinction coefficient (k) curves of the TCOs deposited on (a) i/n /glass and (b) i/p /glass, respectively.

C.3. Optical simulations on bifacial SHJ solar cells with varied TCO/SiO_x stacks

Figure C.3(a-c) shows GenPro4 optical simulation results of monofacial SHJ devices based on different TCO/SiO_x stacks [211]. We applied the same type of TCO at the front and rear sides. The thickness of rear TCO was kept at 150 nm, to maintain sufficient internal reflection and avoid plasmonic absorption in the rear metal [82]. On the front side, double layer antireflection coating was utilized, which composes of varied TCO/SiO_x stacks. As labelled in the contour plots, in the case of optimum single-layer AR coating with a 75 nm-thick TCO on the front side, the implied photocurrent densities in c-Si absorber (J_{c-Si}) were calculated to be 38.5 mA/cm², 39.6 mA/cm², and 40.3 mA/cm², for ITO-, IFO-, and IWO-based solar cells, respectively. By adding a SiO_x layer, they were correspondingly improved to optimal values of 39.5 mA/cm², 40.3 mA/cm², and 41.0 mA/cm², with reduced TCO thicknesses at 40 nm for ITO and IFO, 60 nm for IWO, respectively. The improved J_{c-Si} values could be attributed to a further reduction of the reflectance, as well as a reduced parasitic absorption. This is in agreement with our previous investigation [123]. On the other hand, within a certain SiO_x thickness range of around 90-130 nm, all the devices could maintain decent optical responses with continuously decreased TCO thickness (even to the extreme *TCO-free* case).

From a comparison among Figure C.3(a-c), one can see that the ITO-based devices show lowest J_{c-Si} , which could be attributed to the higher N_e in the ITO layer, as compared to IFO and IWO layers (as shown in Figure 7.1). As compared to the IWO layer, the IFO layer shows lower N_e when deposited on glass substrates. While the N_e of the IFO layer notably increases when deposited on top of thin-film silicon layers, leading to a more absorptive nature. In contrast, the N_e of the IWO layer mildly decreases when deposited on top of thin-film silicon layers, indicating a more transparent nature of the TCO layer. Consequently, the optimal IWO-based device displays the highest A_{c-Si} , although the IWO layer does not possess the lowest N_e at the initial stage when deposited on glass substrates. This emphasizes the importance that the manipulation of the TCO properties

need to be taken into consideration in device investigations, which is in accordance with the observations from Cruz *et al.* [87].

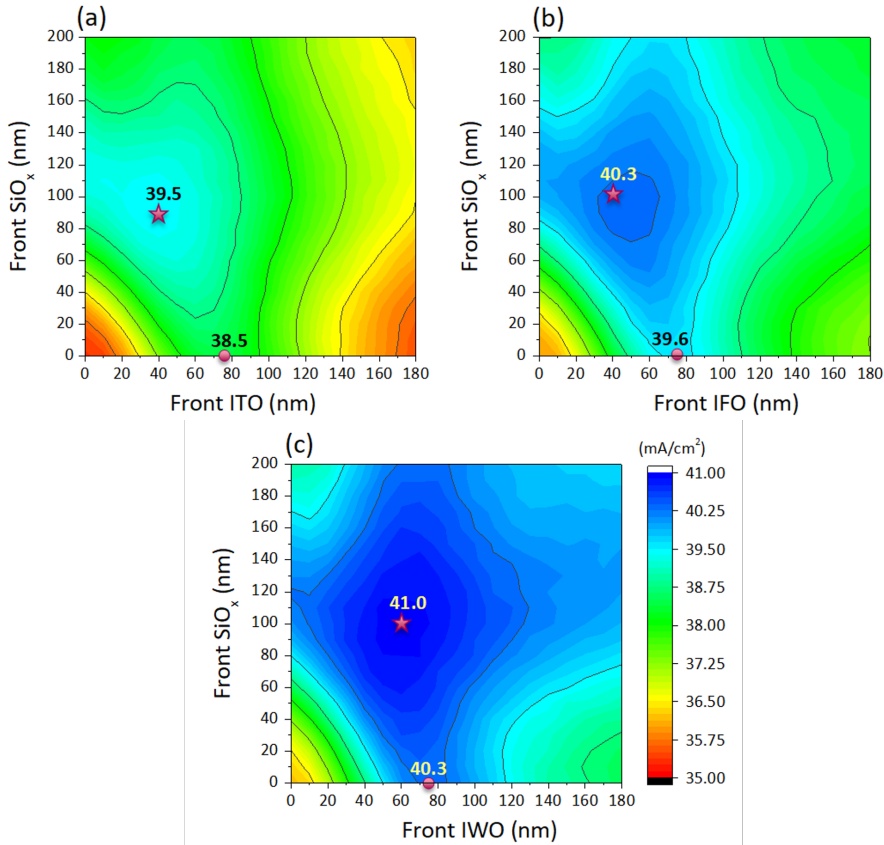


Figure C.3: The simulated implied photocurrent densities in c-Si absorber (J_{c-Si}) as a function of front side TCO and SiO_x thicknesses for (a) ITO-, (b) IFO-, and (c) IWO-based monofacial SHJ devices. The dots indicate the cases of single ARC use, the stars show the positions corresponding to optimal TCO/ SiO_x use. The values show the J_{c-Si} values that correspond to the dots or stars.

As labelled in the contour plots, in the case of optimum single-layer AR coating with a 75 nm-thick TCO on the front side, the implied photocurrent densities in c-Si absorber (J_{c-Si}) were calculated to be 38.5 mA/cm², 39.6 mA/cm², and 40.3 mA/cm², for ITO-, IFO-, and IWO-based solar cells, respectively. By adding an SiO_x layer, they were correspondingly improved to optimal values of 39.5 mA/cm², 40.3 mA/cm², and 41.0 mA/cm², with reduced TCO thicknesses at 40 nm for ITO and IFO, 60 nm for IWO, respectively.

For bifacial cell simulations, we used constant 100 nm-thick SiO_x layers on top of TCO and on both sides of the wafer. This thickness was chosen from the following procedures: (i) choose the optimal TCO/ SiO_x stacks in monofacial cell as shown in Figure 7.2, and get ($t_{\text{TCO,front},0}$, $t_{\text{SiO}_x,\text{front},0}$); (ii) optimize rear side TCO/ SiO_x stacks with rear side illumination

in a bifacial cell structure, front side layers are fixed with $(t_{\text{TCO,front},0}, t_{\text{SiO}_x,\text{front},0})$. As a results, one gets optimized $(t_{\text{TCO,back},0}, t_{\text{SiO}_x,\text{back},0})$; (iii) use a `fminsearch` algorithm to find out the optimal points from four variables with varied TCO/SiO_x stacks on both sides, in which $(t_{\text{TCO,front},0}, t_{\text{SiO}_x,\text{front},0}, t_{\text{TCO,back},0}, t_{\text{SiO}_x,\text{back},0})$ acts as the starting point. After `fminsearch`, all the optimized SiO_x thicknesses fell into the range of 90-115 nm (detailed data not shown). Therefore, constant 100 nm-thick SiO_x layers on both sides of the wafer were fixed in our bifacial cell simulation settings, while front and rear TCO thicknesses act as variable parameters.

C.4. Monofacial SHJ solar cell results

Figure C.4(a-d) show the measured monofacial rear emitter SHJ solar cell results. For each cell, we used the same type of TCO on both sides, where 150 nm-thick TCO was constantly applied at the rear side the cell. For the front TCO, three thicknesses were tested, i.e., 25 nm, 50 nm, and 75 nm. *n*-side is the illuminated side in the solar cell measurements. From Figure C.4(a), the V_{OC} values are generally below 720 mV, which is above 20 mV drop as compared to the implied- V_{OC} values at ~ 740 mV before metallization. This may indicate an selectivity issue in our cells, which still needs to be tackled in specific investigation. From Figure C.4(b), the J_{SC} comparisons among the three types of devices are basically in agreement with our optical simulations as shown in Figure C.3. From Figure C.4(c), each type of TCO-based SHJ devices maintain a relatively stable FF among the devices within one type of TCO-based SHJ devices even for the 25 nm-thick TCO. However, the FF values of the IFO-based devices are generally lower than ITO- and IWO-based devices, while their pFF values are comparable with the other two groups of devices. This indicates that with respect to the ITO- and IWO-based devices, there are higher series resistances in the IFO-based devices dominating those losses. Combined with the results from Figure 7.3 and Figure 7.4, we presume that the c-Si absorber acts as the lateral electron transport layer, while the FF is mainly determined by the $\rho_{c,n}$ differences in the vertical carrier transport direction. For the IFO-based devices, with the IFO layer thickness increasing from 25 nm and 50 nm to 75 nm, although the *n*-contact property changes from non-ohmic to ohmic behaviour, the $\rho_{c,n}$ is much higher than that of ITO- and IWO-based contact samples. This explains why the FF is low and series resistance is high in the IFO-based devices. In addition, it is noteworthy that on the rear side of the devices, 150 nm-thick TCO is in contact with *p*-type silicon layers. The corresponding average $\rho_{c,p}$ values are measured 306 m Ω cm², 168 m Ω cm², and 173 m Ω cm², for ITO-, IFO-, and IWO-based contact samples, respectively. Therefore, the optimal FF in the IWO-based devices could be attributed to its low ρ_c values in both *n*-contact at the front side and *p*-contact at the rear side. As a consequence, the best monofacial SHJ device was observed among the IWO-based devices, in which the 50 nm-thick IWO and 100 nm-thick SiO_x layers are applied on the illuminated side.

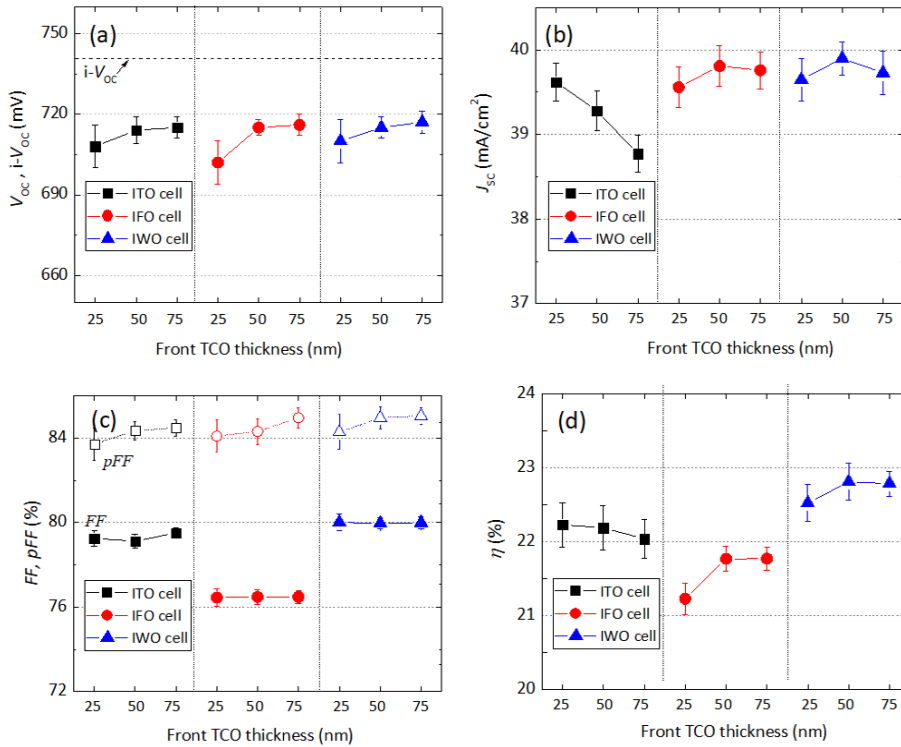


Figure C.4: The measured (a) open-circuit voltage, V_{OC} , and implied- V_{OC} , $i-V_{OC}$, (b) short-circuit current density, J_{SC} , (c) fill factor, FF, and pseudo fill factor (pFF), and (d) power conversion efficiency, η , of monofacial SHJ device with varied TCO thicknesses of 25 nm, 50 nm, and 75 nm. The results are based on three devices on the same wafer from the one batch of processes.

Figure C.5(a-c) depicts the measured EQE and simulated absorbance curves of the champion cells among each type of TCO-based SHJ devices, in which ITO-based cell based on 25 nm-thick ITO layer, IFO-based cell based on 50 nm-thick IFO layer, and IWO-based cell based on 50 nm-thick IWO layer are presented. The comparisons between the simulated and measured data could be evaluated from different wavelength regions. In the short wavelength region (below 550 nm), with respect to the measured EQE curves, the simulated absorbance of c-Si absorber is a bit lower than the optical response from EQE measurements. This difference could be attributed to two aspects: (i) the Genpro4 simulation only count the absorbance into c-Si absorber in the model [211], whereas there is some additional contributing optical response from the intrinsic amorphous silicon layer [369], which was not taken into account in our optical simulations [211]; (ii) the layer property may change in real corresponding layer stacks.

In the near infrared (NIR) wavelength region (above 750 nm), with respect to the measured EQE curves, from the ITO-, IFO-, to IWO-based devices, the simulated absorbance curves show more pronounced overestimation of the optical responses. We speculate that this increasing overestimation trend is related to the fact that the reflection- n -type

SE has limited sensitivity for weak light absorption [183, 189]. From Figure C.2, the IFO layers are less absorptive than the ITO layers, and among the TCO layers, the IWO layers show the least absorption in the NIR range. It is plausible that the sensitivity of the SE measurements decreases when measuring the very transparent IFO and IWO layers. The speculation may also be supported by the enlarged differences between the $J_{SC,EQE}$ and A_{c-Si} values from ITO-, IFO-, and IWO-based devices. Thirdly, in the NIR wavelength region, there could also be slight overestimation in our simulated current due to the fact that there would be non-negligible plasmonic absorption of rear metal when thin TCO layer (<150 nm) was utilized [82]. But it was omitted in our optical simulation. Lastly, the current collection efficiency in the devices could deviate from 100%, which also occupies a small portion in the discrepancies between the overall simulated and measured curves [370].

As a result of the above-mentioned aspects, the overall differences between the $J_{SC,EQE}$ and A_{c-Si} values are 0.2 mA/cm^2 , 0.9 mA/cm^2 , and 0.9 mA/cm^2 , for ITO-, IFO-, and IWO-based devices, respectively. Additionally, looking back at our optical simulation results in Figure 7.2 and Figure C.3, there is optical overestimations to different extents for the SHJ devices with different TCOs. Specifically, there could be a relatively high overestimation in the devices with the most transparent IWO layers, then the overestimation can be a bit lower in the IFO-based devices, and the simulated result on ITO-based devices is relatively reliable.

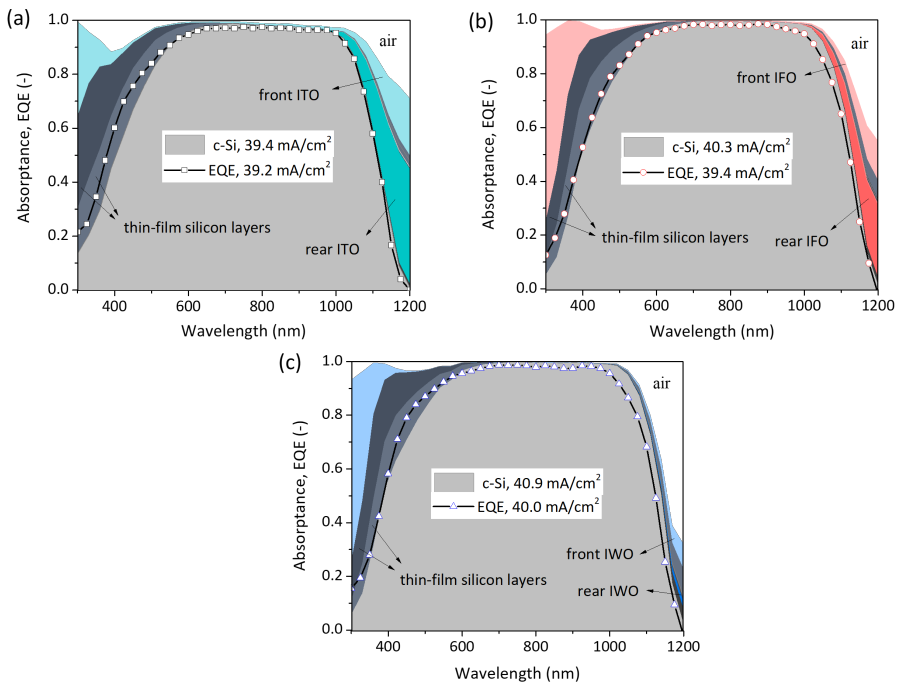


Figure C.5: The measured EQE and simulated absorbance curves of (a) ITO-based cell based on 25 nm-thick ITO layer, (b) IFO-based cell based on 50 nm-thick IFO layer, and (c) IWO-based cell based on 50 nm-thick IWO layer.

D

Controllable bifacial Cu-plating for c-Si solar cells (I)

This appendix was published as one article in *Solar RRL** [371]

Abstract

Bifacial copper(Cu)-plated crystalline silicon (c-Si) solar cell has been an attractive topic to concurrently reduce silver (Ag) consumption and maintain good device performance. However, it is still challenging to realize a high aspect ratio (*AR*) of the metal fingers. In this work, we electrochemically fabricate a new type of hybrid-shaped Cu finger in a bifacial plating process. Cyclic voltammetry was employed to disclose the electrochemical behaviors of cupric ions in monofacial (MF) and simultaneous BF Cu-plating processes, such that the controllability of the plating process could be assessed. The optimal hybrid Cu finger composes of a rectangular bottom part and a round top part, such that an utmost effective *AR* value of 1.73 is reached. In BF Cu-plating, two sub-three-electrode electrochemical cells were employed to realize equal metal finger heights on both sides of the wafer. Compared to our low thermal-budget screen-printing metallization, the Cu-plated silicon heterojunction devices showed both optical and electrical advantages (based on lab-scale tests). The champion bifacial Cu-plated device shows a front side efficiency of 22.1%, and a bifaciality factor of 0.99.

*C. Han, G. Yang, P. Procel, D. O'Connor, Y. Zhao, A. Gopalakrishnan, X. Zhang, M. Zeman, L. Mazzarella, and O. Isabella, "Controllable simultaneous bifacial Cu-plating for high efficiency crystalline silicon solar cells," *Solar RRL*, 2100810, 2022. February 12, 2022, doi:10.1002/solr.202100810.

D.1 Introduction

Silver (Ag) consumption in the photovoltaic (PV) industry, which takes around 10% of the yearly global Ag production, is becoming a great concern in the PV community [167, 301, 372]. In 2020, the global solar PV capacity was approximately 135 GW, and an annual production of PV systems of around 3 TW per annum is predicted around 2030 [167, 301, 373], which is tens of times higher than the current capacity. Even if we ignore the evolution in c-Si PV technologies (for instance, silicon heterojunction or iTOPCon consume more silver than PERC per wafer), the global silver production cannot satisfy the vast demand in future decades. Thus, it is imperative to reduce Ag usage. In order to concurrently reduce Ag consumption [167, 373] and reach high PV device performance, bifacial copper(Cu)-plated solar cell has been an attractive topic in recent years [374–376]. High efficiency above 24% have been achieved on industrial 6” bifacial Cu-plated silicon heterojunction (SHJ) solar cells [375]. In March 2022, Australian startup SunDrive has obtained an efficiency of 26.07% on commercial-sized bifacial silicon heterojunction solar cell with Ag-free Cu metallization technology [377].

To realize a bifacial plating process, the approach can be realized in a 2-step process, i.e., firstly do plating on one side of the wafer (with the other side protected or biased) and then plate on the other side [378–380]. The other way to do bifacial plating is a 1-step process, i.e., do simultaneous plating on both sides of the wafer [374–376, 381]. The first bifacial plating attempt in PV devices was electroless plating. Back to 1990s, Ebong *et al.* [382] at UNSW tried simultaneous electroless chemical nickel (Ni)/Cu-plating on both sides of the wafer. But they failed to get the same deposition rates on *n*- and *p*-sides of the wafer [383]. In 2017, Tous *et al.* and Russell *et al.* from IMEC reported successful bifacial electroless Ni plating with applying a proprietary selective activation step on silicon surfaces [381, 384]. Since 2010s, the 2-step bifacial plating with a combination of a light-induced plating and a field-induced plating on two sides of the wafer [380, 385, 386], as well as the 1-step simultaneous bifacial electrochemical plating on both sides of the wafer [374–376, 387], have been extensively developed. The institutes (such as Fraunhofer ISE, CSEM, UNSW, SIMIT [387]), and companies (such as MECO, Sunpreme) are working on the bifacial Cu-plating development [388]. However, despite the devoted efforts, the Cu-plating development is still not ripe enough to compete with traditional screen printing technology. The market share of Cu-plated solar cells is still conservatively considered [389], which is predicted to about 12% in 2031 [7]. The factors that hamper the progress of plating technique include processes, equipment, and reliability issues [7]. Therefore, research on these aspects is essential to the development of the alternative Cu-plating metallization approach in next decade(s).

Regarding the 1-step simultaneous bifacial electrochemical plating process, provided the wafer is double-sided coated with a full area thin metal seed layer and fully immersed in the electrolyte solution, the wafer could be basically treated as a conductor in the electroplating process, which may introduce influences in the two electrochemical deposition processes on both sides of the wafer. Assuming one does monofacial electroplating on one wafer side, with the other side immersed in the solution but unprotected (or unbiased), the other side of the wafer can also be plated. Such a “bifacial” plating may be challenging to control due to the complex uncertainties in the wafer surface condition, electrolyte and the distribution of electric field [390–393]. Therefore, it is imperative to carry out

investigation to understand the electrochemical behaviors of the reactive species in the bifacial electroplating processes and realize them in a controllable way.

In addition, from the finger dimension point of view, high aspect ratio (AR , i.e., the ratio of height and width) is always desirable to ensure sufficient conductivity and minimize shadow losses at the illuminated side(s) of solar cells [394]. In general, there are two basic types of metal finger cross-sections in PV devices: (i) rectangle-like shape [390], from self-aligned metal growth in specific contact pattern; (ii) half-circular shape, from free isotropic growth of metal after initial nucleation at specific nucleation point (or hole) [395]. The latter type is optically preferable because with an encapsulated wavy metal finger joint by half-sphere-shaped metal points, Blakers *et al.* calculated the effective shading to be below 36% [395]. However, plating the half-sphere-shaped metal points at the designed position requires an extremely narrow starting finger width at pointed places [395]. This increases the complexity in the control of metal plating process. Besides, such a half-circular shape geometrically sets an intrinsic constant AR value of the finger. To minimize the effective shading loss of the plated Cu finger, pioneers in Atotech [396] and Fraunhofer ISE [388] have been devoting efforts to change the isotropic growth of Cu to anisotropic feature via electrolyte tuning. Other alternative approaches are also in progress.

In this work, we employ two sub-three-electrode electrochemical cells in simultaneous bifacial Cu-plating processes. Via cyclic voltammetric study, we provide an alternative method to monitor whether the simultaneous bifacial Cu-plating process is well controlled. Besides, to reach a high effective aspect ratio of the metal finger, we fabricate a new type of hybrid-shaped Cu finger whose cross-section combines a rectangle-like bottom part and a round top part. Finally, we test the optimal bifacial plated Cu finger in silicon heterojunction solar cells at lab-scale.

D.2 Experimental

D.2.1 Cu-plating process and device fabrication

A basic Cu-plating process consisted of: (i) full area 100 nm-thick Ag seed layer growth by PVD deposition and contact pattern by photolithography on both sides of the wafer. AZ ECI3027 photoresist and TMAH-based MF322 developer were utilized in standard MEMS lithography processes. A constant resistance value of 0.1Ω was ensured at the Ag seed layer surface after PVD and before Cu-plating (measured between randomly distributed points in the contact area); (ii) cyclic voltammetry (CV) scanning or electroplating of Cu; (iii) removal of the photoresist and Ag seed layer at un-plated area. More details about the process sequence could be found elsewhere [288]. A dual-functional sample holder, which can contact the seed layer on each side of the wafer individually with 2 separated potentiostat tools, was designed for satisfying both mono-(MF) and bifacial (BF) electroplating purposes. To ensure a homogenous current distribution in the electrochemical process, a surrounding electric contact was utilized by sandwiching the wafer between two metal rings, whose outer circles match the shape of the wafer. It is worth noting that a parasitic Cu-plating on the wafer edge occurred, no matter whether the full area PVD Ag seed layer was deposited with or without the wafer edge exclusion. The wafer edge deposition is also reported by Hatt, *et al.* [397] and Gröbel, *et al.* [385]. Besides, we assume that the wafer itself and its surrounding functional layers do not participate in the Cu-plating process, for the following two reasons: (i) in an electrochemical cell, the

applied charges from the potentiostat are mainly consumed by electrochemical reactions at the Ag seed layer surface; (ii) the energy barriers between wafer and other functional layers (such as thin-film silicon layers and transparent conductive oxide layer) block the residual electron flow from the Ag seed layer to the functional layers underneath.

Figure D.1(a) depicts the basic experimental configuration of our Cu-plating processes, in which two sets of standard 3-electrode cells were utilized with reference Ag/AgCl electrodes (RE). All voltages are reported with respect to the Ag/AgCl RE. Regarding the sample geometry in CV study, we used 1 cm × 1 cm square full area contact design in the middle of the wafer substrate. In both MF and BF experiments, the wafer was double-side coated with photoresist. In MF case, only one side was opened with the above-mentioned square contact design; in BF case, both sides of the wafer were opened with the contact design. Two independent Metrohm Autolab potentiostat tools, PGSTAT101 and PGSTAT204, were utilized to separately control the two electrochemical cells on both sides of the wafer. The bifacial plating by utilizing two potentiostat tools are also reported in literature[398]. The working electrodes (WEs) were the two sides of the 100 nm-thick silver-coated pyramidally-textured 4-inch wafer, at which the electrolysis of interest took place within the contact region patterned via photolithography. We carried out the CV study and plating processes at room temperature under quiescent conditions to eliminate any forced convection in the electrolyte solution. However, prior to each experimental batch, the electrolyte solution was stirred for 10 minutes to form a uniform solution; during one experimental batch, the stirring was done for 2 minutes in the interval for loading a fresh sample substrate.

For monofacial CV scans, the back side of the wafer was fully protected with photoresist. The counter electrodes (CEs) were graphite sheets for CV scan and were sacrificing copper sheets for Cu electroplating process. The dimensions of the CEs are 10 cm × 10 cm × ~1 mm. Electrodeposition was carried out from an unstirred aqueous solution composed of an Intervia™ 8502 starter solution (50 g/L Cu²⁺, 100 g/L H₂SO₄, 50 ppm Cl⁻) and 9000E leveller (3 mL/L). The pH of the solution was lower than 1. In CV study, due to an upper current limitations of our potentiostat tools, we used 40-folded diluted solution. Although the concentration difference influences the redox potential of the cupric ions in the solution [390, 399], it is still meaningful to use the preliminary CV results from diluted solution to understand the initial electrochemical behaviours of the species, and to qualitatively study the comparative electrochemical behaviours of the redox species in MF and BF deposition processes. Besides, due to the commercial solution use, blank solution scan was omitted in our CV investigation. The CV scan started at 0 V, then progressed in a cathodic direction to -0.7 V, and then back to 0 V. The scan rate controls how fast the applied potential is scanned, and was kept at 2.5 mV/s unless otherwise specified. Before collecting the data with varied scan rates, we performed several CV scans to exclude the influence of Ag seed layer and possible contaminant at the working electrode surface. This was done until the scans overlapped. To minimize the influence from the resistive losses in the electrical connection in both 3-electrochemical cells, the external resistance beside the solution was controlled below 0.5 Ω. The electrode distances of the two sub-cells were kept equal in BF deposition processes, which is also the same with the electrode distance in MF deposition case. After each deposition, the samples were rinsed with deionized water and dried in air.

Figure D.1(b) displays the SHJ solar cell structure of our PV devices. For the device fabrication, after the above-mentioned double-side texturization of the wafers, we subsequently clean them in two baths of HNO₃ 99% (RT, 10 min) and HNO₃ 69.5% (110 °C, 10 min). Wafers were dipped in 0.55% HF for 4 min prior to the plasma enhanced chemical vapour deposition (PECVD) step. Then, the SHJ cell precursors with front 10 nm-thick *i/n* stack and rear 26 nm-thick *i/p* stack thin-film silicon layers were prepared from PECVD. Nominal 75 nm-thick ITO films were sputtered on both sides of the wafers. Hard masks were utilized in sputtering step to pattern the cell areas. A geometrical factor of 1.7 was used in the thin-film silicon layer growth and ITO sputtering on textured wafer surface, with respect to that on flat wafer. After sputtering, the wafers went through either the Cu-plating process as described above, or a lab-scale, standard low-temperature screen printing (SP) process. The cell area is defined by photolithography or SP screen as 4 cm². For each type of the solar cell, we applied the same metal design on both sides of the wafer. The solar cell images are shown in Figure E.1. For the Cu-plated solar cells, the finger pitch is 915 μm on both sides of the wafer; while for the screen-printed solar cells, the finger pitch is 1740 μm on both sides of the wafer. The growth of Cu used the optimal “2-step” electrochemical deposition, which will be introduced Section D.3.2. In the SP case, a curing condition of 170 °C for 30 min was utilized to make the metal contact. Specifically, we firstly performed the SP on the *n*-side of the wafer, dried the paste on the wafer in an oven at 170 °C for 5 minutes, then carried out the SP on the *p*-side of the wafer, and did the curing at 170 °C for 30 minutes.

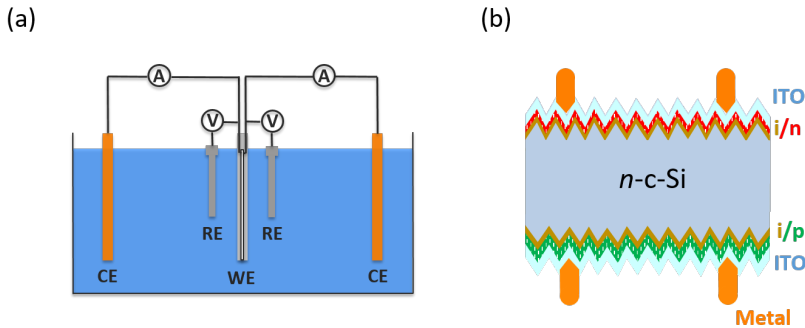


Figure D.1: (a) Schematic experimental configuration of our Cu-plating processes, in which the WE, CE, and RE represent working electrode, counter electrode, and reference electrode, respectively; and (b) the SHJ solar cell structure of our PV devices.

D.2.2 Characterizations

Finger characterizations: The finger height was measured with a Dektak 150 step-profiler. Morphological images of the metal fingers and wafer surfaces were detected with a field-emission scanning electron microscope (FE-SEM) via Hitachi Regulus 8230, and a low resolution SEM system from JEOL Ltd., respectively. The optical microscope images of the metal fingers were characterized by a confocal laser microscope (Keyence VK-X250). The resistivity of the metal fingers were obtained from 4-point probe measurements via the electrical setup as we used for current-voltage (*I-V*) measurements of solar cells.

Via a Kelvin connection, the cable resistance in the circuit loop of the measurement setup is excluded. The reported finger resistivity (ρ) data were calculated from measured finger resistance (R) values via $\rho = R \cdot S / l$, where S represents the cross-section area of the finger, and l denotes the finger length, which was kept at a constant value of 1 cm. Finger samples with different contact width values were utilized (15-50 μm for plated copper finger, and 50-100 μm for screen-printed silver finger). In addition, for the plated Cu finger, we performed the tape test to evaluate the finger adhesion [288]. It consists of placing a tape on the wafer and then pulling it. If the metal is attached to the tape, the test is considered failed, and the adhesion is considered poor; on the other hand, if the test is passed, the adhesion is considered good.

Bifacial solar cell measurements: The I - V characteristics of our 4 cm^2 SHJ devices were measured using the dedicated sample stage for the bifacial device measurements as described in Section 3.3.3. As mentioned, there is one type of special substrate which shows a reflectance of below 3.5% along the wavelength range of 700-1200 nm was utilized in the bifacial device measurements. The reflectance and transmittance curves of the mentioned substrate is provided as Figure E.2. Besides, SunsVoc measurements were performed on our complete bifacial solar cells via a Sinton Suns-Voc-150 Illumination-Voltage Tester. Note that in SunsVoc measurements, the rear side reflection from the brass chuck was not excluded.

D.3 Results and discussion

D.3.1 Cyclic voltammetric study

Figure D.2(a) shows the first two subsequent CV scans in monofacial (MF) deposition process. On the first scan, the forward scanning current starts from a near zero value, and displays a seemingly cathodic deposition peak feature at ~ -0.32 V. While on the second scan, the cathodic deposition peak features appears at ~ -0.11 V and ~ -0.27 V. This indicates that Cu becomes easier to be plated on the initially grown Cu, rather than the original PVD Ag seed layer. This observation agrees with the report from Dobson *et al.* [400], and could be treated as an overpotential deposition (OPD) of Cu on Ag. The OPD phenomenon could be explained by the lower binding energy of a Cu adatom on Ag than the Cu bulk cohesive energy [401, 402]. Figure D.2(b) shows the comparative CV scans between MF and BF deposition processes. There are two specific local deposition peak features appearing at different voltages during a forward potential scan, which could correspond to the two electron transfer steps involved in reduction of the cupric ions in the solution [403, 404]. The redox reactions are provided in Figure D2(b). One can see that, with simultaneous control on the two electrochemical cells, the cathodic current on both sides of the wafer are almost identical. Besides, with respect to the MF deposition, the cathodic current in BF deposition is smaller, and the current peaks shift to lower deposition voltage values. This manifests that although the CV features of the both side scannings in bifacial process overlap with each other, they are not equal to the case of single electrochemical cell. In other words, the BF Cu deposition rates on both sides of the wafer can be controlled at the same level, but they are not the same as that of MF deposition. It is noteworthy that our CV study only provides qualitative analysis in recognizing the difference in MF and BF deposition processes, since we utilized a diluted electrolyte solution in CV study (due to the upper current limit in our potentiostat tools). Investigations with the real electrolyte concentrations of electroactive species may

provide more detailed understanding on how the electrochemical interaction occurs in different electrochemical reactions during MF and BF depositions.

Figure D.2(c) shows the CV scans on one side of wafer in BF deposition process, with varied scan rates (ν). The data on the other side of the wafer basically overlaps with the data in Figure D.2(c), thus is not shown. One can see that, with varied ν values, the voltage that corresponds to the peak current (i_p) changes. This is a characteristic of electrochemical irreversibility feature of the Cu electrodeposition process. It means that the electron transfer at the WE is slow compared to mass transport, thus significantly more negative applied potentials than the theoretical redox potential may be required for appreciable current to flow [390, 399]. Figure D.2(d) depicts the data points of i_p versus $\nu^{1/2}$, and corresponding linear fitting line. According to the Randles-Sevcik equation for irreversible electrochemical process [405]

$$i_p = -0.496\sqrt{\alpha n'} nFAC\sqrt{\frac{nFD\nu}{RT}} \quad (D.1)$$

in which F is the Faraday constant, R is the universal gas constant, T is the temperature, A is the electrode area, C is the bulk concentration of the solution, D is the diffusion coefficient of the electroactive species, α is the transfer coefficient, n' is the number of electrons transferred before the rate determining step. For ν increasing from 2.5 mV/s to 20 mV/s, the relation i_p versus $\nu^{1/2}$ shows a linear behaviour, indicating that the redox species are freely diffusing in the solution [390, 406]. The case of 50 mV/s shows an obvious deviation from the fitted line of other data points. This might be caused by the fact that the Randles-Sevcik equation is derived from assuming the concentration of the electroactive species in the bulk is the same as that at the surface of the electrode. When ν is too high, the assumption may not be applicable and the linear formula does not hold anymore [405]. In addition, it is noteworthy that there is some noticeable cathodic deposition feature change between the curves from the same parameter setting, such as between the “BF-side 1” curve in Figure D.2(b) and the “2.5 mV/s” curve in Figure D.2(c). This is possibly caused by the WE surface condition change or the adsorption of solvent impurities on the CEs [390]. For comparison purpose, the CV curves of MF deposition process with varied scan rates are provided as Figure E.3. Basically, the MF depositions occur at more negative voltages than that in BF deposition cases, which is in accordance with the observations of Figure D.2(b). Besides, the MF deposition process also shows an irreversible characteristic. However, we would like to point out that, due to the upper current limitations of our potentiostat tools, we used diluted solution in the CV study, rather than the formal Cu-plating bath (see Experimental part). The bulk concentration change influences both the absolute redox potential and i_p values [390]. Therefore, the results from Figure D.2(c-d) only provide tentative understanding of the electrochemical plating processes. But the indications from comparative CV results could be still legitimate, which include: (i) the initial Cu growth on Ag seed layer belongs to overpotential deposition; (ii) the simultaneous deposition processes on both side of the wafer are basically identical in BF deposition, but they differ from MF deposition process; (iii) the BF deposition tends to occur at smaller voltages than MF case, and the cathodic current is smaller than in MF case.

D.3.2 Optimal bifacial Cu-plating with 2-step deposition approach

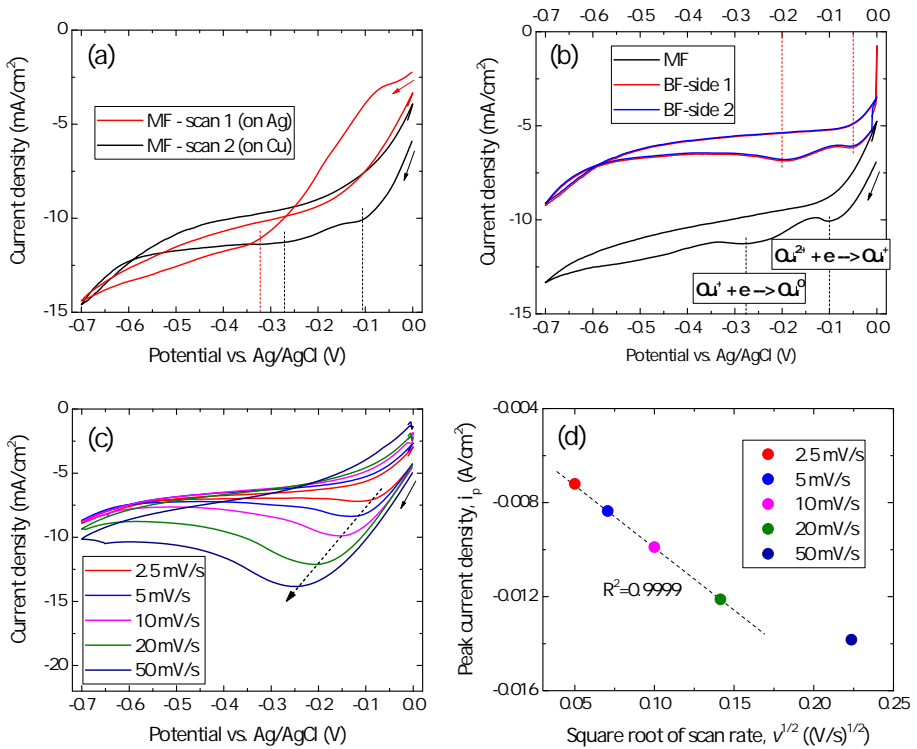


Figure D.2: (a) The first two subsequent CV scans in monofacial (MF) deposition process; (b) comparative CV scans between MF and bifacial (BF) deposition processes; (c) CV scans with varied scan rates, and (d) the cathodic peak currents (i_p) versus the square root of the scan rate ($v^{1/2}$) in bifacial deposition.

We optimized galvanostatic bifacial Cu-plating process, utilizing Cu sheets as sacrificing CE. -0.4 A and 20 min was found to be the best current-time condition to produce ~30 μm finger height (similar as that of our screen-printed Ag). However, the adhesion and uniformity of the finger height over the active area of the solar cell were found to be poor. The adhesion of plated metal on a substrate could be influenced by multi-factors, such as crystallographic coherency at the interface between plated metal and the substrate [407], nuclei germination and coalesce control in the metal growth [408, 409], and geometrical contact design [393]. As indicated by literature and the CV study results in Figure D.2(a), we performed two-step depositions. Prior to the optimal galvanostatic “1-step” process (-0.4 A, 20 min), we added either another galvanostatic process (-0.2 A, 2 min) or a potentiostatic process (-0.35 V, 2 min), namely, “2-step(I)” and “2-step(II)”, respectively. Figure D.3(a) is the photo of one solar cell on one side of the wafer, and Figure D.3(b) shows a typical finger height distribution along the middle finger as indicated in Figure D.3(a). One can see that, as compared to “1-step” case, the finger height uniformity are significantly improved with the 2-step approaches. Besides, in our adhesion test with a tape, the fingers from “1-step” deposition mode tended to easily detach off the substrate. While for the fingers deposited from “2-step” modes, no detachment was observed, i.e., the tape test

was passed. The “2-step” approaches were also reported from literature [408, 409], with the purpose of improving adhesion between Cu and the underlying foreign substrate and forming homogenous Cu growth. The rationale of the improvement could be attributed to the manipulation of the island nucleation and growth in the electrochemical deposition, which dictate the structure and properties of the plated metal [410]. However, we note that even with the “2-step” modes, the uniformity of our Cu finger height is still not ideally controlled, i.e., the finger height at the edge part of the solar cell is still 4~6 μm lower than that of the central region. This could be related to the intrinsic un-uniform current distribution between the finger and the adjacent busbar regions in plating process [393]. Further attempts to improve the homogeneity, such as applying narrower busbar or using busbar-free cell design, are under investigation.

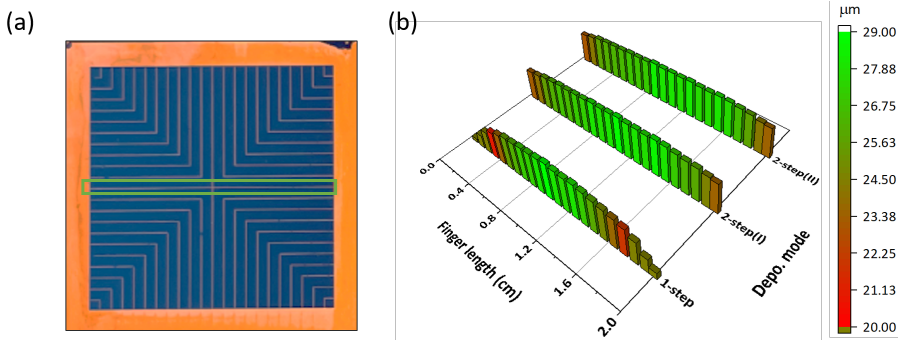


Figure D.3: (a) Image of one solar cell (active area $2 \times 2 \text{ cm}^2$) on one side of the wafer. (b) Finger height distribution along the 2 cm-long middle finger (indicated by the green rectangle in (a)) for different deposition modes.

Since galvanostatic mode is widely utilized in compact metal electrode electrodepositions, we set the “2-step(I)” as the optimal plating process. The faradaic current efficiency (CE_F) is defined as the ratio of the experimentally obtained amount of material deposited to its theoretical calculation according to Faraday’s equation. It is mathematically expressed as [411]

$$CE_F = \frac{mFz}{MI t} \quad (\text{D.2})$$

where m represents the measured mass of elements deposited at the cathode, F is Faraday’s constant (96485 C mol^{-1}), z is the valency of the ions, M is the molar mass of the substance, I is the applied current, and t expresses the deposition time. Accordingly, the CE_F of our BF plating process was calculated to be 89.4%. We note that the CE_F of MF plating process from the same plating parameter setting as in BF plating was determined to be 99.7%, indicating an ideal utilization of the applied current. This is another indication (beside Figure D2(b)) that the electrochemical process on one side of the wafer in BF deposition is not equal to single MF deposition. Additionally, the CE_F of MF plating is much higher than the current efficiency of 30% in our previously reported MF Cu-plating process [288]. The CE_F improvement could be mainly ascribed to the fresh

and optimal commercial electrolyte solution use, as well as the modification in circuit connections.

D.3.3 Morphological manipulation

Figure D.4(a-c) shows the morphological manipulation of the plated Cu finger. Figure D.4(a) illustrates the cross-section of a typical half-sphere metal finger with encapsulant or glass, in which A and B fractions could effectively reduce the shadow loss of the finger owing to downward trajectory of light path and total reflection at glass/air interface, respectively. While the fraction C could be assumed to be a lambertian emitter, where the incoming light is completely reflected out in each angle [412, 413]. According to Blakers *et al.* [395] and Woehl *et al.* [413], when a half-sphere shaped finger is covered with encapsulant, only a top portion (fraction C) in the half-circular cross-section is acting as a shadow area. The geometrical portions of the areas A, B and C are calculated in Figure E.4. Figure D.4(b-c) shows the SEM images of the cross-section of two types of hybrid fingers. We controlled the finger shape via tuning the contact pattern (mask layer) from lithography procedure. The prototype sketches of Finger D.4(b) and Finger D.4(c) are shown in Figure E.5(a) and Figure E.5(b), respectively. Each hybrid finger consists of a rectangle bottom part and a round top part, such that the novel structure could maintain the favourable optical advantage from half-circular shaped finger, meanwhile high aspect ratio (AR) could be potentially achieved. We would like to introduce an effective aspect ratio (AR_{eff}) definition for the optical evaluation of our hybrid metal fingers. The expression is as follows:

$$AR_{\text{eff}} = \frac{h_{\text{finger}}}{\max(w_{\text{top}}, w_{\text{bot.}})} \quad (\text{D.3})$$

where h_{finger} denotes the total height of the metal finger, w_{top} and $w_{\text{bot.}}$ are the calculated width of the shadow area C (i.e., $w_{\text{top}} = w_{\text{C}}$) at the top round part and the measured width of the finger at the bottom rectangular part, respectively. The $\max(w_{\text{top}}, w_{\text{bot.}})$ represents the maximum of the values of w_{top} and $w_{\text{bot.}}$. The AR_{eff} describes the ratio of the finger height and the actual shadow area width when covered with encapsulant. The AR_{eff} is $\frac{h_{\text{finger}}}{w_{\text{top}}}$ for single round shaped finger, and is $\frac{h_{\text{finger}}}{w_{\text{bot.}}}$ for single rectangular shaped finger. Provided normal incoming light is applied, the refractive index of the glass is 1.5 and the metal surface is ideally smooth and reflective, one can calculate the w_{C} to be $\sim 0.36D$ for the finger in Figure D.4(a), where D is the diameter of the half-circle (see Supporting Information, Figure E.3). Thus, the AR_{eff} of the ideally half-sphere shaped metal finger can be determined to be 1.4. For the widely utilized rectangular shaped metal finger, the AR_{eff} is equal to AR, and is generally 0.2~1 [288, 378, 387, 414–417]. For the hybrid fingers as shown in Figure D.4(b) and (c), the w_{top} values are calculated to be 34.3 μm and 15.4 μm , respectively. The corresponding measured h_{finger} values are 41 and 33 μm , and the AR_{eff} values are obtained as 1.2 and 1.1, respectively. Therefore, the AR_{eff} values of the hybrid fingers of Figure D.4(b-c) are comparable and fall in-between that of single rectangular shaped and single half-sphere shaped fingers.

However, the hybrid Cu finger in Figure D.4(c) is more optically favourable than the one in Figure D.4(b) for three reasons. First, from the finger growth mode point of view, the finger in Figure D.4(b) tends to have a large overall width (81 μm) and a greater w_{top} than $w_{\text{bot.}}$. The former leads to a large diameter (D) value of the geometrical circle,

and the latter limits the further improvement of AR_{eff} . In contrast, the hybrid finger in Figure D.4(c) could potentially reach higher AR_{eff} values due to its notably lower w_{top} than w_{bot} . Second, from the device design point of view, with respect to the finger in Figure D.4(b), the smaller overall finger width ($46\ \mu\text{m}$) in Figure D.4(c) could allow smaller finger-to-finger distance, i.e., denser finger distribution. Such that the device could be more tolerant of functional layers with high sheet resistance [418]. This can be of special importance for the emerging bifacial TCO-less/free SHJ solar cell topic in recent years [125, 170]. Third, in reality, the w_{top} could be higher than the calculated value, which is more detrimental when using the hybrid finger as shown in Figure D.4(b). The above-mentioned calculation of w_{top} is based on the assumption that the metal surface is ideally smooth and reflective. However, the actual plated metal finger can be grown into different microscopic morphologies, depending on the growth kinetics and substrate properties. In the case of Figure D.4(b), the $\max(w_{\text{top}}, w_{\text{bot}})$ is determined by w_{top} . The widening of w_{top} means decreasing AR_{eff} , thus is not desirable in the actual device utilization. All in all, with respect to the hybrid finger in Figure D.4(b), the finger growth mode in Figure D.4(c) could potentially achieve metal finger with higher AR_{eff} , resulting in both optical and electrical benefits at device level.

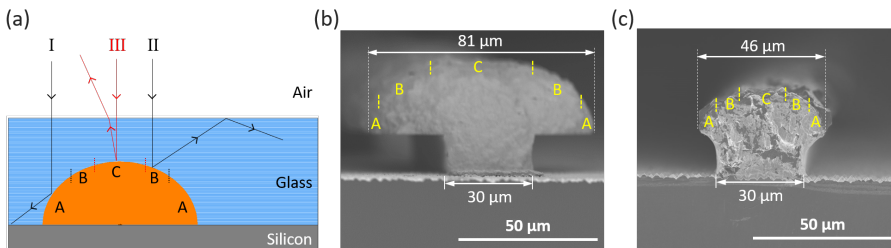


Figure D.4: (a) Schematic cross-sectional view of an encapsulated half-sphere-shaped metal finger, in which A, B, and C indicate areas with different reflection properties, after [413]. (b) and (c) SEM images of the cross section of our hybrid fingers.

D.3.4 Plated Cu and screen-printed Ag fingers, and SHJ devices (lab-scale)

Based on the favourable finger growth mode in Figure D.4(c), we further optimized the plated Cu finger with using a smaller feature of w_{bot} in the rectangular bottom part. Figure D.5(a) and Figure D.5(c) show the SEM and the optical microscope images of our optimized hybrid plated Cu finger. The AR_{eff} value is calculated to be 1.73. It is worth noting that this method of making hybrid-shaped metal fingers can also be applied to different (smaller) geometrical sizes. By properly tuning the mask design, a flexible approach to grow various expected metal contacts for high performance PV devices could be facilitated.

For comparison, the images of our lab-standard low thermal-budget SP-Ag finger are provided as Figure D.5(b) and Figure D.5(d). The AR_{eff} value of the SP-Ag finger is 0.36. Moreover, from Figure D.5(c-d), with respect to the SP-Ag case, the Cu fingers have a well-defined shape, and the plated Cu is super-conformal, void-free, and in compact contact with the wafer surface. This implies a good electrical contact between plated Cu and the underlying Ag(seed)/ITO/doped silicon film stacks. Additionally, from dedicated contact

design with different contact width and 4-point probe measurements, the estimated resistivity of our plated Cu finger is calculated to be $1.7 \pm 0.1 \mu\Omega \text{ cm}$, which is comparable to the Cu bulk material. In contrast, the resistivity of our lab-scale standard SP-Ag finger is $10.0 \pm 5.0 \mu\Omega \text{ cm}$. There are two aspects to be noted. First, as mentioned in the Experimental section, the raw finger resistivity values are calculated from the measured finger resistance and related geometrical dimensions, the latter could intrinsically bring uncertainties due to the non-standard/non-uniform geometrical shapes of the fingers. Second, the resistivity value of our screen-printed Ag finger is limited by issues such as setup, paste, curing condition in the laboratory, and cannot be representative of state-of-the-art screen-printed Ag finger as obtained in an optimized industrial environment.

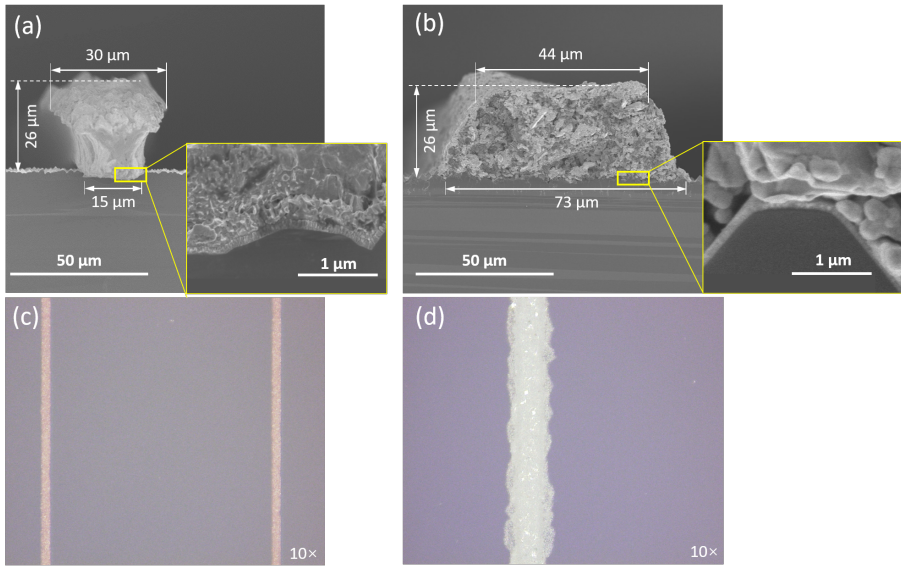


Figure D.5: (a) SEM and (c) optical microscope images of our optimal hybrid Cu finger, and (b) SEM and (d) optical microscope images of the lab-standard SP-Ag finger.

Table D.1 shows the comparative bifacial SHJ solar cell results with plated Cu and SP-Ag metallization approaches, from *n*-side illumination. The Cu-plated cell outperforms the SP cell both optically and electrically. Specifically, with respect to the cell with SP-Ag, the higher open-circuit voltage (V_{OC}) in the Cu-plated cell could be attributed to its less recombination centres at the metal and silicon interfaces. Supportive information could be found in Figure E.6, in which one can clearly see the damaged pyramid structures by metal penetration of SP-Ag into the silicon substrate. In addition, we note that the implied V_{OC} ($i-V_{OC}$) values were 740 mV of the SHJ cell precursors before metallization procedure. Surprisingly, the difference between $i-V_{OC}$ and V_{OC} was observed to be $>20 \text{ mV}$, even for the Cu-plated cells. This manifests that the quasi-Fermi level splitting of majority and minority carriers in the absorber was not effectively transferred to the external voltage [10, 311]. Detailed diagnosis remains to be performed.

Regarding the optical response, the higher short-circuit current density (J_{SC}) in Cu-

plated cells could be explained by its lower metal coverage of 1.6% than the 4.4% of the SP-Ag solar cells. In addition, it is noteworthy that the solar cells were not encapsulated, thus the measured J_{SC} is somehow compensated by counting both the fractions B and C as shadow areas, rather than only counting the fraction C as shadow portion in the top finger part (see discussion related to Figure D.4(a)). The finger shape has been reported to play an important role in the optical properties in the module [412, 413]. We believe that the optical advantage of the Cu-plated cell over the screen-printed cell is potentially higher when measured with encapsulated cells [412, 413]. As for the fill factor (FF) of the cells, with respect to the screen-printed cells, the Cu-plated SHJ cell shows a significant average FF improvement by 4.65%_{abs.}. It has been theoretically and experimentally proven that the c-Si absorber itself could provide sufficient lateral electron transport towards the metal electrodes [170, 313]. For the p -side, we calculated the diffusion length of the holes to be 1080 μm . This value is bigger than the finger gap of 915 μm in plated Cu grid, but smaller than the finger gap of 1740 μm in printed Ag grid. Therefore, the low FF in the screen-printed cell should be mainly caused by the large finger gap on the p -side of the cell. Additional factors such as finger resistance, the contact resistivity at the layer interfaces, and the selectivity of the functional layers in the cell precursors, remain to be investigated. The measured pseudo fill factor (pFF) values are $85.10\% \pm 0.36\%$ and $84.07\% \pm 0.12\%$, and the calculated series resistance ($R_{S, \text{SunsVoc}}$) values were calculated to be $0.93 \pm 0.02 \Omega \text{ cm}^2$ and $1.71 \pm 0.02 \Omega \text{ cm}^2$, for Cu-plated solar cell and SP counterpart, respectively. The overall power conversion efficiency shows an average improvement of 1.9%_{abs.}. Figure D.6 shows the corresponding comparative I - V curves and cell parameters of our champion devices, from n -side illumination. One can clearly see the optical and electrical advantages in Cu-plated cell over the screen-printed counterpart. The champion bifacial Cu-plated SHJ device shows a power conversion efficiency of 22.10% from n -side illumination. Measuring from p -side illumination, the bifaciality factor was calculated to be 0.99. In addition, it may be important to note that the data in Table D.1 and Figure D.4 are from this laboratory case study. In other words, one cannot treat the comparative data as evidence of technical outperformance of Cu-plating technique over screen-printing technique. Besides, the issues we have in our lab-scale, standard, screen-printed solar cells may not exist at an industrial level. Thus, the purpose of the above analysis only lies in gaining insights about the cause of the observed difference in our solar cell performance.

Table D.1: Solar cell parameters of 4 cm^2 SHJ devices with plated Cu and SP-Ag metallization approaches. The cell precursors were fabricated from one batch. The designed metal coverage values are 1.6% and 4.4%, respectively. The reported values are the average based on three cells illuminated from the n -side. The standard deviation is calculated for each external parameter.

Metal	Open-circuit voltage [V_{OC} , mV]	Short-circuit current density [J_{SC} , mA/cm^2]	Fill factor [FF , %]	Efficiency [η , %]
Plated Cu	716 ± 1.5	38.07 ± 0.04	80.76 ± 0.04	22.02 ± 0.06
SP-Ag	710 ± 3.5	37.24 ± 0.02	76.11 ± 0.07	20.12 ± 0.10

D.4 Conclusions

In summary, via cyclic voltammetry approach, we studied the electrochemical behaviors on both sides of the wafer in the one-step simultaneous Cu-plating process, based on

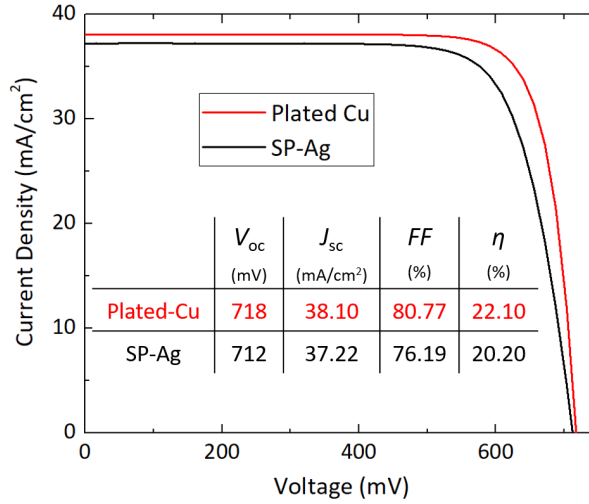


Figure D.6: Champion bifacial SHJ solar cell results with plated Cu and SP-Ag metallization approaches, illuminated from the n -side. The cell area is 4 cm^2 , and the designed metal coverage values are 1.6% and 4.4%, respectively.

which the evaluation on the double-side plating control can be made. The results show that the the initial Cu growth on Ag seed layer is an overpotential deposition. With a 2-step deposition approach, we improved finger adhesion and achieved relatively uniformly distributed Cu fingers. With appropriate morphological manipulation on the plated Cu finger, we fabricated a new type of hybrid-shaped Cu finger, which consists of a rectangular bottom part and a round top part with an utmost effective aspect ratio value of 1.73. Finally, with respect to our lab-scale, standard, low-temperature screen-printed silicon heterojunction solar cells, the Cu-plated devices showed both optical and electrical advantages. The champion bifacial Cu-plated device shows a power conversion efficiency of 22.1% from front side (i/n) illumination, and a bifaciality factor of 0.99.

E

Controllable bifacial Cu-plating for c-Si solar cells (II)

This appendix provides supporting information of Appendix D, which was included in the publication of *Solar RRL** [371]

E.1. Bifacial SHJ solar cell images from front side (*i/n*)

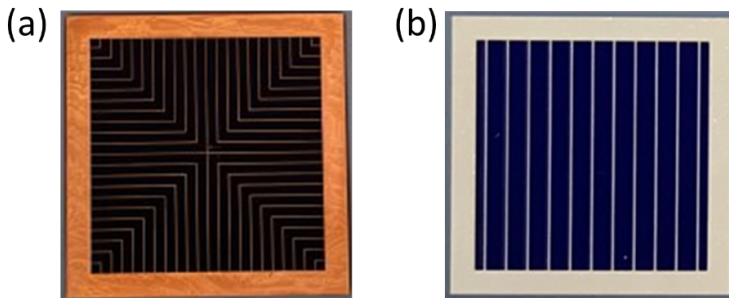


Figure E.1: Images of the front sides (*i/n*) of our (a) Cu-plated and (b) screen-printed SHJ solar cells. For each type of solar cell, the rear side (*i/p*) is using the same metal grid as that applied on the front side.

*C. Han, G. Yang, P. Procel, D. O'Connor, Y. Zhao, A. Gopalakrishnan, X. Zhang, M. Zeman, L. Mazzarella, and O. Isabella, "Controllable simultaneous bifacial Cu-plating for high efficiency crystalline silicon solar cells," *Solar RRL*, 2100810, 2022. February 12, 2022, doi:10.1002/solr.202100810.

E.2. Reflectance and transmittance curves of the substrate that was used in bifacial solar cell measurements

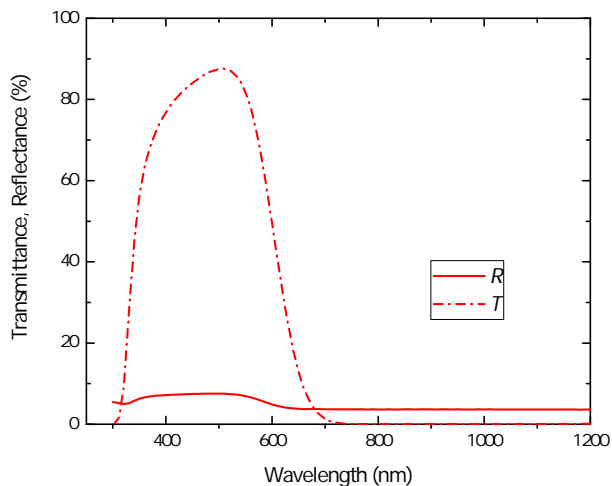


Figure E.2: Reflectance (R) and transmittance (T) curves of the substrate that was used in bifacial solar cell measurements.

E.3. CV scans with varied scan rates in monofacial deposition process

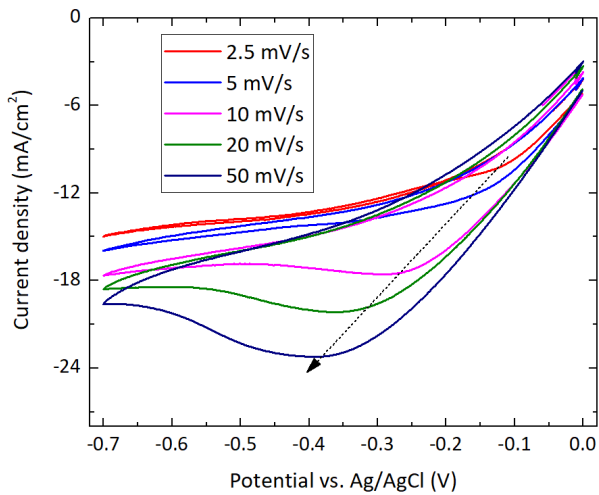
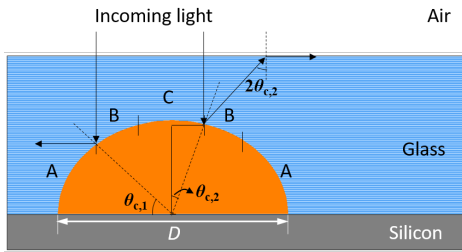


Figure E.3: CV scans with varied scan rates in monofacial deposition process.

E.4. Geometrical calculations of areas A, B, and C



Area A: Downward trajectory of light

Critical angle $\theta_{c,1}$:

$$\tan \theta_{c,1} = 1, \text{ thus } \theta_{c,1} = 45^\circ$$

Area B: Total internal reflection

Critical angle $\theta_{c,2}$:

$$n_{\text{Air}} \cdot \sin 90^\circ = n_{\text{Glass}} \cdot \sin 2\theta_{c,2},$$

$$\text{thus, } \theta_{c,2} = 20.9^\circ$$

Area C: Reflection loss (shadow area)

Width of area C w_c :

$$w_c = 2 \times (0.5D \times \sin \theta_{c,2}) = 0.36 D$$

Figure E.4: Geometrical calculations of areas A, B, and C.

E

E.5. Prototype sketches of two types of hybrid-shaped fingers

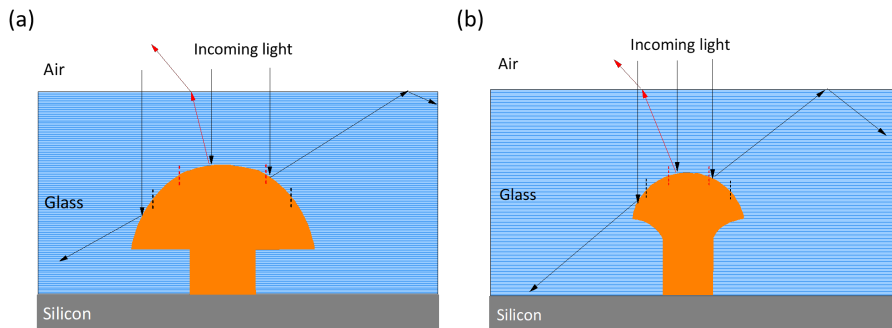


Figure E.5: Prototype sketches of two types of hybrid-shaped fingers.

E.6. SEM images of the silicon surface after SP-Ag and ITO removal

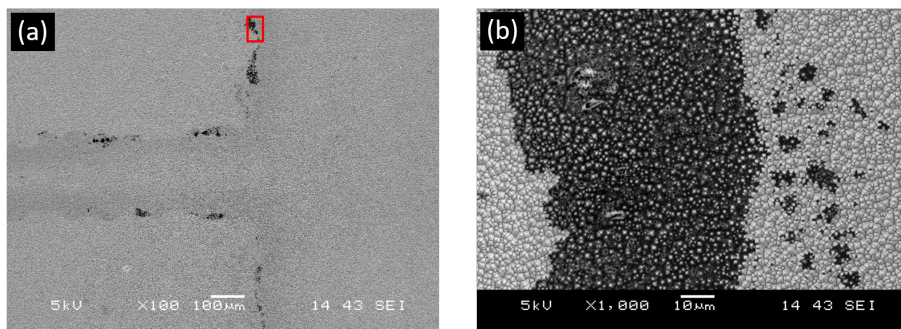


Figure E.6: SEM images of the silicon surface after SP-Ag and ITO removal, at magnifications of (a) 100×, and (b) 1000× at the labelled area in (a).

References

- [1] A. H. Smets, K. Jäger, O. Isabella, R. A. Swaaij, and M. Zeman, *Solar Energy: The physics and engineering of photovoltaic conversion, technologies and systems* (UIT Cambridge, 2015).
- [2] IEA, *Key World Energy Statistics 2020*, Report (International Energy Agency, 2020).
- [3] bp Energy Outlook, <https://www.bp.com/en/global/corporate/energy-economics/energy-outlook/introduction/overview.html> (2020).
- [4] O. Sarmad, *2020 a "critical year for addressing climate change"*, (2020).
- [5] C. Kamaraki, M. T. Klug, T. Green, L. Miranda Perez, and C. Case, *Perovskite/silicon tandem photovoltaics: Technological disruption without business disruption*, Applied Physics Letters **119**, 070501 (2021).
- [6] J. Goldemberg, *World energy assessment (2000): Energy and the challenge of sustainability*, United Nations Development Programme (2001), online report.
- [7] VDMA, *International Technology Roadmap for Photovoltaic (ITRPV) - 12 Edition*, Report (VDMA, 2021).
- [8] M. Victoria, N. Haegel, I. M. Peters, R. Sinton, A. Jäger-Waldau, C. del Cañizo, C. Breyer, M. Stocks, A. Blakers, I. Kaizuka, K. Komoto, and A. Smets, *Solar photovoltaics is ready to power a sustainable future*, Joule **5**, 1041 (2021).
- [9] A. Richter, R. Müller, J. Benick, F. Feldmann, B. Steinhauser, C. Reichel, A. Fell, M. Bivour, M. Hermle, and S. W. Glunz, *Design rules for high-efficiency both-sides-contacted silicon solar cells with balanced charge carrier transport and recombination losses*, Nature Energy **6**, 429 (2021).
- [10] M. Hermle, F. Feldmann, M. Bivour, J. C. Goldschmidt, and S. W. Glunz, *Passivating contacts and tandem concepts: Approaches for the highest silicon-based solar cell efficiencies*, Applied Physics Reviews **7**, 021305 (2020).
- [11] K. Yoshikawa, W. Yoshida, T. Irie, H. Kawasaki, K. Konishi, H. Ishibashi, T. Asatani, D. Adachi, M. Kanematsu, H. Uzu, and K. Yamamoto, *Exceeding conversion efficiency of 26% by heterojunction interdigitated back contact solar cell with thin film si technology*, Solar Energy Materials and Solar Cells **173**, 37 (2017).
- [12] S. De Wolf, A. Descoedres, Z. C. Holman, and C. Ballif, *High-efficiency silicon heterojunction solar cells: A review*, green **2**, 7 (2012).

- [13] J. Haschke, J. P. Seif, Y. Riesen, A. Tomasi, J. Cattin, L. Tous, P. Choulat, M. Aleman, E. Cornagliotti, A. Uruena, R. Russell, F. Duerinckx, J. Champliand, J. Levrat, A. A. Abdallah, B. Aïssa, N. Tabet, N. Wyrsh, M. Despeisse, J. Szlufcik, S. De Wolf, and C. Ballif, *The impact of silicon solar cell architecture and cell interconnection on energy yield in hot & sunny climates*, Energy & Environmental Science **10**, 1196 (2017).
- [14] A. Danel, *Bifaciality optimization of silicon heterojunction solar cells*, in *36th European Photovoltaic Solar Energy Conference and Exhibition* (2019) pp. 224–228.
- [15] A. Danel, S. Harrison, F. Gerenton, A. Moustafa, R. Varache, J. Veirman, and C. Roux, *Silicon heterojunction solar cells with open-circuit-voltage above 750 mv*, in *Proc. 35th European Photovoltaic Solar Energy Conference and Exhibition* (2018) pp. 444–447.
- [16] E. Sandra, *Trina solar achieves 25.5% efficiency in n-type topcon solar cell*, (2022), web report.
- [17] A. Bhambhani, *Heterojunction cell efficiency jumps to 26.30% within a week*, (2021), web report.
- [18] Z. Yang, J. Yan, W. Yang, Y. Zeng, J. Sun, X. Wang, X. Yang, J. C. Greer, J. Sheng, B. Yan, and J. Ye, *Back-contact structures for optoelectronic devices: Applications and perspectives*, Nano Energy **78**, 105362 (2020).
- [19] A. Polman, M. Knight, E. C. Garnett, B. Ehrler, and W. C. Sinke, *Photovoltaic materials: Present efficiencies and future challenges*, Science **352**, aad4424 (2016).
- [20] A. D. Vos, *Detailed balance limit of the efficiency of tandem solar cells*, Journal of Physics D: Applied Physics **13**, 839 (1980).
- [21] A. Richter, M. Hermle, and S. W. Glunz, *Reassessment of the limiting efficiency for crystalline silicon solar cells*, IEEE Journal of Photovoltaics **3**, 1184 (2013).
- [22] S. Bhattacharya and S. John, *Beyond 30% conversion efficiency in silicon solar cells: A numerical demonstration*, Sci Rep **9**, 12482 (2019).
- [23] M. L. Hsieh, A. Kaiser, S. Bhattacharya, S. John, and S. Y. Lin, *Experimental demonstration of broadband solar absorption beyond the lambertian limit in certain thin silicon photonic crystals*, Sci Rep **10**, 11857 (2020).
- [24] R. Peibst, *Still in the game*, Nature Energy **6**, 333 (2021).
- [25] E. Köhnen, *Tandem cells approaching 30% efficiency*, <https://www.pv-magazine.com/2020/01/30/tandems-cells-approaching-30-efficiency/> (2021), web report.
- [26] J. Benick, B. Hoex, M. C. M. van de Sanden, W. M. M. Kessels, O. Schultz, and S. W. Glunz, *High efficiency n-type si solar cells on Al₂O₃-passivated boron emitters*, Applied Physics Letters **92**, 253504 (2008).

- [27] D. Herrmann, D. R. C. Falconi, S. Lohmüller, D. Ourinson, A. Fell, H. Höffler, A. A. Brand, and A. Wolf, *Spatially resolved determination of metallization-induced recombination losses using photoluminescence imaging*, IEEE Journal of Photovoltaics **11**, 174 (2021).
- [28] W. Shockley and H. J. Queisser, *Detailed balance limit of efficiency of p-n junction solar cells*, Journal of Applied Physics **32**, 510 (1961).
- [29] S.-S. Wang, J.-J. Ho, J.-J. Liou, J.-S. Ho, S.-Y. Tsai, H.-S. Hung, C.-H. Yeh, and K. L. Wang, *Effects of sheet resistance on mc-Si selective emitter solar cells using laser opening and one-step diffusion*, International Journal of Photoenergy **2015**, 208270 (2015).
- [30] R. Peibst, *Implementation of n^+ and p^+ poly junctions on front and rear side of double-side contacted industrial silicon solar cells*, Proc. 32nd Eur. Photovolt. Sol. Energy Conf. , 323–327 (2016).
- [31] S. Reiter, N. Koper, R. Reineke-Koch, Y. Larionova, M. Turcu, J. Krügener, D. Tetzlaff, T. Wietler, U. Höhne, J.-D. Kähler, R. Brendel, and R. Peibst, *Parasitic absorption in polycrystalline si-layers for carrier-selective front junctions*, Energy Procedia **92**, 199 (2016).
- [32] X. Yu, T. J. Marks, and A. Facchetti, *Metal oxides for optoelectronic applications*, Nature materials **15**, 383 (2016).
- [33] M. Morales-Masis, S. De Wolf, R. Woods-Robinson, J. W. Ager, and C. Ballif, *Transparent electrodes for efficient optoelectronics*, Advanced Electronic Materials **3**, 1600529 (2017).
- [34] K. Ellmer, *Past achievements and future challenges in the development of optically transparent electrodes*, Nature Photonics **6**, 809 (2012).
- [35] K. L. Chopra, S. Major, and D. K. Pandya, *Transparent conductors—a status review*, Thin Solid Films **102**, 1 (1983).
- [36] R. Bel Hadj Tahar, T. Ban, Y. Ohya, and Y. Takahashi, *Tin doped indium oxide thin films: Electrical properties*, Journal of Applied Physics **83**, 2631 (1998).
- [37] J. E. Medvedeva, *Combining optical transparency with electrical conductivity: Challenges and prospects*, Transparent Electronics , 1 (2010).
- [38] D. C. Look and B. Claflin, *P-type doping and devices based on ZnO*, physica status solidi (b) **241**, 624 (2004).
- [39] O. Bierwagen and J. S. Speck, *Mg acceptor doping of In_2O_3 and overcompensation by oxygen vacancies*, Applied Physics Letters **101**, 102107 (2012).
- [40] J. Zhang, J. Shi, D.-C. Qi, L. Chen, and K. H. L. Zhang, *Recent progress on the electronic structure, defect, and doping properties of Ga_2O_3* , APL Materials **8**, 020906 (2020).

- [41] K. Bädeker, *Über die elektrische leitfähigkeit und die thermoelektrische kraft einiger schwermetallverbindungen*, *Annalen der Physik* **327**, 749 (1907).
- [42] X. Li, Y. Yan, A. Mason, T. Gessert, and T. Coutts, *High mobility cdo films and their dependence on structure*, *Electrochemical and Solid State Letters* **4**, C66 (2001).
- [43] E. Fortunato, D. Ginley, H. Hosono, and D. C. Paine, *Transparent conducting oxides for photovoltaics*, *MRS Bulletin* **32**, 242 (2011).
- [44] Y. Furubayashi, T. Hitosugi, Y. Yamamoto, K. Inaba, G. Kinoda, Y. Hirose, T. Shimada, and T. Hasegawa, *A transparent metal: Nb-doped anatase TiO₂*, *Applied Physics Letters* **86**, 252101 (2005).
- [45] W. Chen, Y. Wu, Y. Yue, J. Liu, W. Zhang, X. Yang, H. Chen, E. Bi, I. Ashraful, M. Grätzel, and L. Han, *Efficient and stable large-area perovskite solar cells with inorganic charge extraction layers*, *Science* **350**, 944 (2015).
- [46] Z. Galazka, K. Irmscher, M. Pietsch, T. Schulz, R. Uecker, D. Klimm, and R. Fornari, *Effect of heat treatment on properties of melt-grown bulk In₂O₃ single crystals*, *Crys-tEngComm* **15**, 2220 (2013).
- [47] R. Groth, *Untersuchungen an halbleitenden indiumoxydschichten*, *physica status solidi (b)* **14**, 69 (1966).
- [48] A. Wibowo Setia Budhi, *Hydrogenated Indium Oxide (IO: H) TCO for Thin Film Solar Cell*, master, Delft University of Technology (2016).
- [49] E. Kobayashi, Y. Watabe, T. Yamamoto, and Y. Yamada, *Cerium oxide and hydrogen co-doped indium oxide films for high-efficiency silicon heterojunction solar cells*, *Solar Energy Materials and Solar Cells* **149**, 75 (2016).
- [50] K. Persson, *Materials data on In₂O₃ (sg:206) by materials project*, (2014).
- [51] P. Reunchan, X. Zhou, S. Limpijumnong, A. Janotti, and C. G. Van de Walle, *Vacancy defects in indium oxide: An ab-initio study*, *Current Applied Physics* **11**, S296 (2011).
- [52] S. C. Dixon, D. O. Scanlon, C. J. Carmalt, and I. P. Parkin, *n-type doped transparent conducting binary oxides: an overview*, *Journal of Materials Chemistry C* **4**, 6946 (2016).
- [53] S. Kasap and P. Capper, *Transparent conductive oxides*, in *Handbook of electronic and photonic materials (2nd Edition)* (Springer, Switzerland, 2017) pp. 1391–1395.
- [54] H. Köstlin, R. Jost, and W. Lems, *Optical and electrical properties of doped In₂O₃ films*, *physica status solidi (a)* **29**, 87 (1975).
- [55] E. Burstein, *Anomalous optical absorption limit in insb*, *Physical Review* **93**, 632 (1954).
- [56] N. F. Mott, *Review lecture: Metal–insulator transitions*, *Proceedings of the Royal Society of London. A. Mathematical and Physical Sciences* **382**, 1 (1982).

- [57] P. P. Edwards and M. J. Sienko, *Universality aspects of the metal-nonmetal transition in condensed media*, Physical Review B **17**, 2575 (1978).
- [58] N. Preissler, O. Bierwagen, A. T. Ramu, and J. S. Speck, *Electrical transport, electrothermal transport, and effective electron mass in single-crystalline In_2O_3 films*, Physical Review B **88**, 085305 (2013).
- [59] A. Klein, C. Korber, A. Wachau, F. Sauberlich, Y. Gassenbauer, S. P. Harvey, D. E. Profit, and T. O. Mason, *Transparent conducting oxides for photovoltaics: Manipulation of fermi level, work function and energy band alignment*, Materials **3**, 4892 (2010).
- [60] B. Macco, H. C. M. Knoop, and W. M. M. Kessels, *Electron scattering and doping mechanisms in solid-phase-crystallized $\text{In}_2\text{O}_3\text{:H}$ prepared by atomic layer deposition*, ACS Applied Materials & Interfaces **7**, 16723 (2015).
- [61] C. Han, G. Yang, A. Montes, P. Procel, L. Mazzarella, Y. Zhao, S. Eijt, H. Schut, X. Zhang, M. Zeman, and O. Isabella, *Realizing the potential of RF-sputtered hydrogenated fluorine-doped indium oxide as an electrode material for ultrathin SiO_x /poly-Si passivating contacts*, ACS Applied Energy Materials **3**, 8606 (2020).
- [62] T. Pisarkiewicz, K. Zakrzewska, and E. Leja, *Scattering of charge carriers in transparent and conducting thin oxide films with a non-parabolic conduction band*, Thin Solid Films **174**, 217 (1989).
- [63] S. Limpijumnong, P. Reunchan, A. Janotti, and C. G. Van de Walle, *Hydrogen doping in indium oxide: An ab initio study*, Physical Review B **80**, 193202 (2009).
- [64] I. Makkonen, E. Korhonen, V. Prozheeva, and F. Tuomisto, *Identification of vacancy defect complexes in transparent semiconducting oxides ZnO , In_2O_3 and SnO_2* , J Phys Condens Matter **28**, 224002 (2016).
- [65] E. Korhonen, F. Tuomisto, O. Bierwagen, J. S. Speck, and Z. Galazka, *Compensating vacancy defects in Sn- and Mg-doped In_2O_3* , Physical Review B **90**, 245307 (2014).
- [66] K. Ellmer, A. Klein, and B. Rech, *Transparent conductive zinc oxide: basics and applications in thin film solar cells*, Vol. 104 (Springer Science & Business Media, 2007) pp. 59–66, 187–194.
- [67] D. Zhang and H. Ma, *Scattering mechanisms of charge carriers in transparent conducting oxide films*, Applied physics A **62**, 487 (1996).
- [68] G. K. Deyu, J. Hunka, H. Roussel, J. Brötz, D. Bellet, and A. Klein, *Electrical properties of low-temperature processed Sn-doped In_2O_3 thin films: The role of microstructure and oxygen content and the potential of defect modulation doping*, Materials (Basel, Switzerland) **12**, 2232 (2019).
- [69] V. A. Johnson and K. Lark-Horovitz, *Transition from classical to quantum statistics in germanium semiconductors at low temperature*, Physical Review **71**, 374 (1947).

- [70] A. Abdolazadeh Ziabari and S. M. Rozati, *Carrier transport and bandgap shift in n-type degenerate ZnO thin films: The effect of band edge nonparabolicity*, Physica B: Condensed Matter **407**, 4512 (2012).
- [71] K. G. Saw, N. M. Aznan, F. K. Yam, S. S. Ng, and S. Y. Pung, *New insights on the burstein-moss shift and band gap narrowing in indium-doped zinc oxide thin films*, PLoS One **10**, 0141180 (2015).
- [72] L. Gupta, A. Mansingh, and P. K. Srivastava, *Band gap narrowing and the band structure of tin-doped indium oxide films*, Thin Solid Films **176**, 33 (1989).
- [73] I. Hamberg, C. G. Granqvist, K. F. Berggren, B. E. Sernelius, and L. Engström, *Band-gap widening in heavily Sn-doped In_2O_3* , Physical Review B **30**, 3240 (1984).
- [74] A. Walsh, J. L. F. Da Silva, and S.-H. Wei, *Origins of band-gap renormalization in degenerately doped semiconductors*, Physical Review B **78**, 075211 (2008).
- [75] A. Aliano, A. Catellani, and G. Cicero, *Characterization of amorphous In_2O_3 : An ab initio molecular dynamics study*, Applied Physics Letters **99**, 211913 (2011).
- [76] F. H. Wardenga, V. M. Frischbier, M. Morales-Masis, and A. Klein, *In situ hall effect monitoring of vacuum annealing of $In_2O_3:H$ thin films*, Materials **8**, 561 (2015).
- [77] J. Rosen and O. Warschkow, *Electronic structure of amorphous indium oxide transparent conductors*, Physical Review B **80**, 115215 (2009).
- [78] K. Nomura, H. Ohta, A. Takagi, T. Kamiya, M. Hirano, and H. Hosono, *Room-temperature fabrication of transparent flexible thin-film transistors using amorphous oxide semiconductors*, Nature **432**, 488 (2004).
- [79] S. Arooj, T. Xu, X. Hou, Y. Wang, J. Tong, R. Chu, and B. Liu, *Green emission of indium oxide via hydrogen treatment*, RSC Advances **8**, 11828 (2018).
- [80] A. Walsh, J. L. Da Silva, S. H. Wei, C. Korber, A. Klein, L. F. Piper, A. DeMasi, K. E. Smith, G. Panaccione, P. Torelli, D. J. Payne, A. Bourlange, and R. G. Egdell, *Nature of the band gap of In_2O_3 revealed by first-principles calculations and x-ray spectroscopy*, Phys Rev Lett **100**, 167402 (2008).
- [81] H. C. M. Knoops, B. W. H. van de Loo, S. Smit, M. V. Ponomarev, J.-W. Weber, K. Sharma, W. M. M. Kessels, and M. Creatore, *Optical modeling of plasma-deposited ZnO films: Electron scattering at different length scales*, Journal of Vacuum Science & Technology A: Vacuum, Surfaces, and Films **33**, 021509 (2015).
- [82] Z. C. Holman, M. Filipič, A. Descoedres, S. De Wolf, F. Smole, M. Topič, and C. Ballif, *Infrared light management in high-efficiency silicon heterojunction and rear-passivated solar cells*, Journal of Applied Physics **113**, 013107 (2013).
- [83] R. E. Hummel and K. H. Guenther, *Handbook of optical properties: thin films for optical coatings*, Vol. 1 (CRC Press, 1995).

- [84] M. I. Hossain, A. Hongsingthong, W. Qarony, P. Sichanugrist, M. Konagai, A. Salleo, D. Knipp, and Y. H. Tsang, *Optics of perovskite solar cell front contacts*, ACS Appl Mater Interfaces **11**, 14693 (2019).
- [85] S. H. Brewer and S. Franzen, *Indium tin oxide plasma frequency dependence on sheet resistance and surface adlayers determined by reflectance ftr spectroscopy*, The Journal of Physical Chemistry B **106**, 12986 (2002).
- [86] G. Rupprecht, *Untersuchungen der elektrischen und lichtelektrischen leitfähigkeit dünner indiumoxydschichten*, Zeitschrift für Physik **139**, 504 (1954).
- [87] A. Cruz, F. Ruske, A. Eljarrat, P. P. Michalowski, A. B. Morales-Vilches, S. Neubert, E. Wang, C. T. Koch, B. Szyszka, R. Schlatmann, and B. Stannowski, *Influence of silicon layers on the growth of ITO and AZO in silicon heterojunction solar cells*, IEEE Journal of Photovoltaics **10**, 703 (2020).
- [88] L. Tutsch, H. Sai, T. Matsui, M. Bivour, M. Hermle, and T. Koida, *The sputter deposition of broadband transparent and highly conductive cerium and hydrogen co-doped indium oxide and its transfer to silicon heterojunction solar cells*, Progress in Photovoltaics: Research and Applications **29**, 835 (2021).
- [89] D. Erfurt, T. Koida, M. D. Heinemann, C. Li, T. Bertram, J. Nishinaga, B. Szyszka, H. Shibata, R. Klenk, and R. Schlatmann, *Impact of rough substrates on hydrogen-doped indium oxides for the application in CIGS devices*, Solar Energy Materials and Solar Cells **206**, 110300 (2020).
- [90] W. R. Grove, *On the electro-chemical polarity of gases*, Philosophical Transactions of the Royal Society of London , 87 (1852).
- [91] P. Michel, *Coating by cathode disintegration*, (1939).
- [92] J. S. Chapin, *The planar magnetron*, Research Development **25**, 37 (1974).
- [93] G. J. Exarhos and X.-D. Zhou, *Discovery-based design of transparent conducting oxide films*, Thin solid films **515**, 7025 (2007).
- [94] D. Depla, S. Mahieu, and J. Greene, *Sputter deposition processes*, in *Handbook of deposition technologies for films and coatings* (Elsevier, 2010) pp. 253–296.
- [95] T. Welzel and K. Ellmer, *Comparison of ion energies and fluxes at the substrate during magnetron sputtering of ZnO:Al for dc and rf discharges*, Journal of Physics D: Applied Physics **46**, 315202 (2013).
- [96] M. Huang, Z. Hameiri, A. G. Aberle, and T. Mueller, *Comparative study of amorphous indium tin oxide prepared by pulsed-DC and unbalanced RF magnetron sputtering at low power and low temperature conditions for heterojunction silicon wafer solar cell applications*, Vacuum **119**, 68 (2015).
- [97] D. Yan, A. Cuevas, S. P. Phang, Y. Wan, and D. Macdonald, *23% efficient p-type crystalline silicon solar cells with hole-selective passivating contacts based on physical vapor deposition of doped silicon films*, Applied Physics Letters **113**, 061603 (2018).

- [98] S. Chunduri, *High efficiency solar technologies: from PERC, HJT to TOPCon and IBC*, (2020), TaiyangNews, webinar report.
- [99] A. Cuevas, D. Yan, S. Phang, Y. Wan, and D. Macdonald, *Silicon solar cells by "DESIJN" (deposited silicon junctions)*, (2018).
- [100] A. Tabata, J. Nakano, T. Misutani, and K. Fukaya, *Preparation of B-doped microrystalline silicon thin films by RF magnetron sputtering*, in *IEEE 4th World Conference on Photovoltaic Energy Conference*, Vol. 2 (2006) pp. 1639–1641.
- [101] J. Hoß, J. Baumann, M. Berendt, U. Graupner, R. Köhler, J. Lossen, M. Thumsch, and E. Schneiderlöchner, *Sputtering of silicon thin films for passivated contacts*, (2019).
- [102] S. Choi, O. Kwon, K. H. Min, M. S. Jeong, K. T. Jeong, M. G. Kang, S. Park, K. K. Hong, H.-e. Song, and K.-H. Kim, *Formation and suppression of hydrogen blisters in tunnelling oxide passivating contact for crystalline silicon solar cells*, *Scientific Reports* **10**, 1 (2020).
- [103] I. Hamberg and C. G. Granqvist, *Evaporated Sn-doped In_2O_3 films: Basic optical properties and applications to energy-efficient windows*, *Journal of Applied Physics* **60**, R123 (1986).
- [104] Y. Smirnov, L. Schmengler, R. Kuik, P.-A. Repecaud, M. Najafi, D. Zhang, M. Theelen, E. Aydin, S. Veenstra, S. De Wolf, and M. Morales-Masis, *Scalable pulsed laser deposition of transparent rear electrode for perovskite solar cells*, *Advanced Materials Technologies* **6**, 2000856 (2021).
- [105] Y. Smirnov, P.-A. Repecaud, L. Tutsch, I. Florea, K. P. Zanoni, A. Paliwal, H. J. Bolink, P. R. i Cabarrocas, M. Bivour, and M. Morales-Masis, *Wafer-scale pulsed laser deposition of ito for solar cells: reduced damage vs. interfacial resistance*, *Materials Advances* (2022).
- [106] K. Iwata, T. Sakemi, A. Yamada, P. Fons, K. Awai, T. Yamamoto, M. Matsubara, H. Tampo, K. Sakurai, S. Ishizuka, and S. Niki, *Doping properties of ZnO thin films for photovoltaic devices grown by URT-IP (ion plating) method*, *Thin Solid Films* **451-452**, 219 (2004).
- [107] J. G. Kim, J. E. Lee, S. M. Jo, B. D. Chin, J. Y. Baek, K. J. Ahn, S. J. Kang, and H. K. Kim, *Room temperature processed high mobility W-doped In_2O_3 electrodes coated via in-line arc plasma ion plating for flexible oleds and quantum dots leds*, *Sci Rep* **8**, 12019 (2018).
- [108] Y. Shigesato, S. Takaki, and T. Haranoh, *Electrical and structural properties of low resistivity tin-doped indium oxide films*, *Journal of Applied Physics* **71**, 3356 (1992).
- [109] P. Nath and R. F. Bunshah, *Preparation of In_2O_3 and tin-doped In_2O_3 films by a novel activated reactive evaporation technique*, *Thin Solid Films* **69**, 63 (1980).

- [110] Z. Li, K. Tong, R. Shi, Y. Shen, Y. Zhang, Z. Yao, J. Fan, M. Thwaites, and G. Shao, *Reactive plasma deposition of high quality single phase CuO thin films suitable for metal oxide solar cells*, Journal of Alloys and Compounds **695**, 3116 (2017).
- [111] L. Davis, *Properties of transparent conducting oxides deposited at room temperature*, Thin Solid Films **236**, 1 (1993).
- [112] J. Yu, J. Bian, L. Jiang, Y. Qiu, W. Duan, F. Meng, and Z. Liu, *Tungsten-doped indium oxide thin film as an effective high-temperature copper diffusion barrier*, ECS Solid State Letters **3**, N15 (2014).
- [113] Z. Lu, F. Meng, Y. Cui, J. Shi, Z. Feng, and Z. Liu, *High quality of iwo films prepared at room temperature by reactive plasma deposition for photovoltaic devices*, Journal of Physics D: Applied Physics **46**, 075103 (2013).
- [114] K. Iwata, T. Sakemi, A. Yamada, P. Fons, K. Awai, T. Yamamoto, S. Shirakata, K. Matsumbara, H. Tampo, K. Sakurai, S. Ishizuka, and S. Niki, *Improvement of ZnO TCO film growth for photovoltaic devices by reactive plasma deposition (rpd)*, Thin Solid Films **480-481**, 199 (2005).
- [115] S. K. Chunduri and M. Schmela, *Heterojunction Solar Technology*, Report (TaiyangNews, 2020).
- [116] T. Kamioka, Y. Isogai, Y. Hayashi, Y. Ohshita, and A. Ogura, *Effects of damages induced by indium-tin-oxide reactive plasma deposition on minority carrier lifetime in silicon crystal*, AIP Advances **9**, 105219 (2019).
- [117] K. Onishi, Y. Hara, T. Nishihara, H. Kanai, T. Kamioka, Y. Ohshita, and A. Ogura, *Evaluation of plasma induced defects on silicon substrate by solar cell fabrication process*, Japanese Journal of Applied Physics **59**, 071003 (2020).
- [118] J. Bartsch, U. Heitmann, L. Jakob, R. Mahmoud Algazzar, L. Tutsch, R. Hermann, S. Kluska, M. Bivour, B. Bläsi, H. Hauser, S. Janz, and M. Glatthaar, *Spray pyrolysis, spray coating, dielectric layer, tandem solar cells*, (2020).
- [119] G. G. Untila, T. N. Kost, and A. B. Chebotareva, *F-In-codoped ZnO (FIZO) films produced by corona-discharge-assisted ultrasonic spray pyrolysis and hydrogenation as electron-selective contacts in FIZO/SiO_x/p-Si heterojunction crystalline silicon solar cells with 10.5% efficiency*, Solar Energy **181**, 148 (2019).
- [120] G. G. Untila, T. N. Kost, A. B. Chebotareva, M. B. Zaks, A. M. Sitnikov, and O. I. Solodukha, *Effect of conditions of deposition and annealing of indium oxide films doped with fluorine (IFO) on the photovoltaic properties of the IFO/p-Si heterojunction*, Semiconductors **42**, 406 (2008).
- [121] J. Yu, J. Zhou, J. Bian, L. Zhang, Y. Liu, J. Shi, F. Meng, J. Liu, and Z. Liu, *Improved opto-electronic properties of silicon heterojunction solar cells with SiO_x/tungsten-doped indium oxide double anti-reflective coatings*, Japanese Journal of Applied Physics **56**, 08MB09 (2017).

- [122] C. Han, Y. Zhao, L. Mazzarella, R. Santbergen, A. Montes, P. Procel, G. Yang, X. Zhang, M. Zeman, and O. Isabella, *Room-temperature sputtered tungsten-doped indium oxide for improved current in silicon heterojunction solar cells*, *Solar Energy Materials and Solar Cells* **227**, 111082 (2021).
- [123] D. Zhang, I. A. Digdaya, R. Santbergen, R. A. C. M. M. van Swaaij, P. Bronsveld, M. Zeman, J. A. M. van Roosmalen, and A. W. Weeber, *Design and fabrication of a SiO_x/ITO double-layer anti-reflective coating for heterojunction silicon solar cells*, *Solar Energy Materials and Solar Cells* **117**, 132 (2013).
- [124] A. Cruz, D. Erfurt, P. Wagner, A. B. Morales-Vilches, F. Ruske, R. Schlatmann, and B. Stannowski, *Optoelectrical analysis of TCO + silicon oxide double layers at the front and rear side of silicon heterojunction solar cells*, *Solar Energy Materials and Solar Cells* **236**, 111493 (2022).
- [125] C. Han, R. Santbergen, M. van Duffelen, P. Procel, Y. Zhao, G. Yang, X. Zhang, M. Zeman, L. Mazzarella, and O. Isabella, *Towards bifacial silicon heterojunction solar cells with reduced TCO use*, (2022), progress in Photovoltaics: Research and Applications, accepted.
- [126] P. Procel, H. Xu, A. Saez, C. Ruiz-Tobon, L. Mazzarella, Y. Zhao, C. Han, G. Yang, M. Zeman, and O. Isabella, *The role of heterointerfaces and subgap energy states on transport mechanisms in silicon heterojunction solar cells*, *Progress in Photovoltaics: Research and Applications* **28**, 935 (2020).
- [127] D. Menzel, M. Mews, B. Rech, and L. Korte, *Electronic structure of indium-tungsten-oxide alloys and their energy band alignment at the heterojunction to crystalline silicon*, *Applied Physics Letters* **112**, 011602 (2018).
- [128] M. Bivour, S. Schröer, and M. Hermle, *Numerical analysis of electrical TCO/ a-Si:H(p) contact properties for silicon heterojunction solar cells*, *Energy Procedia* **38**, 658 (2013).
- [129] S. Kirner, M. Hartig, L. Mazzarella, L. Korte, T. Frijnts, H. Scherg-Kurmes, S. Ring, B. Stannowski, B. Rech, and R. Schlatmann, *The influence of ITO dopant density on JV characteristics of silicon heterojunction solar cells: experiments and simulations*, *Energy Procedia* **77**, 725 (2015).
- [130] C. Messmer, M. Bivour, C. Luderer, L. Tutsch, J. Schön, and M. Hermle, *Influence of interfacial oxides at TCO/doped Si thin film contacts on the charge carrier transport of passivating contacts*, *IEEE Journal of Photovoltaics* **10**, 1 (2019).
- [131] E. Böhmer, F. Siebke, B. Rech, C. Beneking, and H. Wagner, *More insights into the ZnO/a-SiC:H(B) interface - an improved TCO/p contact*, *MRS Proceedings* **426**, 519 (1996).
- [132] Y. Zhao, P. Procel, C. Han, L. Mazzarella, G. Yang, A. Weeber, M. Zeman, and O. Isabella, *Design and optimization of hole collectors based on nc-SiO_x:H for high-efficiency silicon heterojunction solar cells*, *Solar Energy Materials and Solar Cells* **219**, 110779 (2021).

- [133] W.-K. Oh, S. Q. Hussain, Y.-J. Lee, Y. Lee, S. Ahn, and J. Yi, *Study on the ito work function and hole injection barrier at the interface of ITO/a-Si:H(p) in amorphous/crystalline silicon heterojunction solar cells*, *Materials Research Bulletin* **47**, 3032 (2012).
- [134] D. Deligiannis, J. van Vliet, R. Vasudevan, R. A. C. M. M. van Swaaij, and M. Zeman, *Passivation mechanism in silicon heterojunction solar cells with intrinsic hydrogenated amorphous silicon oxide layers*, *Journal of Applied Physics* **121**, 085306 (2017).
- [135] S. De Wolf and M. Kondo, *Boron-doped a-Si:H/c-Si interface passivation: Degradation mechanism*, *Applied Physics Letters* **91**, 112109 (2007).
- [136] R. Rößler, C. Leendertz, L. Korte, N. Mingirulli, and B. Rech, *Impact of the transparent conductive oxide work function on injection-dependent a-Si:H/c-Si band bending and solar cell parameters*, *Journal of Applied Physics* **113**, 144513 (2013).
- [137] I. P. Sobkowicz, A. Salomon, and P. R. i. Cabarrocas, *Apparent doping-dependence of the a-Si:H/c-Si interface degradation upon ITO sputtering*, in *IEEE 40th Photovoltaic Specialist Conference (PVSC)* (2014) pp. 0645–0648.
- [138] M. Wimmer, M. Bär, D. Gerlach, R. G. Wilks, S. Scherf, C. Lupulescu, F. Ruske, R. Félix, J. Hüpkens, G. Gavrilă, M. Gorgoi, K. Lips, W. Eberhardt, and B. Rech, *Hard x-ray photoelectron spectroscopy study of the buried Si/ZnO thin-film solar cell interface: Direct evidence for the formation of Si–O at the expense of Zn–O bonds*, *Applied Physics Letters* **99**, 152104 (2011).
- [139] M. H. Rein, M. V. Hohmann, A. Thøgersen, J. Mayandi, A. O. Holt, A. Klein, and E. V. Monakhov, *An in situ X-ray photoelectron spectroscopy study of the initial stages of rf magnetron sputter deposition of indium tin oxide on p-type Si substrate*, *Applied Physics Letters* **102**, 021606 (2013).
- [140] H. Schriemer, B. Halliop, R. Kleiman, A. Gougam, N. Kherani, and S. Zukotynski, *Indium tin oxide and the amorphous-crystalline silicon heterojunction*, (2010).
- [141] T. Nishihara, H. Kanai, Y. Ohshita, K. Nakamura, T. Kamioka, T. Hara, S. Yamaguchi, M. Koharada, and A. Ogura, *Evaluation of correlation between fill factor and high mobility transparent conductive oxide film deposition temperature in the silicon heterojunction solar cells*, *Materials Science in Semiconductor Processing* **132**, 105887 (2021).
- [142] L. Tutsch, F. Feldmann, M. Bivour, W. Wolke, M. Hermle, and J. Rentsch, *Integrating transparent conductive oxides to improve the infrared response of silicon solar cells with passivating rear contacts*, (2018).
- [143] L. Tutsch, F. Feldmann, J. Polzin, C. Luderer, M. Bivour, A. Moldovan, J. Rentsch, and M. Hermle, *Implementing transparent conducting oxides by DC sputtering on ultrathin SiO_x / poly-Si passivating contacts*, *Solar Energy Materials and Solar Cells* **200**, 109960 (2019).

- [144] T. F. Wietler, B. Min, S. Reiter, Y. Larionova, R. Reineke-Koch, F. Heinemeyer, R. Brendel, A. Feldhoff, J. Krügener, D. Tetzlaff, and R. Peibst, *High temperature annealing of ZnO:Al on passivating POLO junctions: Impact on transparency, conductivity, junction passivation, and interface stability*, IEEE Journal of Photovoltaics **9**, 89 (2019).
- [145] S. Sheng, H. Hao, H. Diao, X. Zeng, Y. Xu, X. Liao, and T. L. Monchesky, *XPS depth profiling study of n/TCO interfaces for p-i-n amorphous silicon solar cells*, Applied Surface Science **253**, 1677 (2006).
- [146] Y. Zhao, L. Mazzarella, P. Procel, C. Han, F. D. Tichelaar, G. Yang, A. Weeber, M. Zeman, and O. Isabella, *Ultra-thin electron collectors based on nc-Si:H for high-efficiency silicon heterojunction solar cells*, Progress in Photovoltaics, in press (2021).
- [147] A. G. Silva, K. Pedersen, Z. S. Li, and P. Morgen, *Oxidation of the surface of a thin amorphous silicon film*, Thin Solid Films **520**, 697 (2011).
- [148] C. G. Van de Walle and R. A. Street, *Silicon-hydrogen bonding and hydrogen diffusion in amorphous silicon*, Physical Review B **51**, 10615 (1995).
- [149] R. Wehrspohn, S. Deane, I. French, I. Gale, J. Hewett, M. Powell, and J. Robertson, *Relative importance of the Si-Si bond and Si-H bond for the stability of amorphous silicon thin film transistors*, Journal of Applied Physics **87**, 144 (2000).
- [150] A. Illiberi, P. Kudlacek, A. Smets, M. Creatore, and M. Van De Sanden, *Effect of ion bombardment on the a-Si: H based surface passivation of c-Si surfaces*, Applied Physics Letters **98**, 242115 (2011).
- [151] Y. Takagi, Y. Sakashita, H. Toyoda, and H. Sugai, *Generation processes of super-high-energy atoms and ions in magnetron sputtering plasma*, Vacuum **80**, 581 (2006).
- [152] B. Demareux, S. De Wolf, A. Descoeurdes, Z. Charles Holman, and C. Ballif, *Damage at hydrogenated amorphous/crystalline silicon interfaces by indium tin oxide overlayer sputtering*, Applied Physics Letters **101**, 171604 (2012).
- [153] S. Nunomura, I. Sakata, and K. Matsubara, *Plasma-induced electronic defects: Generation and annihilation kinetics in hydrogenated amorphous silicon*, Physical Review Applied **10**, 054006 (2018).
- [154] L. Tutsch, M. Bivour, W. Wolke, M. Hermle, and J. Rentsch, *Influence of the transparent electrode sputtering process on the interface passivation quality of silicon heterojunction solar cells*, in 33rd European PV Solar Energy Conference and Exhibition (2017).
- [155] H. Li, W. Duan, A. Lambertz, J. Hüpkes, K. Ding, U. Rau, and O. Astakhov, *Influence of room temperature sputtered Al-doped zinc oxide on passivation quality in silicon heterojunction solar cells*, IEEE Journal of Photovoltaics **9**, 1485 (2019).

- [156] J. Haschke, R. Lemerle, B. Aïssa, A. A. Abdallah, M. M. Kivambe, M. Boccard, and C. Ballif, *Annealing of silicon heterojunction solar cells: Interplay of solar cell and indium tin oxide properties*, IEEE Journal of Photovoltaics **9**, 1202 (2019).
- [157] S. Li, Z. Tang, J. Xue, J. Gao, Z. Shi, and X. Li, *Comparative study on front emitter and rear emitter n-type silicon heterojunction solar cells: The role of folded electrical fields*, Vacuum **149**, 313 (2018).
- [158] A. H. T. Le, V. A. Dao, D. P. Pham, S. Kim, S. Dutta, C. P. Thi Nguyen, Y. Lee, Y. Kim, and J. Yi, *Damage to passivation contact in silicon heterojunction solar cells by ITO sputtering under various plasma excitation modes*, Solar Energy Materials and Solar Cells **192**, 36 (2019).
- [159] M. Tamakoshi and N. Matsuki, *Impact of sputter-induced ion bombardment at the heterointerfaces of a-Si:H/c-Si solar cells with double-layered In₂O₃:Sn structures*, Japanese Journal of Applied Physics **54**, 08kd09 (2015).
- [160] V. A. Dao, H. Choi, J. Heo, H. Park, K. Yoon, Y. Lee, Y. Kim, N. Lakshminarayanan, and J. Yi, *rf-magnetron sputtered ITO thin films for improved heterojunction solar cell applications*, Current Applied Physics **10**, S506 (2010).
- [161] S.-H. Lim, H.-J. Seok, M.-J. Gwak, D.-H. Choi, S.-K. Kim, D.-H. Kim, and H.-K. Kim, *Semi-transparent perovskite solar cells with bidirectional transparent electrodes*, Nano Energy, 105703 (2020).
- [162] H. Fujiwara and M. Kondo, *Effects of a-si: H layer thicknesses on the performance of a-si:h/c-si heterojunction solar cells*, Journal of Applied Physics **101**, 054516 (2007).
- [163] V. Linss, M. Bivour, H. Iwata, and K. Ortner, *Comparison of low damage sputter deposition techniques to enable the application of very thin a-si passivation films*, (2019).
- [164] E. Aydin, C. Altinkaya, Y. Smirnov, M. A. Yaqin, K. P. Zanoni, A. Paliwal, Y. Firdaus, T. G. Allen, T. D. Anthopoulos, H. J. Bolink, *et al.*, *Sputtered transparent electrodes for optoelectronic devices: Induced damage and mitigation strategies*, Matter **4**, 3549 (2021).
- [165] H. Kanai, T. Nishihara, and A. Ogura, *Evaluation of process damage induced by sputtering of transparent conductive oxide films for crystalline silicon solar cells*, ECS Journal of Solid State Science and Technology **10**, 035002 (2021).
- [166] D. Caudevilla, E. García-Hemme, E. San Andrés, F. Pérez-Zenteno, I. Torres, R. Barrio, R. García-Hernansanz, S. Algaidy, J. Olea, D. Pastor, *et al.*, *Indium tin oxide obtained by high pressure sputtering for emerging selective contacts in photovoltaic cells*, Materials Science in Semiconductor Processing **137**, 106189 (2022).
- [167] P. Verlinden, *Future challenges for photovoltaic manufacturing at the terawatt level*, Journal of Renewable and Sustainable Energy **12**, 053505 (2020).
- [168] J. F. Weaver, *World has installed 1TW of solar capacity*, (2022).

- [169] M. Lokanc, R. Eggert, and M. Redlinger, *The availability of indium: The present, medium term, and long term*, Report (National Renewable Energy Lab.(NREL), Golden, CO (United States), 2015).
- [170] S. Li, M. Pomaska, A. Lambertz, W. Duan, K. Bittkau, D. Qiu, Z. Yao, M. Luysberg, P. Steuter, M. Köhler, K. Qiu, R. Hong, H. Shen, F. Finger, T. Kirchartz, U. Rau, and K. Ding, *Transparent-conductive-oxide-free front contacts for high-efficiency silicon heterojunction solar cells*, *Joule* **5**, 1535 (2021).
- [171] J. Bartsch, M. Kamp, D. Hartleb, C. Wittich, A. Mondon, B. Steinhauser, F. Feldmann, A. Richter, J. Benick, M. Glatthaar, M. Hermle, and S. W. Glunz, *21.8% efficient n-type solar cells with industrially feasible plated metallization*, *Energy Procedia* **55**, 400 (2014).
- [172] D. Meza, A. Cruz, A. Morales-Vilches, L. Korte, and B. Stannowski, *Aluminum-doped zinc oxide as front electrode for rear emitter silicon heterojunction solar cells with high efficiency*, *Applied Sciences* **9**, 862 (2019).
- [173] A. Mazzi, *Modeling and production of metal nanoparticles through laser ablation and applications to photocatalytic water oxidation*, Ph.D. thesis, University of Trento (2017).
- [174] L. Conde, *An introduction to plasma physics and its space applications*, (2020).
- [175] D. Chen, M. Vaqueiro Contreras, A. Ciesla, P. Hamer, B. Hallam, M. Abbott, and C. Chan, *Progress in the understanding of light- and elevated temperature-induced degradation in silicon solar cells: A review*, *Progress in Photovoltaics: Research and Applications*, 1 (2020).
- [176] S. Huang, W. Liu, X. Li, Z. Li, Z. Wu, W. Huang, Y. Yang, K. Jiang, J. Shi, L. Zhang, F. Meng, and Z. Liu, *Prolonged annealing improves hole transport of silicon heterojunction solar cells*, *physica status solidi (RRL) – Rapid Research Letters*, 2100015 (2021).
- [177] J. Schube, L. Tutsch, T. Fellmeth, M. Bivour, F. Feldmann, T. Hatt, F. Maier, R. Keding, F. Clement, and S. W. Glunz, *Low-resistivity screen-printed contacts on indium tin oxide layers for silicon solar cells with passivating contacts*, *IEEE Journal of Photovoltaics* **8**, 1208 (2018).
- [178] J. Geissbühler, S. D. Wolf, A. Faes, N. Badel, Q. Jeangros, A. Tomasi, L. Barraud, A. Descoedres, M. Despeisse, and C. Ballif, *Silicon heterojunction solar cells with copper-plated grid electrodes: Status and comparison with silver thick-film techniques*, *IEEE Journal of Photovoltaics* **4**, 1055 (2014).
- [179] A. Descoedres, Z. C. Holman, L. Barraud, S. Morel, S. De Wolf, and C. Ballif, *>21% efficient silicon heterojunction solar cells on n- and p-type wafers compared*, *IEEE Journal of Photovoltaics* **3**, 83 (2013).

- [180] H. Steinkemper, M. Hermle, and S. W. Glunz, *Comprehensive simulation study of industrially relevant silicon solar cell architectures for an optimal material parameter choice*, Progress in Photovoltaics: Research and Applications **24**, 1319 (2016).
- [181] T. Tiedje, E. Yablonovitch, G. D. Cody, and B. G. Brooks, *Limiting efficiency of silicon solar cells*, IEEE Transactions on Electron Devices **31**, 711 (1984).
- [182] J. A. Sap, O. Isabella, K. Jäger, and M. Zeman, *Extraction of optical properties of flat and surface-textured transparent conductive oxide films in a broad wavelength range*, Thin Solid Films **520**, 1096 (2011).
- [183] H. Fujiwara and R. W. Collins, *Spectroscopic Ellipsometry for Photovoltaics: Volume 1: Fundamental Principles and Solar Cell Characterization*, Vol. 212 (Springer, 2019) pp. 206–207.
- [184] S. Cornelius, *Charge transport limits and electrical dopant activation in transparent conductive (Al, Ga): ZnO and Nb: TiO₂ thin films prepared by reactive magnetron sputtering*, Ph.D. thesis, Technische Universität Dresden (2014).
- [185] R. A. Synowicki, *Suppression of backside reflections from transparent substrates*, physica status solidi c **5**, 1085 (2008).
- [186] T. Koida, M. Kondo, K. Tsutsumi, A. Sakaguchi, M. Suzuki, and H. Fujiwara, *Hydrogen-doped In₂O₃ transparent conducting oxide films prepared by solid-phase crystallization method*, Journal of Applied Physics **107**, 033514 (2010).
- [187] A. S. Ferlauto, G. M. Ferreira, J. M. Pearce, C. R. Wronski, R. W. Collins, X. Deng, and G. Ganguly, *Analytical model for the optical functions of amorphous semiconductors from the near-infrared to ultraviolet: Applications in thin film photovoltaics*, Journal of Applied Physics **92**, 2424 (2002).
- [188] A. Cruz Bournazou, *Transparent conductive oxides for silicon heterojunction solar cells: interaction between materials and device*, Ph.D. thesis, Technische Universität Berlin (2021).
- [189] G. Bader, P. Ashrit, and T. Vo-Van, *Transmission and reflection ellipsometry of thin films and multilayer systems*, Applied Optics **37**, 1146 (1998).
- [190] F. Smits, *Measurement of sheet resistivities with the four-point probe*, Bell System Technical Journal **37**, 711 (1958).
- [191] O. Philips' Gloeilampenfabrieken, *A method of measuring specific resistivity and hall effect of discs of arbitrary shape*, Philips Res. Rep **13**, 1 (1958).
- [192] F. Werner, *Hall measurements on low-mobility thin films*, Journal of Applied Physics **122**, 135306 (2017).
- [193] E. H. Hall, *On a new action of the magnet on electric currents*, American Journal of Mathematics **2**, 287 (1879).

- [194] J. N. Avaritsiotis and R. P. Howson, *Composition and conductivity of fluorine-doped conducting indium oxide films prepared by reactive ion plating*, *Thin Solid Films* **77**, 351 (1981).
- [195] K.-U. Ritzau, T. Behrendt, D. Palaferri, M. Bivour, and M. Hermle, *Hydrogen doping of indium tin oxide due to thermal treatment of hetero-junction solar cells*, *Thin Solid Films* **599**, 161 (2016).
- [196] H. Fujiwara and M. Kondo, *Effects of carrier concentration on the dielectric function of ZnO:Ga and In₂O₃:Sn studied by spectroscopic ellipsometry: Analysis of free-carrier and band-edge absorption*, *Physical Review B* **71**, 075109 (2005).
- [197] T. Koida, Y. Ueno, and H. Shibata, *In₂O₃-based transparent conducting oxide films with high electron mobility fabricated at low process temperatures*, *physica status solidi (a)* **215**, 1700506 (2018).
- [198] M. Salerno and S. Dante, *Scanning kelvin probe microscopy: Challenges and perspectives towards increased application on biomaterials and biological samples*, *Materials (Basel)* **11**, 951 (2018).
- [199] J. Matthew, *Surface analysis by auger and x-ray photoelectron spectroscopy. d. briggs and j. t. grant (eds). impublications, chichester, uk and surfacespectra, manchester, uk, 2003. 900 pp., isbn 1-901019-04-7, 900 pp*, *Surface and Interface Analysis* **36**, 1647 (2004).
- [200] A. Gulino, *Structural and electronic characterization of self-assembled molecular nanoarchitectures by x-ray photoelectron spectroscopy*, *Analytical and Bioanalytical Chemistry* **405**, 1479 (2013).
- [201] A. Montes, S. W. H. Eijt, Y. Tian, R. Gram, H. Schut, T. Suemasu, N. Usami, M. Zeman, J. Serra, and O. Isabella, *Point defects in basi2 thin films for photovoltaic applications studied by positron annihilation spectroscopy*, *Journal of Applied Physics* **127**, 085304 (2020).
- [202] A. Richter, S. W. Glunz, F. Werner, J. Schmidt, and A. Cuevas, *Improved quantitative description of auger recombination in crystalline silicon*, *Physical Review B* **86**, 165202 (2012).
- [203] M. Reusch, M. Bivour, M. Hermle, and S. W. Glunz, *Fill factor limitation of silicon heterojunction solar cells by junction recombination*, *Energy Procedia* **38**, 297 (2013).
- [204] A. Cuevas and D. Macdonald, *Measuring and interpreting the lifetime of silicon wafers*, *Solar Energy* **76**, 255 (2004).
- [205] C. Reichel, F. Granek, J. Benick, O. Schultz-Wittmann, and S. W. Glunz, *Comparison of emitter saturation current densities determined by injection-dependent lifetime spectroscopy in high and low injection regimes*, *Progress in Photovoltaics: Research and Applications* **20**, 21 (2012).

- [206] B. A. Veith-Wolf, S. Schäfer, R. Brendel, and J. Schmidt, *Reassessment of intrinsic lifetime limit in n-type crystalline silicon and implication on maximum solar cell efficiency*, Solar Energy Materials and Solar Cells **186**, 194 (2018).
- [207] M. Müller, *Reporting effective lifetimes at solar cell relevant injection densities*, Energy Procedia **92**, 138 (2016).
- [208] F. Feldmann, M. Bivour, C. Reichel, M. Hermle, and S. W. Glunz, *Passivated rear contacts for high-efficiency n-type si solar cells providing high interface passivation quality and excellent transport characteristics*, Solar Energy Materials and Solar Cells **120**, 270 (2014).
- [209] T. S. Liang, M. Pravettoni, J. P. Singh, and Y. S. Khoo, *Meeting the requirements of iec ts 60904-1-2 for single light source bifacial photovoltaic characterisation: evaluation of different back panel materials*, Engineering Research Express **2**, 015048 (2020).
- [210] L. Leec, *Physics of metal-semiconductor contact and circular transmission line model (ctlm)*, (xxx, 2004) Book section Physics of Metal-Semiconductor Contact and Circular Transmission Line Model (CTLM), pp. 10–22.
- [211] R. Santbergen, T. Meguro, T. Suezaki, G. Koizumi, K. Yamamoto, and M. Zeman, *Genpro4 optical model for solar cell simulation and its application to multijunction solar cells*, IEEE Journal of Photovoltaics **7**, 919 (2017).
- [212] A. Alcañiz Moya, *Numerical simulation of c-Si solar cells based on transition metal oxide as carrier selective contact: Drift diffusion and ab initio*, (2020), mater thesis.
- [213] C. Han, L. Mazzarella, Y. Zhao, G. Yang, P. Procel, M. Tijssen, A. Montes, L. Spitaleri, A. Gulino, X. Zhang, O. Isabella, and M. Zeman, *High-mobility hydrogenated fluorine-doped indium oxide film for passivating contacts c-Si solar cells*, ACS Applied Materials & Interfaces **11**, 45586 (2019).
- [214] M. Morales-Masis, S. M. D. Nicolas, J. Holovsky, S. D. Wolf, and C. Ballif, *Low-temperature high-mobility amorphous IZO for silicon heterojunction solar cells*, IEEE Journal of Photovoltaics **5**, 1340 (2015).
- [215] M. F. A. M. van Hest, M. S. Dabney, J. D. Perkins, D. S. Ginley, and M. P. Taylor, *Titanium-doped indium oxide: A high-mobility transparent conductor*, Applied Physics Letters **87**, 032111 (2005).
- [216] M. Morales-Masis, E. Rucavado, R. Monnard, L. Barraud, J. Holovský, M. Despeisse, M. Boccard, and C. Ballif, *Highly conductive and broadband transparent Zr-doped In_2O_3 as front electrode for solar cells*, IEEE Journal of Photovoltaics **8**, 1202 (2018).
- [217] F. Meng, J. Shi, Z. Liu, Y. Cui, Z. Lu, and Z. Feng, *High mobility transparent conductive W-doped In_2O_3 thin films prepared at low substrate temperature and its application to solar cells*, Solar Energy Materials and Solar Cells **122**, 70 (2014).

- [218] Y. Meng, X.-l. Yang, H.-x. Chen, J. Shen, Y.-m. Jiang, Z.-j. Zhang, and Z.-y. Hua, *Molybdenum-doped indium oxide transparent conductive thin films*, Journal of Vacuum Science & Technology A: Vacuum, Surfaces, and Films **20**, 288 (2002).
- [219] G. H. Wang, C. Y. Shi, L. Zhao, H. W. Diao, and W. J. Wang, *Transparent conductive Hf-doped In_2O_3 thin films by rf sputtering technique at low temperature annealing*, Applied Surface Science **399**, 716 (2017).
- [220] S. Singh, A. Raza, A. Sharma, O. Agnihotri, and L. Tewari, *Characterization of fluorine-doped In_2O_3 films synthesized by spray pyrolysis*, Thin Solid Films **105**, 131 (1983).
- [221] T. Maruyama and T. Nakai, *Fluorine-doped indium oxide thin films prepared by chemical vapor deposition*, Journal of Applied Physics **71**, 2915 (1992).
- [222] H. Kobayashi, T. Ishida, K. Nakamura, Y. Nakato, and H. Tsubomura, *Properties of indium tin oxide films prepared by the electron beam evaporation method in relation to characteristics of indium tin oxide/silicon oxide/silicon junction solar cells*, Journal of Applied Physics **72**, 5288 (1992).
- [223] T. Ishida, H. Kobayashi, and Y. Nakato, *Structures and properties of electron-beam-evaporated indium tin oxide films as studied by x-ray photoelectron spectroscopy and work-function measurements*, Journal of Applied Physics **73**, 4344 (1993).
- [224] Y. Shigesato, N. Shin, M. Kamei, P. K. Song, and I. Yasui, *Study on fluorine-doped indium oxide films deposited by rf magnetron sputtering*, Japanese Journal of Applied Physics **39**, 6422 (2000).
- [225] J.-S. Seo, J.-H. Jeon, Y. H. Hwang, H. Park, M. Ryu, S.-H. K. Park, and B.-S. Bae, *Solution-processed flexible fluorine-doped indium zinc oxide thin-film transistors fabricated on plastic film at low temperature*, Scientific reports **3**, 2085 (2013).
- [226] B. Mayer, *Highly conductive and transparent films of tin and fluorine doped indium oxide produced by apcvd*, Thin Solid Films **221**, 166 (1992).
- [227] G. G. Untila, T. N. Kost, A. B. Chebotareva, and E. D. Kireeva, *Contact resistance of indium tin oxide and fluorine-doped indium oxide films grown by ultrasonic spray pyrolysis to diffusion layers in silicon solar cells*, Solar Energy Materials and Solar Cells **137**, 26 (2015).
- [228] G. G. Untila, T. N. Kost, and A. B. Chebotareva, *Concentrator $In_2O_3:F(n+pp+)-c-Si/Al$ solar cells with Al-alloyed BSF and Ag-free multi-wire metallization using transparent conductive polymers*, Solar Energy **174**, 1008 (2018).
- [229] G. Limodio, G. Yang, H. Ge, P. Procel, Y. De Groot, L. Mazzarella, O. Isabella, and M. Zeman, *Front and rear contact si solar cells combining high and low thermal budget si passivating contacts*, Solar Energy Materials and Solar Cells **194**, 28 (2019).
- [230] G. Nogay, *Full-Area Passivating Contacts with High and Low Thermal Budgets: Solutions for High Efficiency c-Si Solar Cells*, Doctoral, EPFL (2018).

- [231] G. Yang, P. Guo, P. Procel, G. Limodio, A. Weeber, O. Isabella, and M. Zeman, *High-efficiency black IBC c-Si solar cells with poly-Si as carrier-selective passivating contacts*, *Solar Energy Materials and Solar Cells* **186**, 9 (2018).
- [232] S. Honda, M. Watamori, and K. Oura, *The effects of oxygen content on electrical and optical properties of indium tin oxide films fabricated by reactive sputtering*, *Thin Solid Films* **281-282**, 206 (1996).
- [233] L. Shen, Y. An, D. Cao, Z. Wu, and J. Liu, *Room-temperature ferromagnetic enhancement and crossover of negative to positive magnetoresistance in N-doped In_2O_3 films*, *The Journal of Physical Chemistry C* **121**, 26499 (2017).
- [234] H. Kato, S. Takemura, and Y. Nakajima, *X-ray photoemission spectroscopy studies of conducting polymer-substrate interfaces: Interfacial electrochemical diffusion*, *Journal of Applied Physics* **81**, 7313 (1997).
- [235] S. P. Singh, L. M. Tiwari, and O. P. Agnihotri, *Optical investigations of $In_2O_3:F$ films*, *Thin Solid Films* **139**, 1 (1986).
- [236] G. G. Untila, T. N. Kost, and A. B. Chebotareva, *Fluorine doped indium oxide films for silicon solar cells*, *Thin Solid Films* **518**, 1345 (2009).
- [237] S. Sugumaran, C. S. Bellan, D. Muthu, S. Raja, D. Bheeman, and R. Rajamani, *Novel hybrid pva–inzno transparent thin films and sandwich capacitor structure by dip coating method: preparation and characterizations*, *RSC Advances* **5**, 10599 (2015).
- [238] M. Myilsamy, V. Murugesan, and M. Mahalakshmi, *Indium and cerium co-doped mesoporous TiO_2 nanocomposites with enhanced visible light photocatalytic activity*, *Applied Catalysis A: General* **492**, 212 (2015).
- [239] S. Sugumaran, C. S. Bellan, D. Muthu, S. Raja, D. Bheeman, and R. Rajamani, *New transparent PVA– $InTiO$ hybrid thin films: influence of $InTiO$ on the structure, morphology, optical, and dielectric properties*, *Polymers for Advanced Technologies* **26**, 1486 (2015).
- [240] M. Pashchanka, R. C. Hoffmann, A. Gurlo, and J. J. Schneider, *Molecular based, chimie douce approach to 0D and 1D indium oxide nanostructures. evaluation of their sensing properties towards CO and H_2* , *Journal of Materials Chemistry* **20**, 8311 (2010).
- [241] P. Drude, *Zur elektronentheorie der metalle*, *Annalen der Physik* **306**, 566 (1900).
- [242] Z. G. Yu, J. Sun, M. B. Sullivan, Y.-W. Zhang, H. Gong, and D. J. Singh, *Dopant chemical potential modulation on oxygen vacancies formation in In_2O_3 : A comparative density functional study*, *Chemical Physics Letters* **621**, 141 (2015).
- [243] W.-F. Wu, B.-S. Chiou, and S.-T. Hsieh, *Effect of sputtering power on the structural and optical properties of RF magnetron sputtered ITO films*, *Semiconductor science and technology* **9**, 1242 (1994).

- [244] S. Amara and M. Bouafia, *Characterisation of TCO AZO/glass structures by spectroscopic ellipsometry*, International Journal of Nanoparticles **6**, 122 (2013).
- [245] E. Parsianpour, D. Raoufi, M. Roostaei, B. Sohrabi, and F. Samavat, *Characterization and structural property of indium tin oxide thin films*, Advances in Materials Physics and Chemistry **07**, 42 (2017).
- [246] E. Shanthi, A. Banerjee, V. Dutta, and K. L. Chopra, *Electrical and optical properties of tin oxide films doped with F and Sb+F*, Journal of Applied Physics **53**, 1615 (1982).
- [247] A. S. Hassanien and A. A. Akl, *Effect of se addition on optical and electrical properties of chalcogenide CdSse thin films*, Superlattices and Microstructures **89**, 153 (2016).
- [248] M. Thirumoorthi and J. Thomas Joseph Prakash, *Structure, optical and electrical properties of indium tin oxide ultra thin films prepared by jet nebulizer spray pyrolysis technique*, Journal of Asian Ceramic Societies **4**, 124 (2016).
- [249] M. I. Hossain, W. Qarony, V. Jovanov, Y. H. Tsang, and D. Knipp, *Nanophotonic design of perovskite/silicon tandem solar cells*, Journal of Materials Chemistry A **6**, 3625 (2018).
- [250] C. P. Liu, Y. Foo, M. Kamruzzaman, C. Y. Ho, J. Zapien, W. Zhu, Y. Li, W. Walukiewicz, and K. M. Yu, *Effects of free carriers on the optical properties of doped CdO for full-spectrum photovoltaics*, Physical Review Applied **6**, 064018 (2016).
- [251] P. Procel, G. Yang, O. Isabella, and M. Zeman, *Theoretical evaluation of contact stack for high efficiency IBC-SHJ solar cells*, Solar Energy Materials and Solar Cells **186**, 66 (2018).
- [252] P. P. Moya, H. Xu, L. Mazzarella, L.-L. Senaud, B. Paviet-Salomon, H. S. Radhakrishnan, M. Filipic, M. Xu, M. Boccard, A. Fioretti, R. Monnard, J.-C. Stang, P. Wagner, D. Meza, D. Lachenal, B. Strahm, W. Duan, A. Lambertz, A. Fejfar, K. Ding, M. Despeisse, I. Gordon, L. Korte, C. Ballif, O. Isabella, and M. Zeman, *On the correlation between contact resistivity and high efficiency IBC-SHJ solar cells*, in *Proceedings of the 36th European Photovoltaic Solar Energy Conference and Exhibition* (2019) pp. 255–258.
- [253] L. Barraud, Z. C. Holman, N. Badel, P. Reiss, A. Descoeudres, C. Battaglia, S. De Wolf, and C. Ballif, *Hydrogen-doped indium oxide/indium tin oxide bilayers for high-efficiency silicon heterojunction solar cells*, Solar Energy Materials and Solar Cells **115**, 151 (2013).
- [254] M. Leilaieoun, J. Y. Zhengshan, and Z. Holman, *Optimization of front TCO layer of silicon heterojunction solar cells for tandem applications*, in *2016 IEEE 43rd Photovoltaic Specialists Conference (PVSC)* (IEEE, 2016) pp. 0681–0684.
- [255] T. G. Allen, J. Bullock, X. Yang, A. Javey, and S. De Wolf, *Passivating contacts for crystalline silicon solar cells*, Nature Energy **4**, 914 (2019).

- [256] G. Limodio, G. Yang, Y. De Groot, P. Procel, L. Mazzarella, A. W. Weber, O. Isabella, and M. Zeman, *Implantation-based passivating contacts for crystalline silicon front/rear contacted solar cells*, *Progress in Photovoltaics: Research and Applications* **28**, 403 (2020).
- [257] W. Yoon, D. Scheiman, Y.-W. Ok, Z. Song, C. Chen, G. Jernigan, A. Rohatgi, Y. Yan, and P. Jenkins, *Sputtered indium tin oxide as a recombination layer formed on the tunnel oxide/poly-Si passivating contact enabling the potential of efficient monolithic perovskite/Si tandem solar cells*, *Solar Energy Materials and Solar Cells* **210**, 110482 (2020).
- [258] J. H. W. De Wit, *The high temperature behavior of In_2O_3* , *Journal of Solid State Chemistry* **13**, 192 (1975).
- [259] S. Li, Z. Shi, Z. Tang, and X. Li, *Study on the hydrogen doped indium oxide for silicon heterojunction solar cell application*, *Journal of Alloys and Compounds* **705**, 198 (2017).
- [260] E. Cartier, J. H. Stathis, and D. A. Buchanan, *Passivation and depassivation of silicon dangling bonds at the Si/SiO_2 interface by atomic hydrogen*, *Applied Physics Letters* **63**, 1510 (1993).
- [261] L. Tutsch, F. Feldmann, B. Macco, M. Bivour, E. Kessels, and M. Hermle, *Improved passivation of n-type poly-Si based passivating contacts by the application of hydrogen-rich transparent conductive oxides*, *IEEE Journal of Photovoltaics* **10**, 986 (2020).
- [262] S. T. Khlayboonme and W. Thowladda, *Comparative study of non-annealing and annealing on properties of ITO deposited by rf magnetron sputtering*, *Key Engineering Materials* **659**, 615 (2015).
- [263] G. Yang, A. Ingenito, N. van Hameren, O. Isabella, and M. Zeman, *Design and application of ion-implanted polysi passivating contacts for interdigitated back contact c-Si solar cells*, *Applied Physics Letters* **108**, 033903 (2016).
- [264] G. Yang, A. Ingenito, O. Isabella, and M. Zeman, *IBC c-Si solar cells based on ion-implanted poly-silicon passivating contacts*, *Solar Energy Materials and Solar Cells* **158**, 84 (2016).
- [265] M. Nakashima, M. Oota, N. Ishihara, Y. Nonaka, T. Hirohashi, M. Takahashi, S. Yamazaki, T. Obonai, Y. Hosaka, and J. Koezuka, *Origin of major donor states in $in-ga-zn$ oxide*, *Journal of Applied Physics* **116**, 213703 (2014).
- [266] B. Clafin and H. Fritzsche, *The role of oxygen diffusion in photoinduced changes of the electronic and optical properties in amorphous indium oxide*, *Journal of electronic materials* **25**, 1772 (1996).
- [267] J. B. Varley, H. Peelaers, A. Janotti, and C. G. Van de Walle, *Hydrogenated cation vacancies in semiconducting oxides*, *Journal of Physics: Condensed Matter* **23**, 334212 (2011).

- [268] A. Uedono, K. Shimayama, M. Kiyohara, Z. Q. Chen, and K. Yamabe, *Study of oxygen vacancies in srTiO_3 by positron annihilation*, Journal of Applied Physics **92**, 2697 (2002).
- [269] J. I. Kim, W. Lee, T. Hwang, J. Kim, S.-Y. Lee, S. Kang, H. Choi, S. Hong, H. H. Park, T. Moon, and B. Park, *Quantitative analyses of damp-heat-induced degradation in transparent conducting oxides*, Solar Energy Materials and Solar Cells **122**, 282 (2014).
- [270] O. Bierwagen and J. S. Speck, *High electron mobility $\text{In}_2\text{O}_3(001)$ and (111) thin films with nondegenerate electron concentration*, Applied Physics Letters **97**, 072103 (2010).
- [271] S. Husein, M. Stuckelberger, B. West, L. Ding, F. Dauzou, M. Morales-Masis, M. Duchamp, Z. Holman, and M. I. Bertoni, *Carrier scattering mechanisms limiting mobility in hydrogen-doped indium oxide*, Journal of applied physics **123**, 245102 (2018).
- [272] C. N. Liu, B. Ozkaya, S. Steves, P. Awakowicz, and G. Grundmeier, *Combined in situ FTIR-spectroscopic and electrochemical analysis of nanopores in ultra-thin SiO₂-like plasma polymer barrier films*, Journal of Physics D: Applied Physics **46**, 084015 (2013).
- [273] K. Ishikawa, H. Ogawa, and S. Fujimura, *Contribution of interface roughness to the infrared spectra of thermally grown silicon dioxide films*, Journal of Applied Physics **85**, 4076 (1999).
- [274] T. N. Truong, D. Yan, C. Samundsett, R. Basnet, M. Tebyetekerwa, L. Li, F. Kremer, A. Cuevas, D. Macdonald, and H. T. Nguyen, *Hydrogenation of phosphorus-doped polycrystalline silicon films for passivating contact solar cells*, ACS Appl Mater Interfaces **11**, 5554 (2019).
- [275] A. Mewe, M. Stodolny, J. Anker, M. Lenes, X. Pagès, Y. Wu, K. Tool, B. Geerligs, and I. Romijn, *Full wafer size ibc cell with polysilicon passivating contacts*, AIP Conference Proceedings **1999**, 040014 (2018).
- [276] Z. Zhang, M. Liao, Y. Huang, X. Guo, Q. Yang, Z. Wang, T. Gao, C. Shou, Y. Zeng, B. Yan, and J. Ye, *Improvement of surface passivation of tunnel oxide passivated contact structure by thermal annealing in mixture of water vapor and nitrogen environment*, Solar RRL **3**, 1900105 (2019).
- [277] H. Malmbeek, L. Vines, E. V. Monakhov, and B. G. Svensson, *Electronic states at the interface between indium tin oxide and silicon*, Journal of Applied Physics **110**, 074503 (2011).
- [278] H. Park, H. Park, S. J. Park, S. Bae, H. Kim, J. W. Yang, J. Y. Hyun, C. H. Lee, S. H. Shin, Y. Kang, H.-S. Lee, and D. Kim, *Passivation quality control in poly-Si/SiO₂/c-Si passivated contact solar cells with 734 mV implied open circuit voltage*, Solar Energy Materials and Solar Cells **189**, 21 (2019).

- [279] M. Boccard, L. Antognini, V. Paratte, J. Haschke, M. Truong, J. Cattin, J. Dréon, W. Lin, L. L. Senaud, B. Paviet-Salomon, S. Nicolay, M. Despeisse, and C. Ballif, *Hole-selective front contact stack enabling 24.1%-efficient silicon heterojunction solar cells*, IEEE Journal of Photovoltaics , 1 (2020).
- [280] Z. Yao, W. Duan, P. Steuter, J. Hüpkes, A. Lambertz, K. Bittkau, M. Pomaska, D. Qiu, K. Qiu, Z. Wu, H. Shen, U. Rau, and K. Ding, *Influence of oxygen on sputtered titanium-doped indium oxide thin films and their application in silicon heterojunction solar cells*, Solar RRL **5**, 2000501 (2020).
- [281] J. E. N. Swallow, B. A. D. Williamson, S. Sathasivam, M. Birkett, T. J. Featherstone, P. A. E. Murgatroyd, H. J. Edwards, Z. W. Lebens-Higgins, D. A. Duncan, M. Farnworth, P. Warren, N. Peng, T.-L. Lee, L. F. J. Piper, A. Regoutz, C. J. Carmalt, I. P. Parkin, V. R. Dhanak, D. O. Scanlon, and T. D. Veal, *Resonant doping for high mobility transparent conductors: the case of Mo-doped In_2O_3* , Materials Horizons **7**, 236 (2020).
- [282] J. Yu, J. Bian, W. Duan, Y. Liu, J. Shi, F. Meng, and Z. Liu, *Tungsten doped indium oxide film: Ready for bifacial copper metallization of silicon heterojunction solar cell*, Solar Energy Materials and Solar Cells **144**, 359 (2016).
- [283] Y. Zhang, *Electronegativities of elements in valence states and their applications. 2. a scale for strengths of lewis acids*, Inorganic Chemistry **21**, 3889 (1982).
- [284] M. Yang, J. Feng, G. Li, and Q. Zhang, *Tungsten-doped In_2O_3 transparent conductive films with high transmittance in near-infrared region*, Journal of Crystal Growth **310**, 3474 (2008).
- [285] S. Calnan and A. N. Tiwari, *High mobility transparent conducting oxides for thin film solar cells*, Thin Solid Films **518**, 1839 (2010).
- [286] T. Koida, J. Nishinaga, Y. Ueno, H. Higuchi, H. Takahashi, M. Iioka, Y. Kamikawa, H. Shibata, and S. Niki, *Improved efficiency of $Cu(In,Ga)Se_2$ mini-module via high-mobility $In_2O_3:W,H$ transparent conducting oxide layer*, Progress in Photovoltaics: Research and Applications **27**, 491 (2019).
- [287] J. Lerat, G. Christmann, L. Ding, M. Tomassini, J. Diaz Leon, V. Barth, S. Nicolay, and D. Munoz, *Bringing tungsten-doped indium oxide to manufacturing maturity for high efficiency silicon heterojunction solar cells*, EUPVSEC , 1 (2019).
- [288] G. Limodio, Y. D. Groot, G. V. Kuler, L. Mazzarella, Y. Zhao, P. Procel, G. Yang, O. Isabella, and M. Zeman, *Copper-plating metallization with alternative seed layers for c-Si solar cells embedding carrier-selective passivating contacts*, IEEE Journal of Photovoltaics **10**, 372 (2020).
- [289] L. T. Yan and R. E. I. Schropp, *Changes in the structural and electrical properties of vacuum post-annealed tungsten- and titanium-doped indium oxide films deposited by radio frequency magnetron sputtering*, Thin Solid Films **520**, 2096 (2012).

- [290] J. H. Kim, Y.-H. Shin, T.-Y. Seong, S.-I. Na, and H.-K. Kim, *Rapid thermal annealed WO₃-doped In₂O₃ films for transparent electrodes in organic photovoltaics*, Journal of Physics D: Applied Physics **45**, 395104 (2012).
- [291] D. M. Mattox, *Fundamentals of ion plating*, Journal of Vacuum Science and Technology **10**, 47 (1973).
- [292] R. R. Krishnan, V. Kavitha, S. Chalana, R. Prabhu, and V. M. Pillai, *Effect of tungsten doping on the properties of In₂O₃ films*, JOM **71**, 1885 (2019).
- [293] J. Y. W. Seto, *The electrical properties of polycrystalline silicon films*, Journal of Applied Physics **46**, 5247 (1975).
- [294] V. H. Nguyen, U. Gottlieb, A. Valla, D. Muñoz, D. Bellet, and D. Muñoz-Rojas, *Electron tunneling through grain boundaries in transparent conductive oxides and implications for electrical conductivity: the case of ZnO:Al thin films*, Materials Horizons **5**, 715 (2018).
- [295] J. Pan, W. Wang, D. Wu, Q. Fu, and D. Ma, *Tungsten doped indium oxide thin films deposited at room temperature by radio frequency magnetron sputtering*, Journal of Materials Science & Technology **30**, 644 (2014).
- [296] S. Kumar Vishwanath, T. An, W.-Y. Jin, J.-W. Kang, and J. Kim, *The optoelectronic properties of tungsten-doped indium oxide thin films prepared by polymer-assisted solution processing for use in organic solar cells*, J. Mater. Chem. C **5**, 10295 (2017).
- [297] R. Santbergen, R. Mishima, T. Meguro, M. Hino, H. Uzu, J. Blanker, K. Yamamoto, and M. Zeman, *Minimizing optical losses in monolithic perovskite/c-Si tandem solar cells with a flat top cell*, Optics Express **24**, A1288 (2016).
- [298] L. Ding, J. Diaz, G. Christmann, L. L. Senaud, L. Barraud, A. Descoeurdes, N. Badel, M. Despeisse, S. Nicolay, and C. Ballif, *High mobility iwo for improved current in heterojunction technology solar cells*, 28th PVSEC 35th EU PVSEC , 1 (2018).
- [299] A. B. Morales-Vilches, A. Cruz, S. Pingel, S. Neubert, L. Mazzarella, D. Meza, L. Korte, R. Schlattmann, and B. Stannowski, *ITO-free silicon heterojunction solar cells with ZnO:Al/SiO₂ front electrodes reaching a conversion efficiency of 23%*, IEEE Journal of Photovoltaics **9**, 34 (2019).
- [300] E. Gervais, S. Shammugam, L. Friedrich, and T. Schlegl, *Raw material needs for the large-scale deployment of photovoltaics – effects of innovation-driven roadmaps on material constraints until 2050*, Renewable and Sustainable Energy Reviews **137**, 110589 (2021).
- [301] Y. Zhang, M. Kim, L. Wang, P. Verlinden, and B. Hallam, *Design considerations for multi-terawatt scale manufacturing of existing and future photovoltaic technologies: challenges and opportunities related to silver, indium and bismuth consumption*, Energy & Environmental Science **14**, 5587 (2021).

- [302] Z. Wu, W. Duan, A. Lambertz, D. Qiu, M. Pomaska, Z. Yao, U. Rau, L. Zhang, Z. Liu, and K. Ding, *Low-resistivity p-type a-Si:H/AZO hole contact in high-efficiency silicon heterojunction solar cells*, Applied Surface Science **542**, 148749 (2021).
- [303] L.-L. Senaud, G. Christmann, A. Descoedres, J. Geissbuhler, L. Barraud, N. Badel, C. Allebe, S. Nicolay, M. Despeisse, B. Paviet-Salomon, and C. Ballif, *Aluminium-doped zinc oxide rear reflectors for high-efficiency silicon heterojunction solar cells*, IEEE Journal of Photovoltaics , 1 (2019).
- [304] L. Lancellotti, E. Bobeico, M. Della Noce, L. V. Mercaldo, I. Usatii, P. D. Veneri, G. V. Bianco, A. Sacchetti, and G. Bruno, *Graphene as non conventional transparent conductive electrode in silicon heterojunction solar cells*, Applied Surface Science **525**, 146443 (2020).
- [305] T. Jäger, Y. E. Romanyuk, S. Nishiwaki, B. Bissig, F. Pianezzi, P. Fuchs, C. Gretener, M. Döbeli, and A. N. Tiwari, *Hydrogenated indium oxide window layers for high-efficiency Cu(In,Ga)Se₂ solar cells*, Journal of Applied Physics **117**, 205301 (2015).
- [306] M. Bivour, *Towards TCO-free shj solar cells*, (2021).
- [307] P. Wagner, A. Cruz, J. C. Stang, and L. Korte, *Low-resistance hole contact stacks for interdigitated rear-contact silicon heterojunction solar cells*, IEEE Journal of Photovoltaics , 1 (2021).
- [308] C. Liu, W. Liu, W. Chen, S. Hsieh, T. Tsai, and L. Yang, *ITO as a diffusion barrier between si and cu*, Journal of the Electrochemical Society **152**, G234 (2005).
- [309] U. Heitmann, O. Höhn, H. Hauser, S. Kluska, J. Bartsch, and S. Janz, *Electrical and optical analysis of a spray coated transparent conductive adhesive for two-terminal silicon based tandem solar cells*, (2019).
- [310] Z. C. Holman, A. Descoedres, S. De Wolf, and C. Ballif, *Record infrared internal quantum efficiency in silicon heterojunction solar cells with dielectric/metal rear reflectors*, IEEE Journal of Photovoltaics **3**, 1243 (2013).
- [311] M. Bivour, M. Reusch, F. Feldmann, M. Hermle, and S. Glunz, *Requirements for carrier selective silicon heterojunctions*, Proc. 24th Workshop Crystalline Silicon Sol. Cells Modules, Mater. Processes , 1 (2014).
- [312] M. Bivour, S. Schröer, M. Hermle, and S. W. Glunz, *Silicon heterojunction rear emitter solar cells: Less restrictions on the optoelectrical properties of front side TCOs*, Solar Energy Materials and Solar Cells **122**, 120 (2014).
- [313] J. Haschke, G. Christmann, C. Messmer, M. Bivour, M. Boccard, and C. Ballif, *Lateral transport in silicon solar cells*, Journal of Applied Physics **127**, 114501 (2020).
- [314] K.-U. Ritzau, M. Bivour, S. Schröer, H. Steinkemper, P. Reinecke, F. Wagner, and M. Hermle, *TCO work function related transport losses at the a-Si:H/TCO-contact in shj solar cells*, Solar Energy Materials and Solar Cells **131**, 9 (2014).

- [315] G. G. Untila, T. N. Kost, and A. B. Chebotareva, *Fluorine- and tin-doped indium oxide films grown by ultrasonic spray pyrolysis: Characterization and application in bifacial silicon concentrator solar cells*, *Solar Energy* **159**, 173 (2018).
- [316] M. R. Vogt, T. Gewohn, K. Bothe, C. Schinke, and R. Brendel, *Impact of using spectrally resolved ground albedo data for performance simulations of bifacial modules*, (2018).
- [317] H. Sai, P.-W. Chen, H.-J. Hsu, T. Matsui, S. Nunomura, and K. Matsubara, *Impact of intrinsic amorphous silicon bilayers in silicon heterojunction solar cells*, *Journal of Applied Physics* **124**, 103102 (2018).
- [318] M. Weidner, A. Fuchs, T. J. Bayer, K. Rachut, P. Schnell, G. K. Deyu, and A. Klein, *Defect modulation doping*, *Advanced Functional Materials* **29**, 1807906 (2019).
- [319] G. Du, Y. Bai, J. Huang, J. Zhang, J. Wang, Y. Lin, L. Lu, L. Yang, S. Bao, Z. Huang, et al., *Surface passivation of ito on heterojunction solar cells with enhanced cell performance and module reliability*, *ECS Journal of Solid State Science and Technology* **10**, 035008 (2021).
- [320] L. L. Senaud, P. Procel, G. Christmann, A. Descoeurdes, J. Geissbühler, C. Allebé, N. Badel, P. Wyss, M. Boccard, O. Isabella, M. Zeman, S. Nicolay, M. Despeisse, C. Ballif, and B. Paviet-Salomon, *Advanced method for electrical characterization of carrier-selective passivating contacts using transfer-length-method measurements under variable illumination*, *Journal of Applied Physics* **129**, 195707 (2021).
- [321] T. Nishihara, K. Muramatsu, K. Nakamura, Y. Ohshita, S. Yasuno, H. Kanai, Y. Hara, Y. Hibino, H. Kojima, and A. Ogura, *Investigation of the chemical reaction between silver electrodes and transparent conductive oxide films for the improvement of fill factor of silicon heterojunction solar cells*, *ECS Journal of Solid State Science and Technology* **10** (2021), 10.1149/2162-8777/abffae.
- [322] M. Nishiwaki and H. Fujiwara, *Highly accurate prediction of material optical properties based on density functional theory*, *Computational Materials Science* **172**, 109315 (2020).
- [323] M. W. Knight, J. van de Groep, P. C. Bronsveld, W. C. Sinke, and A. Polman, *Soft imprinted ag nanowire hybrid electrodes on silicon heterojunction solar cells*, *Nano Energy* **30**, 398 (2016).
- [324] N. E. Grant, P. P. Altermatt, T. Niewelt, R. Post, W. Kwapil, M. C. Schubert, and J. D. Murphy, *Gallium-doped silicon for high-efficiency commercial passivated emitter and rear solar cells*, *Solar RRL* **5**, 2000754 (2021).
- [325] B. Emiliano, *Longi achieves 25.47% efficiency for gallium-doped p-type heterojunction solar cell*, (2022), web report.
- [326] C. Hong, K.-M. Kang, M. Kim, Y. Wang, T. Kim, C. Lee, and H.-H. Park, *Structural, electrical, and optical properties of si-doped zno thin films prepared via supercycled atomic layer deposition*, *Materials Science and Engineering: B* **273**, 115401 (2021).

- [327] E. Bruhat, T. Desrues, D. Blanc-Pélessier, B. Martel, R. Cabal, and S. Dubois, *TCO contacts on poly-Si layers: High and low temperature approaches to maintain passivation and contact properties*, (2019).
- [328] E. Bruhat, T. Desrues, B. Grange, H. Lignier, D. Blanc-Pélessier, and S. Dubois, *TCO contacts for high efficiency c-Si solar cells: Influence of different annealing steps on the Si substrates and TCO layers properties*, *Energy Procedia* **124**, 829 (2017).
- [329] T. Leichtweiss, R. A. Henning, J. Koettgen, R. M. Schmidt, B. Holländer, M. Martin, M. Wuttig, and J. Janek, *Amorphous and highly nonstoichiometric titania (TiO_x) thin films close to metal-like conductivity*, *Journal of Materials Chemistry A* **2**, 6631 (2014).
- [330] T. Hitosugi, N. Yamada, S. Nakao, K. Hatabayashi, T. Shimada, and T. Hasegawa, *Structural study of TiO₂-based transparent conducting films*, *Journal of Vacuum Science & Technology A: Vacuum, Surfaces, and Films* **26**, 1027 (2008).
- [331] A. U. Ebong, *Double sided buried contact silicon solar cells*, Ph.D. thesis, University of New South Wales (1996).
- [332] W. Kern and E. Tracy, *Titanium dioxide antireflection coating for silicon solar cells by spray deposition*, *RCA Rev.; (United States)* **41** (1980).
- [333] Q. Tang, H. Shen, H. Yao, K. Gao, Y. Jiang, and Y. Liu, *Dopant-free random inverted nanopillar ultrathin c-Si solar cell via low work function metal modified ITO and TiO₂ electron transporting layer*, *Journal of Alloys and Compounds* **769**, 951 (2018).
- [334] E. Schiavo, C. Latouche, V. Barone, O. Crescenzi, A. B. Muñoz-García, and M. Pavone, *An ab initio study of Cu-based delafossites as an alternative to nickel oxide in photocathodes: effects of Mg-doping and surface electronic features*, *Physical Chemistry Chemical Physics* **20**, 14082 (2018).
- [335] K. H. Zhang, K. Xi, M. G. Blamire, and R. G. Egdell, *P-type transparent conducting oxides*, *J Phys Condens Matter* **28**, 383002 (2016).
- [336] F. Johnson, J. Pankow, G. Teeter, B. Benton, and S. A. Campbell, *High stability near-broken gap junction for multijunction photovoltaics*, *Journal of Vacuum Science & Technology A* **37**, 011201 (2019).
- [337] J. Li, X. Wang, S. Shi, X. Song, J. Lv, J. Cui, and Z. Sun, *Optical and wetting properties of CuAlO₂ films prepared by radio frequency magnetron sputtering*, *Journal of the American Ceramic Society* **95**, 431 (2012).
- [338] F. Igbari, M. Li, Y. Hu, Z.-K. Wang, and L.-S. Liao, *A room-temperature CuAlO₂ hole interfacial layer for efficient and stable planar perovskite solar cells*, *Journal of Materials Chemistry A* **4**, 1326 (2016).
- [339] I. Y.-Y. Bu, Y.-C. Lu, Y.-S. Fu, and C.-T. Hung, *Novel CuAlO₂/polyaniline hole transport layer for industrial production of perovskite solar cells*, *Optik* **210**, 164505 (2020).

- [340] M. C. Raval and C. S. Solanki, *Review of ni-cu based front side metallization for c-si solar cells*, Journal of Solar Energy **2013**, 20 (2013).
- [341] B. Im and S. Kim, *Nucleation and growth of Cu electrodeposited directly on W diffusion barrier in neutral electrolyte*, Electrochimica Acta **130**, 52 (2014).
- [342] D. Starosvetsky, N. Sezin, and Y. Ein-Eli, *Seedless copper electroplating on ta from a "single" electrolytic bath*, Electrochimica Acta **55**, 1656 (2010).
- [343] T. E. Hong, K.-Y. Mun, S.-K. Choi, J.-Y. Park, S.-H. Kim, T. Cheon, W. K. Kim, B.-Y. Lim, and S. Kim, *Atomic layer deposition of ru thin film using N₂/H₂ plasma as a reactant*, Thin Solid Films **520**, 6100 (2012).
- [344] B. S. An, Y. Kwon, J. S. Oh, C. Lee, S. Choi, H. Kim, M. Lee, S. Pae, and C. W. Yang, *Characteristics of an amorphous carbon layer as a diffusion barrier for an advanced copper interconnect*, ACS Appl Mater Interfaces **12**, 3104 (2020).
- [345] C. Byrne, B. Brennan, A. P. McCoy, J. Bogan, A. Brady, and G. Hughes, *In situ XPS chemical analysis of MnSiO₃ copper diffusion barrier layer formation and simultaneous fabrication of metal oxide semiconductor electrical test mos structures*, ACS Appl Mater Interfaces **8**, 2470 (2016).
- [346] B. S. An, Y. Kwon, J. S. Oh, M. Lee, S. Pae, and C. W. Yang, *Amorphous TaxMnyOz layer as a diffusion barrier for advanced copper interconnects*, Sci Rep **9**, 20132 (2019).
- [347] M. Hosseini, D. Ando, Y. Sutou, and J. Koike, *Co and CoTi_x for contact plug and barrier layer in integrated circuits*, Microelectronic Engineering **189**, 78 (2018).
- [348] C. Byrne, B. Brennan, R. Lundy, J. Bogan, A. Brady, Y. Y. Gomeniuk, S. Monaghan, P. K. Hurley, and G. Hughes, *Physical, chemical and electrical characterisation of the diffusion of copper in silicon dioxide and prevention via a CuAl alloy barrier layer system*, Materials Science in Semiconductor Processing **63**, 227 (2017).
- [349] J. Yu, J. Li, Y. Zhao, A. Lambertz, T. Chen, W. Duan, W. Liu, X. Yang, Y. Huang, and K. Ding, *Copper metallization of electrodes for silicon heterojunction solar cells: Process, reliability and challenges*, Solar Energy Materials and Solar Cells **224**, 110993 (2021).
- [350] J. Karas, L. Michaelson, K. Munoz, M. Jobayer Hossain, E. Schneller, K. O. Davis, S. Bowden, and A. Augusto, *Degradation of copper-plated silicon solar cells with damp heat stress*, Progress in Photovoltaics: Research and Applications **28**, 1175 (2020).
- [351] P. Loper, S. J. Moon, S. M. de Nicolas, B. Niesen, M. Ledinsky, S. Nicolay, J. Bailat, J. H. Yum, S. De Wolf, and C. Ballif, *Organic-inorganic halide perovskite/crystalline silicon four-terminal tandem solar cells*, Phys Chem Chem Phys **17**, 1619 (2015).

- [352] E. Köhnen, M. Jošt, A. B. Morales-Vilches, P. Tockhorn, A. Al-Ashouri, B. Macco, L. Kegelmann, L. Korte, B. Rech, R. Schlatmann, B. Stannowski, and S. Albrecht, *Highly efficient monolithic perovskite silicon tandem solar cells: analyzing the influence of current mismatch on device performance*, Sustainable Energy & Fuels **3**, 1995 (2019).
- [353] F. Hou, C. Han, O. Isabella, L. Yan, B. Shi, J. Chen, S. An, Z. Zhou, W. Huang, H. Ren, Q. Huang, G. Hou, X. Chen, Y. Li, Y. Ding, G. Wang, C. Wei, D. Zhang, M. Zeman, Y. Zhao, and X. Zhang, *Inverted pyramidally-textured pdms antireflective foils for perovskite/silicon tandem solar cells with flat top cell*, Nano Energy **56**, 234 (2019).
- [354] C. Messmer, L. Tutsch, S. Pingel, D. Erath, J. Schön, A. Fell, J. C. Goldschmidt, B. S. Goraya, F. Clement, A. Lorenz, *et al.*, *Optimized front tco and metal grid electrode for module-integrated perovskite-silicon tandem solar cells*, Progress in Photovoltaics: Research and Applications **x**, in press (2021).
- [355] A. J. Bett, K. M. Winkler, M. Bivour, L. Cojocar, O. S. Kabakli, P. S. Schulze, G. Siefer, L. Tutsch, M. Hermle, S. W. Glunz, *et al.*, *Semi-transparent perovskite solar cells with ito directly sputtered on spiro-ometad for tandem applications*, ACS applied materials & interfaces **11**, 45796 (2019).
- [356] Q. Xu, Y. Zhao, and X. Zhang, *Light management in monolithic perovskite/silicon tandem solar cells*, Solar RRL **4**, 1900206 (2019).
- [357] D. Bryant, P. Greenwood, J. Troughton, M. Wijdekop, M. Carnie, M. Davies, K. Wojciechowski, H. J. Snaith, T. Watson, and D. Worsley, *A transparent conductive adhesive laminate electrode for high-efficiency organic-inorganic lead halide perovskite solar cells*, Advanced Materials **26**, 7499 (2014).
- [358] R. L. Z. Hoyer, K. A. Bush, F. Oviedo, S. E. Sofia, M. Thway, X. Li, Z. Liu, J. Jean, J. P. Mailoa, A. Osherov, F. Lin, A. F. Palmstrom, V. Bulović, M. D. McGehee, I. M. Peters, and T. Buonassisi, *Developing a robust recombination contact to realize monolithic perovskite tandems with industrially common p-type silicon solar cells*, IEEE Journal of Photovoltaics **8**, 1023 (2018).
- [359] S. Albrecht, M. Saliba, J. P. Correa Baena, F. Lang, L. Kegelmann, M. Mews, L. Steier, A. Abate, J. Rappich, L. Korte, R. Schlatmann, M. K. Nazeeruddin, A. Hagfeldt, M. Grätzel, and B. Rech, *Monolithic perovskite/silicon-heterojunction tandem solar cells processed at low temperature*, Energy & Environmental Science **9**, 81 (2016).
- [360] F. Sahli, B. A. Kamino, J. Werner, M. Bräuninger, B. Paviet-Salomon, L. Barraud, R. Monnard, J. P. Seif, A. Tomasi, Q. Jeangros, A. Hessler-Wyser, S. De Wolf, M. Despeisse, S. Nicolay, B. Niesen, and C. Ballif, *Improved optics in monolithic perovskite/silicon tandem solar cells with a nanocrystalline silicon recombination junction*, Advanced Energy Materials **8**, 1701609 (2018).
- [361] L. Mazzarella, Y.-H. Lin, S. Kirner, A. B. Morales-Vilches, L. Korte, S. Albrecht, E. Crossland, B. Stannowski, C. Case, H. J. Snaith, and R. Schlatmann, *Infrared light management using a nanocrystalline silicon oxide interlayer in monolithic*

- perovskite/silicon heterojunction tandem solar cells with efficiency above 25%*, *Advanced Energy Materials* **9**, 1803241 (2019).
- [362] A. Puaud, A. S. Ozanne, L. L. Senaud, D. Muñoz, and C. Roux, *Microcrystalline silicon tunnel junction for monolithic tandem solar cells using silicon heterojunction technology*, *IEEE Journal of Photovoltaics*, 1 (2020).
- [363] C. Luderer, M. Penn, C. Reichel, F. Feldmann, J. C. Goldschmidt, S. Richter, A. Hahnel, V. Naumann, M. Bivour, and M. Hermle, *Controlling diffusion in poly-Si tunneling junctions for monolithic perovskite/silicon tandem solar cells*, *IEEE Journal of Photovoltaics*, 1 (2021).
- [364] D. Grant, K. Catchpole, K. Weber, and T. White, *Design guidelines for perovskite/silicon 2-terminal tandem solar cells: an optical study*, *Optics express* **24**, A1454 (2016).
- [365] M. De Bastiani, A. S. Subbiah, E. Aydin, F. H. Isikgor, T. G. Allen, and S. De Wolf, *Recombination junctions for efficient monolithic perovskite-based tandem solar cells: physical principles, properties, processing and prospects*, *Materials Horizons* **7**, 2791 (2020).
- [366] C. Blaga, G. Christmann, M. Boccard, C. Ballif, S. Nicolay, and B. Kamino, *Palliating the efficiency loss due to shunting in perovskite/silicon tandem solar cells through modifying the resistive properties of the recombination junction*, *Sustainable Energy & Fuels* **5**, 2036 (2021).
- [367] Z. Chen, L. Huang, Q. Zhang, Y. Xi, R. Li, W. Li, G. Xu, and H. Cheng, *Electronic structures and transport properties of n-type-doped indium oxides*, *The Journal of Physical Chemistry C* **119**, 4789 (2015).
- [368] A. Seidl, A. Görling, P. Vogl, J. A. Majewski, and M. Levy, *Generalized kohn-sham schemes and the band-gap problem*, *Physical Review B* **53**, 3764 (1996).
- [369] Z. C. Holman, A. Descoeur, L. Barraud, F. Z. Fernandez, J. P. Seif, S. D. Wolf, and C. Ballif, *Current losses at the front of silicon heterojunction solar cells*, *IEEE Journal of Photovoltaics* **2**, 7 (2012).
- [370] M. R. Vogt, *Development of Physical Models for the Simulation of Optical Properties of Solar Cell Modules*, Ph.D. thesis, University of Hanover (2016).
- [371] C. Han, G. Yang, P. Procel, D. O'Connor, Y. Zhao, A. Gopalakrishnan, X. Zhang, M. Zeman, L. Mazzarella, and O. Isabella, *Controllable simultaneous bifacial Cu-plating for high efficiency crystalline silicon solar cells*, (2021), solar RRL, DOI:10.1002/solr.202100810.
- [372] J. C. Goldschmidt, L. Wagner, R. Pietzcker, and L. Friedrich, *Technological learning for resource efficient terawatt scale photovoltaics*, *Energy & Environmental Science* **14**, 5147 (2021).

- [373] N. M. Haegel, H. Atwater, T. Barnes, C. Breyer, A. Burrell, Y.-M. Chiang, S. De Wolf, B. Dimmler, D. Feldman, S. Glunz, *et al.*, *Terawatt-scale photovoltaics: Transform global energy*, *Science* **364**, 836 (2019).
- [374] J. Yu, J. Bian, Y. Liu, F. Meng, and Z. Liu, *Patterning and formation of copper electroplated contact for bifacial silicon hetero-junction solar cell*, *Solar Energy* **146**, 44 (2017).
- [375] A. Lachowicz, J. Geissbühler, A. Faes, J. Champlaud, F. Debrot, E. Kobayashi, J. Horzel, C. Ballif, and M. Despeisse, *Copper plating process for bifacial hetero-junction solar cells*, in *33rd European Photovoltaic Solar Energy Conference and Exhibition*, Vol. 753 (2017).
- [376] T. Hatt, J. Bartsch, S. Kluska, and M. Glatthaar, *Establishing the “native oxide barrier layer for selective electroplated” metallization for bifacial silicon heterojunction solar cells*, in *AIP Conference Proceedings*, Vol. 2147 (2019) p. 040005.
- [377] D. Carroll, *Sundrive sets 26.07% efficiency record for heterojunction PV cell in mass production*, (2022), web report.
- [378] Z. Li, P.-C. Hsiao, W. Zhang, R. Chen, Y. Yao, P. Papet, and A. Lennon, *Patterning for plated heterojunction cells*, *Energy Procedia* **67**, 76 (2015).
- [379] B. Grübel, G. Cimiotti, C. Schmiga, V. Arya, B. Steinhauser, N. Bay, M. Passig, D. Brunner, M. Glatthaar, and S. Kluska, *Direct contact electroplating sequence without initial seed layer for bifacial TOPCon solar cell metallization*, *IEEE Journal of Photovoltaics* **11**, 584 (2021).
- [380] X. Wang, V. Allen, V. Vais, Y. Zhao, B. Tjahjono, Y. Yao, S. Wenham, and A. Lennon, *Laser-doped metal-plated bifacial silicon solar cells*, *Solar energy materials and solar cells* **131**, 37 (2014).
- [381] L. Tous, R. Russell, E. Cornagliotti, A. Uruena, P. Choulat, M. Haslinger, J. John, F. Duerinckx, and J. Szlufcik, *22.4% bifacial n-PERT cells with ni/ag co-plated contacts and Voc ~ 691 mV*, *Energy Procedia* **124**, 922 (2017).
- [382] A. Ebong, M. Taouk, and S. Wenham, *A low cost metallization scheme for double sided buried contact silicon solar cells*, *Solar energy materials and solar cells* **31**, 499 (1994).
- [383] A. U. Ebong, *Double sided buried contact silicon solar cells*, phd, the University of New South Wales (1994).
- [384] R. Russell, L. Tous, E. Carnagliotti, D. Hendrickx, F. Duerinckx, and J. Szlufcik, *Simultaneous fabrication of n & p contacts for bifacial cells by a novel co-plating process*, in *33rd European Photovoltaic Solar Energy Conference and Exhibition* (2017) pp. 212–217.

- [385] B. Grübel, G. Cimiotti, C. Schmiga, S. Schellinger, B. Steinhauser, A. A. Brand, M. Kamp, M. Sieber, D. Brunner, S. Fox, *et al.*, *Progress of plated metallization for industrial bifacial topcon silicon solar cells*, Progress in Photovoltaics: Research and Applications (2021).
- [386] J. Bartsch, M. Kamp, D. Hartleb, C. Wittich, A. Mondon, B. Steinhauser, F. Feldmann, A. Richter, J. Benick, M. Glatthaar, *et al.*, *21.8% efficient n-type solar cells with industrially feasible plated metallization*, Energy Procedia **55**, 400 (2014).
- [387] J. B. Heng, J. Fu, B. Kong, Y. Chae, W. Wang, Z. Xie, A. Reddy, K. Lam, C. Beitel, C. Liao, C. Erben, Z. Huang, and Z. Xu, *>23% high-efficiency tunnel oxide junction bifacial solar cell with electroplated Cu gridlines*, IEEE Journal of Photovoltaics **5**, 82 (2015).
- [388] T. Hatt, J. Bartsch, S. Schellinger, M. Jahn, L. Tutsch, A. Brand, N. Schröer, E. Schultze, and M. Glatthaar, *Copper electroplating for SHJ solar cells – adequate contact by electrolyte tuning*, (2021), 10th workshop on metallization and interconnection for crystalline silicon solar cells.
- [389] G. Beaucarne, L. Tous, J. Lossen, and G. Schubert, *Summary of the 9th workshop on metallization and interconnection for crystalline silicon solar cells*, in *AIP Conference Proceedings*, Vol. 2367 (AIP Publishing LLC, 2021) p. 020001.
- [390] N. Elgrishi, K. J. Rountree, B. D. McCarthy, E. S. Rountree, T. T. Eisenhart, and J. L. Dempsey, *A practical beginner's guide to cyclic voltammetry*, Journal of Chemical Education **95**, 197 (2017).
- [391] S. Y. Tan, V. Y. Chia, K. Höltt-Ottoä, and F. Anariba, *Teaching the nernst equation and faradaic current through the use of a designette: An opportunity to strengthen key electrochemical concepts and clarify misconceptions*, Journal of Chemical Education **97**, 2238 (2020).
- [392] K. Popov, B. Grgur, and S. S. Djokić, *Fundamental aspects of electrometallurgy* (Springer, 2007) pp. 101–142.
- [393] J. O. Dukovic, *Current distribution and shape change in electrodeposition of thin films for microelectronic fabrication*, Advances in Electrochemical Science and Engineering **3**, 117 (1993).
- [394] G. Beaucarne, G. Schubert, L. Tous, and J. Hoornstra, *Summary of the 8th workshop on metallization and interconnection for crystalline silicon solar cells*, (2019).
- [395] A. W. Blakers, *Shading losses of solar-cell metal grids*, Journal of Applied Physics **71**, 5237 (1992).
- [396] S. Kluska, B. Grübel, G. Cimiotti, C. Schmiga, H. Berg, A. Beinert, I. Kubitzka, P. Müller, and T. Voss, *Plated topcon solar cells & modules with reliable fracture stress and soldered module interconnection*, EPJ Photovoltaics **12**, 10 (2021).

- [397] T. Hatt, V. P. Mehta, J. Bartsch, S. Kluska, M. Jahn, D. Borchert, and M. Glatthaar, *Novel mask-less plating metallization route for bifacial silicon heterojunction solar cells*, in *AIP Conference Proceedings*, Vol. 1999 (AIP Publishing LLC, 2018) p. 040009.
- [398] J. Yu, L. Zhang, T. Chen, J. Bian, J. Shi, F. Meng, Y. Huang, and Z. Liu, *Dual-function light-trapping: Selective plating mask of $\text{SiO}_2/\text{SiN}_x$ stacks for silicon heterojunction solar cells*, *Solar RRL* **3**, 1800261 (2019).
- [399] G. Zangari, *Electrodeposition of alloys and compounds in the era of microelectronics and energy conversion technology*, *Coatings* **5**, 195 (2015).
- [400] K. D. Dobson, Z. Sun, U. Nsofor, U. Das, A. Sinha, M. Gupta, and S. S. Hegedus, *Direct laser patterned electroplated copper contacts for interdigitated back contact silicon solar cells*, in *IEEE 46th Photovoltaic Specialists Conference (PVSC)* (2019) pp. 1112–1119.
- [401] M. Del Pópolo and E. Leiva, *Embedded atom method study of Cu deposition on Ag (111)*, *Journal of Electroanalytical Chemistry* **440**, 271 (1997).
- [402] C. Sánchez and E. Leiva, *Underpotential versus overpotential deposition: a first-principles calculation*, *Journal of Electroanalytical Chemistry* **458**, 183 (1998).
- [403] M.-E. Wagner, R. Valenzuela, T. Vargas, M. Colet-Lagrille, and A. Allanore, *Copper electrodeposition kinetics measured by alternating current voltammetry and the role of ferrous species*, *Journal of The Electrochemical Society* **163**, D17 (2015).
- [404] A. Milchev and T. Zapryanova, *Nucleation and growth of copper under combined charge transfer and diffusion limitations—part ii*, *Electrochimica Acta* **51**, 4916 (2006).
- [405] A. García-Miranda Ferrari, C. W. Foster, P. J. Kelly, D. A. Brownson, and C. E. Banks, *Determination of the electrochemical area of screen-printed electrochemical sensing platforms*, *Biosensors* **8**, 53 (2018).
- [406] L. Sanz, J. Palma, E. García-Quismondo, and M. Anderson, *The effect of chloride ion complexation on reversibility and redox potential of the Cu (II)/Cu (I) couple for use in redox flow batteries*, *Journal of power sources* **224**, 278 (2013).
- [407] N. Okamoto, F. Wang, and T. Watanabe, *Adhesion of electrodeposited copper, nickel and silver films on copper, nickel and silver substrates*, *Materials transactions* **45**, 3330 (2004).
- [408] F. Goncalves de Cerqueira Lima, U. Mescheder, H. Leiste, and C. Müller, *Influence of current density on the adhesion of seedless electrodeposited copper layers on silicon*, *Surface and Coatings Technology* **375**, 554 (2019).
- [409] Y. H. Kwon, S. K. Kim, S.-W. Kim, and H. K. Cho, *Artificially controlled two-step electrodeposition of Cu and Cu/In metal precursors with improved surface roughness for solar applications*, *Journal of The Electrochemical Society* **161**, D447 (2014).

- [410] L. Guo, G. Oskam, A. Radisic, P. M. Hoffmann, and P. C. Searson, *Island growth in electrodeposition*, *Journal of Physics D: Applied Physics* **44**, 443001 (2011).
- [411] M. S. Al Farisi, S. Hertel, M. Wiemer, and T. Otto, *Aluminum patterned electroplating from $AlCl_3(-)[EMIm]Cl$ ionic liquid towards microsystems application*, *Micromachines (Basel)* **9**, 589 (2018).
- [412] O. Schultz-Wittmann, D. De Ceuster, A. Turner, D. Crafts, R. Ong, D. Suwito, L. Pavani, and B. Eggleston, *Fine line copper based metallization for high efficiency crystalline silicon solar cells*, in *27th European Photovoltaic Solar Energy Conference and Exhibition* (2012) pp. 596–9.
- [413] R. Woehl, M. Hörteis, and S. W. Glunz, *Analysis of the optical properties of screen-printed and aerosol-printed and plated fingers of silicon solar cells*, *Advances in OptoElectronics* **2008**, 1 (2008).
- [414] A. Khanna, K.-U. Ritzau, M. Kamp, A. Filipovic, C. Schmiga, M. Glatthaar, A. G. Aberle, and T. Mueller, *Screen-printed masking of transparent conductive oxide layers for copper plating of silicon heterojunction cells*, *Applied Surface Science* **349**, 880 (2015).
- [415] M. Hwang, S. Kim, K. Lee, I. Moon, J. Lim, J. Lee, D. Kyeong, W. Lee, and E. Cho, *Fine and high aspect ratio front electrode formation for improving efficiency of the multicrystalline silicon solar cells*, in *25th European Photovoltaic Solar Energy Conference* (2010) pp. 1792–1795.
- [416] A. Ebong and N. Chen, *Metallization of crystalline silicon solar cells: A review*, (2012).
- [417] Y.-H. Chang, W.-M. Su, P.-S. Huang, and L.-W. Cheng, *Improvement of the solar cell efficiency by fine line print on print technology*, in *IEEE 39th Photovoltaic Specialists Conference (PVSC)* (IEEE, 2013) pp. 2176–2178.
- [418] A. Aguilar, S. Y. Herasimenka, J. Karas, H. Jain, J. Lee, K. Munoz, L. Michaelson, T. Tyson, W. J. Dauksher, and S. Bowden, *Development of Cu plating for silicon heterojunction solar cells*, in *IEEE 43rd Photovoltaic Specialists Conference (PVSC)* (2016) pp. 1972–1975.

Acknowledgements

In 2017, I was told that, as a female, pursuing a PhD after working for 4 years could be quite challenging. It turns out to be true. Nevertheless, I want to add a second half sentence, "but if you decide to go, it will be a rewarding journey, regardless of gender, age". The past five years have been very fruitful for me, thanks to many great persons...

First and foremost I wish to thank Prof. Miro Zeman (Delft University of Technology, TUD), Prof. Xiaodan Zhang (Nankai University), and Prof. Olindo Isabella (TUD), for being my promoters, continuously giving me support, and nurturing me in an open and pleasant manner. I am deeply grateful to Prof. Olindo Isabella and Prof. Miro Zeman, for their supervision and support during this entire thesis, especially for accepting me to continuously work within the PVMD group, where facilities are well equipped, and a stable, pleasant, collaborative and stimulating atmosphere is ensured. My sincere thanks also go to Dr. Luana Mazzarella for being my daily supervisor. Their guidance, trust, enthusiasm, critical perspectives and perceptive insights help me become an independent researcher. Besides, I thank Prof. Kouchi Zhang (TUD) and Dr. Wenbo Wang (Shenzhen Institute of Wide-Bandgap Semiconductors, WinS; and Beijing Delft Institute of Intelligent Science and Technology, BDIIST) for their support during my PhD project.

I would like to thank the members of my jury, Prof. Ivan Gordon (imec/TUD), Prof. Erik Garnett (AMOLF), Dr. Martin Bivour (Fraunhofer ISE), Prof. Ferdinand Grozema (TUD), and Prof. Peter Palensky (TUD), who accepted our invitations and devoted time to read this thesis and provide insightful comments.

Special thanks go to Dr. Paul Procel, for sharing his expertise in past years, especially at the early stage of my PhD. I will never forget the pleasures when I worked out the correct approaches for transfer-length-method studies for the first time, when we came up with the series resistance decoupling method, when I started to treat myself as a "lazy" electron... I am also truly grateful to his continuous support during my research, and his kindness as a trustworthy friend in life.

I thank Dr. Guangtao Yang and Yifeng Zhao, for the productive discussions and practical cell precursor supplies during my thesis work. Aiming at increasing the device performances, our works are closely interconnected. The reliable teamwork makes the seemingly dull journey fruitful and joyful. I also would like to thank them and their partners (Madam Wei Cui and Miss Yiran Zhao) for their help in life since I arrived at Delft in August 2018. Besides, I am very grateful to Dr. Rudi Santbergen who came in my research and started providing support since 2020, when I needed dedicated simulations for bifacial solar cell design with reduced TCO use. He shared his expertise in GenPro4 modelling, which filled the optical simulation part in the thesis. Moreover, preliminary atomistic modelling of TCO materials was realized by Max van Duffelen in his master thesis work (under our co-supervision), which helps us to get deeper understandings of the TCO materials.

My sincere gratitude is due to the powerful technical supporting team. I Thank Martijn Tijssen, Stefaan Herman, Daragh O'Connor and Remko Koornneef for their professional support in the numerous depositions and characterizations. Also many thanks go to the Else Kooi Laboratory (EKL) supporting team, I thank Dr. Paolo Sberna, Robert Verhoeven, Dr. Hitham Amin Hassan, Tom Scholtes, Dr. Aleksandar Jovic, Dr. Johannes van Wingerden, Loek Steenweg, Vinod Narain, Mario Laros, Silvana Milosavljevic, and the other technicians from EKL. Besides, I specially thank Dr. Sten Vollebregt from the Department of Microelectronics, for building up the electrical connections on Cascade setup for my dedicated measurement purpose. I also thank Joost Romijn for his kind help in my electrical measurements, and Joost van Ginkel, Dong Hu, and Dr. Filiberto Ricciardella for the helpful discussions.

Life in PVMD group has been rich and fun. Ana Rita Bento Montes, who helped a lot in the XRD and DB-PAS measurements and analyses, is also a close and thoughtful friend; Dr. Carlos M. Ruiz Tobon, who works on ASA simulation, is a dear officemate who always gave me instant help when I needed. I still remember the afternoon when he walked to send the Covid self-test boxes to me with an injured leg; Andres Calcabrini, my another officemate, who made this Latex template, is a smart and capable colleague, and a warm friend with whom we shared living stories. Besides, his chocolate cake is super tasty! Dr. Gianluca Limodio, who shared his expertise in Cu-plating when I started this work, is always easy-going and friendly; Dr. Yilei Tian, who gave insights into various material characterizations, also helped in the thesis preparation; Thierry de Vrijer is a productive researcher, who brings fun to me with sharing the interesting moments of his kids. Besides, I feel lucky to have inspiring discussions with Dr. Nasim Rezaei, Alba Alcañiz Moya, Klaas Bakker, Dr. Malte Ruben Vogt, Dr. Gregory Pandraud, Dr. Robin Vismara, Liqi Cao, Dr. Zhirong Yao, Manvika Singh, Juan Camillo Ortiz Lizcano, Arturo Martinez Lopez, Yilong Zhou, Jin Yan, Dr. Zameer Ahmad, Dr. Mirco Muttillio, Dr. Yuan Gao, Dr. Fai Tong, Dr. Paula Perez Rodriguez, and Dr. Engin Özkol. Unforgettable things in PVMD also include the spontaneous dinners before pandemic era. We shared many happy moments together with Rita, Luana, Nasim, Paul, Robin, Andres, Carlos, Yifeng, Guangtao, Juan Camillo, also Daniele Sciré and Yudai Yamashita.

I thank Prof. Arthur Weeber especially for the exciting discussions on PV processing and sustainability over last year (in the ProfEd course development). Besides, my acknowledgements also go to Prof. Arno Smets, Dr. Rene van Swaaij, Prof. Ivan Gordon, Dr. Hesan Ziar, and Dr. Patrizio Manganiello. Thanks to the weekly academic meetings within the PVMD group, although we do not have frequent direct discussions, the way how you present the progresses, how you raise questions, and how you put intelligence to interpret experimental data and give suggestions to pinpoint the cause of observations, inspired me a lot in past years.

I thank my students: Max van Duffelen (Cum Laude), Anirudh Gopalakrishnan, and Jing Zhang. The famous physicist Richard Feynman said, "If you want to master something, teach it." I enjoyed the periods that I experienced with them, not only because I got my knowledge more solid via the teaching/supervising activities, but more importantly, because we keep growing together.

I would also like to thank some people although I have never met them in person. I thank Luca Spitaleri and Prof. Antonino Gulino at University of Catania (Italy), for

their help in XPS measurements and analysis; Jeroen Lybaert and Martijn Van der Plas in Metrohm (the Netherlands), for the technical support in the development of our Cu-plating technique; Dr. Stephan Eijt and Dr. Henk Schut from the Department of Radiation Science and Technology in Faculty of Applied Sciences (TUD), for sharing expertise in DB-PAS data analysis; Dr. Jouke R. Heringa in Department of Radiation Science & Technology (TUD) and Antoon Pieter Frehe in EEMCS faculty (TUD), for their support when we attempted to establish the density functional theory simulation model.

I am also grateful to the secretaries' support in administrative affairs. I thank Mark Vielvoije, Sharmila Rattansingh, Margot Witteveen-Visser, Ellen Schwencke-Karlas, Marieke Bijl, Carla Jager, Ilona van der Wenden, and Claudia de Kooter for their help in past years. Besides, I want to thank Bianca Knot, Bruno Morana and Vincent van Croonenburg in EKL team, Ming Lu and Xiaoping Wang in WinS (Shenzhen), and Fang Ding in BDIIST (Beijing). Apart from the secretaries, I also would like to send my gratitude to the late Prof. Bram Ferreira, for his help in the first two years of my PhD.

Now I would like to thank the team in Nankai University. I spent my first year of PhD there. I thank Prof. Xiaodan Zhang and Prof. Ying Zhao for their supervision, guidance, and support; Prof. Guofu Hou, Prof. Fuhai Zhang, Prof. Yi Zhang, Dr. Qian Huang, and Dr. Jian Ni for giving scientific lectures and promoting insightful discussions; Changchun Wei, Huizhi Ren, Yongtong Wang, and Dekun Zhang, for their technical support in the laboratory; Yixuan Huang and Yan Zeng for the administrative assistance; Dr. Lingling Yan, Dr. Fuhua Hou, Manjing Wang, Guanlin Chen, Shengsheng Zhao, Qianshang Ren, Shengzhe Li, Junfan Chen, Shichong An, Dr. Biao Shi, and Dr. Qixing Zhang, for the inspiring discussions and for their help in that uncommon year.

I thank Prof. Baojie Yan and Prof. Pingqi Gao in CNITECH (Ningbo) at the time, for recommending me to my PhD promoters in 2017. I also thank my previous colleagues Dr. Yuheng Zeng, Dr. Xi Yang, Mingdun Liao, and Dr. Jiang Sheng in CNITECH(Ningbo), and friends Dr. Jingjing Tang (CSU) and Dr. Hao Zhang (TUD), for their practical help at the initial stage of my PhD trajectory. During the PhD, I was lucky to meet Dr. Hongyu Tang, Yue Sun, Dr. Fengze Hou, Tianzhu Tang, Dongsheng Zhao, Jian Wang, who helped me at different moments. I specially thank Yinghu Yang and Zhi Zheng, who are the close elder friends, for always giving thoughtful advices and witnessing my growth in past years.

I would like to express my sincere thankfulness to some old friends and my family. I thank Jingna Zheng, Huanan Cheng, Jin Li, Zhimeng Li, and Shuangping Che. Their care and comfort is invaluable to me. Special thanks to my brothers and sisters-in-law for taking care of the whole family, and to my lovely nephew and nieces for always transmitting happiness, purity and vitality in the life. They make me feel at ease although I have not visited the family for 2.5 years (due to the Covid-19 pandemic), such that I could well concentrate on my research work in a foreign country. Finally, my deepest gratitude is to my beloved parents Peixiang Han and Haolan Zhang, for their continuous trust and unconditional support on me, which give me the calm, optimism and courage, to positively face any situations in life.

感念在心，感恩前行！

List of Publications

This chapter lists the publications during my PhD period.

Peer-reviewed journal articles

First-authored peer-reviewed journal articles

1. **C. Han**, R. Santbergen, M. van Duffelen, P. Procel, Y. Zhao, G. Yang, X. Zhang, M. Zeman, L. Mazzarella, and O. Isabella, *Towards bifacial SHJ solar cells with reduced TCO use*, Progress in Photovoltaics: Research and Applications, 1-13, (2022).[†]
2. **C. Han**, G. Yang, P. Procel, D. O'Connor, Y. Zhao, A. Gopalakrishnan, X. Zhang, M. Zeman, L. Mazzarella, and O. Isabella, *Controllable simultaneous bifacial Cu-plating for high efficiency crystalline silicon solar cells*, Solar RRL, 2100810, (2022).[‡]
3. **C. Han**, Y. Zhao, L. Mazzarella, R. Santbergen, A. Montes, P. Procel, G. Yang, X. Zhang, M. Zeman, and O. Isabella, *Room-temperature sputtered tungsten-doped indium oxide for improved current in silicon heterojunction solar cells*, Solar Energy Materials and Solar Cells, **227**, 111082, (2021).
4. **C. Han**, G. Yang, A. Montes, P. Procel, L. Mazzarella, Y. Zhao, S. Eijt, H. Schut, X. Zhang, M. Zeman, and O. Isabella, *Realizing the Potential of RF-Sputtered Hydrogenated Fluorine-Doped Indium Oxide as an Electrode Material for Ultrathin SiO_x/Poly-Si Passivating Contacts*, ACS Applied Energy Materials, **3**(9), 8606-8618, (2020).
5. **C. Han**, L. Mazzarella, Y. Zhao, G. Yang, P. Procel, M. Tijssen, A. Montes, L. Spitaleri, A. Gulino, X. Zhang, O. Isabella, and M. Zeman, *High-Mobility Hydrogenated Fluorine-Doped Indium Oxide Film for Passivating Contacts c-Si Solar Cells*, ACS Applied Materials & Interfaces, **11**(49), 45586-45595, (2019).
6. F. Hou, **C. Han**, O. Isabella, L. Yan, B. Shi, J. Chen, S. An, Z. Zhou, W. Huang, H. Ren, Q. Huang, G. Hou, X. Chen, Y. Li, Y. Ding, G. Wang, C. Wei, D. Zhang, M. Zeman, Y. Zhao, and X. Zhang, *Inverted pyramidally-textured PDMS antireflective foils for perovskite/silicon tandem solar cells with flat top cell*, Nano Energy, **56**, 234-240, (2019). (*co-first author*)

Co-authored peer-reviewed journal articles

1. G. Yang, **C. Han**, P. Procel, Y. Zhao, M. Singh, L. Mazzarella, M. Zeman, and O. Isabella, *Oxygen-alloyed poly-Si passivating contacts for high-thermal budget c-Si heterojunction solar cells*, Progress in Photovoltaics: research and applications, **30**, 141-151, (2022).

[†]This work is also reported by pv magazine via <https://www.pv-magazine.com/2022/03/16/bifacial-heterojunction-solar-cell-with-22-84-efficiency/>.

[‡]This work is also reported by pv magazine via <https://www.pv-magazine.com/2022/03/02/copper-plated-heterojunction-solar-cell-with-22-1-efficiency-0-99-bifaciality-factor/>.

2. L. Yan, **C. Han**, B. Shi, Y. Zhao, and X. Zhang, *Interconnecting layers of different crystalline silicon bottom cells in monolithic perovskite/silicon tandem solar cells*, Superlattices and Microstructures, **151**, 106811, (2021).
3. Y. Zhao, P. Procel, **C. Han**, L. Mazzarella, G. Yang, A. Weeber, M. Zeman, and O. Isabella, *Design and optimization of hole collectors based on nc-SiOx:H for high-efficiency silicon heterojunction solar cells*, Solar Energy Materials and Solar Cells, **219**, 110779, (2021).
4. Y. Zhao, L. Mazzarella, P. Procel, **C. Han**, F.D. Tichelaar, G. Yang, A. Weeber, M. Zeman, and O. Isabella, *Ultra-thin electron collectors based on nc-Si:H for high-efficiency silicon heterojunction solar cells*, Progress in Photovoltaics: research and applications, 1-14, (2021).
5. T. Vrijer, S. Miedema, T. Blackstone, D. Nijen, **C. Han**, and A. Smets, *Advanced current matching in multijunction photovoltaic devices using intermediate reflective layers based on metals, metal-oxides and silicon-oxides*, under review, 2021.
6. Y. Zhao, L. Mazzarella, P. Procel, **C. Han**, G. Yang, A. Weeber, M. Zeman, and O. Isabella, *Doped hydrogenated nanocrystalline silicon oxide layers for high-efficiency c-Si heterojunction solar cells*, Progress in Photovoltaics: research and applications, **28**, 425-435, (2020).
7. J. Chen, S. Zhao, L. Yan, H. Ren, **C. Han**, D. Zhang, C. Wei, G. Wang, G. Hou, and Y. Zhao, *Microstructure evolution and passivation quality of hydrogenated amorphous silicon oxide ($a\text{-SiO}_x\text{:H}$) on $\langle 100 \rangle$ - and $\langle 111 \rangle$ -orientated c-Si wafers*, Chinese Physics B, **29**(3), 038801, (2020).
8. P. Procel, H. Xu, A. Saez, C. Ruiz-Tobon, L. Mazzarella, Y. Zhao, **C. Han**, G. Yang, M. Zeman, and O. Isabella, *The role of heterointerfaces and subgap energy states on transport mechanisms in silicon heterojunction solar cells*, Progress in Photovoltaics: Research and Applications, **28**, 935-945, (2020).
9. L. Mazzarella, A. Alcañiz, P. Procel, E. Kawa, Y. Zhao, U. Tiringler, **C. Han**, G. Yang, P. Taheri, M. Zeman, and O. Isabella, *Strategy to mitigate the dipole interfacial states in (i)a-Si:H/MoOx passivating contacts solar cells*, Progress in Photovoltaics: Research and Applications, **29**, 391-400, (2020).
10. L. Yan, **C. Han**, B. Shi, Y. Zhao, and X.D. Zhang, *A review on the crystalline silicon bottom cell for monolithic perovskite/silicon tandem solar cells*, Materials Today Nano, **7**, 100045, (2019).
11. G. Chen, **C. Han**, L. Yan, Y. Li, Y. Zhao, and X. Zhang, *Simulation and application of external quantum efficiency of solar cells based on spectroscopy*, Journal of Semiconductors, **40**(12), 122701, (2019).

Patent applications

1. **C. Han**, M. Zeman, and O. Isabella, Fabrication method of one kind of transparent conductive oxide film, China, CN 2021103389670, Mar 2021.
2. **C. Han**, M. Zeman, and O. Isabella, Fabrication method and application of high-mobility transparent conductive oxide films, China, CN 2019111257591, Nov 2019.
3. X. Zhang, **C. Han**, F. Hou, C. Wei, H. Ren, Y. Li, Q. Huang, X. Chen, G. Hou, D. Zhang, S. Xu, G. Wang, Y. Ding, W. Xu, J. Luo, and Y. Zhao, Anti-reflective coating for tandem solar cells, China, CN 2018106926219, Jun 2018.

Conference contributions

First-authored conference contributions

1. Oral presentation @ SiliconPV 2022 (highlight talk): **Can Han**, Yifeng Zhao, Rudi Santbergen, Max van Duffelen, Paul Procel, Guangtao Yang, Miro Zeman, Luana Mazzarella, and Olindo Isabella, *Towards high efficiency SHJ solar cells with less TCO use*, Konstanz, Germany, 2022. [§]
2. Oral presentation @ MRS Fall Meeting and Exhibit 2021: **Can Han**, Rudi Santbergen, Max van Duffelen, Yifeng Zhao, Paul Procel, Guangtao Yang, Xiaodan Zhang, Miro Zeman, Luana Mazzarella, and Olindo Isabella, *Towards TCO-less bifacial Cu-plated SHJ solar cells*, online, 2021.
3. Oral presentation @ Metallisation and Interconnection Workshop 2021: **Can Han**, Guangtao Yang, Daragh O'Connor, Yifeng Zhao, Anirudh Gopalakrishnan, Liqi Cao, Paul Procel, Xiaodan Zhang, Miro Zeman, Luana Mazzarella, and Olindo Isabella, *Controllable simultaneous bifacial Cu-plating for high efficiency crystalline silicon solar cells*, Genk, Belgium, 2021.
4. Invited talk @ the 4th international workshop on SHJ solar cells: **Can Han**, Guangtao Yang, Daragh O'Connor, Yifeng Zhao, Anirudh Gopalakrishnan, Liqi Cao, Paul Procel, Xiaodan Zhang, Miro Zeman, Luana Mazzarella, and Olindo Isabella, *Controllable simultaneous bifacial Cu-plating for high efficiency crystalline silicon solar cells*, online, 2021.
5. Invited talk @ Guangdong Province International Photovoltaic Science and Technology Academic Conference: **Can Han**, Rudi Santbergen, Max van Duffelen, Yifeng Zhao, Paul Procel, Guangtao Yang, Xiaodan Zhang, Miro Zeman, Luana Mazzarella, and Olindo Isabella, *Bifacial SHJ solar cells with low indium, low silver consumptions*, online, 2021.
6. Oral presentation @ 38th European PV Solar Energy: **Can Han**, Yifeng Zhao, Luana Mazzarella, Rudi Santbergen, Ana Montes, Paul Procel, Guangtao Yang, Miro Zeman, and Olindo Isabella, *On the Interplay between Room-Temperature Sputtered IWO and Underlying Thin Film Silicon Stacks in Silicon Heterojunction Solar Cells*, online, 2021.
7. Poster presentation @ SiliconPV 2021: **Can Han**, Yifeng Zhao, Luana Mazzarella, Rudi Santbergen, Ana Montes, Paul Procel, Guangtao Yang, Miro Zeman, and Olindo Isabella, *Room-Temperature RF Magnetron Sputtered Tungsten-Doped Indium Oxide for c-Si Photovoltaic Devices*, online, 2021.
8. Oral presentation @ 29th Asian PVSC: **Can Han**, Yifeng Zhao, Paul Procel, Luana Mazzarella, Guangtao Yang, Xiaodan Zhang, Olindo Isabella, and Miro Zeman, *High-mobility Hydrogenated Fluorine-doped Indium Oxide Film for Passivating Contacts c-Si Solar Cells*, Xi'an, China, 2019.

Co-authored conference contributions

1. Submitted abstract @ WCPEC-8: Yifeng Zhao, Paul Procel, Luana Mazzarella, **Can Han**, Guangtao Yang, Liqi Cao, Zhirong Yao, Dong Zhang, Valerio Zardetto, Mehrdad Najafi, Adriana Creatore, René Janssen, Sjoerd Veenstra, Gianluca Coletti, Arthur Weeber, Miro Zeman, and Olindo Isabella, *Effects of (i)a-Si:H deposition temperature on high-efficiency silicon*

[§]This work has won "SiliconPV Award" (3rd place) in SiliconPV 2022.

- heterojunction solar cells for high-efficiency four-terminal tandem solar cells*, Milan, Italy, 2022.
2. Submitted abstract @ WCPEC-8: Liqi Cao, Luana Mazzarella, Paul Procel, Yifeng Zhao, Jin Yan, **Can Han**, Guangtao Yang, Zhirong Yao, Miro Zeman, and Olindo Isabella, *Interface treatment for high efficient dopant free MoOx silicon heterojunction solar cells*, Milan, Italy, 2022.
 3. Submitted abstract @ WCPEC-8: Paul Procel, Alba Alcañiz, Liqi Cao, Luana Mazzarella, Yifeng Zhao, **Can Han**, Guangtao Yang, Rudi Santbergen, Miro Zeman, and Olindo Isabella, *Insights into MoOx/i-aSi:H interface for high efficiency solar cells*, Milan, Italy, 2022.
 4. Poster presentation @ TandemPV2022: Luana Mazzarella, Yifeng Zhao, Manvika Singh, **Can Han**, Guangtao Yang, Dong Zhang, Valerio Zardetto, Mehrdad Najafi, Mariadriana Creatore, Rene Janssen, Sjoerd Veenstra, Gianluca Coletti, Arthur Weeber, Miro Zeman and Olindo Isabella, *Development of c-Si Bottom Cells Based on Carrier-Selective Passivating Layers for Demonstrating High-Efficiency 4T Perovskite/c-Si Solar Cells*, Freiburg, Germany (hybrid), 2022.
 5. Poster presentation @ SiliconPV 2022: Zhirong Yao, Guangtao Yang, **Can Han**, Paul Procel, Yifeng Zhao, Liqi Cao, Roald van der Kolk, Luana Mazzarella, Miro Zeman, and Olindo Isabella, *PECVD Plasma-SiOx/poly-SiOx Passivating Contacts*, Konstanz, Germany, 2022. [¶]
 6. Oral presentation @ SiliconPV 2022: Guangtao Yang, Remon Gram, Paul Procel, **Can Han**, Zhirong Yao, Luana Mazzarella, Yifeng Zhao, Miro Zeman, and Olindo Isabella, *Will pinholes for SiOx/poly-Si Passivating Contact Enhance the Passivation Quality?*, Konstanz, Germany, 2022.
 7. Oral presentation @ SiliconPV 2022: Paul Procel, Alba Alcañiz, Liqi Cao, Luana Mazzarella, Yifeng Zhao, **Can Han**, Guangtao Yang, Rudi Santbergen, Miro Zeman, and Olindo Isabella, *Insights into MoOx/i-aSi:H interface for high efficiency solar cells*, Konstanz, Germany, 2022.
 8. Oral presentation @ MRS Fall Meeting and Exhibit 2021: Liqi Cao, Yifeng Zhao, **Can Han**, Guangtao Yang, Miro Zeman, Luana Mazzarella, and Olindo Isabella, *The application of ultra-thin MoOx in silicon heterojunction solar cells*, online, 2021.
 9. Poster presentation @ 38th European PV Solar Energy: Guangtao Yang, Paul Procel, **Can Han**, Zakaria Asalieh, Yifeng Zhao, Luana Mazzarella, Miro Zeman, and Olindo Isabella, *Evaluation and Demonstration of Bifacial-IBC Solar Cells Featuring Poly-Si Alloy Passivating Contacts*, online, 2021.
 10. Oral presentation @ 38th European PV Solar Energy: Yifeng Zhao, Luana Mazzarella, Paul Procel, **Can Han**, Frans D. Tichelaar, Guangtao Yang, Arthur Weeber, Miro Zeman, and Olindo Isabella, *Ultra-thin electron collectors based on nc-Si:H for high-efficiency silicon heterojunction solar cells*, online, 2021.
 11. Poster presentation @ SiliconPV 2021: Yifeng Zhao, Luana Mazzarella, Paul Procel, **Can Han**, Guangtao Yang, Arthur Weeber, Miro Zeman, and Olindo Isabella, *Optimization strategies for electron collectors based on nc-SiOx:H for high-efficiency silicon heterojunction solar cells*, online, 2021.

[¶]This work has won "SiliconPV Poster Award" in SiliconPV 2022.

12. Oral presentation @ 3rd international workshop on SHJ solar cells: Paul Procel, Rik van Heerden, Alba Alcañiz, Carlos Ruiz, Luana Mazzarella, Yifeng Zhao, **Can Han**, Guangtao Yang, Miro Zeman, and Olindo Isabella, *Defect engineering and transport mechanisms for high efficiency single- and double-junction front/back contacted solar cells*, online, 2020.
13. Oral presentation @ 37th European PV Solar Energy Conference and Exhibition: Guangtao Yang, Saravana K. Senthil Kumar, Paul Procel, Yifeng Zhao, **Can Han**, Manvika Singh, Gianluca Limodio, Luana Mazzarella, Arthur Weeber, Miro Zeman, and Olindo Isabella, *Development of Poly-Si Passivating Contacts on Textured Si Surface for Bottom c-Si Solar Cell Application*, online, 2020.
14. Oral presentation @ 37th European PV Solar Energy Conference and Exhibition: Yifeng Zhao, Paul Procel, **Can Han**, Luana Mazzarella, Guangtao Yang, Arthur Weeber, Miro Zeman, and Olindo Isabella, *Design and optimization of hole collectors based on nc-SiO_x:H for high-efficiency silicon heterojunction solar cells*, online, 2020.
15. Oral presentation @ 37th European PV Solar Energy Conference and Exhibition: Luana Mazzarella, Alba Alcañiz, Paul Procel, Eliora Kawa, Yifeng Zhao, **Can Han**, Guangtao Yang, Miro Zeman, and Olindo Isabella, *Interface treatment to improve the (i)a-Si:H/MoO_x stack for passivating contact solar cells*, online, 2020.
16. Oral presentation @ 47th IEEE PVSC Virtual Meeting: Luana Mazzarella, Alba Alcañiz, Eliora Kawa, Paul Procel, Yifeng Zhao, **Can Han**, Guangtao Yang, Miro Zeman, and Olindo Isabella, *Strategy to mitigate the dipole interfacial states in (i)a-Si:H/MoO_x passivating contacts solar cells*, online, 2020.
17. Oral presentation @ SiliconPV 2020: Yifeng Zhao, Paul Procel, **Can Han**, Luana Mazzarella, Guangtao Yang, Arthur Weeber, Miro Zeman, and Olindo Isabella, *Design and optimization of positive-charge carrier collectors based on nc-SiO_x:H for high-efficiency silicon heterojunction solar cells*, online, 2020.
18. Poster presentation @ the Sunday Conference 2019: Yifeng Zhao, Paul Procel, Luana Mazzarella, **Can Han**, Guangtao Yang, Olindo Isabella, Arthur Weeber, and Miro Zeman, *Positive-charge carrier collections in low-temperature c-Si heterojunction solar cells*, Bussum, 2019.
19. Oral presentation @ 29th Asian PVSC: Luana Mazzarella, Antonios Mandrampazakis, **Can Han**, Paul Procel, Yifeng Zhao, Guangtao Yang, Arthur Weeber, Olindo Isabella, and Miro Zeman, *Development of thin Poly-SiC_x passivating contacts for c-Si solar cells*, Xi'an, China, 2019.
20. Oral presentation @ 2nd international workshop on SHJ solar cells: Paul Procel, Yifeng Zhao, **Can Han**, Luana Mazzarella, Guangtao Yang, Olindo Isabella, and Miro Zeman, *Understanding and optimizing carriers transport in low-thermal budget passivating contacts for high efficiency c-Si solar cells*, online, 2019.
21. Oral presentation @ SiliconPV 2019: Olindo Isabella, Guangtao Yang, Gianluca Limodio, Paul Procel, Luana Mazzarella, Yifeng Zhao, Manvika Singh, **Can Han**, Hao Ge, Peiqing Guo, Yvar de Groot, Gerwin van Kuler, Leo Franco, Antonios Mandrampazakis, Arthur Weeber, and Miro Zeman, *Fully-passivated, black, high-efficiency c-Si solar cells featuring passivating contacts*, Leuven, 2019.

22. Poster presentation @ SiliconPV 2019: Luana Mazzarella, Paul Procel, Yifeng Zhao, Gianluca Limodio, **Can Han**, Guangtao Yang, Arthur Weeber, Olindo Isabella, and Miro Zeman, *Insights into Charge Carrier Transport Mechanisms of SiO₂/Poly-SiCx/TCO Contact Structures for Silicon Solar Cells*, Leuven, 2019.
23. Poster presentation @ SiliconPV 2019: Yifeng Zhao, Luana Mazzarella, Paul Procel, Guangtao Yang, **Can Han**, Gianluca Limodio, Olindo Isabella, Arthur Weeber, and Miro Zeman, *Optoelectrical optimization of nc-SiOx:H layers for silicon heterojunction solar cells*, Leuven, 2019.
24. Poster presentation @ Fourier Transform Spectroscopy 2018: Fuhua Hou, **Can Han**, Lingling Yan, Biao Shi, Yi Ding, Yuelong Li, Ying Zhao, and Xiaodan Zhang, *Light Trapping Enhancement in Perovskite/Silicon Tandem Solar Cells via Optimized PDMS as an Antireflective Layer*, Singapore, 2018.

Curriculum Vitae

Can Han was born in Zhoukou (Henan Province), China on 16-01-1987. In 2010, she received the bachelor degree (Metallurgical Engineering) from Central South University (CSU), Changsha, China. She did the thesis entitled “Thermodynamic and dynamic analysis on metal selenide electrodeposition”. The supervisors were Prof. Yexiang Liu and Prof. Yanqing Lai. In 2013, she got her master degree (Nonferrous Metallurgy) from CSU, under the supervision of Prof. Yexiang Liu and Prof. Yanqing Lai. Her daily-supervisor was Fangyang Liu. The thesis was on “The electrochemical self-assembly of hierarchical dendritic Bi_2Se_3 nanostructures”. In 2013-2017, she worked in Ningbo Institute of Materials Technology & Engineering (CNITECH), CAS, Ningbo, China. The group head was Prof. Jichun Ye. In December 2015, she was entitled as an engineer. As an engineer, she was involved in an enterprise cooperative project on “Wet-chemical black silicon development on diamond-wire sawn polycrystalline silicon wafers”. Since 01-09-2017, she started to pursue a PhD degree in photovoltaic technologies. Her pomoters are Prof. Miro Zeman, Prof. Xiaodan Zhang, and Prof. Olindo Isabella. She also has a daily-supervisor during the thesis work, Dr. Luana Mazzearella. Can spent one year at Nankai University, Tianjin, China. From 01-09-2018, she moved to Delft University of Technology, Delft, the Netherlands. She was consecutively sponsored by Beijing Delft Institute of Intelligent Science and Technology (2017-2019), and Shenzhen Institute of Wide-Bandgap Semiconductors (2019-2021). After completing her PhD project, Can has been working as a researcher at TU Delft since September 2021.

Contact:

Email: 296295845@qq.com

LinkedIn: <https://www.linkedin.com/in/can-han-245a17231/>